

Winter 2007

# Position and orientation correction for pipe profiling robots

Andrew John Dettmer  
*Louisiana Tech University*

Follow this and additional works at: <https://digitalcommons.latech.edu/dissertations>



Part of the [Civil Engineering Commons](#)

---

## Recommended Citation

Dettmer, Andrew John, "" (2007). *Dissertation*. 547.  
<https://digitalcommons.latech.edu/dissertations/547>

This Dissertation is brought to you for free and open access by the Graduate School at Louisiana Tech Digital Commons. It has been accepted for inclusion in Doctoral Dissertations by an authorized administrator of Louisiana Tech Digital Commons. For more information, please contact [digitalcommons@latech.edu](mailto:digitalcommons@latech.edu).

**POSITION AND ORIENTATION CORRECTION  
FOR PIPE PROFILING ROBOTS**

by

**Andrew John Dettmer, M.B.A., B.S.**

**A Dissertation Presented in Partial Fulfillment  
of the Requirements for the Degree  
Doctor of Philosophy**

**COLLEGE OF ENGINEERING AND SCIENCE  
LOUISIANA TECH UNIVERSITY**

**March 2007**

UMI Number: 3264694

### INFORMATION TO USERS

The quality of this reproduction is dependent upon the quality of the copy submitted. Broken or indistinct print, colored or poor quality illustrations and photographs, print bleed-through, substandard margins, and improper alignment can adversely affect reproduction.

In the unlikely event that the author did not send a complete manuscript and there are missing pages, these will be noted. Also, if unauthorized copyright material had to be removed, a note will indicate the deletion.

**UMI**<sup>®</sup>

---

UMI Microform 3264694

Copyright 2007 by ProQuest Information and Learning Company.

All rights reserved. This microform edition is protected against unauthorized copying under Title 17, United States Code.

ProQuest Information and Learning Company  
300 North Zeeb Road  
P.O. Box 1346  
Ann Arbor, MI 48106-1346

LOUISIANA TECH UNIVERSITY

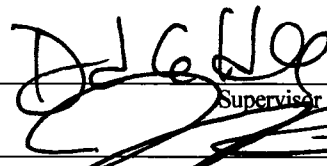
THE GRADUATE SCHOOL

01/23/2007 Date

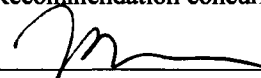
We hereby recommend that the dissertation prepared under our supervision  
by Andrew John Dettmer


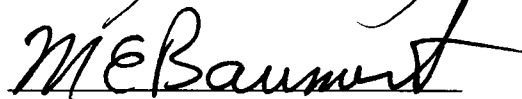
entitled Position and Orientation Correction for Pipe Profiling Robots

be accepted in partial fulfillment of the requirements for the Degree of  
Doctor of Philosophy

  
\_\_\_\_\_  
Supervisor of Dissertation Research  
\_\_\_\_\_  
Head of Department  
Engineering  
\_\_\_\_\_  
Department

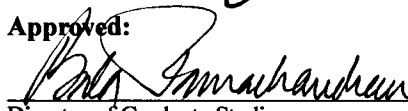
Recommendation concurred in:

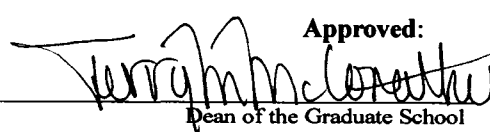
  
\_\_\_\_\_

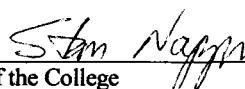
  
  
\_\_\_\_\_

Advisory Committee

  
\_\_\_\_\_

Approved:  
  
\_\_\_\_\_  
Director of Graduate Studies

Approved:  
  
\_\_\_\_\_  
Dean of the Graduate School

  
\_\_\_\_\_  
Dean of the College

## ABSTRACT

Sewer pipelines are prevalent, important, valuable, unnoticed, and often in a state of disrepair. Pipeline inspection is essential for effective management of wastewater systems and is now mandated for many municipalities complying with the Governmental Accounting Standards Board Statement 34 and EPA regulations. Pipe inspection robots are routinely used to inspect underground pipelines for cracks, deformations, leaks, blockages and other anomalies to prevent catastrophic failure and to ensure cost effective maintenance and renewal. Most existing pipe inspection robots only collect video footage of pipe condition. Pipe profiling technology has recently been introduced to allow for measurement of the internal coordinate geometry of pipelines. Accurate radial measurements permit the calculation of several important pipe parameters which aid in the determination of pipe condition and prediction of time to failure. Significant research work has been completed in North America, Europe, Asia and Australia aimed at improving the accuracy and automation of the pipe inspection process. However, standard calibration, verification, reporting and analysis practices must be developed for pipe profilers if coordinate profiling data is to be effectively included in the long term management of pipeline assets.

The objective of this research is to quantify the measurement error incurred by a pipe profiler's misalignment with the pipe axis, present a new methodology to correct the measurement error, develop a prototype profiler to verify the equations derived herein,

and to further the development of pipe profiler technology at the Trenchless Technology Center at Louisiana Tech University. Equations are derived for pipe ovality as a function of the robot's position and orientation with respect to a pipe to demonstrate the magnitude of the error which is introduced by a robot's misalignment with the pipe axis. A new technique is presented to estimate the position and orientation of a profiler using radial measurement devices at each of its ends. This technique is demonstrated by applying homogeneous coordinate transformations to simulated radial measurements based on mathematically generated data that would be obtained by incrementally rotating two parallel radial measuring devices in a perfectly cylindrical pipe. A prototype pipe profiling robot was developed to demonstrate the new position and orientation technique and to experimentally verify the measurement error caused by a robot's misalignment with the pipe axis. This work improves the accuracy and automation of pipe profiling technology and makes a case for the development of industry standard calibration, verification, reporting and analysis practices.

## APPROVAL FOR SCHOLARLY DISSEMINATION

The author grants to the Prescott Memorial Library of Louisiana Tech University the right to reproduce, by appropriate methods, upon request, any or all portions of this Dissertation. It is understood that "proper request" consists of the agreement, on the part of the requesting party, that said reproduction is for his personal use and that subsequent reproduction will not occur without written approval of the author of this Dissertation. Further, any portions of the Dissertation used in books, papers, and other works must be appropriately referenced to this Dissertation.

Finally, the author of this Dissertation reserves the right to publish freely, in the literature, at any time, any or all portions of this Dissertation.

Author *Arden J. Pettit*  
Date 2/20/2007

## TABLE OF CONTENTS

ABSTRACT.....	iii
LIST OF TABLES.....	xi
LIST OF FIGURES.....	xii
ACKNOWLEDGMENTS.....	xix
CHAPTER 1 INTRODUCTION.....	1
1.1 Background and Research Need.....	1
1.2 Objective and Scope.....	6
CHAPTER 2 LITERATURE REVIEW.....	9
2.1 The Need for Accurate Determination of Pipeline Condition.....	10
2.1.1 Effective Management of Pipeline Assets.....	13
2.1.2 Regulatory Directives for Pipe Inspection.....	15
2.1.3 The Influence of Pipe Ovality in CIPP Liner Design.....	18
2.2 Pipe Inspection Methods and Research.....	19
2.2.1 History of Sewer Pipe Inspection.....	19
2.2.2 Commercialized Pipe Profilers.....	22
2.2.3 Pipe Profiling Research.....	27
2.3 Mathematical Principles and Techniques.....	34
2.3.1 Centroid Location from Pipe Profiles.....	34
2.3.2 Homogeneous Coordinate Transformation Matrices.....	37
2.3.3 The atan2 Function.....	40



2.3.4 Quadrature Logic .....	41
2.3.5 Laser Peak Finding Algorithm.....	42
2.4 Conclusions.....	43
<b>CHAPTER 3 QUANTIFYING THE ERROR PRODUCED BY MISALIGNED PIPE PROFILERS .....</b>	<b>45</b>
3.1 Erroneous Ovality Produced by Pipe Profilers .....	46
3.1.1 Measurement-Plane Definition .....	47
3.1.2 Robot Orientation Geometry.....	49
3.1.3 Relating Ellipse Dimensions to Erroneous Ovality .....	53
3.2 Misaligned Pipe Profilers Cause Three-Dimensional Wireframe Distortion .....	56
3.2.1 Distance Measurement Error .....	56
3.2.2 Distance Measurement Error as a Function of Robot Orientation.....	58
3.3 Relating Bump Height and Robot Length to Erroneous Ovality.....	61
3.4 Erroneous Ovality Causes CIPP Liner Over-Design.....	64
3.5 Conclusions.....	66
<b>CHAPTER 4 A NEW STRATEGY FOR POSITION AND ORIENTATION ESTIMATION .....</b>	<b>68</b>
4.1 A New Technique for Position and Orientation Estimation.....	69
4.2 Simulated Elliptical-Shaped Radial Measurements.....	76
4.2.1 Coordinate System Definitions .....	76
4.2.2 Development of an Offset Elliptical Radial Descriptor .....	81
4.2.3 Relating the General Ellipse to the Primed Coordinate System .....	83
4.2.4 Development of the Rear Elliptical Offset.....	85
4.2.5 Development of the Front Elliptical Offset.....	88
4.2.6 Transformation from $x - y - z$ to $x' - y' - z'$ .....	93
4.2.7 Transformation from $x' - y' - z'$ to $x'' - y'' - z''$ .....	94

4.2.8 Transformation from $x''-y''-z''$ to $x'''-y'''-z'''$ .....	98
4.3 Conclusions.....	100
CHAPTER 5 PROTOTYPE HARDWARE DEVELOPMENT.....	103
5.1 Prototype Overview .....	103
5.1.1 Data Flow Onboard the Prototype Robot.....	106
5.1.2 USB Data Acquisition Card and LabVIEW™ Software .....	108
5.2 Original Pipe Repair/Inspection Robot.....	109
5.2.1 Purpose and Background of the Original Robot .....	109
5.2.2 Robot Speed and Direction Controls .....	111
5.3 Global Orientation and Axial Position Measuring Systems .....	115
5.3.1 Accelerometer and Custom Bracket .....	115
5.3.2 Axial Position Encoder .....	118
5.4 Optical Triangulation Measuring System .....	119
5.4.1 Stepper Motors and Supporting Hardware .....	120
5.4.2 Digital Cameras and Supporting Hardware .....	123
5.4.3 Lasers and Transistors for Brightness Control.....	126
5.4.4 Halogen Backlights and Solid State Relay .....	127
5.5 Tactile Measuring System .....	129
5.5.1 Tactile Probe Hardware .....	130
5.6 Conclusions.....	135
CHAPTER 6 EXPERIMENTAL SETUP AND AUTOMATED PROTOTYPE SOFTWARE DEVELOPMENT .....	136
6.1 Experimental Preparation and Procedures.....	136
6.1.1 Pipe Test Stand .....	137
6.1.2 Alignment of Robot's Reference Planes.....	138
6.1.3 Tactile Probe Calibration .....	139

6.1.4 Camera and Laser Calibration.....	141
6.1.5 Accelerometer Normalization and Calibration .....	147
6.1.6 Axial Distance Encoder and Robot Drive Motor Calibration.....	151
6.1.7 Experimental Procedure for Full-Length Pipe Scan .....	152
6.1.8 Acquiring Optical Scans for Incremental Bump-Height Measurements .....	153
6.1.9 Experimental Procedure for Caliper Measurements of Pipe Diameter .....	153
6.2 Software Design and Implementation for Automated Data Collection.....	154
6.2.1 Master Control VI.....	156
6.2.2 Initialize DAC VI and its Sub-VIs.....	161
6.2.3 Sense, Drive, Stop VI and its Sub-VIs.....	165
6.2.4 Collect One Ring VI and its Sub-VIs .....	174
6.2.5 Rewind VI and its Sub-VIs.....	188
6.3 Data Collection Preliminary Results.....	190
6.4 Conclusions.....	191
<b>CHAPTER 7 EXPERIMENTAL DATA POST-PROCESSING AND ERROR ANALYSIS.....</b>	<b>193</b>
7.1 Experimental Data Post-Processing.....	195
7.1.1 Format Raw Data for Transformations .....	195
7.1.2 Application of Transformation Equations.....	198
7.1.3 Ovality Calculations for the Full-Pipe Scan .....	202
7.1.4 Comparison of Measured Ovality to Predicted Ovality.....	203
7.2 Error and Uncertainty Analysis .....	204
7.2.1 Error in Camera-Laser Measurements .....	204
7.2.2 Error in Tactile Probe Measurements .....	206
7.2.3 Uncertainty Propagation Using Kline-McClintock.....	207
7.3 Conclusions.....	209

**CHAPTER 8 CONCLUSIONS, RESEARCH IMPLICATIONS AND  
RECOMMENDATIONS..... 211**

**8.1 Research Conclusions..... 211**

**8.2 Research Implications..... 213**

**8.3 Recommendations for Further Research..... 216**

**REFERENCES ..... 218**

## LIST OF TABLES

Table 2.1 Comparison between atan and atan2 Functions.....	41
Table 6.1 Sample Raw Data File from Data Collection Process .....	191
Table 7.1 Percent Difference Comparison between Types of Measuring Devices .....	202
Table 7.2 Regression Analysis on the Camera Calibration Data.....	205

## LIST OF FIGURES

Figure 1.1 Dilemma Faced When Reading the Output from a Roll/Pitch Sensor .....	3
Figure 1.2 Non-Rigid Link between Robot and Pipe Radial Measurement System .....	4
Figure 1.3 Dilemma Faced When Reading the Output from a Gyroscope .....	5
Figure 1.4 Meander by a Commercialized Pipe Profiler in an Inverted Horseshoe Sewer	6
Figure 2.1 ClearLine Profiler and Sample Image .....	22
Figure 2.2 Colmatec's 3-D Pipe Plot and Profiler in an Inverted Horseshoe Sewer .....	24
Figure 2.3 OMC's Laser Profiler and 3-D Plot.....	25
Figure 2.4 3-D Point Cloud from the RedZone Laser Profiler .....	26
Figure 2.5 PIRAT Laser Scan Showing Bands Caused by Unsteady Camera Movement	29
Figure 2.6 Quadrature Encoder Disc and Logic .....	42
Figure 2.7 Peak Detector VI Inputs and Outputs.....	43
Figure 3.1 Top View of Robot Meander and Resulting Erroneous Ovality .....	46
Figure 3.2 Side View of Robot on Bump or Offset Joint and the Resulting Erroneous Ovality.....	47
Figure 3.3 Cartesian Coordinate System Attached to the Pipe with the Centroid of the Elliptical Measurement Plane Intersecting the Origin.....	48
Figure 3.4 Normal Vector $\bar{n}$ Representing the Measurement-Plane.....	48
Figure 3.5 Projection of the $\bar{n}$ vector onto the Pipe's Vertical $x$ - $y$ Plane .....	49
Figure 3.6 Projection of the $\bar{n}$ vector onto the Pipe's Horizontal $x$ - $z$ Plane .....	50
Figure 3.7 Geometric Relationship Between $\theta_x$ , $\theta_h$ and $\theta_v$ .....	51
Figure 3.8 Relationship between the Ellipse Formed on the Measurement-Plane and the Undeformed Pipe .....	52

Figure 3.9 Relationship between $\bar{n}$ - $x$ Plane and Ellipse Major Axis $A$ .....	52
Figure 3.10 Ovality Plot as a Function of Meander and Pitch Angles .....	55
Figure 3.11 Distance Measurement Error Produced by Robot Meander.....	57
Figure 3.12 Distance Measurement Error Produced by Robot on Bump or Offset Joint .	57
Figure 3.13 Wireframe Distortion Caused by Robot Meander.....	58
Figure 3.14 Relationship between $\bar{n}$ - $x$ Plane and Distance Measurement Error .....	59
Figure 3.15 Distance Error Plot as a Function of Meander and Pitch Angles .....	60
Figure 3.16 Side View of Robot on Bump .....	61
Figure 3.17 3-D Ovality Plot as a Function of Robot Length and Bump Height .....	63
Figure 3.18 2-D Ovality Plot as a Function of Robot Length and Bump Height .....	63
Figure 3.19 Liner Thickness Over-Design Due to Erroneous Ovality .....	66
Figure 4.1 Location of Points $P$ and $Q$ on Robot's Reference Frame .....	71
Figure 4.2 Front and Rear Points of Measurements with Six Degrees of Freedom .....	72
Figure 4.3 Centroid Offsets Depicting Radial Points of Measurements.....	72
Figure 4.4 Centroid Offsets Defined Relative to the Points of Measurements.....	74
Figure 4.5 $\theta_h$ and $\theta_v$ Related to $\bar{z}$ , $\bar{y}$ , $\bar{w}$ , and $\bar{v}$ .....	75
Figure 4.6 3-D View of the Four Coordinate Systems Used for the Robot-Pipe-Gravity System.....	77
Figure 4.7 Location of Points $P$ and $Q$ on Robot's Reference Frame .....	77
Figure 4.8 2-D Rear View of Rear Measurement Plane Introducing $\bar{z}$ and $\bar{y}$ .....	79
Figure 4.9 2-D Rear View of Front Measurement Plane Introducing $\bar{w}$ and $\bar{v}$ .....	80
Figure 4.10 2-D Rear View of Front Measurement Plane Introducing $s$ and $t$ .....	81
Figure 4.11 Offset Ellipse with Origin at $(h, k)$ in Cartesian Coordinates.....	82
Figure 4.12 General Offset Ellipse with Origin at $(h, k)$ in Cylindrical Coordinates .....	83
Figure 4.13 $\theta_h$ and $\theta_v$ Related to $\bar{z}$ , $\bar{y}$ , $\bar{w}$ , and $\bar{v}$ .....	84

Figure 4.14 Rear View of the Rear Elliptical Profile.....	85
Figure 4.15 Rear Elliptical Profile on Primed Coordinate System Rotated by Angle $\phi$ ..	86
Figure 4.16 Rear Simulated Measurements on $y$ - $z$ Coordinate System.....	88
Figure 4.17 Rear View of the Front Measurement Plane .....	89
Figure 4.18 Front Elliptical Profile on Primed Coordinates Rotated by Angle $\phi$ .....	90
Figure 4.19 Front Simulated Measurements on $v$ - $w$ Coordinate System.....	92
Figure 4.20 3-D View of Front and Rear Simulated Data on $x$ - $y$ - $z$ Coord. Sys.....	92
Figure 4.21 3-D View of Front and Rear Simulated Data on $x'$ - $y'$ - $z'$ Coord. Sys. ....	94
Figure 4.22 3-D View of Front and Rear Simulated Data on $x''$ - $y''$ - $z''$ Coord. Sys.....	96
Figure 4.23 Side View of Front and Rear Simulated Data on $x''$ - $y''$ Coord. Sys.....	97
Figure 4.24 Top View of Front and Rear Simulated Data on $x''$ - $z''$ Coord. Sys.....	97
Figure 4.25 Definition of Pipe Pitch Angle with Respect To Gravity.....	98
Figure 4.26 3-D View of Simulated Data on $x'''$ - $y'''$ - $z'''$ Coord. Sys. ....	99
Figure 4.27 Side View of Front and Rear Simulated Data on $x'''$ - $y'''$ Coord. Sys. ....	100
Figure 4.28 Top View of Front and Rear Simulated Data on $x'''$ - $z'''$ Coord. Sys.....	100
Figure 5.1 Fully Assembled Prototype Pipe Profiling Robot .....	105
Figure 5.2 Optical and Tactile Measuring Systems on the Prototype Robot.....	105
Figure 5.3 Data Flow Chart for Electrical Components on Prototype Robot .....	107
Figure 5.4 USB-6009 DAQ Mounted on Prototype Robot.....	108
Figure 5.5 Joint and Crack Repair Attachment.....	110
Figure 5.6 Grinding Arm Attachment.....	110
Figure 5.7 Original Robot with Attachments Removed .....	111
Figure 5.8 Centent CN0105 DC Motor Controller Drawing .....	112
Figure 5.9 RAYEX LB2 DPDT Electromagnetic Relay .....	113
Figure 5.10 SP540-X Solid State Relay.....	114



Figure 5.11 Power Supply for Robot Drive Motor and 24VDC Relays.....	115
Figure 5.12 Tri-axis Accelerometer Pin-out and Coordinate System.....	116
Figure 5.13 Tri-axis Accelerometer Output Response vs. Orientation.....	117
Figure 5.14 Accelerometer Mounting Location and Custom Bracket.....	118
Figure 5.15 Spring Loaded Axial Distance Encoder Assembly .....	119
Figure 5.16 Stepper Motor and NEMA 23 Bracket on Front of Robot .....	120
Figure 5.17 Custom Stepper Motor Support Brackets.....	121
Figure 5.18 Stepper Motor Controller Kit L297/L298N .....	122
Figure 5.19 Circuit Diagram for L297/L298N Stepper Motor Control Kit.....	122
Figure 5.20 MicroPix C-1024 Digital Camera .....	123
Figure 5.21 IEEE 1394 Hub for Digital Cameras.....	124
Figure 5.22 Custom Shaft Couplers Attached to Front Stepper Motor .....	125
Figure 5.23 Wedge-Shaped Mounting Plate Attached to Front Stepper Motor .....	125
Figure 5.24 Camera Support Wing and Laser Mount Spacer.....	126
Figure 5.25 Front Camera-Laser Support Assembly .....	126
Figure 5.26 MOSFET Transistor for Laser Brightness Control .....	127
Figure 5.27 Halogen Light Mounted on Rear Tactile Probe Spacer.....	128
Figure 5.28 KG1010D Solid State Relay for Halogen Light Control.....	129
Figure 5.29 Tactile Probe Assembly Attached to the Optical Measuring System.....	130
Figure 5.30 Tactile Probe Off-the-Shelf Components.....	132
Figure 5.31 Custom Brackets for the Tactile Probe.....	133
Figure 5.32 L298 DC Motor Driver Kit.....	133
Figure 5.33 L298 Pin-out, Wiring Diagram, and Logic Table for Tactile DC Motor ....	134
Figure 6.1 Test Stand and Pipe Used for Experimental Data Collection.....	137
Figure 6.2 Faces Aligned on the Side of the Robot.....	138

Figure 6.3 Tactile Measuring Point References.....	139
Figure 6.4 Tactile Probe Encoder VI Block Diagram .....	141
Figure 6.5. Dimensions of Robot Highlighting Camera/Laser Measuring Points.....	142
Figure 6.6 Camera Calibration Jig (Top View) .....	143
Figure 6.7 Parse Image Set for Camera Calibration Front Panel.....	144
Figure 6.8 Parse Image Set for Camera Calibration Block Diagram.....	144
Figure 6.9 Peak Finder Looped VI Block Diagram .....	146
Figure 6.10 Camera Calibration Curves and Equations.....	147
Figure 6.11 Robot Pitch Angle Related to Accelerometer Output Voltages .....	150
Figure 6.12 Robot Roll Angle Related to Accelerometer Output Voltages .....	150
Figure 6.13 Caliper Measurements of Pipe Diameter.....	154
Figure 6.14 VI Hierarchy for Automated Data Collection Process .....	155
Figure 6.15 Master Control VI Block Diagram.....	157
Figure 6.16 Master Control VI Front Panel.....	159
Figure 6.17 Drive Parameters and File Output Tabs on Master Control VI Front Panel	160
Figure 6.18 Drive and Measurement Delay Tabs on Master Control VI Front Panel ....	160
Figure 6.19 Data to Gather Tab on Master Control VI Front Panel .....	161
Figure 6.20 Initialize DAC VI Block Diagram.....	162
Figure 6.21 Initialize DAC VI Block Diagram.....	163
Figure 6.22 Update AO VI Block Diagram.....	163
Figure 6.23 Boolean Cluster to Port VI Front Panel.....	164
Figure 6.24 Boolean Cluster to Port VI Block Diagram.....	164
Figure 6.25 Write Digital VI Block Diagram .....	165
Figure 6.26 Sense, Drive, Stop VI Block Diagram (1 of 2) .....	166
Figure 6.27 Sense, Drive, Stop VI Block Diagram (2 of 2) .....	167

Figure 6.28 Sense Distance Encoder VI Block Diagram .....	169
Figure 6.29 Single Quad Encoder VI Block Diagram .....	171
Figure 6.30 Pitch and Roll VI Block Diagram (1 of 2) .....	172
Figure 6.31 Pitch and Roll VI Block Diagram (2 of 2) .....	173
Figure 6.32 Collect One Ring VI Block Diagram (1 of 3) .....	175
Figure 6.33 Collect One Ring VI Block Diagram (2 of 3) .....	176
Figure 6.34 Collect One Ring VI Block Diagram (3 of 3) .....	177
Figure 6.35 Tactile Sense and Motion VI Block Diagram (1 of 2) .....	178
Figure 6.36 Tactile Sense and Motion VI Block Diagram (2 of 2) .....	179
Figure 6.37 Single Quad Encoder Linear VI Block Diagram .....	180
Figure 6.38 Add File Line VI Block Diagram.....	181
Figure 6.39 Acquire with Camera and Light VI Block Diagram in Backlight Mode ....	183
Figure 6.40 Acquire with Camera and Light VI Block Diagram in Laser Mode .....	184
Figure 6.41 Store Indexed Image VI Block Diagram.....	185
Figure 6.42 Name Image File VI Block Diagram.....	186
Figure 6.43 Capture and Save VI Block Diagram .....	186
Figure 6.44 Stepper ++ VI Block Diagram (1 of 3).....	187
Figure 6.45 Stepper ++ VI Block Diagram (2 of 3).....	188
Figure 6.46 Stepper ++ VI Block Diagram (3 of 3).....	188
Figure 6.47 Rewind VI Block Diagram.....	189
Figure 6.48 Simple Stepper ++ VI Block Diagram .....	189
Figure 6.49 Sample Images Taken During Data Collection.....	190
Figure 7.1 Format Raw Data for Transformations VI Block Diagram .....	197
Figure 7.2 3-D Plots of Laser Radial Measurements for the Full-Pipe Scan.....	200

Figure 7.3 3-D Plots of Tactile Probe Radial Measurements for the Full-Pipe Scan ..... 201

Figure 7.4 Theoretical and Experimental Ovality Due to a Robot on a Bump..... 204

Figure 7.5 Theoretical and Experimental Ovality Due to a Robot on a Bump with Error  
Bars ..... 209

## ACKNOWLEDGMENTS

First and foremost, I would like to thank my wife Melissa for her constant encouragement and affirmation. She faithfully supported me through my coursework, research and writing of this dissertation. I would like to express gratitude to my fellow Ph.D. candidate and good friend Michael Swanbom for his help in the design and construction of the robot prototype and for his programming assistance with LabVIEW™. I would also like to thank my co-advisor Dr. David Hall for his encouragement, career counseling and proofreading of several dissertation iterations. I would like to thank my co-advisor Dr. Hisham Hegab for his assistance in the establishment of my research problem statement and for his encouragement to publish a research poster and two conference papers.

I wish to express my gratitude to Dr. Ray Sterling for his enthusiasm and support for my research and for providing me with the opportunity to work as a sewer inspection field technician. I would also like to thank Dr. Mike Baumert for his late-night encouragement and support during the writing of this dissertation. I would like to thank Dr. Jun-Ing Ker for his advanced robotics class, particularly for his assistance with the optical triangulation techniques used in computer vision. I am also grateful for the assistance in the Louisiana Tech machine shop by Jimmy Cook and Murray Rasbury.

Finally, I would like to thank my parents and siblings for all of their love and support. Thanks mom and dad for your encouragement, guidance and prayers through this long, incredible journey!

## CHAPTER 1

### INTRODUCTION

Sewer systems are prevalent, important, valuable, unnoticed, and often in a state of disrepair. Many sewer systems are causing catastrophic damage and are in need of inspection and renovation. In-pipe assessment is necessary for observing and predicting pipeline failure and is useful in verifying whether proper installation methods were used for new flexible walled pipes. Pipe inspection is often government mandated and now required of many municipalities complying with new accounting standards.

Pipe inspection has been around for decades but is now becoming more sophisticated and the topic of much research. Several pipe inspection technologies have been developed including CCTV vehicles, infrared cameras, microwave sensors, nuclear sensors, ground penetrating radar, crack detectors, soil void detectors, electric probes, sonic hammers and pipe profilers. Pipe profilers utilize several emerging technologies and are outfitted with advanced sensors to measure pipe radii. Pipe profiling technologies include video calipers, optical triangulation, laser interferometry, sonar beacons, tactile probes, and various methods of autonomous navigation.

#### **1.1 Background and Research Need**

Pipe profiling provides accurate measurements of pipe radii which are used to create three-dimensional wireframe models of pipes, calculate ovality, flow parameters,

and, by scanning the same pipe several times, the rate of deformation. Three-dimensional models of pipes are helpful when the deformations in the pipe are associated with a color gradient. This allows one to visually see the areas of impending failure that need repair. Ovality measurements of the host-pipe are used in the design of thin walled pipe liners and in the determination of the quality of backfill around a new plastic pipe installation. A pipe's flow parameters are vital in the evaluation of a sewer system's capacity, and tracking the rate of pipe deformation can help determine the life left before the pipe fails.

Obtaining accurate pipe profiles is the subject of much research and the objective of several commercially available pipe profilers. One of the key aspects of obtaining accurate profiles is the relationship between the measuring device's coordinate system and the real world coordinate system. Whenever a two or three-dimensional graph is presented, it references a certain coordinate system. Most often, people are the most interested in what the pipe looks like relative to real world coordinates. Therefore, it is necessary for pipe profilers to include techniques to transform the radial measurements to the real world coordinate system. However, if a pipe profiler does not include an algorithm or sensors to determine its position and orientation relative to the pipe, then the profiler will report inaccurate measurements when attempting to report a graph or ovality relative to the real world coordinate system. Three coordinate system relationships are necessary to fully define a pipe's measurements to the real world coordinate system:

1. Fully define the measuring device's coordinate system (camera, laser, or sonar beacon) relative to the pipe profiling robot's coordinate system.
2. Fully define the pipe profiling robot's coordinate system relative to the pipe's coordinate system.



3. Fully define the pipe's coordinate system relative to the real world coordinate system.

Pipe profilers are often outfitted with inertial sensors such as accelerometers or gyroscopes to relate the robot's reference frame to the real world coordinates. These types of sensors only provide partial information for accurate pipe profiles. Gyroscopes and accelerometers are helpful in knowing where the robot is relative to the earth but are not helpful in knowing where the robot is in relation to the pipe. If an accelerometer or gyroscope senses a change in position or orientation, one has no way of knowing if the change is due to the orientation of the pipe relative to the earth or the orientation of the robot relative to the pipe. For example, if a tri-axis accelerometer, or some type of roll/pitch sensor, is the only sensor used to report the pitch angle of the robot, then one has no way of knowing if the robot has changed its angle or if the pipe has changed its angle. A diagram showing this dilemma is shown in Figure 1.1.

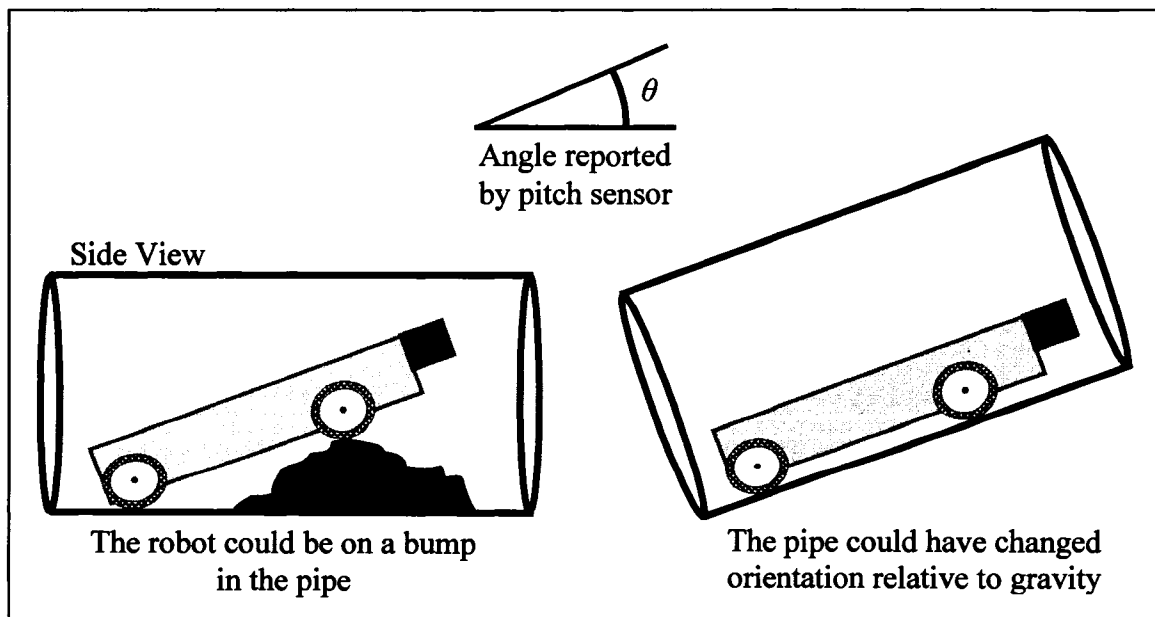


Figure 1.1 Dilemma Faced When Reading the Output from a Roll/Pitch Sensor

The problem would be magnified further if the link between the radial measuring system and the robot was not rigid. This would allow movement between the two systems, thereby misreporting the actual datum from which the pipe radius measurements were made. An example of a commercialized laser profiler exhibiting this potential problem is shown in Figure 1.2 [1].

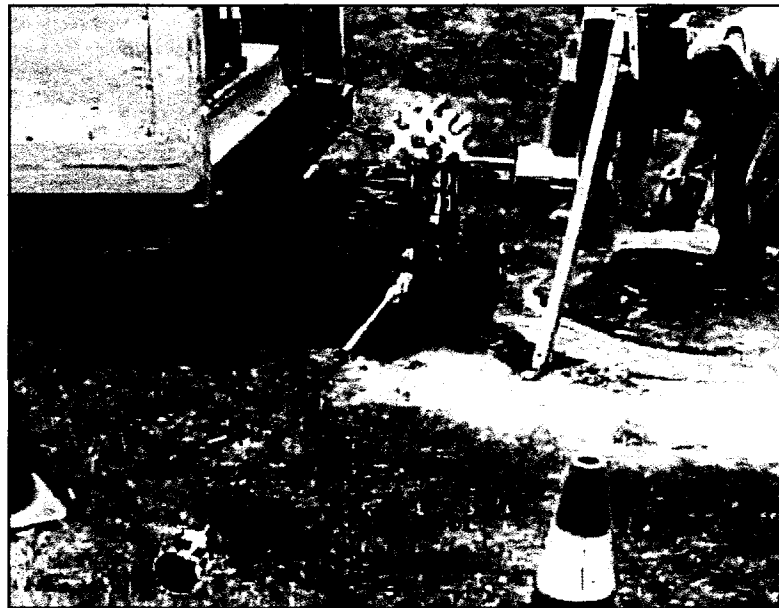


Figure 1.2 Non-Rigid Link between Robot and Pipe Radial Measurement System

A similar situation is encountered when one attempts to interpret the information from an inertial sensor such as a gyroscope. If the gyroscope reports a lateral movement, one has no way of knowing if the pipe's orientation has changed, or if the pipe profiling robot was meandering side-to-side within the pipe. A diagram demonstrating this dilemma and a picture showing a commercialized pipe profiler possibly experiencing this problem are shown in Figures 1.3 and 1.4.

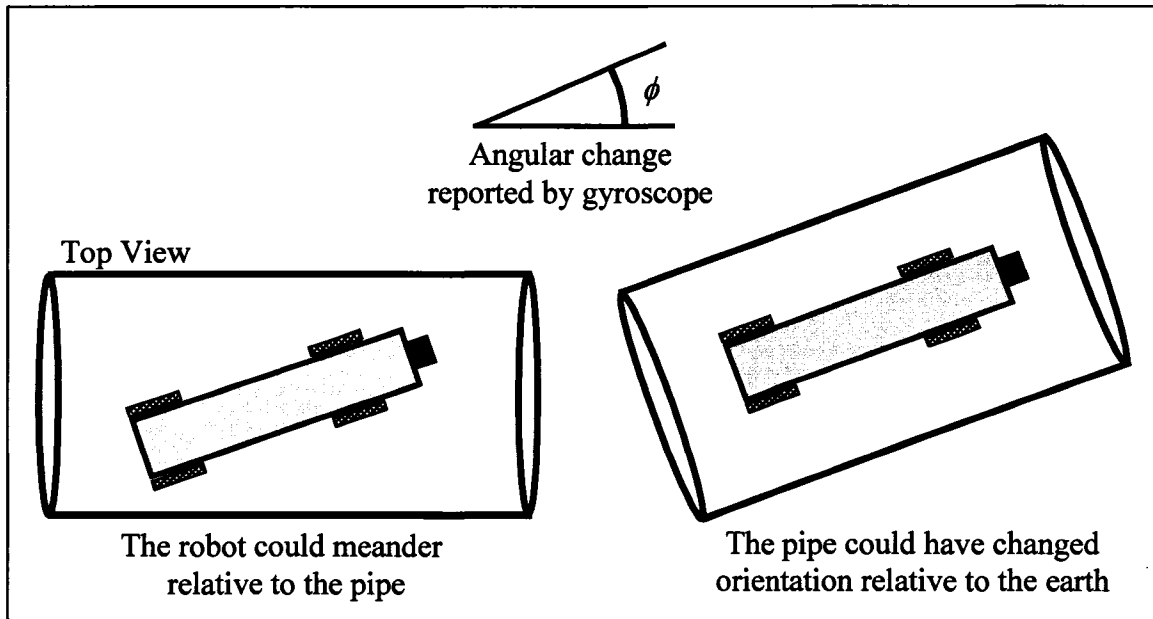


Figure 1.3 Dilemma Faced When Reading the Output from a Gyroscope

The commercial laser profiler shown in Figure 1.4 demonstrates how a robot can meander side-to-side while performing an inspection. As a result, the profiler is no longer parallel with the pipe axis, and it measures a cross-section non-perpendicular to the pipe [2].



Figure 1.4 Meander by a Commercialized Pipe Profiler in an Inverted Horseshoe Sewer

### **1.2 Objective and Scope**

The objective of this research is to quantify the measurement error incurred by a pipe profiler's misalignment with the pipe axis, present a new methodology to correct the measurement error, develop a prototype profiler to verify the equations derived herein, and to further the development of profiler technology. Equations are developed relating the position and orientation of a profiling robot in a cylindrical pipe to the measurement error causing erroneous ovality and three-dimensional wireframe distortion. A new mathematical model to estimate the position and orientation of the pipe profiler is then developed and presented. This model is verified experimentally via a prototype pipe profiling robot developed exclusively for this research. To fulfill this objective the research program was comprised of the following activities:

- Conduct a thorough literature review of the following topics: material demonstrating the need for the accurate determination of pipe condition, past and present pipe inspection research, and techniques used for position and orientation estimation of robots in pipelines.
- Derive equations for erroneous ovality and three-dimensional wireframe distortion as functions of a robot's misalignment with the pipe axis. This derivation was extended to include the effects on CIPP liner design and the length chosen for pipe profiling robots.
- Develop homogenous coordinate transformations to correct for the robot's misalignment with the pipe axis, and provide the steps necessary to implement the technique on existing pipe profilers.
- Apply the coordinate transformations to simulated radial measurements to demonstrate the new position and orientation technique, effectively correcting for the position, pitch and yaw of the robot with respect to the pipe and the pitch and roll of the robot with respect to gravity.
- Design and construct a prototype pipe profiling robot with two types of radial measuring devices at each end demonstrating the new position and orientation estimation technique.
- Develop customized software with National Instrument's LabVIEW™ to automate the data collection process with the prototype pipe profiling robot.
- Perform comparisons and error analyses of both types of radial data collected. The data set taken with the tactile probes was compared to the data set taken with the camera-laser systems. The uncertainty propagation of the radial measurements

through the ASTM ovality equation was also quantified using the Kline-McClintock method.

## CHAPTER 2

### LITERATURE REVIEW

A literature review was conducted to examine the need for pipe inspection, particularly the need for pipe profiling. Past and present methods used to perform pipe inspections are reviewed. The first portion of the literature review examines how sewers are prevalent, valuable, important, unnoticed, and often in a state of disrepair. Inspection of pipelines can identify leaks, cracks and blockages leading to better quantification of flow parameters, ovality and remaining life. Pipe inspection is often government mandated including some select laws requiring pipe profiling for new plastic pipe installations. The need for accurate and repeatable determination of pipe asset condition is demonstrated by examining new governmental accounting regulations for municipalities. The importance of accurate ovality measures in cured in place pipe (CIPP) liners is reviewed, and then specific pipe inspection methods and research are examined. Current practices using CCTV inspection robots along other advanced commercialized systems are evaluated, and then current pipe profiling research is reviewed with a special emphasis on robot position and orientation tracking.

The research presented in this dissertation is distinctive because it presents a novel technique to estimate the pipe profiler's position and orientation relative to the pipe. This provides a more comprehensive pipe inspection technique and correctly reports pipe parameters such as ovality and flow capacity as well as undistorted three-

dimensional pipe wireframes. This technique also provides a repeatable method of measurement as required by new governmental regulations. The author gives a thorough treatment of the misalignment error produced by pipe profilers, and the new position and orientation technique is demonstrated, first with simulated radial measurements, and then, with a prototype. Several researchers have identified the misalignment problem with pipe profilers and proposed methods to account for the error. However, none of the commercial systems currently on the market seem to account for the robot's misalignment with the pipe axis, nor have any researchers suggested the method proposed by this research.

### **2.1 The Need for Accurate Determination of Pipeline Condition**

It is estimated that there are 4.2 billion feet, or 800,000 miles, of sanitary sewer in the U.S. This does not include combined sewers which serve as both storm and sanitary sewer. Recent studies have shown the asset value of sanitary sewers in the U.S. is between \$1 to \$2 trillion, or 16% of the total public works infrastructure [3, 4]. These pipelines are responsible for carrying away wastewater from homes and businesses vital to the personal and economic health of the nation. Many of the wastewater collection systems in the United States were constructed in the early part of the 20<sup>th</sup> century [5] and have been functioning far longer than their intended design life with little or no repair [6].

Non-sewer water often flows into sanitary sewer systems causing a host of problems. This type of flow is called inflow and infiltration (I/I). Inflow is storm water that enters into sanitary sewers at points of direct connections. Sources of inflow include foundation drains, roof drains and basement sump pumps. Infiltration is groundwater that



enters sanitary sewers through cracks or leaks in the sanitary sewer pipes or manholes. Inflow and infiltration cause major problems because they often overburden the sanitary system, thus causing overflows. Sewer overflows put public health at risk and violate state and federal environmental regulations. Inflow and infiltration also cost water treatment facilities and consumers large amounts of money in added treatment costs. This “clean” water must be treated as sewage since it’s in the system.

Leaking sewers, however, weren’t always considered detrimental. Early sewer design purposefully incorporated leakage for the purposes of dilution. Dilution was the most economical, most efficient, and most commonly used method of treating sewer in the 1930s [7]. As cities grew, pollution of lakes, rivers and streams became a major problem. Compression joints were finally developed in the 1950s, and today, pressure tests are part of the regular inspection of sanitary sewers. Many cities however, are still left with the problem of identifying and eliminating the profuse I/I. In most situations, condition assessment, or sewer inspection, is the first step towards the elimination of I/I.

Nearly all wastewater pipelines are buried which makes condition inspection especially difficult and often causes the public to take sewers for granted. After all, pipelines are out of sight and out of mind until there is an overflow, a backup, or a road cave-in [7]. Catastrophic pipeline failure occurs often and is not well-received by the public. However, few are willing to pay the price necessary to inspect and repair the hundreds of thousands of miles of deteriorating pipelines lurking beneath the surface.

The American Society of Civil Engineering (ASCE) in its 2005 assessment of the U.S. infrastructure assigned the grade of “D-” for water and wastewater infrastructure. The U.S. has invested more than \$72 billion in the construction of publicly owned

sewage treatment works (POTWs), including pipelines, since the passage of the Clean Water Act in 1972. However, the physical condition of the nation's 16,000 wastewater treatment systems is poor due to a lack of investment in plant, equipment and other capital improvements over the years. The EPA estimates the U.S. must invest \$390 billion over the next 20 years to replace existing water and wastewater systems and build new ones to meet increasing demands [8].

In 2004 the EPA submitted a report to congress on the impacts and control of combined sewer overflows (CSOs) and sanitary sewer overflows (SSOs). A combined sewer system is defined as a wastewater collection system that is designed to collect and convey sanitary wastewater and storm water through a single pipe. During storm events the systems are designed to overflow when system capacity is exceeded, resulting in a CSO that discharges directly to surface waters. In the U.S. there are over 746 communities in 32 different states, largely concentrated in the Northeast and Great Lakes regions, which have combined sewer systems. The EPA estimates that about 850 billion gallons of untreated wastewater and storm water are released as CSOs each year [9].

A sanitary sewer system is defined as a wastewater collection system that is specifically designed to collect and convey only sanitary wastewater including domestic sewage from homes and industry. Storm water is therefore conveyed through an additional set of pipes. Sanitary sewers can overflow when collection system capacity is exceeded, often due to I/I caused by broken or collapsed pipes. The EPA estimates that there are between 23,000 and 75,000 SSOs each year in the U.S. resulting in the release of between 3 billion and 10 billion gallons of raw sewage.

Since CSOs and SSOs contain raw sewage, their occurrences create public health and environmental concerns. Raw sewage has been known to convey bacteria, viruses, protozoa, intestinal worms, molds, fungi, pathogens, solids, debris, and toxic pollutants to receiving waters. The diseases they may cause range in severity from mild gastroenteritis, causing stomach cramps and diarrhea, to life-threatening ailments such as cholera, dysentery, infections, hepatitis, and severe gastroenteritis. CSOs and SSOs have contributed to beach closures, shellfish bed closures, contamination of drinking water supplies, and other public health concerns. The 2004 EPA Report to Congress had many recommendations to reduce CSOs and SSOs, two of which are pertinent to this research.

1. Develop better technology to identify and measure pipe defects including cracks, leaks, blockages and flow capacity.
2. Develop better operations and management practices which involve inspection and classification of sewer conditions.

### **2.1.1 Effective Management of Pipeline Assets**

Since public infrastructure is the backbone of America's economy and society, asset management has become a hot topic among many researchers, utility managers, and consultants. Building, preserving and protecting the public's investment is one of the main functions of the more than 84,000 state and local governments in the U.S. Approximately \$150 billion are spent annually by governments to build, improve and maintain infrastructure assets. This equates to nearly 10% of their combined annual expenditures [10].

The U.S. EPA defines asset management for wastewater management utilities as "managing infrastructure capital assets to minimize the total cost of owning and operating

them while delivering the service levels customers desire. It is successfully practiced in urban centers, and large and small sewer collection systems to improve operational, environmental, and financial performance”[11].

As part of the EPA's Sustainable Infrastructure Initiative, the Office of Water Works, in collaboration with partner organizations including the American Water Works Association (AWWA), the Buried Asset Management Institute (BAMI), the Water Environment Federation (WEF), the National Science Foundation (NSF), the Water Environment Research Foundation (WERF), and Australia's Commonwealth Scientific and Industrial Research Organization (CSIRO), host and co-sponsor training sessions and facilitate discussions on best practices in Advanced Asset Management.

The EPA has stated that collaboration is necessary to address the nation's water and wastewater issues. The EPA recently signed a statement of intent to collaborate with the Association of Metropolitan Water Agencies (AMWA), the American Public Works Association (APWA), the AWWA, the National Association of Clean Water Agencies (NACWA), the National Association of Water Companies (NAWC), and the WEF to promote effective utility management [12]. Asset management programs with long-range planning, life-cycle costing, proactive operations and maintenance, and capital replacement plans based on cost-benefit analyses will be the most efficient method of meeting this challenge.

Pipeline infrastructure, in particular, is decaying at an accelerating rate and has commanded the attention of asset management researchers [13] and [14]. It is imperative for utility managers, even with stretched thin budgets, to prioritize assets for repair,

rehabilitation or replacement to make cost effective decisions. Condition assessment is usually the first step in the implementation of pipeline infrastructure asset management.

Other researchers are developing planning models for use by water authorities to help predict pipeline failure. A number of these planning models are already available including KANEW, NESSE and PARMS [15] [16]. These models require detailed analysis of pipe assets, and condition assessment is a key component of identifying high risk pipelines. The National Research Council Canada (NRCC) recently completed a project to assist the city of Montreal in determining the condition of its water and sewer systems. They identified pipe profiling as an inspection method that would allow the pipe deformation rates to be tracked. This technique would allow high resolution comparisons between pipe scans made at different times [17].

### **2.1.2 Regulatory Directives for Pipe Inspection**

In 1972 the U.S. Congress passed the Clean Water Act to “sustain economic growth, protect human and environmental health, and restore and maintain the chemical, physical, and biological integrity of the nation’s waters.” The Clean Water Act created the Office of Wastewater Management (OWM) at the EPA [18].

The OWM directs the National Pollutant Discharge Elimination System (NPDES) which regulates the discharge of pollutants into the waters of the U.S. Under the Clean Water Act NPDES permits are issued to industrial, municipal and other point source discharges by either the EPA or an authorized state. NPDES permits are developed to ensure that CSO and SSO discharges to receiving waters such as lakes, streams, rivers, wetlands, bays and oceans are regulated. NPDES permits establish specific discharge limits, monitoring and reporting requirements and may also require that dischargers

undertake measures to reduce or eliminate pollution to receiving waters. Violations of permit conditions are enforceable under the Clean Water Act [19].

To help utility operators and owners manage their wastewater systems, the EPA has recently developed CMOM programs [4] and [20]. CMOM stands for “Capacity, Management, Operations and Maintenance”. It is a flexible framework for municipalities to identify and incorporate widely accepted wastewater industry practices to better manage, operate and maintain collection systems; CMOM also provides the framework needed to investigate capacity constrained areas of the collection system, proactively prevent SSO events, and quickly respond to SSO events.

CMOM programs place a special focus on inspection and testing of sewers to track condition and identify potential problems. These often involve capacity evaluations and investigations to identify bottlenecks or constrictions that limit flow and prevent downstream treatment capacity from being fully utilized. These activities are often realized in a sewer system evolution survey (SSES) performed by a contractor including flow monitoring, smoke testing, manhole inspections, dyed water testing, and CCTV inspection [21].

#### **2.1.2.1 GASB 34 Municipal Accounting Standards**

Another recent development causing pipe inspection to be more prolific are new accounting standards for municipalities being adopted in the U.S. An organization called the Governmental Accounting Standards Board (GASB) was formed in 1984 as a nonprofit private organization to bring order to financial reporting by state and local governments in the wake of the largest loan default in American history, the Washington Public Power Supply System.

In June 1999, GASB published the 277 page, Statement 34. This work had been the result of over 20 years of research. Statement 34 was described by GASB Chairman Tom Allen as “the most significant change to occur in the history of governmental financial accounting. It represents a dramatic shift in the way state and local governments present financial information.” GASB 34 will help fill the needs of municipal credit analysts and cause governments to be more accountable in the management of public assets.

GASB 34 introduced a new system of governmental financial accountability where infrastructure assets will be accounted for in financial reports. Governments will now be able to emphasize the need for long term maintenance, not just short term focus to obtain votes. For many municipalities, implementation of GASB 34 will mark the first systematic accounting of public dollars spent for infrastructure assets. The false economy of deferred maintenance will be revealed as a long term mistake disguised as a short term benefit [22].

GASB 34 requires a condition assessment of sewer assets at least every three years using a consistent basis of measurement and scale that can be repeated. These strict specifications are causing many municipalities to review and make use of the advanced technologies being developed for sewer inspection, including pipe profiling technology.

#### **2.1.2.2 Laser Profiling Mandates**

Pipe profiling is not just useful for inspection of old pipes; it is useful for new installations as well. New large diameter, rigid and flexible pipe installations are required to be laser profiled for jobs let after July 1, 2006 in the State of Florida, U.S.A. The laser profilers attempt to accurately measure ovality which is an indicator of the quality of

backfill [23]. The State of Arizona does not mandate laser profiling but recommends it for new installations of corrugated high density polyethylene pipe [24].

WRc, formerly the Water Research Centre in the UK, is a research based group providing consultancy in the water, waste and environmental sectors. WRc assists the UK government in setting regulations regarding the “adoption” of sewers. In their recent book “Sewers for Adoption,” WRc specifies the requirement that all plastic pipes in the UK must be profiled before they are adopted for management by a “Sewerage Undertaker or Sewerage Agent Council” [25] and [26]. This is causing rapid growth in the use and development of laser and other profiling tools.

All of these recent regulations and recommendations to use pipe profiling equipment for pipe inspection have served to infuse the industry with increased funding and spawned new products and research. Several commercialized profilers have been developed and are described in Section 2.2.2. Researchers working specifically on the technologies associated with pipe profiles are detailed in Section 2.2.3.

### **2.1.3 The Influence of Pipe Ovality in CIPP Liner Design**

Cured in place pipe (CIPP) is the most frequently used rehabilitation method of sewer pipes in the U.S. [5]. The standard design utilizes ASTM F1216-03 [27], though several have noted its limitations [28] and [29]. The ASTM F1216-03 design equation for a partially deteriorated pipe is given by Eq. (2.1).

$$P_{cr} = \frac{2 \cdot K \cdot E_L}{1 - \nu^2} \cdot \frac{1}{(SDR - 1)^3} \cdot \frac{C}{N} \quad (2.1)$$

where



$$C = \text{ovality reduction factor} = \frac{\left[ \left( 1 - \frac{q}{100} \right) \right]^3}{\left[ \left( 1 + \frac{q}{100} \right) \right]^2}, \quad P_{cr} = \text{groundwater load, psi (MPa),}$$

K = enhancement factor of the soil and existing pipe adjacent to the new pipe (a minimum value of seven is recommended where there is full support of the existing pipe),  $\nu$  = Poisson's ration (0.3 average), SDR = standard dimension ratio of CIPP = D/t = outside liner diameter / average liner thickness,  $q$  = percent ovality of original pipe =  $\frac{[MaximumInsideDiameter - MeanInsideDiameter] \times 100}{MeanInsideDiameter}$ , N = factor of safety,  $E_L$  =

long-term modulus of elasticity for CIPP, psi (MPa). The CIPP liner design equation uses ovality  $q$  as one of its main influence factors. Thus, thicker liners must be installed in more ovalized host-pipes.

Pipe profiling has been identified as a technology which can provide accurate determination of pipe ovality for use in the design of CIPP and thermoplastic (PVC and HDPE) liners. This is especially important to help optimize design, minimize costs, and reduce risks. If pipe profilers misreport ovality, it can cause CIPP liners to be designed incorrectly thereby increasing cost or risk. The influence of pipe profiler inaccuracies on CIPP liner design is derived in Chapter 3.

## **2.2 Pipe Inspection Methods and Research**

### **2.2.1 History of Sewer Pipe Inspection**

The first U.S. manufacture of CCTV equipment was in 1946 by a major manufacturer of large power plant boiler systems [30]. The company discovered that

CCTV had been used aboard naval ships for remote viewing and began to manufacture remote CCTV viewing systems for boilers. In the 1950s, the RCA Corporation manufactured the Vidicon imaging tube which was put in a waterproof housing and used to inspect sewers. In 1964, a CCTV equipment business was spun off of the boiler manufacturer and began to market CCTV inspection rigs to municipalities and contractors inspecting sewers. Today, CCTV cameras use solid state imaging arrays which are robust and dependable. The cameras are typically mounted on a sled or tractor and driven or pulled through a sewer pipe. The cameras are usually controlled via a tether connected to a remote vehicle at the surface. CCTV has become the standard in SSES programs around the world and is the most commonly used technique for inspecting the internal condition of a sewer [9].

As popular and pervasive as CCTV is today, it has several limitations and shortcomings. Researchers have pointed out that many CCTV operators are often paid between \$1 to \$ 2.50 per foot of pipe that they inspect [9], [3] and [31]. This can obviously serve as a disincentive to take the time needed for an accurate condition assessment. Sinha points out that CCTV inspections are subject to lapses in operator concentration, inexperience, and inability of the image to reveal important defects [6]. Wirahadikusumah points out that CCTV is heavily dependant on the skill of the technician and the clarity of the TV picture [32]. These situations cause wide variances in inspection results and low consistency among condition reports.

Makar and Eiswirth discuss the difficulty in comparing two CCTV inspections of the same sewer at different times and lament the subjective nature of the results [17] and [33]. Xu notes that the human eye is not suitable for assessing pipe deformations of less

than 5% and that TV monitors can easily produce picture distortions of up to 10% [34]. Henry and Luxmoore report that the human eye can only decipher diameter changes of  $\pm 10\%$ , and this error actually increases to  $\pm 20\%$  when video distortion is involved [35]. Clearly, there is a need for more advanced technology to address these issues; thus, pipe inspection has been the topic of much research and development in the past two decades.

One of the first developments toward a more advanced sewer inspection platform was the Sewer Scanner & Evaluation Technology (SSET©) developed by the CORE Corporation. The SSET© utilizes a digital scanning camera to obtain a flat, “unfolded image” of the pipeline’s interior. The SSET© utilizes a fish-eye lens and a fiber optic gyroscope indicating pipe sag locations or siphons. The technology was evaluated by CEITEC, a center within the Civil Engineering Research Foundation (CERF), in collaboration with the Trenchless Technology Center (TTC), and is commercially available today [36] and [37]. The latest SSET© platforms include advanced software which allows for the automatic identification of cracks, lateral condition, root intrusion and joint condition [38]. Even with these advanced capabilities, the SSET© does not possess the ability to accurately measure pipe ovality or produce accurate three-dimensional wireframe models of pipelines.

Another recent development in advanced sewer inspection is the PANAROMO© by RapidView Inspection Systems and IBAK USA [39]. PANAROMO© is a high speed three-dimensional optical scanner intended to replace the pan-and-tilt CCTV systems. Similar to the SSET©, the PANAROMO© software can provide spherical and unfolded pipe views [40]. The PANAROMO© does not include any sensors to measure pipe ovality or produce accurate wireframe models of pipelines.

### **2.2.2 Commercialized Pipe Profilers**

Due to the growing need to obtain accurate measures of pipe ovality and precise pipe wireframe models, several companies worldwide are developing new ways to solve the problem. Today, a sophisticated sub-category of pipe inspection robots have been developed, and many are commercially available including pipe profilers from CleanFlow Systems Ltd. (New Zealand), Colmatec Inc. (Canada), Optical Metrology Centre (UK), and RedZone Robotics (US).

The ClearLine laser profiling tool was designed and manufactured by CleanFlow Systems Ltd. of New Zealand. This laser profiler uses a measuring technique known as optical triangulation involving the use of a CCTV camera and a ring laser module. The laser light is projected onto a conical mirror which reflects a narrow circular ring of light onto the pipe's interior surface. A digital camera is used to snap individual images where the laser light contacts the pipe. Since the position and orientation of the camera is known with respect to the laser module, the pipe coordinates relative to the camera-laser system can be calculated. The ClearLine profiler concept and a sample image taken by the ClearLine profiler is shown in Figure 2.1 [1].

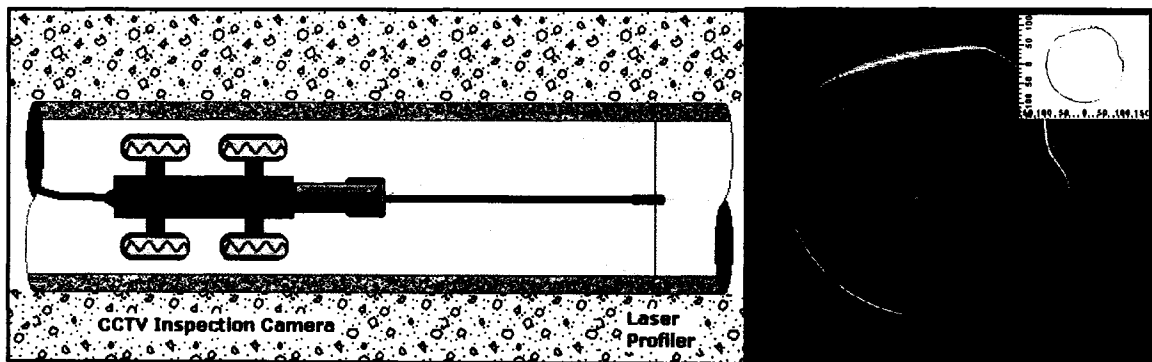


Figure 2.1 ClearLine Profiler and Sample Image

CleanFlow Systems manufactures laser profiling tools for small, medium, and large diameter pipes. They include customized software to generate two and three-dimensional plots of the pipe as well as calculate pipe ovality. The ClearLine profilers have been tested in several case studies in Germany, New Zealand, Australia, and the United States [1] and [41]. The ClearLine laser profiler was recently approved for use by WRc, a research group in the UK [29]. CleanFlow Systems are currently developing a sonar attachment to profile submerged pipes and are working with agencies in the UK on a plastic pipe deformation study [26].

Colmatec Inc. in Canada has also developed a commercialized laser profiler. Similar to the ClearLine profiler, the 4<sup>th</sup> generation Colmatec profiler uses optical triangulation to measure pipe radii relative to the camera-laser system and produces two and three dimensional plots of pipe deformation. One main difference in the Colmatec system is the use of a spinning laser head which produces a light ring by rapidly rotating a spot laser. Two case studies involving the profiling of plastic pipe in Canada were presented by Ouellet as well as the profiling of an inverted horseshoe sewer in Boston, MA, USA [2]. A picture of the Colmatec profiler and a three-dimensional plot from Colmatec's CoolVision software are shown in Figure 2.2 [2].



Figure 2.2 Colmatec's 3-D Pipe Plot and Profiler in an Inverted Horseshoe Sewer

A third company, Optical Metrology Centre of the UK, offers a pipe profiling tool dubbed the OMC Laser Profiler 15/50. This device incorporates a spinning head which houses a CCD sensor and a spot laser projected radially onto the pipe wall. The OMC profiler was tested by Thames Water Research and Technology and by Subterra, “experts in the area of sewer inspection” [42]. The OMC laser profiler has also been used to measure the ovality induced in steel pipes during the pipe-reeling process. Technip Offshore UK Ltd. participated in a case study with OMC in which they compared the ovality as measured by the OMC profiler to finite element predictions. This study produced results which seemed to validate the operation of the OMC laser profiler [43]. OMC also offers customized software which provides two and three-dimensional plots of the pipe measurements made as well as ovality reports. A picture of the OMC laser profiler and an associated three-dimensional plot is shown in Figure 2.3 [42].

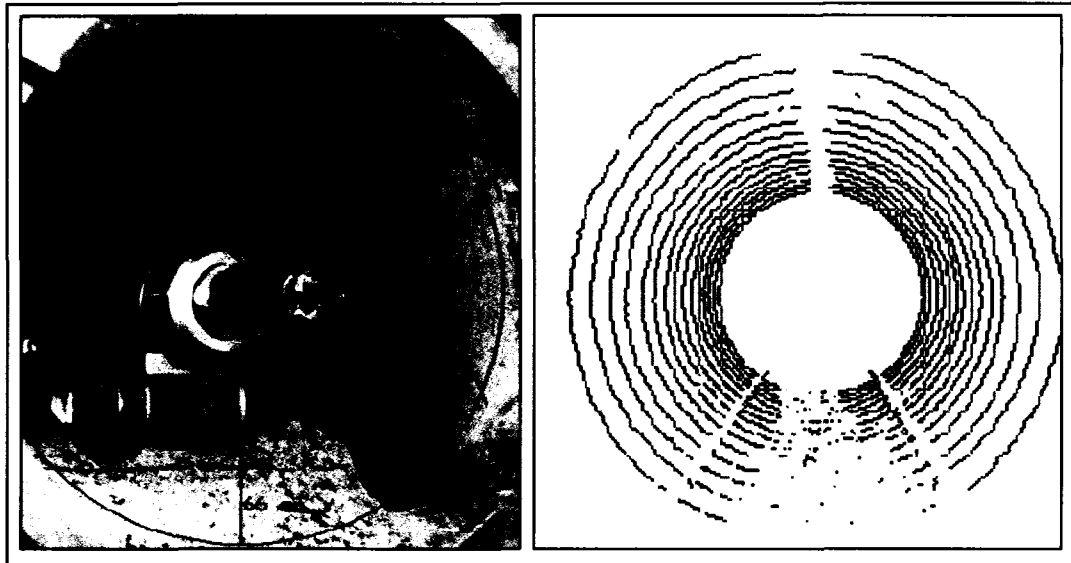


Figure 2.3 OMC's Laser Profiler and 3-D Plot

Much research has been performed by Clarke and Gooch at the Optical Metrology Centre to refine the measurement precision of the OMC Laser Profiler 15/50 [44] and [45]. Clarke has also performed research in the application of various tunnel profiling methods and concludes that laser profiling is one of the most robust and efficient systems [46].

RedZone Robotics of Pennsylvania, USA has also recently developed robotic profilers for use in pipelines. The City of Fort Worth, Texas, USA, recently participated in a pilot project with RedZone Robotics to test their new profiler with great success showing corrosion and pipe deformations in large diameter sewers [47]. The RedZone system uses laser profiling above the water line and sonar profiling below the water line. Their laser profiling tool utilizes laser interferometry which calculates the distance from the sensor to areas of interest in the pipe [48]. This measurement method enables the profiler to create a three-dimensional point cloud on the interior surface of the pipe

allowing for shape extrapolation. A picture of a three-dimensional point cloud from the RedZone profiler is shown in Figure 2.4 [48].

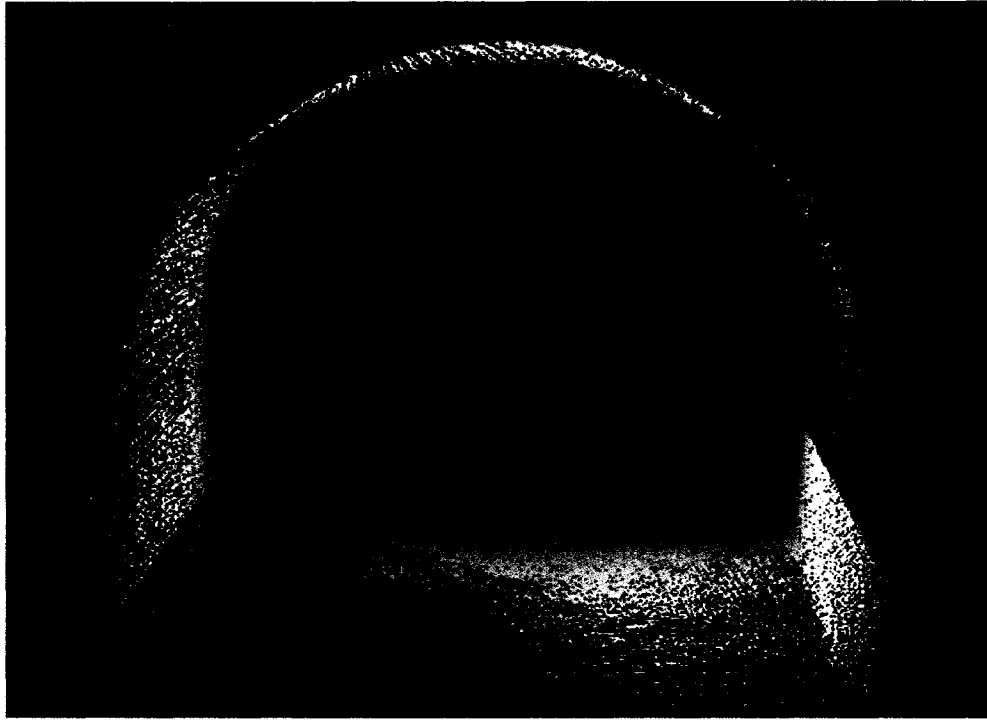


Figure 2.4 3-D Point Cloud from the RedZone Laser Profiler

So far in practice, the ClearLine profiler by CleanFlow Systems does not appear to have incorporated any sensors capable of relating the robot's coordinate system to the world's coordinate system, while using the ring laser to make radial measurements perpendicular to the camera-laser system. Also, the system deployed seems to have no way to guarantee that the camera laser system remains perpendicular to the pipe. Apparently, pitch and roll sensors have been discussed for use in their profilers to identify and throw out "bad" measurements. However, as stated in Section 1.1, pitch and roll sensors only provide partial information when attempting to relate all of the



coordinate systems necessary to produce accurate measures of ovality and three-dimensional pipe plots.

The OMC laser profiler seems to take the same approach in that they have pitch and roll sensors on board the robot [43], but seem to have no method to account for the misalignment of the profiler with the pipe axis. Gooch, one of the researchers working on an early version of the OMC profiler, mentions the need for estimating the position and orientation of the robot with respect to the pipe [45]. Gooch proposes using a four camera system with reflective targets in strategic locations but has not reported on the implementation of such system. Colmatec's laser profiler boasts of a "full telemetry system which records all of the data necessary for the three-dimensional model" [2]. However, they do not detail how this is performed, and based on pictures of the device and several case studies [2], it is suspected the Colmatec profiler cannot correct for its misalignment with the pipe axis.

The RedZone profiler utilizes an inertial measurement unit (IMU) during laser and sonar profiling, but these types of sensors only relate the robot's coordinate system to the world's coordinate system [48]. It is possible that the point cloud measurements taken by the RedZone profiler could be used to establish its position and orientation within the pipe. A method to identify a pipe profiler's orientation with an array of laser points was presented by Tsubouchi, but due to the proprietary nature of RedZone's system, it is unknown if they utilize this technique [49].

### **2.2.3 Pipe Profiling Research**

One of the concerns noted in the survey of pipe profiling literature is the issue of relating coordinate systems to one another to produce definitive real world coordinates

instead of a set of measurements simply related to the robot's coordinate system. Many pipe profiling robots are outfitted with inertial sensors capable of relating the robot's coordinate systems to gravity (accelerometers or roll sensors) or identify a change in direction (gyroscopes). However, one has no way of knowing whether the change in position or orientation has to do with a change in the pipe's coordinate system or a change in the robot's coordinate system. Several researchers have identified this problem and have presented various ways to address it; whereas, some have chosen to ignore it all together.

The PIRAT (Pipe Inspection Real Time Assessment Technique) project was begun in Australia in 1993 [50] and [31]. It was a 3 year, \$3 million (USD) project developed by CSIRO and Melbourne Water to automatically and quantitatively assess sewer pipes. PIRAT was designed with a rotating prism reflecting a laser spot to make radial measurements above the water line and a sonar transducer for making radial measurements underwater. PIRAT was originally designed to incorporate sensor based motion correction to keep the profiler parallel with the pipe axis. However, due to budget and schedule constraints the motion correction system was not implemented. Kirkham notes the shaky camera movement during sewer inspections, the need to keep the camera steady, and close as possible to the pipe's centerline. Kirkham describes "bands caused by scanner movement" relative to the pipe. The lighter color in the bands is an indication that the laser scanner periodically moved closer to the pipe wall during inspections. These bands are displayed in the sample image from a PIRAT laser scan shown in Figure 2.5 [51].

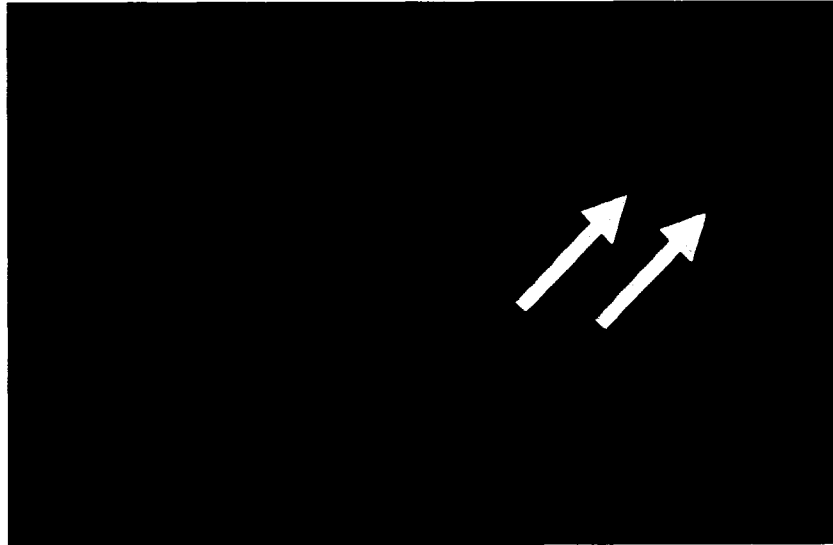


Figure 2.5 PIRAT Laser Scan Showing Bands Caused by Unsteady Camera Movement

Most laser profiling research has used the optical triangulation method for measuring pipe radii. Hibino measured large tunnels with a point laser reflecting off of a rotating mirror [52]. This profiler was adapted from a system designed to inspect road surfaces and was modified to measure tunnels. Hibino points out that it is important to keep the laser scanner aligned with the tunnel's axis to get accurate results. His solution was to mechanically adjust the laser with an axis control system to keep the laser perpendicular to the pipe wall. The yaw and pitch angles were controlled with gyroscopes and the vertical and horizontal planes were aligned using ultrasonic distance sensors. This system seemed to function well in a large diameter tunnel but seemed impractical for smaller sewer pipes.

To extract pipe joint information from conventional CCTV video tape, Pan and Xu take advantage of the semi-predictable sewer environment [53], [34]. Pan uses a Hough-based circle detection algorithm to track pipe joint geometry from several CCTV images. Pan also notes the misalignment error which is common between the CCTV

robot platform and the pipe's axis. He says the misalignment can vary up to  $20^\circ$ , thereby reinforcing the need for a position and orientation tracking system for pipe profilers.

Henry developed a pipe profiling adapter for CCTV cameras that utilized halogen bulb light ring projection and optical triangulation [35]. Henry analyzed the light ring shape on the interior of the pipe using a radial descriptor from centroid analysis which allowed any pipe deformation to be represented in terms of a Fourier series [35]. During pipe scans, Henry notes the misalignment of the profiler with the pipe axis but says the angular deviation is only about  $1^\circ$  unless a significant obstacle is encountered. He chooses to ignore the "small" deviations, but notes it would be possible to include image center analysis to detect misalignment with the pipe axis. Hartrumpf, on the other hand, assumes the pipe profiling robot is "guided centrally through the cylindrical sewer pipe" providing perpendicular pipe radial measurements [54].

Cooper, Pridmore, and Taylor also identify the misalignment problem which is evident by translations and rotations of a CCTV sled drug by a chain through the sewer [55], [56], and [57]. They say this is caused by the pull point location on the sled not being coincident with its center of gravity. They also note the travel of the sled up the sides of the pipe causing the sled to roll and often slide back down. They note the importance of quantifying these misalignments with the pipe axis to have an accurate three-dimensional picture of the pipe. Cooper, Pridmore, and Taylor then present a novel method to establish the relative orientations of the camera and pipe axes. They describe a "vanishing point" in the CCTV images caused by brick mortar lines running axially along the surface of brick sewers. This method, however, requires longitudinal lines such as those in a brick sewer and is not practical for other types of pipe.

Kampfer describes a laser distance sensor incorporated into the head of a pan-and-tilt CCTV inspection system [58]. The system is purportedly used to determine the deformation in plastic pipelines and build three-dimensional wireframe models. He notes that the distance measured with the system is in need of coordinate transforms to describe the spatial coordinates, but he does not describe any system on the robot providing transformation angles or distances other than the camera's pan-and-tilt angles. It is assumed this robot cannot account for its misalignment with the pipe axis, thereby producing inaccurate measures of ovality and distorted three-dimensional wireframes.

A joint R&D project in Germany produced a multi-sensor sewer inspection robot named KARO [59]. This robot utilized concentric laser rings with optical triangulation to detect pipe deformations. Kuntze mentions a navigation module capable of mapping the actual Cartesian coordinates of the robot in the sewer, but does not detail how this is achieved. It is suspected to involve inertial sensors which only provide partial data as described in this dissertation's problem statement presented in Chapter 1.

KARO employed fuzzy logic to fuse and interpret data from several different sensors including the laser rings, ultrasonic distance sensors, and a microwave sensor for inspecting for soil voids behind the pipe wall. Eventually parts of the KARO project were incorporated into a new project called SAM [14] and [60]. SAM includes a host of technologies including a CCTV camera, a microwave backscatter device, hydro-chemical sensors, an acoustic impact transducer, optical triangulation algorithms, and geophysical and radioactive probes. Burn notes the low measurement resolution of many laser profiling systems, but says that SAM's new sensors "should solve this problem". It is

unlikely that any of SAM's sensors are used to identify the robot's position and orientation within the pipe, thereby not solving the problem posed in Chapter 1.

Zhang uses a multiple laser ring generator constructed of a conical reflector and diffraction grating to measure pipe radii [61]. The system was tested on a five inch petroleum pipe, but it is difficult to tell if this system was designed to scan sewer pipes. This profiler requires keeping four wheels in constant contact with the top and bottom of the pipe to keep the camera-laser system parallel with the pipe axis. Since these wheels may conflict with service laterals in a real sewer environment, this system is impractical for sewer pipe inspection.

The MAKRO robot was developed as a prototype autonomous sewer surveyor and was geared toward modern concrete sewers [62], [63], and [64]. MAKRO was a multi-segmented robot which was flexible both vertically and horizontally. The robot was outfitted with a laser which projected a crosshair down the pipe axis. A geometric model was presented by Kolesnik which allowed for the robot's orientation to be established relative to the pipe [65]. This model presents a real solution to the problem posed in this dissertation, but the work on MAKRO has ceased. This crosshair sensor was incorporated onto another robotic platform called KURT [66]. Kolesnik uses the 3-D orientation data from the laser crosshair to aid in autonomous navigation, but does not discuss correcting three-dimensional wireframe models or measuring pipe ovality.

Tsubouchi presents an inspection robot designed for gas pipes [49]. This pipe profiler utilizes a laser spot array generated by a fiber diffraction grating. Optical triangulation is performed on each spot where it comes in contact with the pipe and, using a least squares method, defines a vector parallel to the pipe relative to the robotic

platform. This seems to be a valid way to compensate for the robot's misalignment with the pipe axis, but it is not implemented on any of the current profiling systems.

Roberts presents a laser profiler for the inspection of tubes at chemical plants [67]. By using optical triangulation with a spinning laser probe, the inner diameters of several pipes were profiled to examine creep and material loss. The system was tested at a large methanol processing plant in New Zealand and at a fertilizer plant in Texas, USA. It appears from Robert's paper that the laser profilometer was constrained to remain parallel to the pipe axis since the chemical pipes had predictable geometry.

Zhang also presents a system to profile small tubes by projecting a laser onto a conical reflector to produce a laser ring. Most of his work deals with tubes smaller than one inch in diameter. Zhang discusses the need for coordinate transformations to describe the measurements made with his light conicoid in real world coordinates, but assumes the laser profiler remains parallel to the pipe axis [61].

Duran presents a method to scan sewer pipes with a conical laser to identify cracks [68] and [69]. Sharp changes in the pixel intensity values are used to identify potential cracks in the pipe. In a review of pipe profiling methods, Duran notes that image deformations will occur if the profiler is not aligned with the axis of the pipe. Duran also notes that robot misalignments with the pipe axis are common in harsh environments such as sewers but do not drastically affect crack detection. This work further bolsters the problem statement posited in this dissertation in that a method is needed to relate the robot's coordinate system to the pipe's coordinate system.

The Kings College in London is working toward the design of an autonomous robot for pipe inspection [70]. As part of their system, they are developing an ultrasonic

profiling tool for measuring pipe radii underwater. Their work focuses mainly on the reliability of the sonar measurements and does not discuss position and orientation corrections for the robotic platform relative to the pipe. Price discusses the development of a rotating sonic caliper (RPC) for sewer inspection [71]. However, the RPC is simply placed on a conventional CCTV tractor and does not include any position or orientation tracking devices.

### **2.3 Mathematical Principles and Techniques**

As part of the research process for this dissertation, several mathematical principles were investigated and employed. A special case of Green's Theorem is used to establish the centroid of the typical ring-shaped radial data obtained by a pipe profiler. Homogeneous coordinate transformations are described along with their use in applying the sensor data onboard the prototype profiler to correct erroneous ovality and pipe wireframes. The atan2 function is introduced and compared with the typical atan function used in many programming languages. Quadrature logic, used by several rotary encoders on board the prototype profiler, is explained. And finally, a peak finding algorithm used to identify the location of a laser line in a digital image is introduced.

#### **2.3.1 Centroid Location from Pipe Profiles**

The location of the centroid of a two dimensional area can be calculated by the moment-area method which utilizes the relations in Eqs. (2.2), (2.3) and (2.4).

$$A = \iint_{\mathcal{D}} dx dy \quad (2.2)$$

$$Q_x = \bar{y}A = \iint_{\mathcal{D}} y dx dy \quad (2.3)$$



$$Q_y = \bar{x}A = \iint_D x \, dx \, dy \quad (2.4)$$

where  $D$  is the region consisting of the area's boundary and its interior,  $(\bar{x}, \bar{y})$  are the coordinates of the centroid, and  $(Q_x, Q_y)$  are the first moment of areas about the  $x$  and  $y$  axes, respectively.

In the case of pipe profiles, the points of measurement can be considered to be the boundary of the area by using the discrete case of Green's Theorem. Green's Theorem, a special case of Stoke's Theorem, gives the relationship between a line integral around a simple closed curve  $C$  and a double integral over the plane region  $R$  bounded by  $C$ . If  $L$  and  $M$  have continuous partial derivatives on  $D$ , then Eq. (2.5) can be written.

$$\iint_D \left( \frac{\partial M}{\partial x} - \frac{\partial L}{\partial y} \right) dA = \oint_C L \, dx + M \, dy \quad (2.5)$$

where  $C$  is a smooth simple closed curve and  $D$  is the region consisting of  $C$  and its interior.  $M(x, y)$  and  $L(x, y)$  are functions that are continuous and have continuous first partial derivatives throughout an open region  $R$  containing  $D$ .

This allows Eqs. (2.2), (2.3) and (2.4) to be re-written as Eqs. (2.6), (2.7) and (2.8).

$$A = \iint_D dx \, dy = -\oint_C y \, dx \quad (2.6)$$

where  $L(x, y) = -y$  and  $M(x, y) = 0$ , and

$$Q_x = \bar{y}A = \iint_D y \, dx \, dy = -\frac{1}{2} \int y^2 \, dx \quad (2.7)$$

where  $L(x, y) = -\frac{1}{2}y^2$  and  $M(x, y) = 0$ , and

$$Q_y = \bar{x}A = \iint_D x \, dx \, dy = \frac{1}{2} \int x^2 \, dy \quad (2.8)$$

where  $L(x, y) = 0$  and  $M(x, y) = \frac{1}{2}x^2$

It is important to note that  $C$  does not have to be a single closed curve; it can be composed of piecewise curves  $C_i$  connected together to form a closed loop. This causes Green's formula to become Eq. (2.9).

$$\oint_C L(x, y) dx + M(x, y) dy = \sum \int_{C_i} L(x, y) dx + M(x, y) dy \quad (2.9)$$

If  $C_i$  is composed solely of lines defined by points  $(x_i, y_i)$  and  $(x_{i+1}, y_{i+1})$ , then Green's formula can be written as Eq. (2.10).

$$\oint_C L(x, y) dx + M(x, y) dy = \sum \int_{x_i}^{x_{i+1}} (L(x, y) dx + M(x, y)y'(x)) dx \quad (2.10)$$

A line between any two points on the edge of the pipe profile can be defined by Eq. (2.11).

$$y = y_i + \left( \frac{y_{i+1} - y_i}{x_{i+1} - x_i} \right) (x - x_i) \quad (2.11)$$

This allows Eqs. (2.6), (2.7) and (2.8) to be re-written as Eqs. (2.12), (2.13) and (2.14).

$$A = -\oint_C y dx = -\sum_{i=0}^{n-1} \int_{x_i}^{x_{i+1}} y dx = -\frac{1}{2} \sum_{i=0}^{n-1} (y_i + y_{i+1})(x_{i+1} - x_i) \quad (2.12)$$

$$\begin{aligned} Q_x &= -\frac{1}{2} \oint_C y^2 dx = -\frac{1}{2} \sum_{i=0}^{n-1} \int_{x_i}^{x_{i+1}} \left[ y_i + \left( \frac{y_{i+1} - y_i}{x_{i+1} - x_i} \right) (x - x_i) \right]^2 dx \\ &= -\frac{1}{6} \sum_{i=0}^{n-1} (x_{i+1} - x_i) (y_i^2 + y_i y_{i+1} + y_{i+1}^2) \end{aligned} \quad (2.13)$$

$$\begin{aligned} Q_y &= \frac{1}{2} \oint_C x^2 dy = \frac{1}{2} \sum_{i=0}^{n-1} \int_{y_i}^{y_{i+1}} \left[ x_i + \left( \frac{y_{i+1} - y_i}{x_{i+1} - x_i} \right) (y - y_i) \right]^2 dy \\ &= \frac{1}{6} \sum_{i=0}^{n-1} (y_{i+1} - y_i) (x_i^2 + x_i x_{i+1} + x_{i+1}^2) \end{aligned} \quad (2.14)$$

where  $n$  is the number of measurement points around the pipe profile. These equations allow the centroid's coordinates  $(\bar{x}, \bar{y})$  to be calculated for each pipe profile. Substituting Eqs. (2.12), (2.13) and (2.14) into Eqs. (2.2), (2.3) and (2.4) gives Eqs. (2.15) and (2.16).

$$\bar{x} = \frac{Q_y}{A} = \frac{\frac{1}{6} \sum_{i=0}^{n-1} (y_{i+1} - y_i)(x_i^2 + x_i x_{i+1} + x_{i+1}^2)}{\frac{1}{2} \sum_{i=0}^{n-1} (y_i + y_{i+1})(x_{i+1} - x_i)} \quad (2.15)$$

$$\bar{y} = \frac{Q_x}{A} = \frac{\frac{1}{6} \sum_{i=0}^{n-1} (x_{i+1} - x_i)(y_i^2 + y_i y_{i+1} + y_{i+1}^2)}{\frac{1}{2} \sum_{i=0}^{n-1} (y_i + y_{i+1})(x_{i+1} - x_i)} \quad (2.16)$$

Equations (2.15) and (2.16) were used in Chapter 7 to locate the centroid of each of the pipe profiles based on the pipe coordinate data collected by the prototype profiler.

### **2.3.2 Homogeneous Coordinate Transformation Matrices**

Several coordinate systems are defined in this dissertation. It is desirable to have an efficient and effective method to relate each of the coordinate systems and the simulated radial measurement points taking into account multiple variables. The method chosen involves converting the measurement points into homogeneous coordinates and operating on these coordinates with 4x4 transformation matrices.

Homogeneous coordinates are frequently used in computer graphics because they allow affine transformations to be performed through matrix operations. Homogeneous coordinates embed each three-dimensional coordinate into a 4x1 vector. Instead of representing each point  $(x, y, z)$  in three-dimensional space with a single three-dimensional vector, such as Eq. (2.17).

$$\text{Point coordinates} = \begin{bmatrix} x \\ y \\ z \end{bmatrix} \quad (2.17)$$

homogeneous coordinates allow each  $(x,y,z)$  point to be represented by any of an infinite number of four-dimensional vectors. Adopting this formulation results in Eq. (2.18).

$$\text{Point coordinates} = \begin{bmatrix} T \cdot x \\ T \cdot y \\ T \cdot z \\ T \end{bmatrix} \quad (2.18)$$

where  $T$  is any number, usually equal to one.

Any three-dimensional linear transformation can be represented by a 4x4 homogeneous transformation matrix including rotation, translation, skew, and perspective distortion. The generic format representation of a homogeneous transformation equation for mapping the three-dimensional coordinate  $(x,y,z)$  to the three-dimensional coordinate  $(x',y',z')$  is described by Eq. (2.19).

$$\begin{bmatrix} T' \cdot x' \\ T' \cdot y' \\ T' \cdot z' \\ T' \end{bmatrix} = \begin{bmatrix} T'' \cdot a & T'' \cdot b & T'' \cdot c & T'' \cdot d \\ T'' \cdot e & T'' \cdot f & T'' \cdot g & T'' \cdot h \\ T'' \cdot i & T'' \cdot j & T'' \cdot k & T'' \cdot m \\ T'' \cdot n & T'' \cdot p & T'' \cdot q & T'' \end{bmatrix} \begin{bmatrix} T \cdot x \\ T \cdot y \\ T \cdot z \\ T \end{bmatrix} \quad (2.19)$$

If any two matrices or vectors in Eq. (2.19) are known, the third matrix or vector can be computed, and then the redundant  $T$  element in the solution can be eliminated by dividing all elements of the matrix by the last element.

Of the four types of linear transformations possible with 4x4 homogeneous coordinates, translation and rotation are the only two types needed for this analysis. Translations can be performed on a three-dimensional coordinate  $(x,y,z)$  using the 4x4 homogeneous coordinate transformation matrix described in Eq. (2.20).

$$\begin{bmatrix} x' \\ y' \\ z' \\ 1 \end{bmatrix} = \begin{bmatrix} 1 & 0 & 0 & x-shift \\ 0 & 1 & 0 & y-shift \\ 0 & 0 & 1 & z-shift \\ 0 & 0 & 0 & 1 \end{bmatrix} \begin{bmatrix} x \\ y \\ z \\ 1 \end{bmatrix} \quad (2.20)$$

where *x-shift* is the translation of the three-dimensional coordinate (*x,y,z*) along the *x-axis*, *y-shift* is the translation along the *y-axis*, and *z-shift* is the translation along the *z-axis*.

A series of rotations can also be performed on a three-dimensional coordinate (*x,y,z*) using the 4x4 homogeneous coordinate transformation matrix in Eq. (2.21).

$$\begin{bmatrix} x' \\ y' \\ z' \\ 1 \end{bmatrix} = M \begin{bmatrix} x \\ y \\ z \\ 1 \end{bmatrix} \quad (2.21)$$

where

$$M = \begin{bmatrix} \cos \gamma \cos \beta + \sin \gamma \sin \alpha \sin \beta & \sin \gamma \cos \beta - \cos \gamma \sin \alpha \sin \beta & \cos \alpha \sin \beta & 0 \\ -\sin \gamma \cos \alpha & \cos \gamma \cos \alpha & \sin \alpha & 0 \\ \sin \gamma \sin \alpha \cos \beta - \cos \gamma \sin \beta & -\cos \gamma \sin \alpha \cos \beta - \sin \gamma \sin \beta & \cos \alpha \cos \beta & 0 \\ 0 & 0 & 0 & 1 \end{bmatrix}$$

$\alpha$  = positive angle of rotation (counter-clockwise) around the x-axis

$\beta$  = positive angle of rotation (counter-clockwise) around the y-axis

$\gamma$  = positive angle of rotation (counter-clockwise) around the z-axis

Matrix *M* in Eq. (2.21) is the product of three separate transformation matrices each with a rotation around a single axis and is given by Eq. (2.22).

$$M = M1 \cdot M2 \cdot M3 \quad (2.22)$$

where

$$M1 = \begin{bmatrix} \cos \beta & 0 & \sin \beta & 0 \\ 0 & 1 & 0 & 0 \\ -\sin \beta & 0 & \cos \beta & 0 \\ 0 & 0 & 0 & 1 \end{bmatrix} \quad (2.23)$$

$$M2 = \begin{bmatrix} 1 & 0 & 0 & 0 \\ 0 & \cos \alpha & \sin \alpha & 0 \\ 0 & -\sin \alpha & \cos \alpha & 0 \\ 0 & 0 & 0 & 1 \end{bmatrix} \quad (2.24)$$

$$M3 = \begin{bmatrix} \cos \gamma & \sin \gamma & 0 & 0 \\ -\sin \gamma & \cos \gamma & 0 & 0 \\ 0 & 0 & 1 & 0 \\ 0 & 0 & 0 & 1 \end{bmatrix} \quad (2.25)$$

Matrix  $M$  in Eq. (2.21) is the product of three separate transformation matrices each with a rotation around a single axis.  $M1$  is the rotation around the  $y$ -axis,  $M2$  is the rotation around the  $x$ -axis and  $M3$  the rotation around the  $z$ -axis. It must be noted that since matrix multiplication is not commutative, the order in which the series of rotations is performed is important. The last matrix in the series is applied first. Therefore, for the example in Eq. (2.21),  $M3$  is applied to three-dimensional coordinate  $(x,y,z)$  first,  $M2$  applied second, and  $M1$  applied last.

### **2.3.3 The atan2 Function**

The atan2 function is a two-parameter function for computing the arctangent or atan in many programming languages including Mathcad®. The atan2 function calculates the arctangent of the two variables  $x$  and  $y$ . It is similar to calculating  $\tan^{-1}\left(\frac{y}{x}\right)$ , except that the signs of both arguments are used to determine the quadrant of the result. The atan2 function is preferred over the atan or arctangent function since it correctly identifies

the sign of the result in all quadrants and returns unambiguous results. The function atan returns values in the range  $\left(-\frac{\pi}{2}, \frac{\pi}{2}\right)$ . Whereas, the function atan2(x,y) is defined as the arctangent of y/x with a range of  $(-\pi, \pi)$  determined by the following conditional statements:

if  $x = y = 0$ , then the result is indefinite since the function is dividing 0 by 0,

if  $x > 0$  and  $y = 0$ , then atan2 = 0,

if  $x < 0$  and  $y = 0$ , then atan2 =  $\pi$ , else

if  $y < 0$ , then  $-\pi < \text{atan2} < 0$ ,

if  $y > 0$ , then  $0 < \text{atan2} < \pi$ .

A comparison between the atan and atan2 functions is demonstrated in Table 2.1.

Table 2.1 Comparison between atan and atan2 Functions

$\theta$	$x = \cos(\theta)$	$y = \sin(\theta)$	atan(y/x)	atan2(x,y)
0	1	0	0	0
$\pi/4$	0.707	0.707	$\pi/4$	$\pi/4$
$\pi/2$	0	1	$\pi/2$	$\pi/2$
$3\pi/4$	-0.707	0.707	$-\pi/4$	$3\pi/4$
$\pi$	-1	0	0	$\pi$
$5\pi/4$	-0.707	-0.707	$\pi/4$	$-3\pi/4$
$3\pi/2$	0	-1	$\pi/2$	$-\pi/2$
$7\pi/4$	0.707	-0.707	$-\pi/4$	$-\pi/4$
$2\pi$	1	0	0	0

If the atan2 result is positive, the angle is measured counterclockwise from the x-axis. If the result is negative the angle is measured clockwise from the x-axis.

#### **2.3.4 Quadrature Logic**

There are three optical encoders onboard the prototype profiling robot developed for this research. Each of the encoders utilizes a type of incremental encoder called a

quadrature encoder. Quadrature encoders allow for the determination of the speed and direction of travel. To accomplish this, quadrature encoders utilize two photo detectors and two code tracks. The two code tracks are positioned  $90^\circ$  out of phase, and the pulses produced are used to indicate angular position and direction of travel (clockwise or counter-clockwise). A picture showing the two encoder tracks and pulse differences is shown in Figure 2.6.

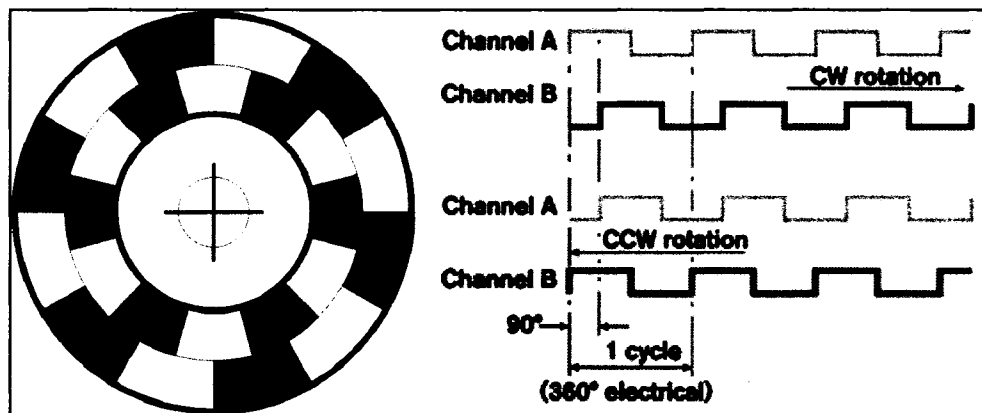


Figure 2.6 Quadrature Encoder Disc and Logic

### **2.3.5 Laser Peak Finding Algorithm**

A peak finding algorithm from LabVIEW™ was used to extract the image coordinates of the intersection of the laser line with the interior surface of the pipe. The peak finding algorithm performs a least squares fit with a quadratic polynomial to sequential groups of data points; in this case, the data points of interest are red pixel values along a single raster line of the image. The peak detector was employed to search each of the 35,200 digital images taken during the data collection process and fit a quadratic curve to the red pixels defining the laser line. The location of the peak is



identified in pixel coordinates and then later converted to real world coordinates. The wiring diagram of the LabVIEW™ peak detector VI is shown in Figure 2.7.

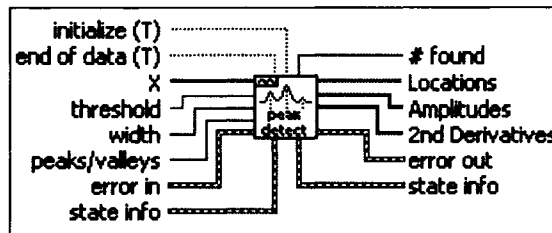


Figure 2.7 Peak Detector VI Inputs and Outputs

X specifies the array to be analyzed. In this case, one raster, or row of red pixel values in the image, is passed to the X input. The number of data points used in the quadratic polynomial fit is specified by the width input. Peaks with heights lower than the threshold level are ignored. The # found output delivers an integer indicating the number of peaks above the threshold which are found. The Locations output provides an index array with pixel locations of valid peaks. Since the peak algorithm uses a quadratic fit, it interpolates between pixels; thus, the index locations are not integers. The Amplitudes output provides an array with the amplitudes of the found peaks, and the 2nd Derivatives output gives a measurement of the sharpness of the peaks.

## 2.4 Conclusions

During the past decade, at least four companies have made pipe profilers commercially available. The need for accurate pipe inspection has grown rapidly and is in need of further research. In the past two decades, significant research work has been completed in North America, Europe, Asia and Australia aimed at improving the accuracy and automation of pipe inspection robots. The previous three sections give a

brief review of this research. A number of conclusions have been drawn by various researchers and have been accepted both in the academic and engineering field including:

1. Sewers are prevalent, valuable, important, unnoticed, and often in a state of disrepair.
2. Current CCTV inspection methods are inadequate for gathering quantitative data.
3. A number of commercial pipe profiling technologies have been implemented in the past five years; these technologies are an important part of the solution to the huge problem of pipe asset condition assessment.
4. Pipe profiling robots move with respect to the pipe. A strategy must be adopted to relate the pipe's coordinate system to the robot's coordinate system to correctly report pipe ovality and produce accurate three-dimensional pipe wireframes.

## CHAPTER 3

### QUANTIFYING THE ERROR PRODUCED BY MISALIGNED PIPE PROFILERS

The literature shows that pipe profiling robots can become misaligned with the axis of the pipe while performing pipe inspections. This movement can cause several problems including the following:

1. Reporting of inaccurate pipe ovality measurements.
2. Reporting of incorrect distance measurements to defect locations along the pipe.
3. Distorting three-dimensional wireframe models.
4. Over-designing cured in place pipe liners used to rehabilitate pipelines as per ASTM F126-03.

Each of the aforementioned problems is quantified in the four sections of this Chapter; however, the magnitude of the error derived is relatively small. The equations developed here demonstrate that substantial misalignment of the robot relative to the pipe is necessary before significant amounts of measurement error can accumulate. Since GASB 34 requires a condition assessment of sewer assets at least every three years using a consistent basis of measurement and scale that can be repeated, quantification of the measurement error is still of interest.

### 3.1 Erroneous Ovality Produced by Pipe Profilers

A pipe profiling robot attempts to accurately measure internal pipe wall dimensions. If the robot veers from being parallel to the axis of the pipe, whether in the vertical plane or the horizontal plane, the machine vision system will incorrectly measure the pipe's dimensions and cause erroneous ovality to be reported. Both of these situations are depicted graphically in Figures 3.1 and 3.2. Figure 3.1 depicts a situation where the robot has meandered away from being parallel with the pipe axis in the horizontal plane with magnitude  $\theta_h$ . This angle is often referred to as the yaw or meander angle.

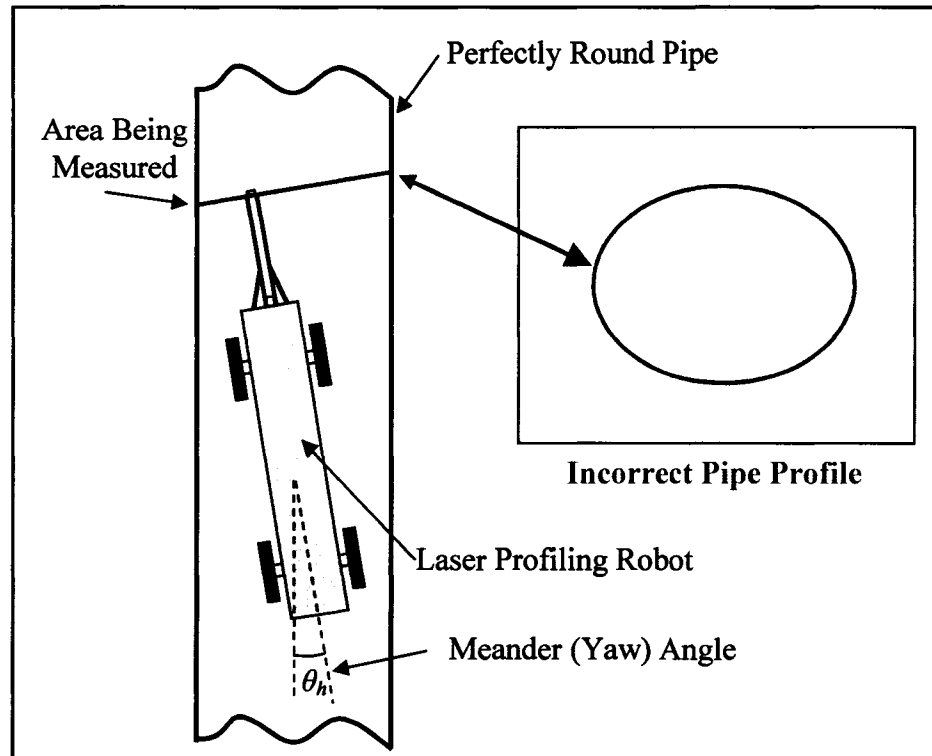


Figure 3.1 Top View of Robot Meander and Resulting Erroneous Ovality

Figure 3.2 depicts where the robot has encountered an anomaly in the bottom of the pipe such as a bump or offset joint causing a rotation of the robot in the vertical plane with magnitude  $\theta_v$ . This angle of rotation is often referred to as the pitch angle.

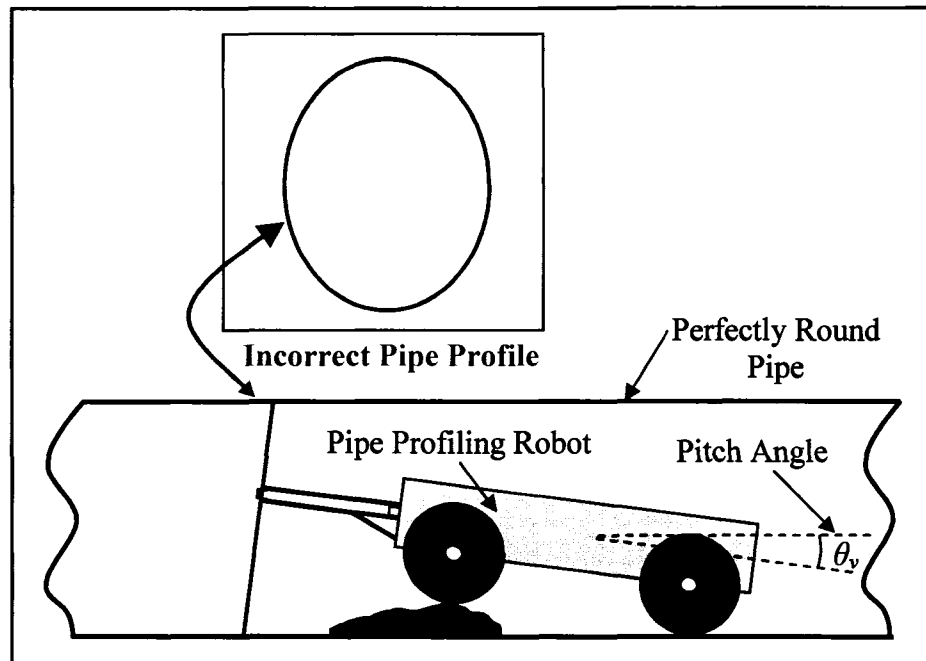


Figure 3.2 Side View of Robot on Bump or Offset Joint and the Resulting Erroneous Ovality

Therefore, it is prudent to quantify the amount of erroneous ovality caused by the robot's misalignment with the pipe axis in terms of the pitch and meander angles ( $\theta_v, \theta_h$ ).

### **3.1.1 Measurement-Plane Definition**

The robot's orientation relative to the pipe is first described in terms of the measurement plane. The measurement plane is defined by a plane passing through the area under consideration for measurement by a pipe profiling robot. The measurement plane could be defined by a plane of laser light, a plane formed by rotating a sonar transducer, a plane formed by rotating a tactile probe, or a plane formed by any other

device measuring a pipe's internal profile. Assuming the pipe is perfectly cylindrical, the measurement plane will form an ellipse where it intersects the pipe as shown in Figure 3.3.

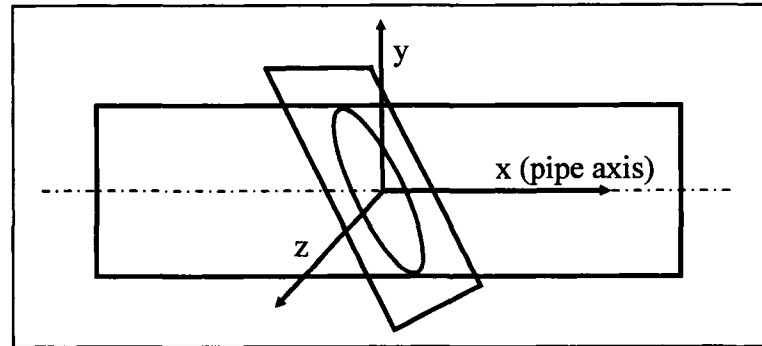


Figure 3.3 Cartesian Coordinate System Attached to the Pipe with the Centroid of the Elliptical Measurement Plane Intersecting the Origin

A plane which passes through the origin of the  $x$ - $y$ - $z$  coordinate system attached to the pipe can be expressed by Eq. (3.1).

$$ax + by + cz = 0 \quad (3.1)$$

The measurement plane can be represented by a normal vector  $\vec{n}$  noted in Eq. (3.2).

$$\vec{n} = a\hat{i} + b\hat{j} + c\hat{k} \quad (3.2)$$

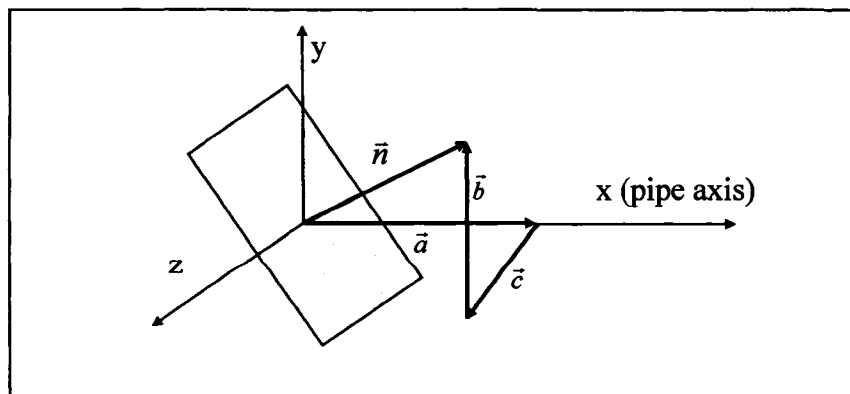


Figure 3.4 Normal Vector  $\vec{n}$  Representing the Measurement-Plane

Assuming  $\bar{n}$  is a unit vector, then Eq. (3.3.) is true.

$$a^2 + b^2 + c^2 = 1 \quad (3.3)$$

This relationship can be written in terms of the pitch and meander angles  $(\theta_v, \theta_h)$  by closer analysis of the vertical and horizontal pipe planes.

### 3.1.2 Robot Orientation Geometry

By examining the  $x$ - $y$  plane from Figure 3.4, one can see the relationship between the vertical rotation of the robot  $(\theta_v)$  and the measurement plane's normal vector  $\bar{n}$ . A diagram showing the  $x$ - $y$  plane geometry is shown in Figure 3.5.

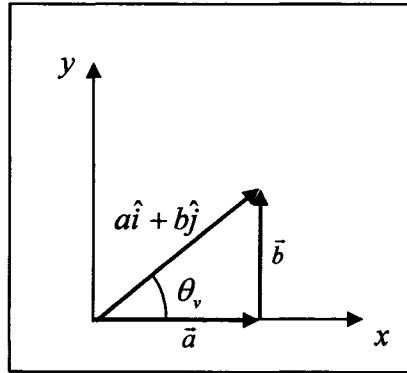


Figure 3.5 Projection of the  $\bar{n}$  vector onto the Pipe's Vertical  $x$ - $y$  Plane

It is clear from Figure 3.5 that Eq. (3.4) is true.

$$\tan(\theta_v) = \frac{b}{a} \quad (3.4)$$

By observing the  $x$ - $z$  plane, one can see the relationship between the horizontal orientation of the robot  $\theta_h$  and  $\bar{n}$ . A diagram showing the  $x$ - $z$  plane geometry is shown in Figure 3.6.

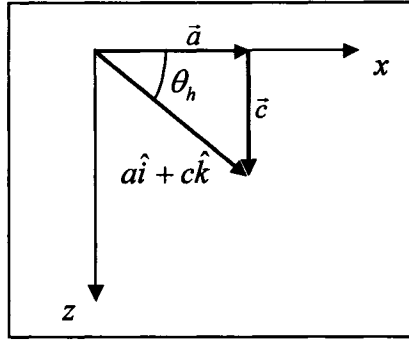


Figure 3.6 Projection of the  $\bar{n}$  vector onto the Pipe's Horizontal  $x$ - $z$  Plane

It is clear from Figure 3.6 that Eq. (3.5) is true.

$$\tan(\theta_h) = \frac{c}{a} \quad (3.5)$$

Solving Eqs. (3.3), (3.4) and (3.5) simultaneously gives Eqs. (3.6), (3.7) and (3.8).

$$a = \pm [1 + \tan(\theta_v)^2 + \tan(\theta_h)^2]^{-1/2} \quad (3.6)$$

$$b = \pm \tan(\theta_h) \cdot [1 + \tan(\theta_v)^2 + \tan(\theta_h)^2]^{-1/2} \quad (3.7)$$

$$c = \pm \tan(\theta_v) \cdot [1 + \tan(\theta_v)^2 + \tan(\theta_h)^2]^{-1/2} \quad (3.8)$$

The positive values of Eqs. (3.6), (3.7) and (3.8) are used to describe the orientation of the measurement-plane's normal vector  $\bar{n}$  as shown in Figure 3.4; the negative values in these expressions point in a negative coordinate direction and are not of interest in this work. A new angle  $\theta_x$  is introduced to relate the normal vector  $\bar{n}$  directly to the  $x$ -axis. This relationship is depicted in Figure 3.7.



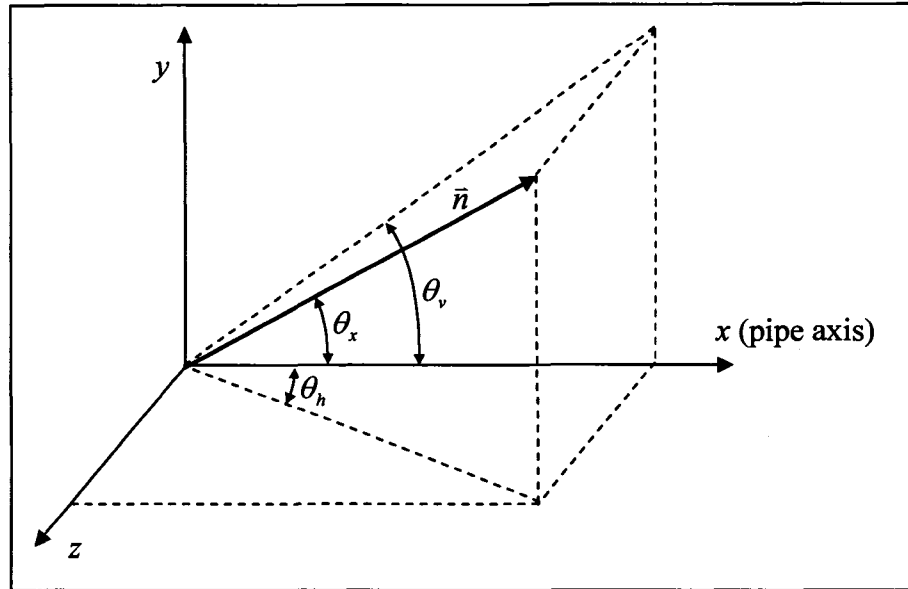


Figure 3.7 Geometric Relationship Between  $\theta_x$ ,  $\theta_h$  and  $\theta_v$

Here,  $\theta_x$  is expressed by the directional cosine equation in Eq. (3.9).

$$\cos \theta_x = \frac{a}{\sqrt{a^2 + b^2 + c^2}} \quad (3.9)$$

which, when considering that the denominator is one, reduces to Eq. (3.10).

$$\theta_x = \cos^{-1} a = \cos^{-1} [1 + \tan(\theta_v)^2 + \tan(\theta_h)^2]^{-1/2} \quad (3.10)$$

Equation (3.10) describes the angle between the measurement plane and the pipe axis in terms of the pitch and meander angles  $\theta_v$  and  $\theta_h$ . To relate these angles to ASTM ovality, they must first be related to the ellipse formed on the measurement plane.

The elliptical profile formed on the measurement-plane can be described mathematically by an ellipse which has a major axis  $A$  and a minor axis  $B$ . The ellipse is defined such that  $B$  is equal to the radius  $r$  of the undeformed pipe as demonstrated in Figure 3.8.

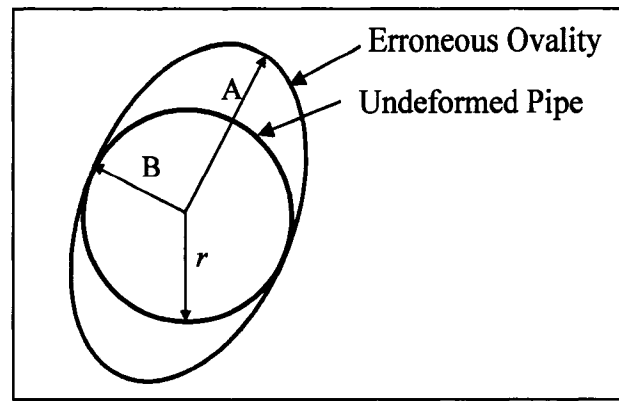


Figure 3.8 Relationship between the Ellipse Formed on the Measurement-Plane and the Undeformed Pipe

Rotating the geometry shown in Figure 3.7 clockwise about the  $x$ -axis until the  $\bar{n}$  vector lies in the vertical plane results in Figure 3.9. Here, the  $\bar{n}$ - $x$  plane is co-planar with the  $A$ - $x$  plane and the ellipse's major axis  $A$  can be directly related to  $\theta_x$ . While it is intuitive that this relationship is true for when  $\theta_x$  is equal to  $\theta_y$ , since the major axis of the ellipse will coincide with the crown and invert of the pipe, the relationship also applies for combined pitch and yaw rotations as depicted in Figure 3.9.

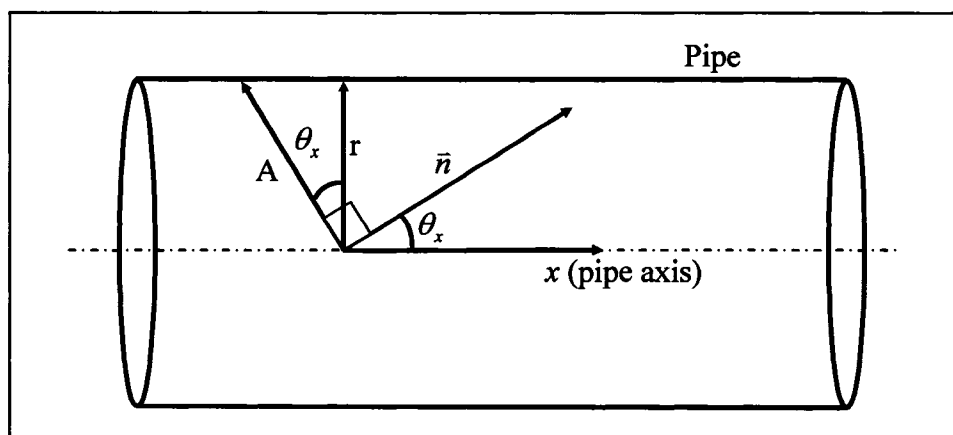


Figure 3.9 Relationship between  $\bar{n}$ - $x$  Plane and Ellipse Major Axis  $A$

Considering the geometry of Figure 3.9, it is evident that the major axis can be written as Eq. (3.11).

$$A = \frac{r}{\cos \theta_x} \quad (3.11)$$

Substituting the expression for  $\cos(\theta_x)$  in Eq. (3.10) yields Eq. (3.12).

$$A = r \cdot [1 + \tan(\theta_v)^2 + \tan(\theta_h)^2]^{1/2} \quad (3.12)$$

Equation (3.12) is an expression which describes the magnitude of the ellipse's major axis  $A$  as a function of the radius of the undeformed pipe  $r$  the horizontal yaw angle  $\theta_h$  and the vertical pitch angle  $\theta_v$ .

### **3.1.3 Relating Ellipse Dimensions to Erroneous Ovality**

The ellipse formed as a result of the robot's misalignment of the pipe can be related to the erroneous ovality perceived by the profiler through Eq. (3.12). According to ASTM F1216-03, the ovality  $q$  of the host-pipe is described by the Eqs. (3.13) and (3.14).

$$q = 100 \times \frac{\text{Maximum Inside Diameter} - \text{Mean Inside Diameter}}{\text{Mean Inside Diameter}} \quad (3.13)$$

$$q = 100 \times \frac{\text{Mean Inside Diameter} - \text{Minimum Inside Diameter}}{\text{Mean Inside Diameter}} \quad (3.14)$$

To relate the ellipse formed on the measurement plane to ASTM ovality, the maximum inside diameter is set equal to the major axis of the ellipse  $A$ ; and the mean inside diameter will be equal to the average of the major axis  $A$  and the minor axis  $B$ . Therefore, the percentage of erroneous ovality  $q_e$  is related to the ellipse by Eq. (3.15).

$$q_e = 100 \times \frac{2A - \left(\frac{2A + 2B}{2}\right)}{\left(\frac{2A + 2B}{2}\right)} \quad (3.15)$$

which reduces to Eq. (3.16).

$$q_e = 100 \times \frac{A - B}{A + B} \quad (3.16)$$

Replacing the major axis  $A$  in Eq. (3.16) with its value from Eq. (3.12) and substituting pipe radius  $r$  for the minor axis  $B$  gives Eq. (3.17).

$$q_e = 100 \times \frac{r \cdot [1 + \tan(\theta_v)^2 + \tan(\theta_h)^2]^{1/2} - r}{r \cdot [1 + \tan(\theta_v)^2 + \tan(\theta_h)^2]^{1/2} + r} \quad (3.17)$$

which reduces to Eq. (3.18).

$$q_e = 100 \times \frac{[1 + \tan(\theta_v)^2 + \tan(\theta_h)^2]^{1/2} - 1}{[1 + \tan(\theta_v)^2 + \tan(\theta_h)^2]^{1/2} + 1} \quad (3.18)$$

Equation (3.18) relates erroneous ovality to the robot's orientation relative to the pipe. It is interesting to note that erroneous ovality  $q_e$  is solely a function of  $\theta_h$  and  $\theta_v$ , and not a function of pipe radius  $r$ . A three-dimensional surface plot of Eq. (3.18) is shown in Figure 3.10 to demonstrate the impact the pitch and meander angles have on the erroneous ovality perceived by a misaligned profiler.

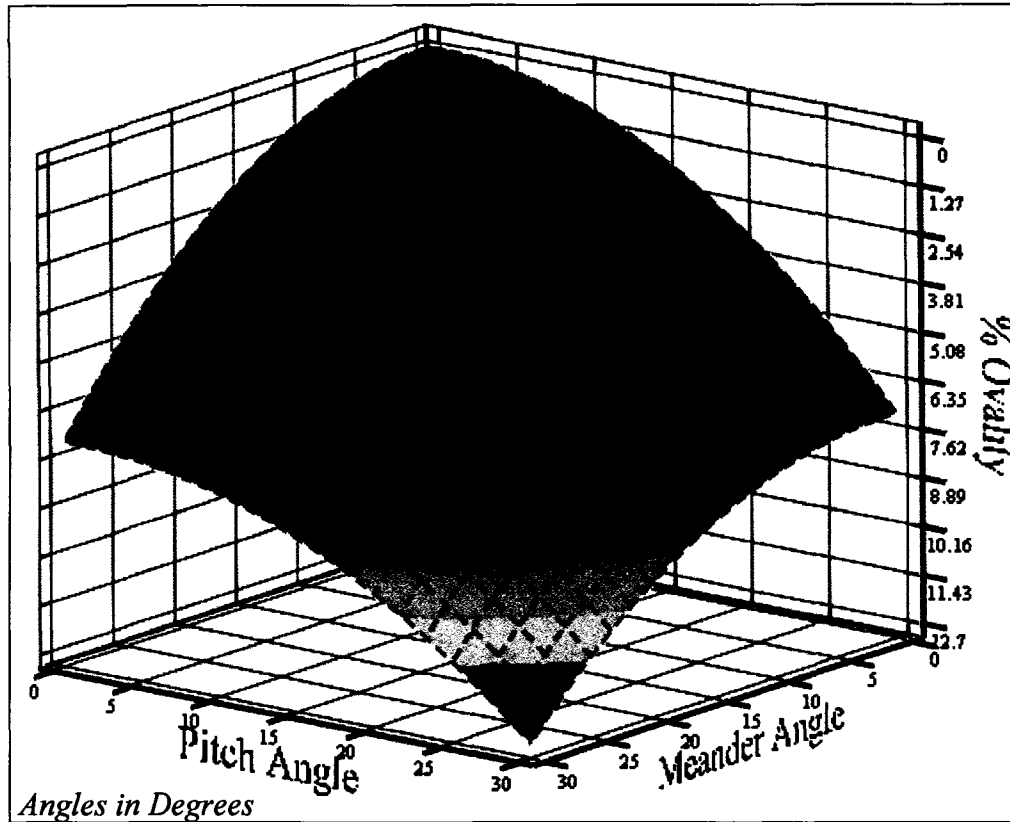


Figure 3.10 Ovality Plot as a Function of Meander and Pitch Angles

From Figure 3.10 it is clear that the highest magnitude for erroneous ovality occurs when the meander angle and pitch angle are both large. When the meander and pitch angles are small, the erroneous ovality is also small. The relationship depicted by Figure 3.10 confirms the expectation that increasing pitch and yaw angles will lead to increasing erroneous ovality. The amount of ovality introduced, however, seems to be small for average misalignments with the pipe axis.

### **3.2 Misaligned Pipe Profilers Cause Three-Dimensional Wireframe Distortion**

#### **3.2.1 Distance Measurement Error**

When a pipe profiling robot inspects a pipe, the locations of defects along the length of the pipe are typically measured from a known point in space such as a manhole. The length of pipe traversed by the robot is usually measured with a distance sensor such as an odometer on a tether attached to the robot. However, if the robot happens to veer from being parallel to the axis of the pipe, there exists a distance discrepancy regarding where exactly a given cross section or ring is measured. Both horizontal deflections and vertical deflections by the robot causes distance discrepancies to occur. These situations are depicted in Figures 3.11 and 3.12. The distance error is represented by the variable  $e$  which will be derived as a function of the horizontal misalignment  $\theta_h$  and vertical misalignment  $\theta_v$ .

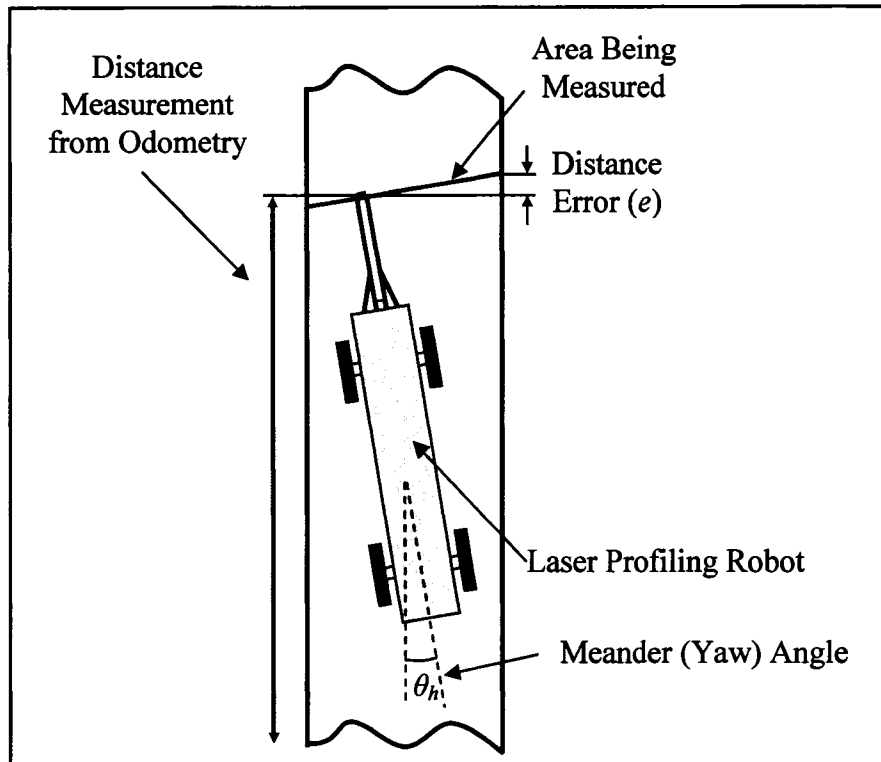


Figure 3.11 Distance Measurement Error Produced by Robot Meander

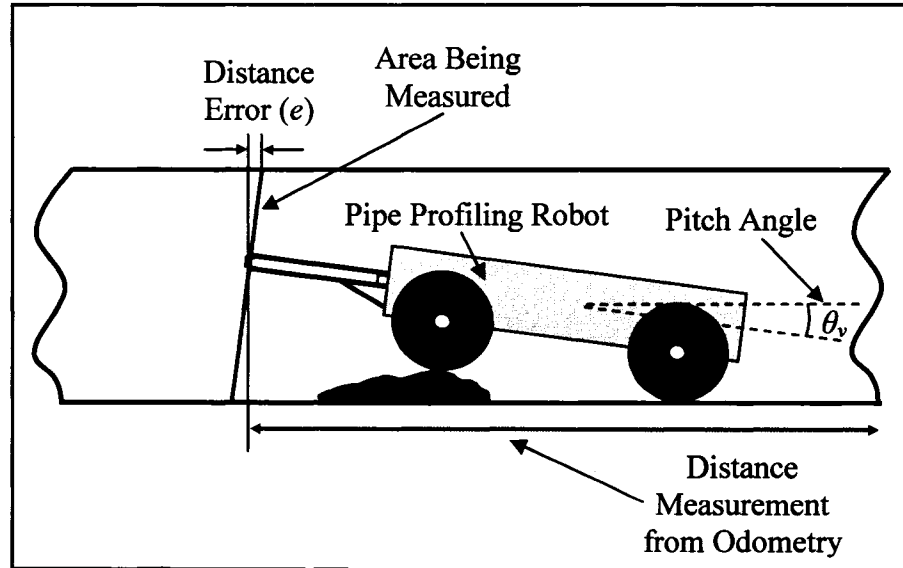


Figure 3.12 Distance Measurement Error Produced by Robot on Bump or Offset Joint

Not only does the distance error cause defects to be located inaccurately along the length of the pipe, but it also causes distortion of the three-dimensional wireframe. This problem is illustrated in Figure 3.13 where point  $P_1$  is measured at distance  $L_1$  but actually exists at distance  $L_2$  because of robot meander.

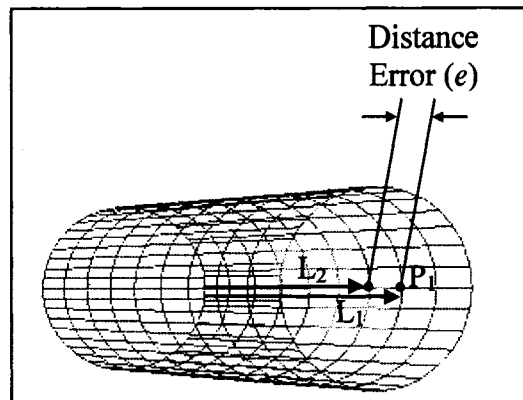


Figure 3.13 Wireframe Distortion Caused by Robot Meander

### **3.2.2 Distance Measurement Error as a Function of Robot Orientation**

To derive the distance measurement error  $e$  as a function of robot orientation, the same geometry as described in Section 3.1 is used. The transformation of the measurement plane coordinate system is described in Section 3.1.2 and shown in Figure 3.14. The maximum distance error  $e$  is denoted at the top of Figure 3.14.



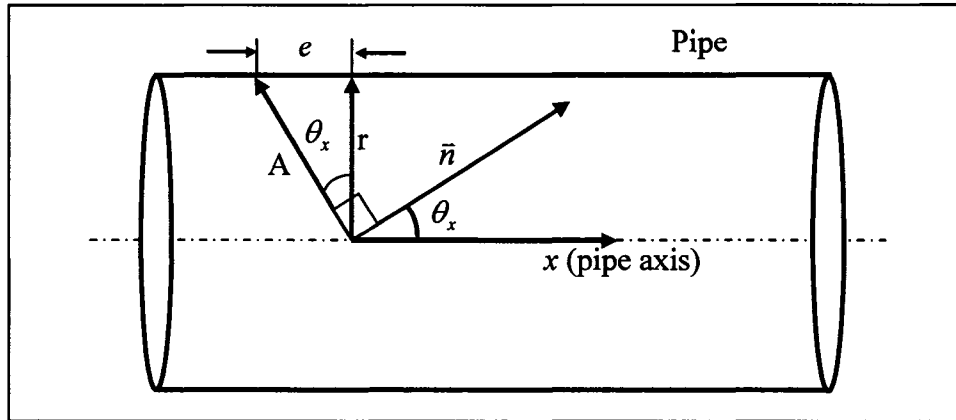


Figure 3.14 Relationship between  $\bar{n}$ - $x$  Plane and Distance Measurement Error

From Figure 3.14 it is clear that the relationship between the maximum distance measurement error  $e$  and the robot's orientation relative to the  $x$ -axis is given by Eq. (3.19).

$$e = r \cdot \tan \theta_x \quad (3.19)$$

Replacing  $\theta_x$  in Eq. (3.19) with its value from Eq. (3.10) gives Eq. (3.20).

$$e = r \cdot \tan(\cos^{-1} a) \quad (3.20)$$

where  $a$  is the  $x$ -component of vector  $\bar{n}$  describing the orientation of the measurement plane from Section 3.1.

Using the forward-inverse trigonometric identity [72] gives Eq. (3.21).

$$\tan(\cos^{-1} a) = \frac{\sqrt{1-a^2}}{a} \quad (3.21)$$

Equation (3.20) can be simplified to yield Eq. (3.22).

$$e = r \cdot \frac{\sqrt{1-a^2}}{a} \quad (3.22)$$

Replacing  $a$  in Eq. (3.22) with its value from Eq. (3.6) gives Eq. (3.23).

$$e = r \cdot \frac{\sqrt{1 - (1 + \tan(\theta_v)^2 + \tan(\theta_h)^2)^{-1}}}{[1 + \tan(\theta_v)^2 + \tan(\theta_h)^2]^{-1/2}} \quad (3.23)$$

Equation (3.23) allows for the calculation of the distance measurement error  $e$  in terms of pipe radius  $r$ , horizontal meander angle  $\theta_h$ , and vertical pitch angle  $\theta_v$ . A three-dimensional surface plot is shown in Figure 3.15 to demonstrate the impact the robot's misalignment with the pipe axis has on the distance measurement error.

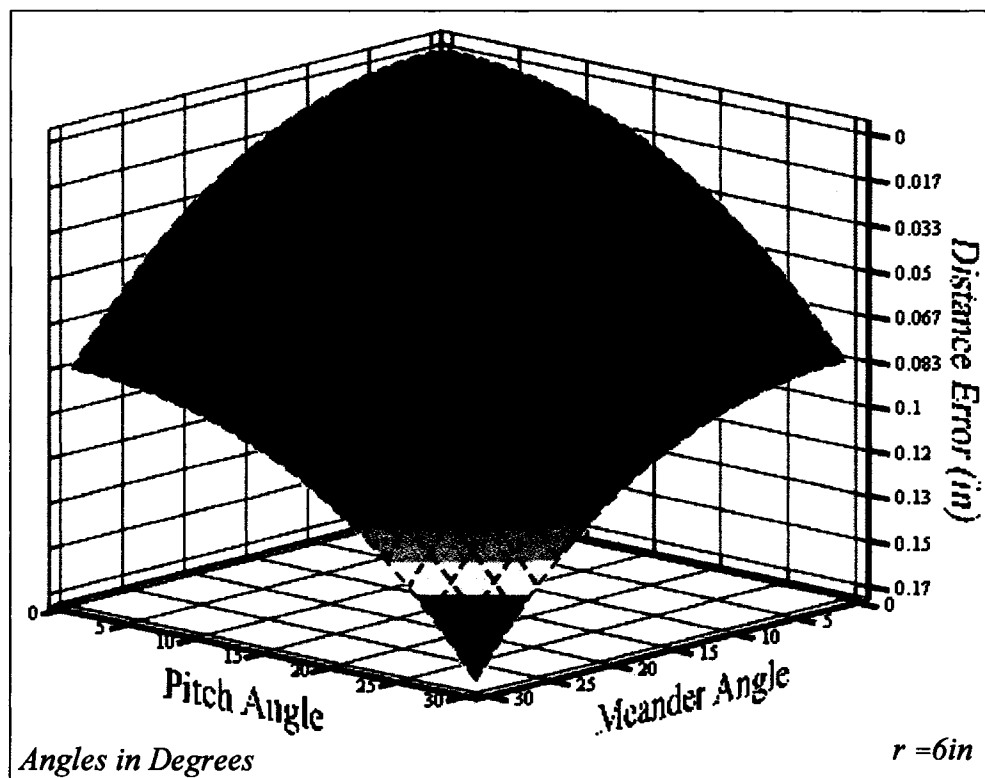


Figure 3.15 Distance Error Plot as a Function of Meander and Pitch Angles

From Figure 3.15 it is clear that the highest magnitude for distance error occurs when the meander angle and pitch angle are both large; conversely, when the meander and pitch angles are small, the distance error is also small. The total amount of distance error introduced, however, seems small for average misalignments with the pipe axis.

### 3.3 Relating Bump Height and Robot Length to Erroneous Ovality

One of the most common vertical deviations which can occur during a pipe inspection is when the pipe profiling robot encounters a bump or offset joint as seen in Figure 3.16.

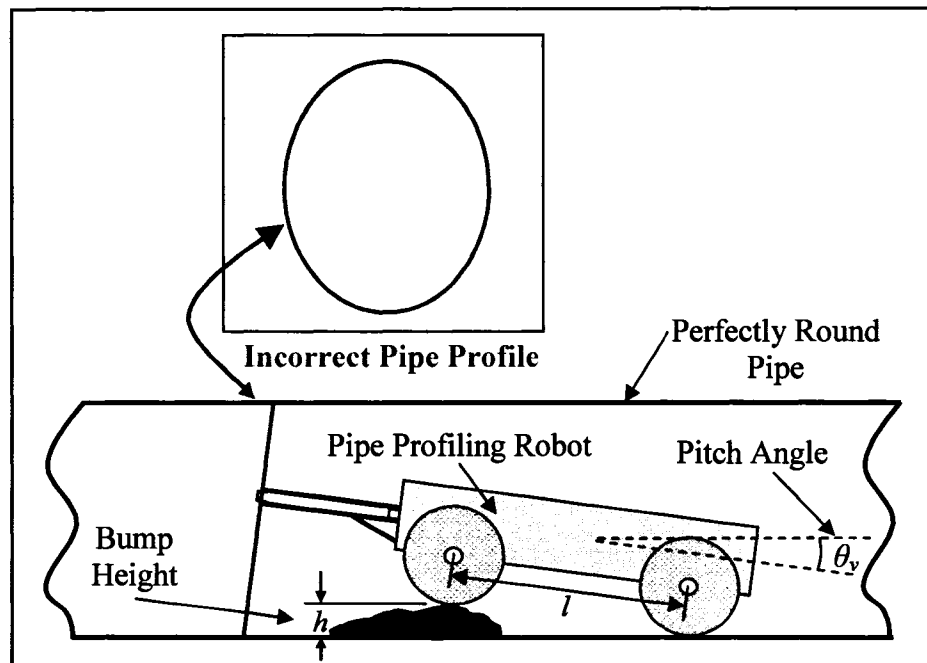


Figure 3.16 Side View of Robot on Bump

Figure 3.16 is similar to Figure 3.2 where ovality is related to the vertical pitch angle  $\theta_v$ . In Figure 3.16, however,  $\theta_v$  is shown to be a function of the bump height  $h$  and the robot length between the wheels  $l$  where

$$\theta_v = \sin^{-1} \frac{h}{l} \quad (3.24)$$

Using the expression derived for the erroneous ovality  $q_e$  perceived by the misaligned profiler,  $\theta_v$  in Eq. (3.18) can be replaced with its value from Eq. (3.24) to give Eq. (3.25).

$$q_e = 100 \times \frac{\left[ 1 + \tan\left(\sin^{-1} \frac{h}{l}\right)^2 + \tan(\theta_h)^2 \right]^{\frac{1}{2}} - 1}{\left[ 1 + \tan\left(\sin^{-1} \frac{h}{l}\right)^2 + \tan(\theta_h)^2 \right]^{\frac{1}{2}} + 1} \quad (3.25)$$

Since Eq. (3.25) is a function of three variables  $\theta_h$ ,  $h$ , and  $l$ ,  $\theta_h$  will be held constant at zero (no meander) to isolate the effects bump height  $h$  and robot length  $l$  have in producing erroneous ovality. Setting  $\theta_h$  to zero allows Eq. (3.25) to be simplified to give Eq. (3.26).

$$q_e = 100 \times \frac{\left(\frac{l^2}{l^2 - h^2}\right)^{\frac{1}{2}} - 1}{\left(\frac{l^2}{l^2 - h^2}\right)^{\frac{1}{2}} + 1} \quad (3.26)$$

Plotting Eq. (3.26) in terms of bump height  $h$  and robot length  $l$  results in Figures 3.17 and 3.18. Clearly, increasing bump height causes an increase in erroneous ovality; conversely, an increase in robot length causes a decrease in erroneous ovality. These results assist robot design engineers in understanding the influence of robot wheel spacing on the accuracy of profiling results.

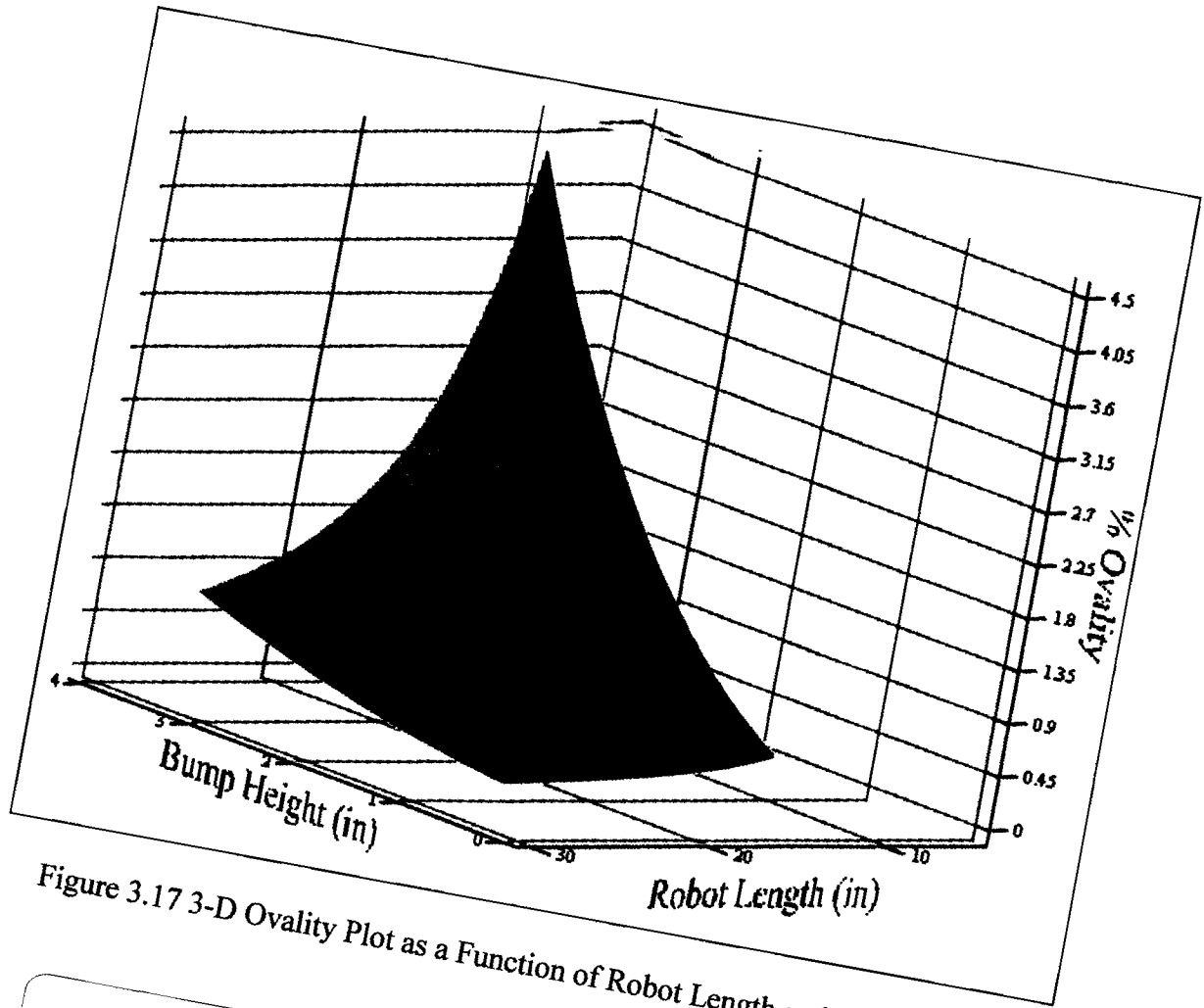


Figure 3.17 3-D Ovality Plot as a Function of Robot Length and Bump Height

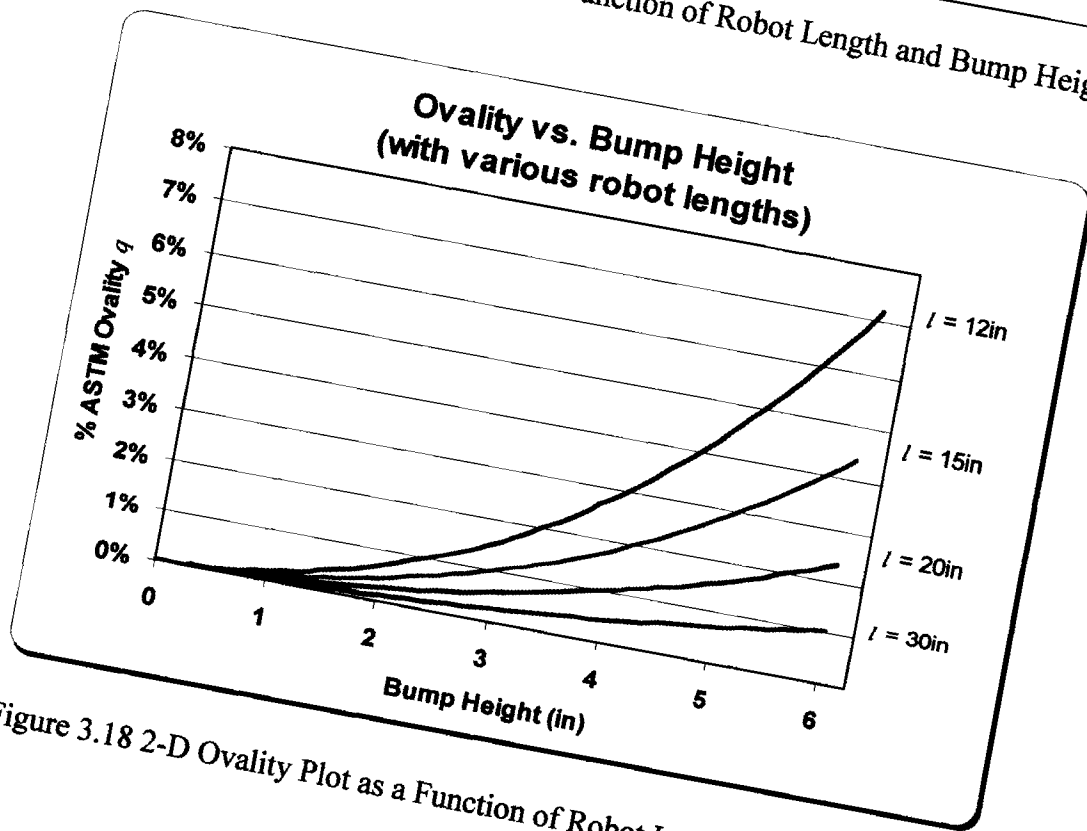


Figure 3.18 2-D Ovality Plot as a Function of Robot Length and Bump Height

From Figures 3.17 and 3.18 it is clear that shorter robots tend to cause more erroneous ovality than do longer robots. However, the total amount of ovality introduced is relatively small when considering the size of the bumps accounted for in Figures 3.17 and 3.18.

### **3.4 Erroneous Ovality Causes CIPP Liner Over-Design**

The erroneous ovality produced by a robot's misalignment with the pipe axis can cause pipe liners to be designed thicker than necessary. Over-designing a CIPP liner can cause unnecessary costs by wasting time and material. According to ASTM F1216-03, which was presented in Chapter 2 but is repeated here for clarity, the design equation for liners installed in partially deteriorated gravity pipes is Eq. (3.27).

$$P_{cr} = \frac{2 \cdot K \cdot E_L}{1 - \nu^2} \cdot \frac{1}{(SDR-1)^3} \cdot \frac{C}{N} \quad (3.27)$$

To see how erroneous ovality affects pipe liner design, one can find the overweighed liner thickness  $t_2$  as a function of the correct liner thickness  $t_1$  required if no erroneous ovality were present. This is accomplished by setting two liner design equations equal to each other with differing environments and pipe conditions as in Eq. (3.28).

$$\frac{2K_1 E_{L1}}{1 - \nu_1^2} \cdot \frac{1}{(SDR_1 - 1)^3} \cdot \frac{C_1}{N_1 P_1} = \frac{2K_2 E_{L2}}{1 - \nu_2^2} \cdot \frac{1}{(SDR_2 - 1)^3} \cdot \frac{C_2}{N_2 P_2} \quad (3.28)$$

which can be re-written as Eq. (3.29).

$$\frac{2K_1 E_{L1}}{2K_2 E_{L2}} \cdot \frac{1 - \nu_2^2}{1 - \nu_1^2} \cdot \frac{C_1 N_2 P_2}{C_2 N_1 P_1} = \frac{(SDR_1 - 1)^3}{(SDR_2 - 1)^3} \quad (3.29)$$

Assuming the same environmental conditions and pipe material, one can write  $OD_2 = OD_1$ ,  $P_2 = P_1$ ,  $N_2 = N_1$ ,  $E_{L2} = E_{L1}$ ,  $K_2 = K_1$ ,  $\nu_2 = \nu_1$ . Using the standard dimension ratio relationship,  $SDR = \frac{OD}{t}$ , Eq. 3.29 is simplified to give Eq. (3.30).

$$\frac{C_1}{C_2} = \frac{\left(\frac{OD}{t_1} - 1\right)^3}{\left(\frac{OD}{t_2} - 1\right)^3} \quad (3.30)$$

Solving Eq. (3.30) for  $t_2$  gives Eq. (3.31).

$$t_2 = \frac{OD}{\left(\frac{OD}{t_1} - 1\right) \cdot \left(\frac{C_2}{C_1}\right)^{1/3} + 1} \quad (3.31)$$

Assuming the original pipe has no ovality allows  $C_2 = 1$ , and plugging in the ovality reduction factor for  $C_1$  gives Eq. (3.32).

$$t_2 = \frac{OD}{\left(\frac{OD}{t_1} - 1\right) \cdot \frac{\left(1 + \frac{q}{100}\right)^2}{\left(1 - \frac{q}{100}\right)} + 1} \quad (3.32)$$

Assuming  $OD = ID$  of the host pipe = 12",  $t_1 = 0.25"$ ,  $q_e$  can be varied according to Eq. (3.21) which takes into account the robot's meander with respect to the pipe. To compare the over-designed liner  $t_2$  to the correct liner dimension  $t_1$ , the following percent difference equation will be used in Eq. (3.33).

$$CIPP \text{ Liner Thickness Percent Difference} = \frac{|t_2 - t_1|}{t_1} \quad (3.33)$$

A plot of the CIPP liner thickness over-design versus the meander angle of the misaligned robot is shown in Figure 3.19.

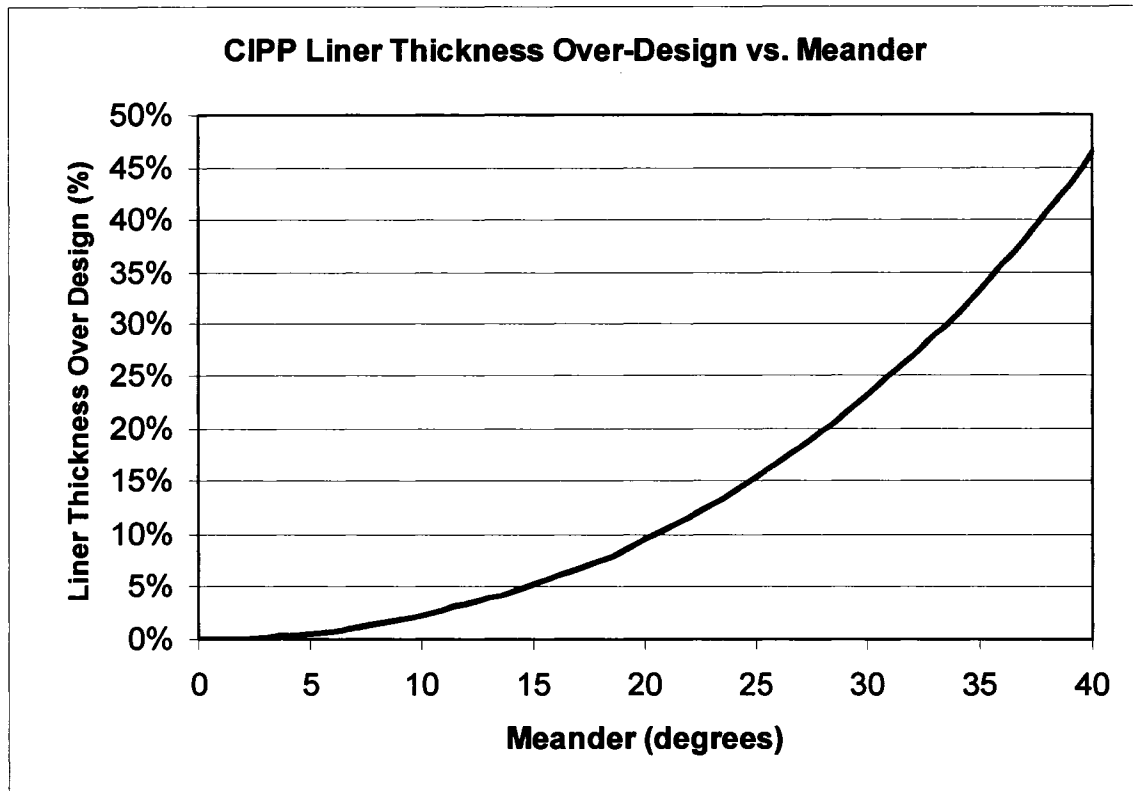


Figure 3.19 Liner Thickness Over-Design Due to Erroneous Ovality

From Figure 3.19 it seems that even with a significant meander angle, the extra thickness required by the CIPP is not very substantial.

### 3.5 Conclusions

Several researchers have identified the fact that pipe profiling robots move relative to the pipe while performing pipe inspections. When the robot's axis is no longer parallel to the pipe axis, four distinct problems can ensue:

1. The reporting of erroneous ovality in a perfectly cylindrical pipe.
2. Incorrect distance measurements to defect locations along the pipe.



3. Three-dimensional wireframe distortion of pipe profiles.
4. The over-design of cured in place pipe liners used to rehabilitate pipelines as per ASTM F126-03.

These four problems were quantified in this chapter, but were found to have relatively low magnitudes, even with substantial misalignments of the robot relative to the pipe. However, as pipe profiling technology continues to improve and is further developed, position and orientation estimation techniques will provide an accurate and repeatable method of sewer assessment as required by GASB 34.

## CHAPTER 4

### A NEW STRATEGY FOR POSITION AND ORIENTATION ESTIMATION

Several researchers have noted the need for estimating the position and orientation of a pipe profiler to accurately report ovality, the location of pipe defects, and prevent three-dimensional wireframe distortion. Several methods have been posited by researchers to estimate the position and orientation of a robot; these methods were reviewed in Chapter 2. This chapter presents a new technique to establish four of the six degrees of freedom between the robot and the pipe using radial measuring devices at both ends of the profiler.

This first section of Chapter 4 presents the methodology of the proposed position and orientation estimation technique and the steps necessary for its implementation on a pipe profiler. The new technique assumes the pipe profiler is outfitted with the following sensors:

1. Radial measuring devices at both ends of the robot.
2. An odometric sensor to measure the length of the pipe traversed by the robot.

The aim of this first section is to provide the details needed to correctly orient the radial measurements taken by a pipe profiler relative to the axis of the pipe.

The second section demonstrates the new position and orientation technique by applying homogeneous coordinate transformations to simulated radial measurements. Four distinct coordinate systems are defined to delineate the multiple measurement reference frames for a robot-pipe-earth system. The simulated radial measurements are based on mathematically generated data that would be obtained by incrementally rotating two radial measuring devices in a perfectly cylindrical pipe. The three-dimensional simulated radial measurements are plotted on the four different coordinate reference frames to provide visual confirmation that the new position and orientation estimation technique is valid.

#### **4.1 A New Technique for Position and Orientation Estimation**

To determine the robot's position and orientation relative to the pipe, two coordinate systems must be fully defined. There are six possible degrees of freedom (DOF) between the robot and the pipe, three translations and three rotations; knowledge of all six DOF allows the two coordinate systems to be fully defined. This would allow for the correction of erroneous ovality and distance measurement error as described in Chapter 3. The six DOF for the robot-pipe system are as follows:

1. Axial translation  $x$  of the robot down the pipe.
2. Vertical translation  $y$  of the robot relative to the pipe.
3. Horizontal translation  $z$  of the robot relative to the pipe.
4. Horizontal meander or yaw angle  $\theta_h$  of the robot relative to the pipe.
5. Vertical pitch angle  $\theta_v$  of the robot relative to the pipe.
6. Roll angle  $\theta_r$  of the robot relative to the pipe.

Sewer inspection robots are usually outfitted with odometric sensors such as encoders to measure the  $x$ -distance traveled by the robot down the pipe. Such a device is capable of measuring the distance traveled along the pipe to the rear of the robot but must be transformed to compensate for distance measurement error. The new position and orientation technique presented here assumes the  $x$ -distance to the rear of the robot is known.

Typically, measuring  $\theta_r$ , the roll angle of the robot relative to the pipe is not useful. The new position and orientation technique presented here assumes  $\theta_r$  is zero. However, the roll angle of the robot relative to gravity  $\theta_R$  is of interest for correcting the twist of three dimensional wireframes and is employed in Section 4.2 as part of the robot-pipe-earth system. This leaves four of the six DOF to be defined using the new position and orientation technique:

1. Vertical translation  $y$  of the robot relative to the pipe.
2. Horizontal translation  $z$  of the robot relative to the pipe.
3. Horizontal meander or yaw angle  $\theta_h$  of the robot relative to the pipe.
4. Vertical pitch angle  $\theta_v$  of the robot relative to the pipe.

The points of radial measurement on the rear and front of the robot are labeled point P and point Q, respectively. The points of radial measurements, P and Q, correspond to the center of rotation of the system that gathers radial pipe measurements, such as a side-facing camera-laser scanner or a tactile probe. The line between P and Q defines the “robot axis” and is shown in Figure 4.1.

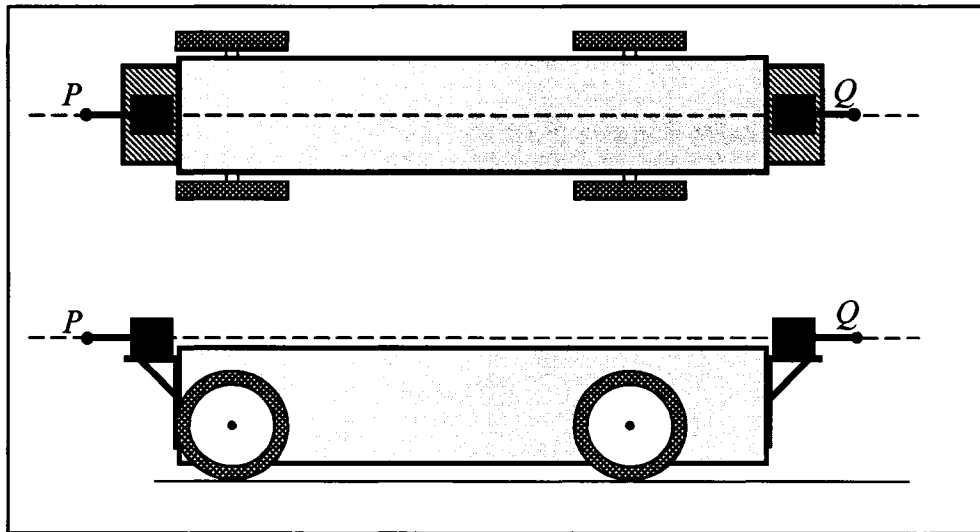


Figure 4.1 Location of Points  $P$  and  $Q$  on Robot's Reference Frame

Since the robot is free to move relative to the pipe according to the six DOF mentioned, the robot's axis between point  $P$  and  $Q$  is represented by a straight line within the pipe as shown in Figure 4.2. The red lines represent the planes of measurement and are also shown in Figure 4.2.

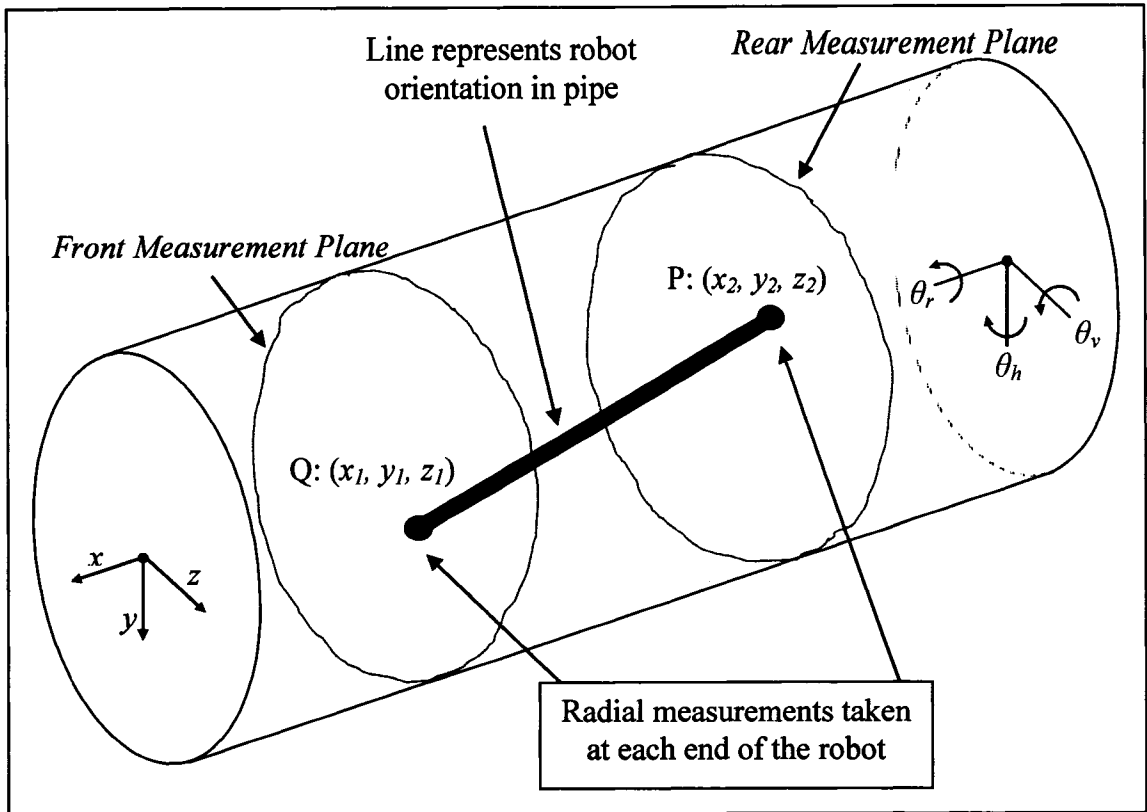


Figure 4.2 Front and Rear Points of Measurements with Six Degrees of Freedom

By taking radial measurements at the front and rear of the robot, the centroid of each “ring” of data on the planes of measurement can be related to the points of radial measurements P and Q as shown in Figure 4.3

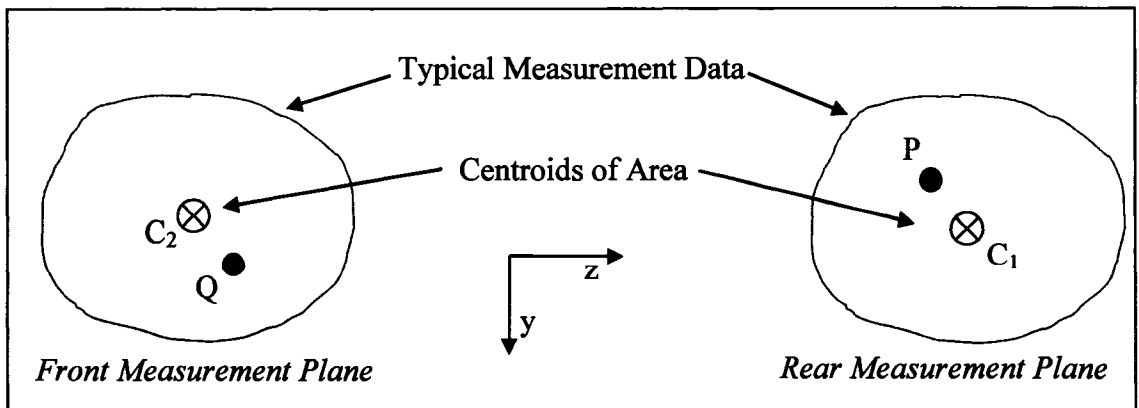


Figure 4.3 Centroid Offsets Depicting Radial Points of Measurements

The centroid locations  $C_1$  and  $C_2$  relative to points P and Q can be calculated using the discrete form of Green's Theorem introduced in Chapter 2 but repeated here for clarity in Eqs. (4.1) and (4.2).

$$\bar{z} = \frac{Q_y}{A} = \frac{\frac{1}{6} \sum_{i=0}^{n-1} (y_{i+1} - y_i)(z_i^2 + z_i z_{i+1} + z_{i+1}^2)}{\frac{1}{2} \sum_{i=0}^{n-1} (y_i + y_{i+1})(z_{i+1} - z_i)} \quad (4.1)$$

$$\bar{y} = \frac{Q_z}{A} = \frac{\frac{1}{6} \sum_{i=0}^{n-1} (z_{i+1} - z_i)(y_i^2 + y_i y_{i+1} + y_{i+1}^2)}{\frac{1}{2} \sum_{i=0}^{n-1} (y_i + y_{i+1})(z_{i+1} - z_i)} \quad (4.2)$$

where the  $(y, z)$  coordinates at angular increment  $i$  and  $i+1$  are used define the contribution of the  $i^{\text{th}}$  line segment to the  $\bar{y}$  and  $\bar{z}$  centroidal distances. Here,  $i$  is the number of radial measurements taken per ring at a given  $x$  translation along the length of the pipe.

Since the P and Q offsets relative to the centroids are not necessarily the same, the rear offset for point P, as measured from  $C_1$ , will be denoted as  $(\bar{y}, \bar{z})$ . Similarly, the front offset for point Q, as measured from  $C_2$ , will be denoted as  $(\bar{w}, \bar{v})$ . These offsets are shown in Figure 4.4.

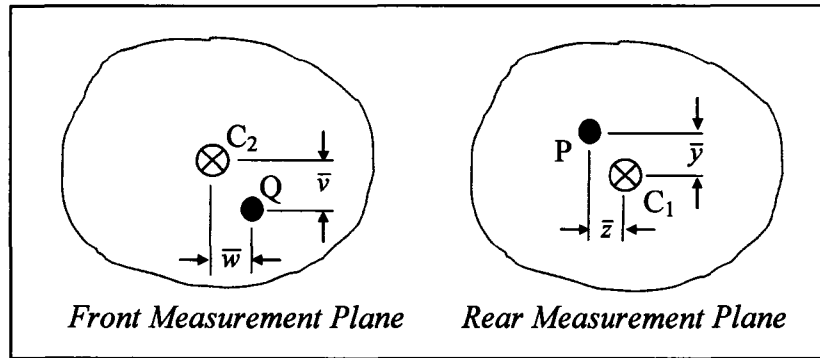


Figure 4.4 Centroid Offsets Defined Relative to the Points of Measurements

The horizontal meander angle  $\theta_h$  and vertical pitch angle  $\theta_v$  of the robot with respect to the pipe can be written in terms of the centroid offsets. Using the coordinate system developed in Chapter 3,  $\theta_h$  and  $\theta_v$  can be written as expressions of  $\bar{z}$ ,  $\bar{y}$ ,  $\bar{w}$ , and  $\bar{v}$  as in Eqs. (4.3) and (4.4).

$$\theta_h = \tan^{-1} \left( \frac{\bar{w} - \bar{z}}{|\overline{PQ}|} \right) \quad (4.3)$$

$$\theta_v = \tan^{-1} \left( \frac{\bar{v} - \bar{y}}{|\overline{PQ}|} \right) \quad (4.4)$$

where  $|\overline{PQ}|$  = length of the robot between the two points of measurement.  $\theta_h$  and  $\theta_v$  are illustrated in Figure 4.5.



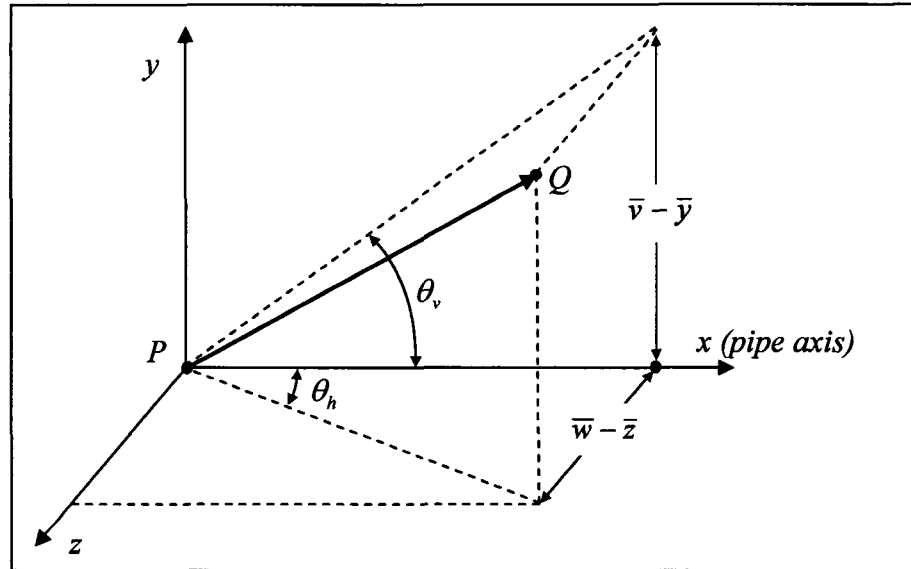


Figure 4.5  $\theta_h$  and  $\theta_v$  Related to  $\bar{z}$ ,  $\bar{y}$ ,  $\bar{w}$ , and  $\bar{v}$

This completes the description of the variables required for the new position and orientation estimation technique. Implementation of the technique on an existing pipe profiling robot includes the following:

1. Install a second radial measuring device on the profiler so that radial measurements can be taken at the front and rear of the robot. Care must be taken to ensure the two radial measuring systems are installed parallel to each other and perpendicular to the robotic platform.
2. Measure and record the distance between the two centers of radial measurement (point P and point Q).
3. Calculate the centroidal offsets  $\bar{z}$ ,  $\bar{y}$ ,  $\bar{w}$ , and  $\bar{v}$  using Eqs. (4.1) and (4.2).
4. Calculate the horizontal meander angle  $\theta_h$  and vertical pitch angle  $\theta_v$  of the robot with respect to the pipe using Eqs. (4.3) and (4.4).

5. Transform the radial measurement data by rotating it about the horizontal and vertical axes by  $\theta_v$  and  $\theta_h$ , respectively, using the homogenous coordinate transformations introduced in Chapter 2.

The transformed data from step five effectively removes the unwanted influences of robot pitch and yaw from laser profiling measurements.

## **4.2 Simulated Elliptical-Shaped Radial Measurements**

Next, the coordinate transformations are demonstrated using simulated radial measurements; simulated measurements are provided to visually confirm the transformation procedures. This section first defines several coordinate systems for a system considering (1) the profiling robot, (2) a perfectly cylindrical pipe, (3) the orientation of the elliptical simulated radial measurements, and (4) gravity.

After the coordinate systems are defined, offset radial descriptors are developed to simulate the radial measurements taken by a robot in a cylindrical pipe. The simulated data points are then systematically transformed from one coordinate system to the next until the profiling data is correctly referenced to the pipe axis and gravity. Appropriate graphs and diagrams accompany each of the coordinate transformations to illustrate the new position and orientation estimation technique and to provide visual confirmation that the transformations were applied correctly.

### **4.2.1 Coordinate System** **Definitions**

Section 4.1 defined two coordinate systems, one attached to the robot and one attached to the pipe. A third reference frame used in this research is defined by a Cartesian coordinate system relative to earth's gravitational field. Two of the robot's

angles relative to gravity are measured using a tri-axis accelerometer configured as a roll and pitch sensor. A fourth coordinate system is defined to orient the simulated radial measurements relative to the robot. To fully define the robot-pipe-gravity system, the relationships between all four coordinate systems must be defined. The four coordinate systems defined for this research are depicted in Figures 4.6 and 4.7.

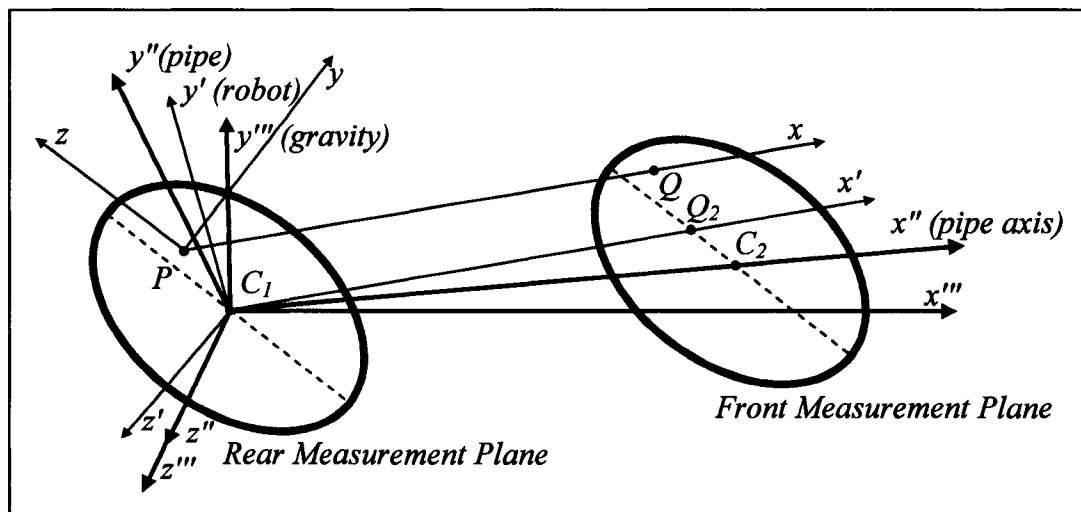


Figure 4.6 3-D View of the Four Coordinate Systems Used for the Robot-Pipe-Gravity System

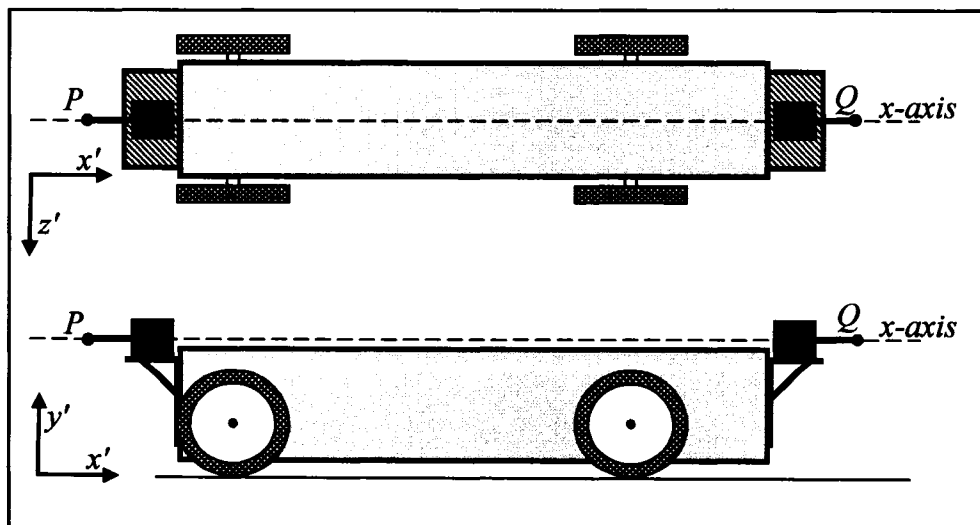


Figure 4.7 Location of Points  $P$  and  $Q$  on Robot's Reference Frame

The four coordinate systems used in this research are:

1. The un-primed coordinate system,  $x$ - $y$ - $z$ , originates at the rear point of radial measurement, point P. The  $z$ -axis is oriented such that it is parallel to the major axis of the simulated elliptical data. The  $x$ -axis passes through the center of rotation of the front and rear radial measurement devices. Thus, point Q defines the location center of rotation of the front radial measurement device. The  $x$ -axis is the only axis that is physically attached to the robot.
2. The primed coordinate system,  $x'$ - $y'$ - $z'$ , originates at the rear centroid  $C_1$  so that the  $x'$ -axis is parallel to the  $x$ -axis; here, the  $x'$  axis is simply translated from P to  $C_1$ . The  $y'$ -axis points away from the top plane of the robot, and the  $z'$ -axis points away from the right side of the robot. That is, the  $y'$ - and  $z'$ -axes are defined based solely on robot geometry.
3. Transforming from  $x'$ - $y'$ - $z'$  coordinate system to account for roll, pitch and yaw results in the  $x''$ - $y''$ - $z''$  coordinate system. As described later, the rotations to transform between the primed and double primed coordinate systems are performed with roll being first followed by pitch and yaw. After the three rotations, the  $x''$ -axis is coincident with the pipe axis and extends through the front centroid  $C_2$ . The  $z''$ -axis is set to be perpendicular to the pipe axis (the  $x''$ -axis) and to gravity.
4. Transforming from  $x''$ - $y''$ - $z''$  coordinate system to account for the pitch of the pipe relative to gravity results in the  $x'''$ - $y'''$ - $z'''$  coordinate system (a rotation about the  $z''$ -axis). The triple-primed coordinate system originates at the rear centroid  $C_1$  and is oriented such that the  $y'''$ -axis corresponds to the gravity vector. The  $x'''$  and

$z'''$  axes are oriented perpendicular to each other and to gravity. Since neither the roll angle of the pipe with respect to gravity nor the pipe's yaw angle relative to gravity can be resolved, the  $x'''$ - $y'''$ -plane remains co-planar to the  $x''$ - $y''$ -plane. The angle between the  $x'''$ -axis and the  $x''$ -axis varies according to the pitch angle of the pipe relative to gravity as does the angle between the  $y'''$ -axis and  $y''$ -axis.

To determine the magnitudes of the values required for the coordinate transformations, each of the points on front and rear measurement planes must be fully defined. The rear measurement plane uses  $x$ - $y$ - $z$  notation and the front measurement plane uses  $u$ - $v$ - $w$  notation. Figure 4.8 depicts rear measurement plane geometry; here, the  $x$ -axis goes straight into the page at P.

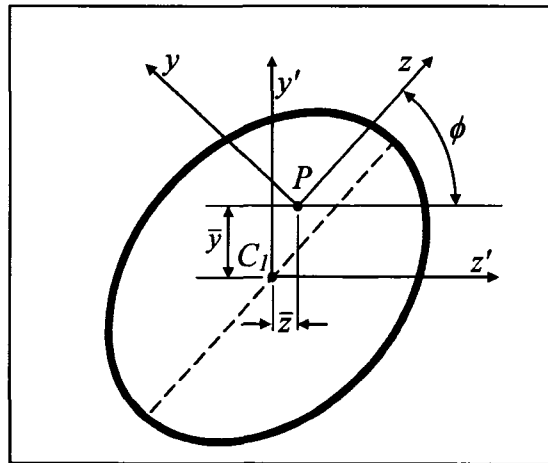


Figure 4.8 2-D Rear View of Rear Measurement Plane Introducing  $\bar{z}$  and  $\bar{y}$

Figure 4.8 exhibits several important geometric relationships.  $\bar{z}$  and  $\bar{y}$  are the horizontal and vertical distances in the  $y'$ - $z'$  plane from the rear centroid  $C_1$  to the rear point of radial measurement P. The  $z$ -axis is parallel to the ellipse's major axis and is angularly offset from being parallel to the  $z'$  axis by the angle  $\phi$ .  $\phi$  is only useful for

orienting the simulated radial measurements and is not necessary for the transformation of a pipe profiler's actual radial measurement; it is presented here for clarity.  $\phi$  is defined after the front measurement plane is described in Figure 4.9.

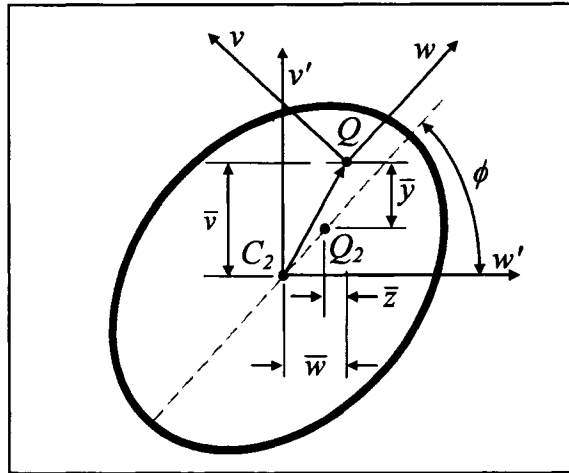


Figure 4.9 2-D Rear View of Front Measurement Plane Introducing  $\bar{w}$  and  $\bar{v}$

Figure 4.9 exhibits several important geometric relationships.  $\bar{w}$  and  $\bar{v}$  are the horizontal and vertical distances in the  $v'$ - $w'$  plane from the front centroid  $C_2$  to the front point of radial measurement  $Q$ . The  $w$ -axis is parallel to the ellipse's major axis and is angularly offset from the  $w'$  axis by the angle  $\phi$ . Point  $Q_2$  is offset from the point of radial measurement  $Q$  by  $\bar{z}$  and  $\bar{y}$ , the horizontal and vertical distances from the rear centroid  $C_1$  to the point of radial measurement  $P$  as seen in Figure 4.8. The length difference between  $\bar{v}$  and  $\bar{y}$  and between  $\bar{w}$  and  $\bar{z}$  can be used to find angle  $\phi$  as shown in Figure 4.10.

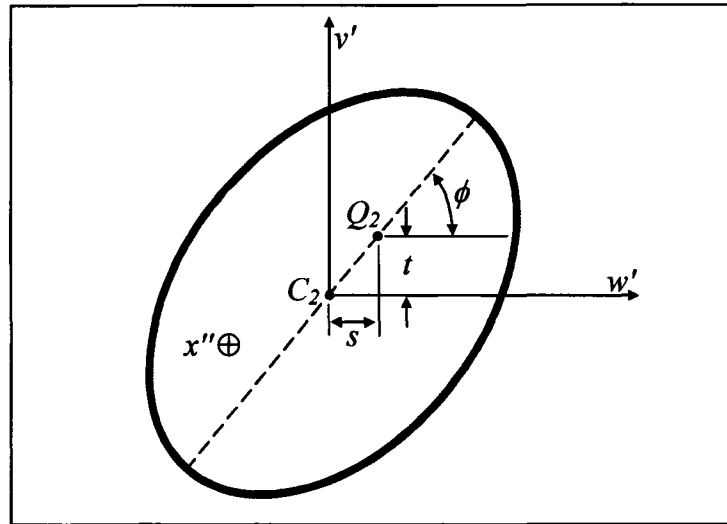


Figure 4.10 2-D Rear View of Front Measurement Plane Introducing  $s$  and  $t$

It is clear from Figure 4.10 that Eqs. (4.5) and (4.6) are true.

$$t = \bar{v} - \bar{y} \quad (4.5)$$

$$s = \bar{w} - \bar{z} \quad (4.6)$$

Using these relationships, the angle  $\phi$  can be written as Eq. (4.7).

$$\phi = \tan^{-1}\left(\frac{t}{s}\right) \quad (4.7)$$

#### **4.2.2 Development of an Offset Elliptical Radial Descriptor**

Radial measurements taken by a profiler in a perfectly cylindrical pipe have an elliptical profile. For the purposes of generalizing the elliptical points expected by a pipe profiler, it is necessary to use the general form of the ellipse equation which allows for an offset origin at  $(h, k)$ . Such an ellipse is defined by Eq. (4.8).

$$\frac{(z - h)^2}{A^2} + \frac{(y - k)^2}{B^2} = 1 \quad (4.8)$$

This ellipse is in Cartesian form and is depicted graphically in Figure 4.11.

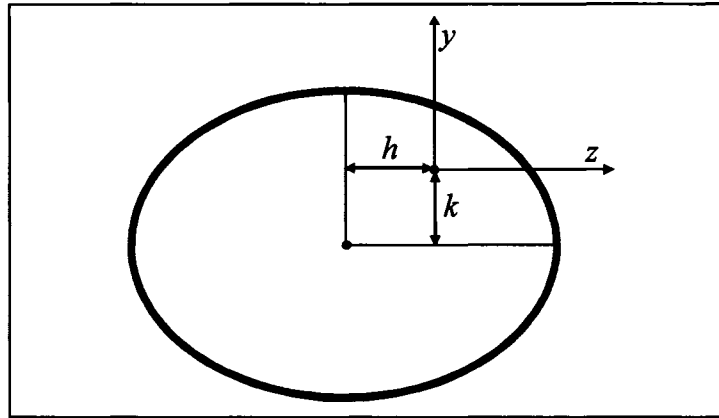


Figure 4.11 Offset Ellipse with Origin at  $(h, k)$  in Cartesian Coordinates

Since the data collection with the experimental pipe profiling robot is gathered by incrementally rotating a stepper motor and taking radial measurements of the pipe, the ellipse must be transformed to cylindrical coordinates. The following general cylindrical-to-Cartesian coordinate conversion will be used in conjunction with the Cartesian offset center ellipse model in Eqs (4.9) and (4.10).

$$y = r \sin \theta \quad (4.9)$$

$$z = r \cos \theta \quad (4.10)$$

Substituting Eqs. (4.9) and (4.10) into Eq. (4.8) yields Eq. (4.11).

$$\frac{(r \cos \theta - h)^2}{A^2} + \frac{(r \sin \theta - k)^2}{B^2} = 1 \quad (4.11)$$

This coordinate transformation is depicted graphically in Figure 4.12.



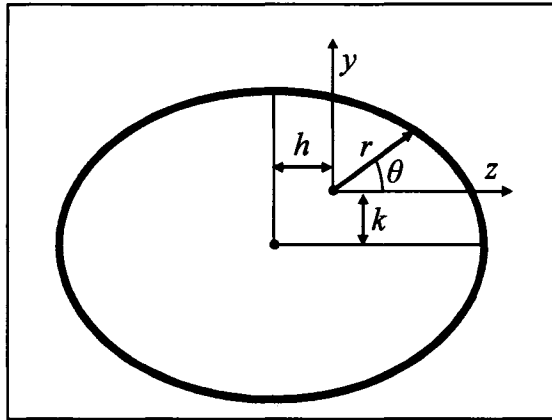


Figure 4.12 General Offset Ellipse with Origin at  $(h, k)$  in Cylindrical Coordinates

Solving Eq. (4.11) for  $r$  is algebraically intensive. Mathcad's® symbolic solver [73] was utilized to find the solution to this problem which can be written as Eq. (4.12).

$$r = \frac{A^2 \sin \theta \cdot k + B^2 \cos \theta \cdot h \pm D}{-A^2 \cos^2 \theta + A^2 + B^2 \cos^2 \theta} \quad (4.12)$$

where

$$D = \left[ A^2 B^2 \left( 2 \sin \theta \cdot k \cos \theta \cdot h - h^2 + \cos^2 \theta \cdot h^2 + A^2 - A^2 \cos^2 \theta - k^2 \cos^2 \theta \right) \right]^{\frac{1}{2}}$$

Since  $r$  is always positive for pipe profiling experiments, only the  $+D$  term is used for the simulated radial measurements.

#### **4.2.3 Relating the General Ellipse to the Primed Coordinate System**

The ellipse's minor axis  $B$  is equal to the radius of the undeformed pipe  $r$  as illustrated in Chapter 3. The magnitude of the ellipse's major axis  $A$  can be determined from the relationship derived in Chapter 3 in terms of the robot's horizontal meander angle  $\theta_h$  and the robot's vertical pitch angle  $\theta_v$ , with respect to the pipe and is repeated here for clarity in Eq. (4.13).

$$A = r \cdot [1 + \tan(\theta_v)^2 + \tan(\theta_h)^2]^{1/2} \quad (4.13)$$

This relationship was derived assuming the robot's horizontal and vertical angular deviations with respect to the pipe,  $\theta_h$  and  $\theta_v$ , were known. Using the coordinate systems developed in Section 4.2.1,  $\theta_h$  and  $\theta_v$  can be written as expressions of  $\bar{z}$ ,  $\bar{y}$ ,  $\bar{w}$ , and  $\bar{v}$  in the primed coordinate system as in Eqs. (4.14) and (4.15).

$$\theta_h = \tan^{-1} \left( \frac{\bar{w} - \bar{z}}{|\overline{PQ}|} \right) \quad (4.14)$$

$$\theta_v = \tan^{-1} \left( \frac{\bar{v} - \bar{y}}{|\overline{PQ}|} \right) \quad (4.15)$$

where  $|\overline{PQ}| \approx |\overline{C_1C_2}|$  using small angle approximations.  $\theta_h$  and  $\theta_v$  are illustrated in

Figure 4.13.

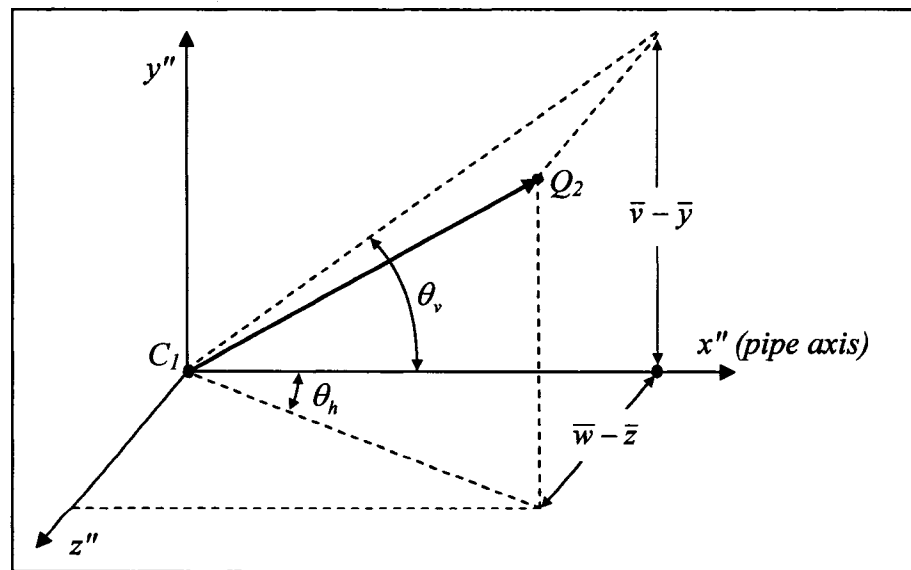


Figure 4.13  $\theta_h$  and  $\theta_v$  Related to  $\bar{z}$ ,  $\bar{y}$ ,  $\bar{w}$ , and  $\bar{v}$

#### **4.2.4 Development of the Rear Elliptical Offset**

To plot the simulated radial measurements it is necessary to first develop expressions for the ellipse's vertical and horizontal offsets ( $h$ ,  $k$ ) relative to the centroid. This requires deeper analysis of the front and rear elliptical profiles and the coordinate systems associated with the centroids and points of radial measurements. The rear profile has the geometry shown in Figure 4.14.

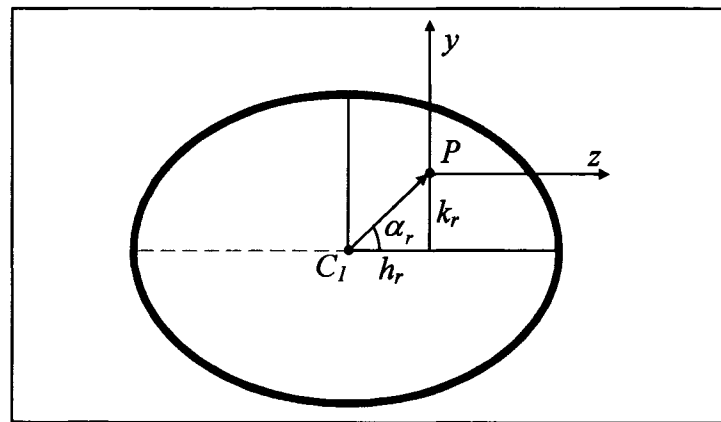


Figure 4.14 Rear View of the Rear Elliptical Profile

Point P is the rear point of radial measurement by the pipe profiler, point  $C_1$  is the centroid of the rear pipe profile,  $k_r$  is the  $y$ -offset from the major axis,  $h_r$  is the  $z$ -offset from the minor axis, and  $\alpha_r$  is the angle formed between the line  $\overline{C_1P}$  and the major axis. Examining Figure 4.14 provides the relations in Eqs. (4.16) and (4.17).

$$k_r = -|\overline{C_1P}| \sin \alpha_r \quad (4.16)$$

$$h_r = -|\overline{C_1P}| \cos \alpha_r \quad (4.17)$$

To calculate  $\overline{|C_1P|}$  and  $\alpha_r$ , in terms of  $\bar{z}$  and  $\bar{y}$ , the  $x$ - $y$ - $z$  coordinate system must be related to the primed coordinate system as shown in Figure 4.15.

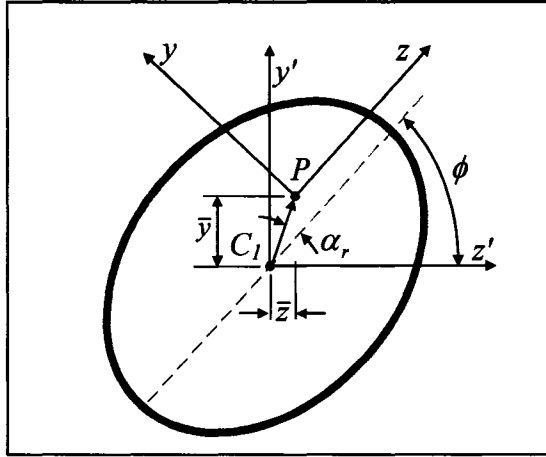


Figure 4.15 Rear Elliptical Profile on Primed Coordinate System Rotated by Angle  $\phi$

From Figure 4.15  $\alpha_r$  can be related to  $\phi$  by Eq. (4.18).

$$\alpha_r + \phi = \tan^{-1}\left(\frac{\bar{y}}{\bar{z}}\right) \quad (4.18)$$

$\overline{|C_1P|}$  is related to  $\bar{y}$  and  $\bar{z}$  by Eq. (4.19).

$$\overline{|C_1P|} = \sqrt{\bar{y}^2 + \bar{z}^2} \quad (4.19)$$

Substituting Eqs. (4.19) and (4.18) into (4.16) and (4.17) gives Eqs. (4.20) and (4.21).

$$k_r = -\sqrt{\bar{y}^2 + \bar{z}^2} \cdot \sin\left(\tan^{-1}\left(\frac{\bar{y}}{\bar{z}}\right) - \phi\right) \quad (4.20)$$

$$h_r = -\sqrt{\bar{y}^2 + \bar{z}^2} \cdot \cos\left(\tan^{-1}\left(\frac{\bar{y}}{\bar{z}}\right) - \phi\right) \quad (4.21)$$

Substituting Eqs. (4.5), (4.6) and (4.7) into Eqs. (4.20) and (4.21) gives Eqs. (4.22) and (4.23).

$$k_r = -\sqrt{\bar{y}^2 + \bar{z}^2} \cdot \sin\left(\tan^{-1}\left(\frac{\bar{y}}{\bar{z}}\right) - \tan^{-1}\left(\frac{\bar{v} - \bar{y}}{\bar{w} - \bar{z}}\right)\right) \quad (4.22)$$

$$h_r = -\sqrt{\bar{y}^2 + \bar{z}^2} \cdot \cos\left(\tan^{-1}\left(\frac{\bar{y}}{\bar{z}}\right) - \tan^{-1}\left(\frac{\bar{v} - \bar{y}}{\bar{w} - \bar{z}}\right)\right) \quad (4.23)$$

Equations (4.22) and (4.23) constitute the form of  $k_r$  and  $h_r$  with variables solely in the primed coordinate system including  $\bar{z}$ ,  $\bar{y}$ ,  $\bar{w}$  and  $\bar{v}$ . However, it is important to use the atan2 function in place of the atan function when dealing with problems that range from 0 to  $2\pi$  as is the case with the simulated radial measurements; see Chapter 2 for a discussion of the atan2 function. Since the atan2 function is undefined when both arguments are equal to zero, it is necessary to add a conditional statement to return a zero for this special case. Therefore, the final form of  $k_r$  and  $h_r$  as used in the Mathcad® worksheet with the radial measurement data simulator is noted in Eqs. (4.24) and (4.25).

$$k_r = -\sqrt{\bar{y}^2 + \bar{z}^2} \cdot \sin\left[\text{if}(\bar{y} \text{ or } \bar{z} \neq 0, \text{ then } \text{atan2}(\bar{z}, \bar{y}), \text{ else } 0) - \text{atan2}(\bar{w} - \bar{z}, \bar{v} - \bar{y})\right] \quad (4.24)$$

$$h_r = -\sqrt{\bar{y}^2 + \bar{z}^2} \cdot \cos\left[\text{if}(\bar{y} \text{ or } \bar{z} \neq 0, \text{ then } \text{atan2}(\bar{z}, \bar{y}), \text{ else } 0) - \text{atan2}(\bar{w} - \bar{z}, \bar{v} - \bar{y})\right] \quad (4.25)$$

These values of  $k_r$  and  $h_r$  from Eqs. (4.24) and (4.25) are inserted into Eq. (4.12) for  $h$  and  $k$  to provide an expression for the rear simulated radial measurements.

To demonstrate the output of the rear radial measurement simulator, assumptions must be made as to the position and orientation of the robot within a perfectly cylindrical pipe. For example purposes, the following input data will be used:

- *Pipe ID = 12in* therefore  $B = 6in$
- Length between radial measurement points:  $|\overline{PQ}| = 32.358in$
- $\bar{z} = 0.5in$ ,  $\bar{y} = 2in$ ,  $\bar{w} = 3in$ , and  $\bar{v} = 3.5in$
- Number of radial points to plot:  $i = 30$

Using the aforementioned input data, 30 radial points were plotted with a Mathcad® algorithm implementing Eq. (4.12) with  $k_r$  and  $h_r$ . As a result,  $A = 6.024in$ ,  $k_r = -1.458in$ ,  $h_r = -1.458in$ ,  $\theta_h = 4.418^\circ$ , and  $\theta_v = 2.654^\circ$ . The results of the rear simulated data with the given inputs are shown in Figure 4.16.

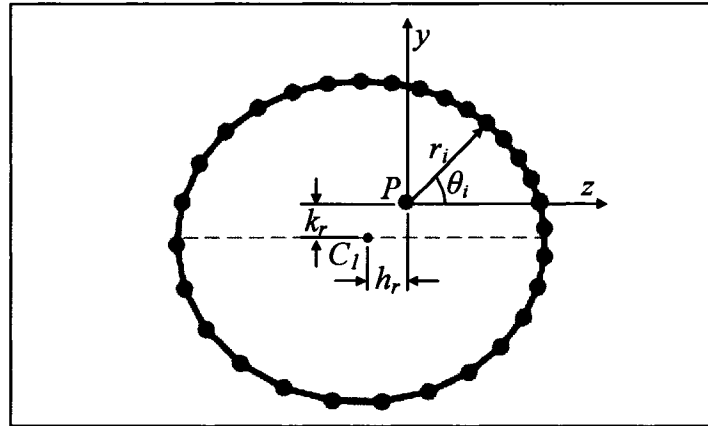


Figure 4.16 Rear Simulated Measurements on  $y$ - $z$  Coordinate System

As expected, the points nearest the point of radial measurement, point P, in Figure 4.16 are stacked closer together than those furthest from point P due to the constant angular increment  $\theta_i$ .

#### **4.2.5 Development of the Front Elliptical Offset**

Now that the simulated data is developed for the rear, a similar process is used to simulate the front radial measurement points. The front pipe profile as viewed from the back of the robot is depicted in Figure 4.17.

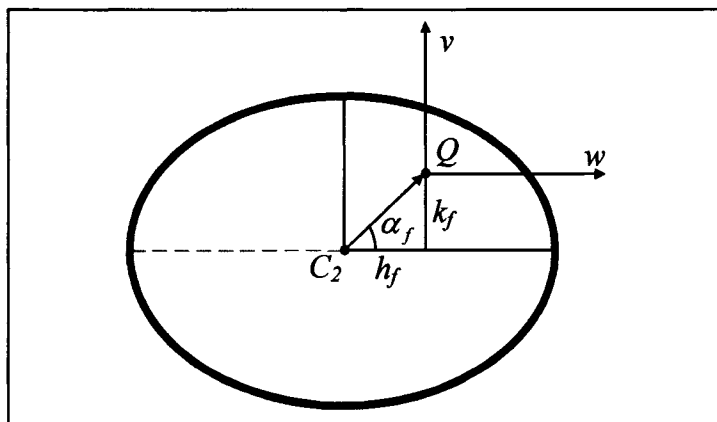


Figure 4.17 Rear View of the Front Measurement Plane

Point  $Q$  is the front point of radial measurement, point  $C_2$  is the centroid of the front pipe profile,  $k_f$  is the  $v$ -offset from the major axis,  $h_f$  is the  $w$ -offset from the minor axis, and  $\alpha_f$  is the angle formed between the line  $\overline{C_2Q}$  and the major axis.

Examining Figure 4.17 provides the relations of Eqs. (4.26) and (4.27).

$$k_f = -|\overline{C_2Q}| \sin \alpha_f \quad (4.26)$$

$$h_f = -|\overline{C_2Q}| \cos \alpha_f \quad (4.27)$$

To calculate  $|\overline{C_2Q}|$  and  $\alpha_f$  in terms of  $\bar{v}$  and  $\bar{w}$ , the  $v$ - $w$  coordinate system must be related to the primed coordinate system as shown in Figure 4.18.

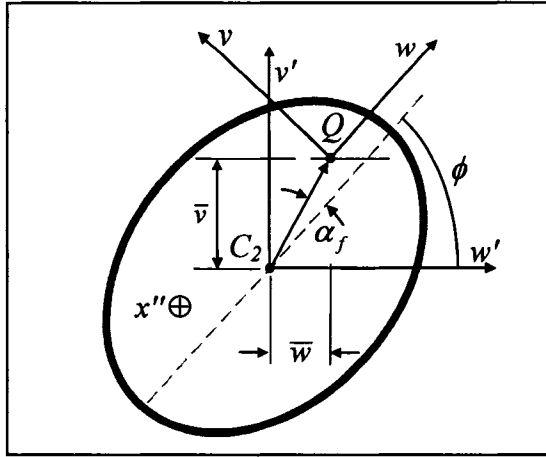


Figure 4.18 Front Elliptical Profile on Primed Coordinates Rotated by Angle  $\phi$

From Figure 4.18  $\alpha_f$  can be related to  $\phi$  by Eq. (4.28).

$$\alpha_f + \phi = \tan^{-1}\left(\frac{\bar{v}}{\bar{w}}\right) \quad (4.28)$$

$|\overline{C_2Q}|$  is related to  $\bar{v}$  and  $\bar{w}$  as in Eq. (4.29).

$$|\overline{C_2Q}| = \sqrt{\bar{v}^2 + \bar{w}^2} \quad (4.29)$$

Substituting Eqs. (4.28) and (4.29) into (4.27) and (4.26) gives Eqs. (4.30) and (4.31).

$$k_f = -\sqrt{\bar{v}^2 + \bar{w}^2} \cdot \sin\left(\tan^{-1}\left(\frac{\bar{v}}{\bar{w}}\right) - \phi\right) \quad (4.30)$$

$$h_f = -\sqrt{\bar{v}^2 + \bar{w}^2} \cdot \cos\left(\tan^{-1}\left(\frac{\bar{v}}{\bar{w}}\right) - \phi\right) \quad (4.31)$$

Substituting Eqs. (4.5), (4.6) and (4.7) into Eqs. (4.30) and (4.31) gives Eqs. (4.32) and (4.33).

$$k_f = -\sqrt{\bar{v}^2 + \bar{w}^2} \cdot \sin\left(\tan^{-1}\left(\frac{\bar{v}}{\bar{w}}\right) - \tan^{-1}\left(\frac{\bar{v} - \bar{y}}{\bar{w} - \bar{z}}\right)\right) \quad (4.32)$$



$$h_f = -\sqrt{\bar{v}^2 + \bar{w}^2} \cdot \cos\left(\tan^{-1}\left(\frac{\bar{v}}{\bar{w}}\right) - \tan^{-1}\left(\frac{\bar{v} - \bar{y}}{\bar{w} - \bar{z}}\right)\right) \quad (4.33)$$

Equation (4.32) and (4.33) constitute the final form of  $k_f$  and  $h_f$  with variables solely in the primed coordinate system including  $\bar{z}$ ,  $\bar{y}$ ,  $\bar{w}$ , and  $\bar{v}$ . As was the case with the rear  $h$  and  $k$  values, it is necessary to add a conditional statement to prevent the atan2 function from being undefined. Therefore, the final form of  $k_f$  and  $h_f$  as used in the Mathcad® sheet with the radial measurement data simulator is noted in Eqs. (4.34) and (4.35).

$$k_f = -\sqrt{\bar{v}^2 + \bar{w}^2} \cdot \sin\left[\text{if}(\bar{v} \text{ or } \bar{w} \neq 0, \text{ then } \text{atan2}(\bar{w}, \bar{v}), \text{ else } 0) - \text{atan2}(\bar{w} - \bar{z}, \bar{v} - \bar{y})\right] \quad (4.34)$$

$$h_f = -\sqrt{\bar{v}^2 + \bar{w}^2} \cdot \cos\left[\text{if}(\bar{v} \text{ or } \bar{w} \neq 0, \text{ then } \text{atan2}(\bar{w}, \bar{v}), \text{ else } 0) - \text{atan2}(\bar{w} - \bar{z}, \bar{v} - \bar{y})\right] \quad (4.35)$$

These values of  $k_f$  and  $h_f$  from Eqs. (4.34) and (4.35) are inserted into Eq. (4.12) for  $h$  and  $k$  to provide an expression for the front simulated radial measurements.

To demonstrate the front radial measurement simulator, the same assumptions will be made as to the position and orientation of the robot within a fictitious, perfectly cylindrical pipe as with the rear simulated radial measurements. Thirty radial points were plotted with a Mathcad® algorithm implementing Eq. (4.12) with  $k_f$  and  $h_f$ . As a result,  $A = 6.024in$ ,  $k_r = -1.458in$ ,  $h_r = -1.458in$ ,  $\theta_h = 4.418^\circ$ , and  $\theta_v = 2.654^\circ$  and resulted in Figure 4.19.

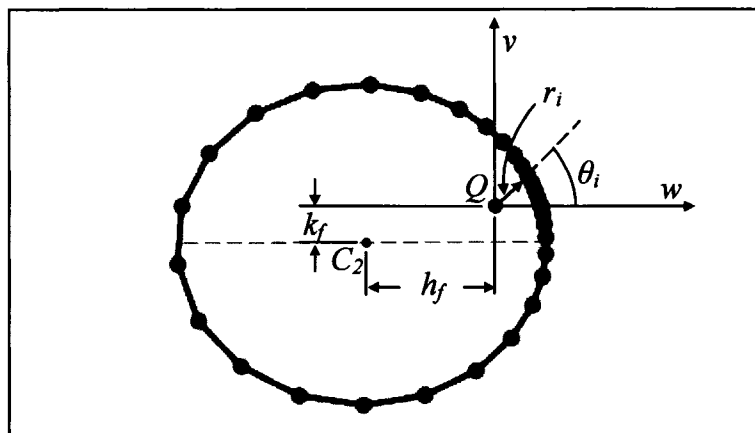


Figure 4.19 Front Simulated Measurements on  $v$ - $w$  Coordinate System

As expected, the points nearest Point Q in Figure 4.19 are stacked closer together than those furthest from Point P. Combining the front and rear simulated data together yields the three-dimensional plot shown in Figure 4.20.

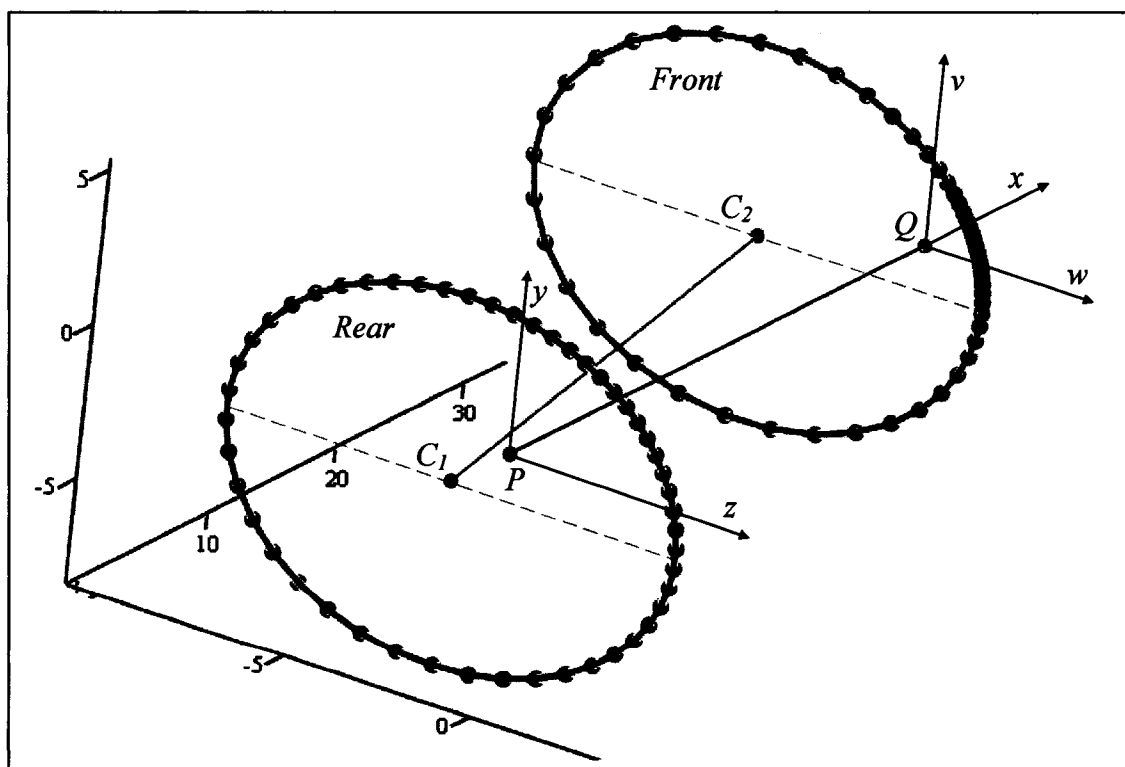


Figure 4.20 3-D View of Front and Rear Simulated Data on  $x$ - $y$ - $z$  Coord. Sys.

The  $x$ -axis originates at point P, the rear point of radial measurement, and extends through the front point of radial measurement, point Q. The front centroid, point  $C_2$ , and rear centroid, point  $C_1$ , lie on the pipe axis, and the major axes are denoted with dashed lines. The  $z$ -axis is parallel to the ellipses' major axes.

#### **4.2.6 Transformation from $x - y - z$ to $x' - y' - z'$**

Using the three-dimensional points developed for the front and rear simulated radial measurements, several transformations will be applied to relate the simulated radial measurements to real world coordinates. The first transformation to be applied involves a translation along the  $y'$ -axis and a translation along the  $z'$ -axis. The  $y'$ -shift and  $z'$ -shift are necessary to move the origin from point P to  $C_1$ . The variables used in the following transformation are noted in Eqs. (4.36), (4.37) and (4.38).

$$y'\text{-shift} = \bar{y} \quad (4.36)$$

$$z'\text{-shift} = \bar{z} \quad (4.37)$$

$$x\text{-rotation} = \phi \quad (4.38)$$

Applying the three dimensional homogeneous coordinate system transformation method gives Eq. (4.39).

$$\begin{bmatrix} x' \\ y' \\ z' \\ 1 \end{bmatrix} = T1 \begin{bmatrix} x \\ y \\ z \\ 1 \end{bmatrix} \quad (4.39)$$

where

$$T1 = \begin{bmatrix} 1 & 0 & 0 & 0 \\ 0 & \cos \phi & \sin \phi & 0 \\ 0 & -\sin \phi & \cos \phi & 0 \\ 0 & 0 & 0 & 1 \end{bmatrix} \cdot \begin{bmatrix} 1 & 0 & 0 & 0 \\ 0 & 1 & 0 & \bar{y} \\ 0 & 0 & 1 & \bar{z} \\ 0 & 0 & 0 & 1 \end{bmatrix} = \begin{bmatrix} 1 & 0 & 0 & 0 \\ 0 & \cos \phi & \sin \phi & \cos \phi \cdot \bar{y} + \sin \phi \cdot \bar{z} \\ 0 & -\sin \phi & \cos \phi & -\sin \phi \cdot \bar{y} + \cos \phi \cdot \bar{z} \\ 0 & 0 & 0 & 1 \end{bmatrix}$$

Equation (4.39) transforms each of the simulated three-dimensional points from the  $x$ - $y$ - $z$  coordinate system to the  $x'$ - $y'$ - $z'$  coordinate system as shown in Figure 4.21.

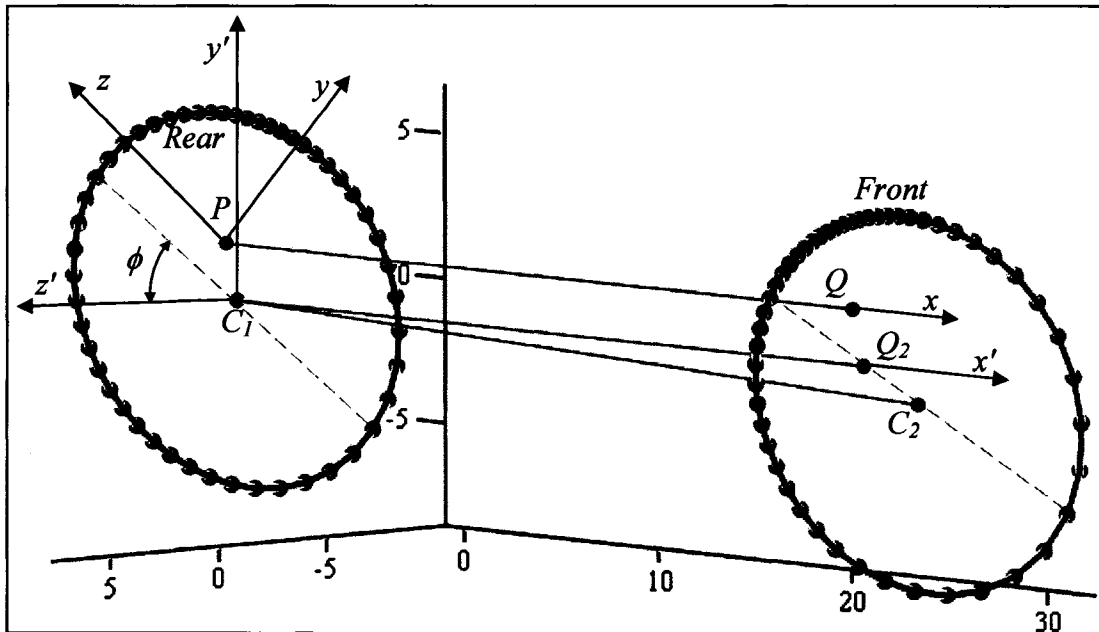


Figure 4.21 3-D View of Front and Rear Simulated Data on  $x'$ - $y'$ - $z'$  Coord. Sys.

The ellipses' major axes are denoted with dashed lines. For this example, the following inputs were used:  $B = 6in$ ,  $\overline{PQ} = 32.358in$ ,  $\bar{z} = 0.5in$ ,  $\bar{y} = 2in$ ,  $\bar{w} = 3in$ ,  $\bar{v} = 3.5in$  and  $i = 30$ .

#### **4.2.7 Transformation from $x'$ - $y'$ - $z'$ to $x''$ - $y''$ - $z''$**

The next transformation applied to the simulated radial measurements involves a rotation to compensate for the robot's roll angle with respect to gravity and rotations

about two axes to compensate for the robot's misalignment with the pipe. The first rotation angle has a magnitude of  $\theta_r$  and is rotated around the  $x'$ -axis.  $\theta_r$  is known as the robot's roll angle with respect to gravity and is measured by a roll sensor. The second rotation angle has a magnitude of  $\theta_h$  and is rotated around the  $y''$ -axis. This angle was referred to in Chapter 3 as the horizontal yaw or meander angle of the robot relative to the pipe. The third rotation angle has a magnitude of  $\theta_v$  and is rotated around the  $z''$ -axis. This angle was referred to in Chapter 3 as the vertical pitch angle of the robot relative to the pipe. Applying the three-dimensional homogeneous coordinate system transformation method gives Eq. (4.40).

$$\begin{bmatrix} x'' \\ y'' \\ z'' \\ 1 \end{bmatrix} = T2 \begin{bmatrix} x' \\ y' \\ z \\ 1 \end{bmatrix} \quad (4.40)$$

where

$$T2 = \begin{bmatrix} \cos\theta_v & -\sin\theta_v & 0 & 0 \\ \sin\theta_v & \cos\theta_v & 0 & 0 \\ 0 & 0 & 1 & 0 \\ 0 & 0 & 0 & 1 \end{bmatrix} \cdot \begin{bmatrix} \cos\theta_h & 0 & -\sin\theta_h & 0 \\ 0 & 1 & 0 & 0 \\ \sin\theta_h & 0 & \cos\theta_h & 0 \\ 0 & 0 & 0 & 1 \end{bmatrix} \cdot \begin{bmatrix} 1 & 0 & 0 & 0 \\ 0 & \cos\theta_r & \sin\theta_r & 0 \\ 0 & -\sin\theta_r & \cos\theta_r & 0 \\ 0 & 0 & 0 & 1 \end{bmatrix} =$$

$$\begin{bmatrix} \cos\theta_v \cos\theta_h & -\sin\theta_v \cos\theta_r + \cos\theta_v \sin\theta_h \sin\theta_r & -\sin\theta_v \sin\theta_r - \cos\theta_v \sin\theta_h \cos\theta_r & 0 \\ \sin\theta_v \cos\theta_h & \cos\theta_v \cos\theta_r + \sin\theta_v \sin\theta_h \sin\theta_r & \cos\theta_v \sin\theta_r - \sin\theta_v \sin\theta_h \cos\theta_r & 0 \\ \sin\theta_h & -\cos\theta_h \sin\theta_r & \cos\theta_h \cos\theta_r & 0 \\ 0 & 0 & 0 & 1 \end{bmatrix}$$

Section 4.2.2 provided Eqs. (4.41) and (4.42).

$$\theta_h = \tan^{-1} \left( \frac{\bar{w} - \bar{z}}{|PQ|} \right) \quad (4.41)$$

$$\theta_v = \tan^{-1} \left( \frac{\bar{v} - \bar{y}}{|PQ|} \right) \quad (4.42)$$

Equation (4.40) transforms each of the simulated radial measurements from the  $x'-y'-z'$  coordinate system to the  $x''-y''-z''$  coordinate system. The simulated radial measurements after these transformations are displayed in Figures 4.22 to 4.24.

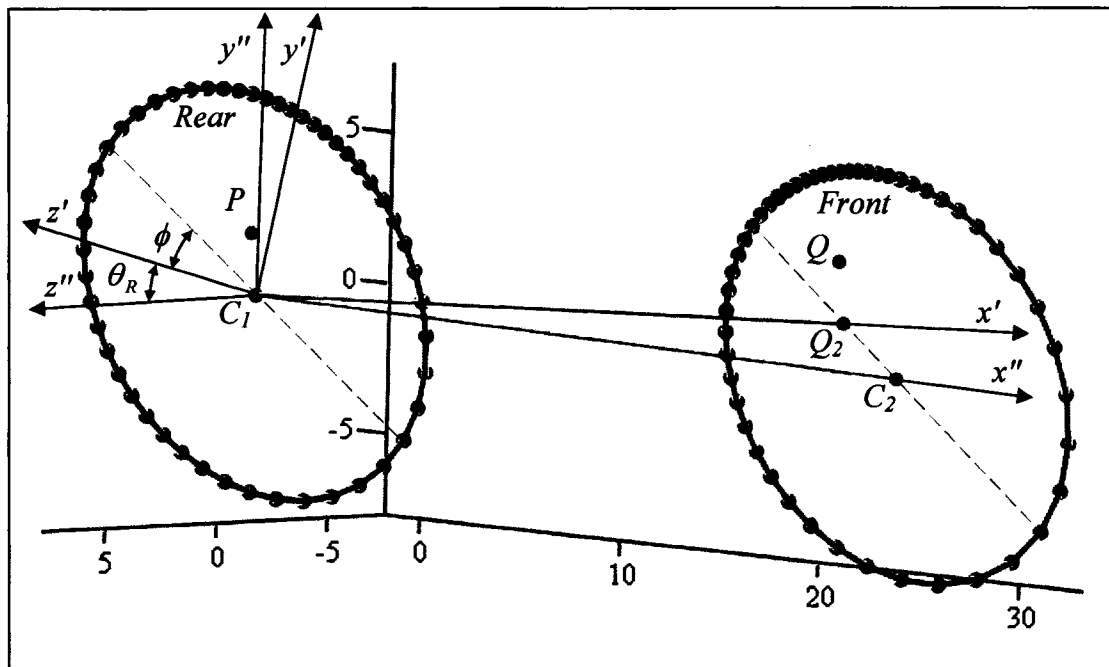


Figure 4.22 3-D View of Front and Rear Simulated Data on  $x''-y''-z''$  Coord. Sys.

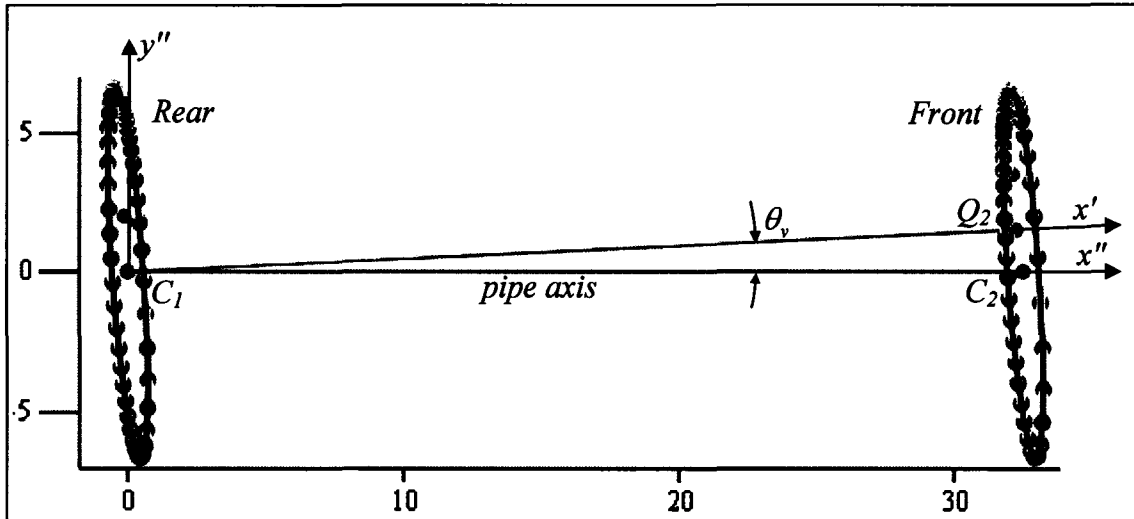


Figure 4.23 Side View of Front and Rear Simulated Data on  $x''$ - $y''$  Coord. Sys.

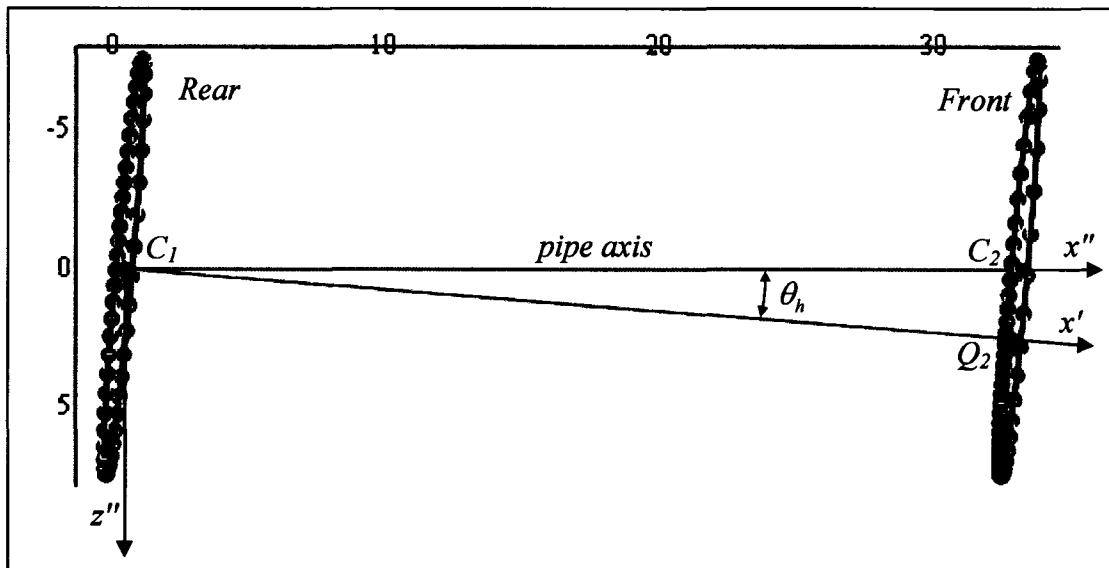


Figure 4.24 Top View of Front and Rear Simulated Data on  $x''$ - $z''$  Coord. Sys.

The  $x''$ -axis originates at the rear centroid  $C_1$  and extends through  $C_2$ . The major axes are denoted with dashed lines. For this example  $\theta_R$ , the roll of the robot with respect to gravity is assumed to be  $10^\circ$ , and all of the other variables are the same as the previous example.

#### 4.2.8 Transformation from $x''-y''-z''$ to $x'''-y'''-z'''$

The last transformation to apply to the simulated radial measurement points involves a rotation about a single axis. The rotation angle has a magnitude of  $\psi$  and is a rotation around the  $z''$ -axis.  $\psi$  is defined as the vertical pitch angle between the pipe and a vector perpendicular to gravity in Figure 4.25.

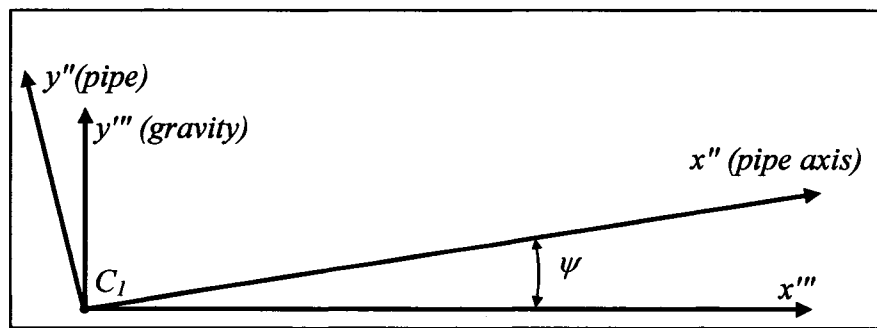


Figure 4.25 Definition of Pipe Pitch Angle with Respect To Gravity

$\psi$  is measured on the robot via an onboard inclinometer. Since an inclinometer will record any vertical pitch angle, the robot's vertical pitch angle  $\theta_v$  with respect to the pipe will also be captured in the inclinometer's output angle. Therefore, to isolate  $\psi$ ,  $\theta_v$  needs to be subtracted from the inclinometer output. For the radial measurement data simulator example,  $\psi$  is assumed to be  $7.5^\circ$ . Applying the three-dimensional homogeneous coordinate system transformation method gives Eq. (4.43).

$$\begin{bmatrix} x''' \\ y''' \\ z''' \\ 1 \end{bmatrix} = T_3 \begin{bmatrix} x'' \\ y'' \\ z'' \\ 1 \end{bmatrix} \quad (4.43)$$



where

$$T3 = \begin{bmatrix} \cos \psi & -\sin \psi & 0 & 0 \\ \sin \psi & \cos \psi & 0 & 0 \\ 0 & 0 & 1 & 0 \\ 0 & 0 & 0 & 1 \end{bmatrix}$$

Equation (4.43) transforms each of the simulated three-dimensional points from the  $x''$ - $y''$ - $z''$  coordinate system to the  $x'''$ - $y'''$ - $z'''$  coordinate system as depicted in Figures 4.26 to 4.28.

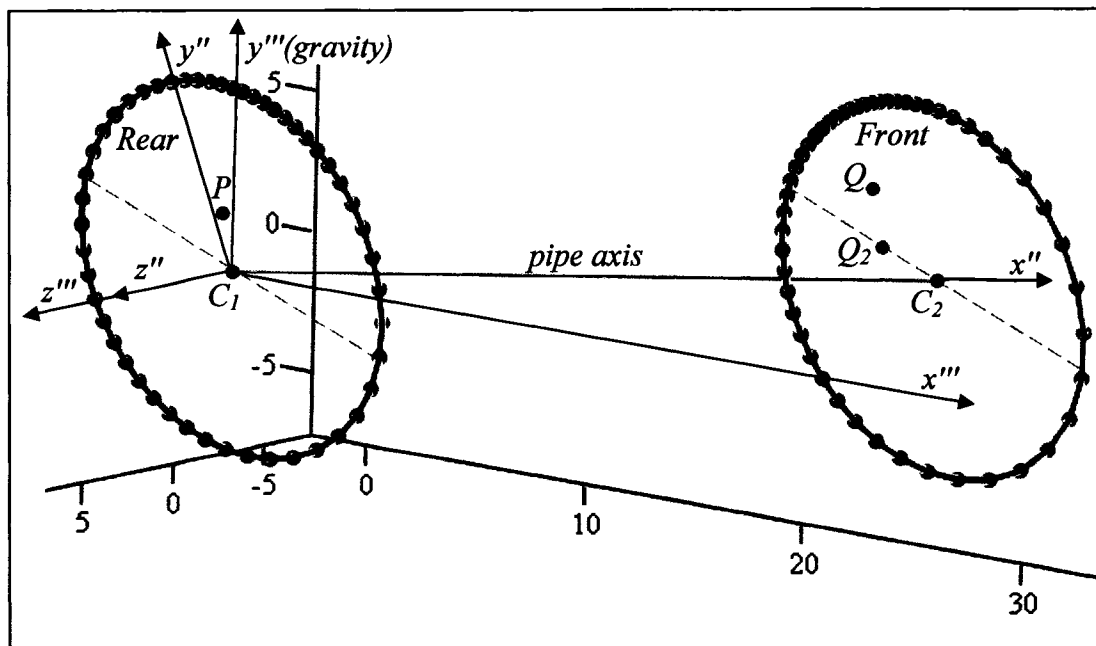


Figure 4.26 3-D View of Simulated Data on  $x'''$ - $y'''$ - $z'''$  Coord. Sys.

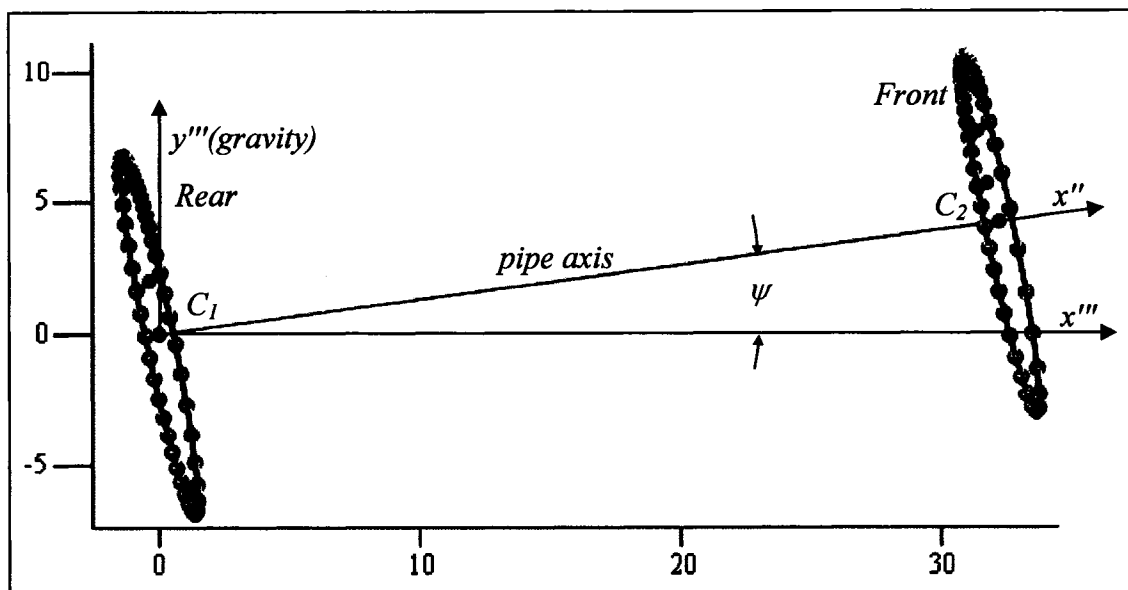


Figure 4.27 Side View of Front and Rear Simulated Data on  $x'''$ - $y'''$  Coord. Sys.

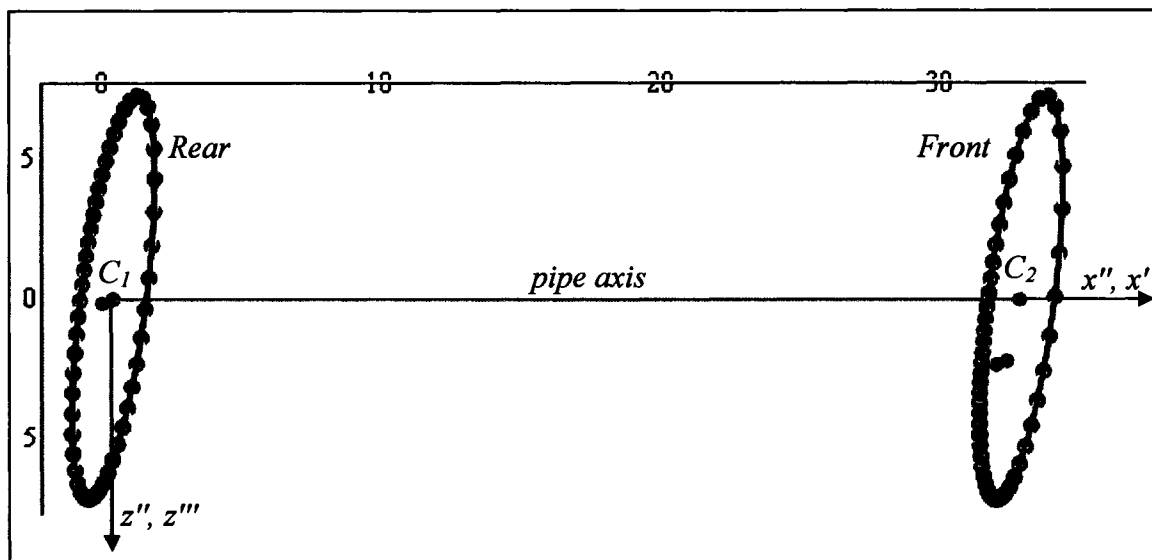


Figure 4.28 Top View of Front and Rear Simulated Data on  $x'''$ - $z'''$  Coord. Sys.

### 4.3 Conclusions

This chapter presented a new technique for estimating the position and orientation of a pipe profiling robot. This technique utilized radial measuring devices positioned at

each end of the profiling robot. Implementation of this technique on an existing pipe profiling robot includes the following:

1. Install a second radial measuring device on the profiler so that radial measurements can be taken at the front and rear of the robot. Care must be taken to ensure the two radial measuring systems are installed parallel to each other and perpendicular to the robotic platform.
2. Measure and record the distance between the two centers of radial measurement (point P and point Q).
3. Calculate the centroidal offsets  $\bar{z}$ ,  $\bar{y}$ ,  $\bar{w}$ , and  $\bar{v}$  using Eqs. (4.1) – (4.2).
4. Calculate the horizontal meander angle  $\theta_h$  and vertical pitch angle  $\theta_v$  of the robot with respect to the pipe using Eqs. (4.3) and (4.4).
5. Transform the radial measurement data by rotating it about the horizontal and vertical axes by  $\theta_v$  and  $\theta_h$ , respectively, using the homogenous coordinate transformations introduced in Chapter 2.

The transformed data from step five effectively removes the unwanted influences of robot pitch and yaw from laser profiling measurements.

The second section demonstrated the new position and orientation technique by applying homogeneous coordinate transformations to simulated radial measurements. Four distinct coordinate systems were defined to delineate the multiple measurement reference frames for a robot-pipe-earth system. The simulated radial measurements were based on mathematically generated data that would be obtained by incrementally rotating two radial measuring devices in a perfectly cylindrical pipe. The three-dimensional simulated radial measurements were then plotted on the four different coordinate

reference frames to provide visual confirmation that the new position and orientation estimation technique is valid.

Several coordinate systems were defined for the robot-pipe-earth system to help delineate the various measurement reference frames. Roll sensors and inclinometers were described as they relate the robot's orientation to gravity. Gyroscopes were not used in this research, though it is important to note their usefulness. Gyroscopes could be used to determine the robot's horizontal meander with respect to the earth and, when combined with the new technique presented in this chapter, could determine the pipe's horizontal meander with respect to the earth.

## CHAPTER 5

### PROTOTYPE HARDWARE DEVELOPMENT

#### **5.1 Prototype Overview**

A prototype pipe profiling robot was developed to demonstrate the new position and orientation estimation technique as presented in Chapter 4. The design, fabrication, assembly, software development, calibration and testing were performed solely by the author and Michael Swanbom, another Ph.D. candidate at Louisiana Tech University. The machining processes utilized in the construction of the prototype included the use of an end mill, drill press, thread tap, welder, band saw, sheet metal bender, sander, and grinder. This prototype was developed, in part, from an existing pipe inspection/repair robot donated to Louisiana Tech University by SCOOTER Video Inspection Systems in Tehachapi, California.

To meet the objectives set forth in this research, several modifications and additions were made to the existing robot including the following:

- Digital controls and customized software were developed in lieu of the existing analog controller. This made the task of automated data collection much easier to accomplish and provided a user friendly interface which was easily customizable. The new control system included one USB data acquisition card (DAQ), one IEEE 1394 (FireWire) hub, three DC motor controllers, two stepper motor

drivers, three solid-state SPST relays, two electromagnetic DPDT relays and two MOSFET transistors.

- A longitudinal position sensor was mounted on a custom spring loaded lever arm. This position sensor was comprised of an optical encoder which measured the axial distance traveled by the robot down the pipe.
- A tri-axis accelerometer, mounted on a custom bracket, was attached to the top of the robot. This sensor was configured to provide pitch and roll angles of the robot relative to gravity.
- Two custom optical measuring systems comprised of line lasers, halogen lights and digital cameras were designed and installed at each end of the robot.
- Two custom tactile measuring systems utilizing a DC motor, rack and pinion drive mechanism, and an optical encoder were installed at each end of the robot.
- An electronics housing box was attached to the top of the robot to provide mounting locations for the USB DAQ, IEEE 1394 hub, breadboard, stepper motor controllers, tactile drive motor controllers, five relays, two MOSFET transistors, and the robot drive motor controller.
- Peripheral attachments, including a grinding arm and grout packer, were removed from the existing robot.

A picture of the fully functioning, complete prototype is shown in Figure 5.1.

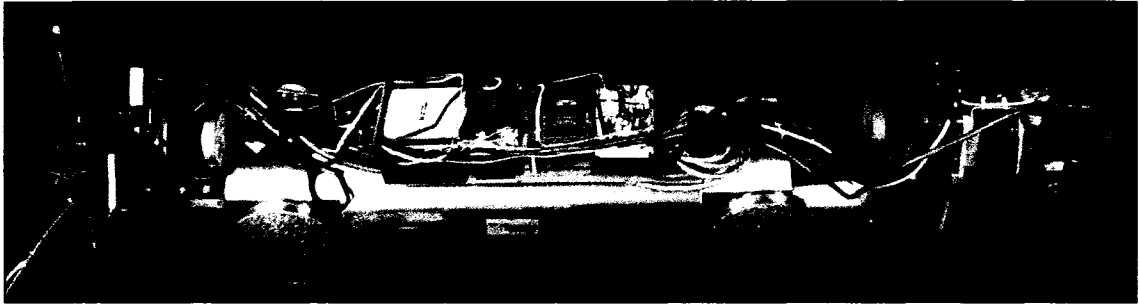


Figure 5.1 Fully Assembled Prototype Pipe Profiling Robot

A picture highlighting the front camera-laser measuring system and front tactile measuring system is shown in Figure 5.2.

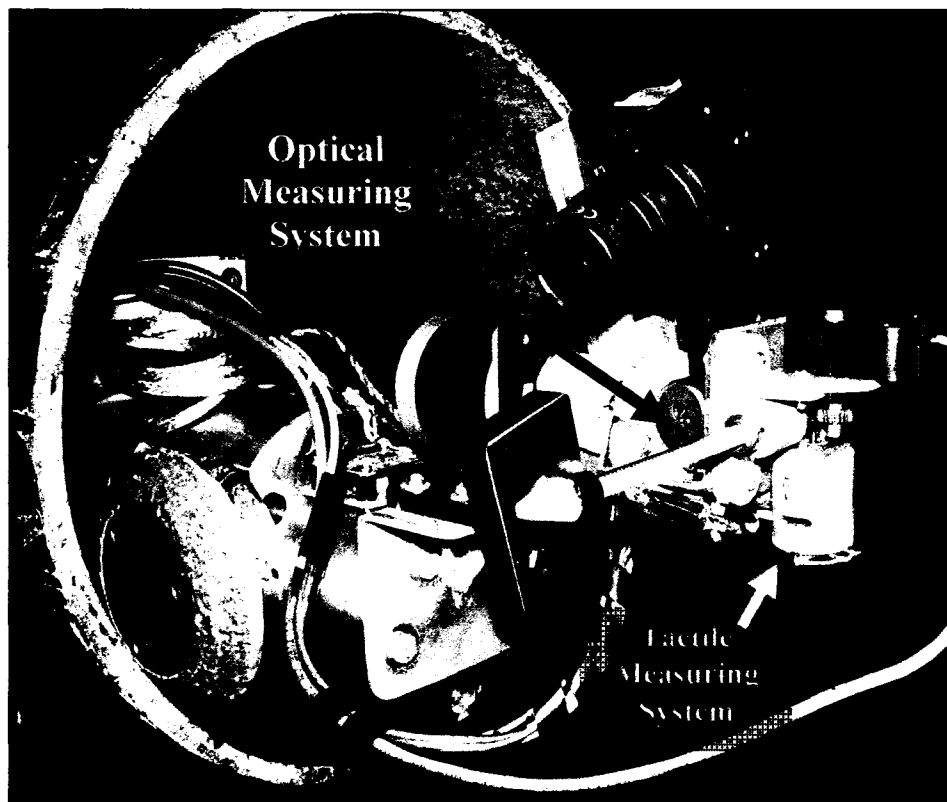


Figure 5.2 Optical and Tactile Measuring Systems on the Prototype Robot

### **5.1.1 Data Flow Onboard the Prototype Robot**

The prototype robot was designed to be controlled from a laptop personal computer (PC). The PC was linked to the DAQ via a universal serial bus (USB) cable and a FireWire cable. The USB DAQ provided digital control of the two tactile probe driver motors, two halogen lights, the direction and speed of the two stepper motors, and the direction of robot's drive motor. The speed of the robot's drive motor and brightness of both line laser diodes were controlled by two analog output channels from the USB DAQ. Additionally, the USB DAQ accepted six digital inputs from the axial distance encoder, front tactile probe encoder, and rear tactile probe encoder. The USB DAQ also received three analog inputs from the tri-axis accelerometer. An IEEE 1394 hub provided communication to and from the digital cameras. All data flow aboard the prototype robot is mapped in Figure 5.3.



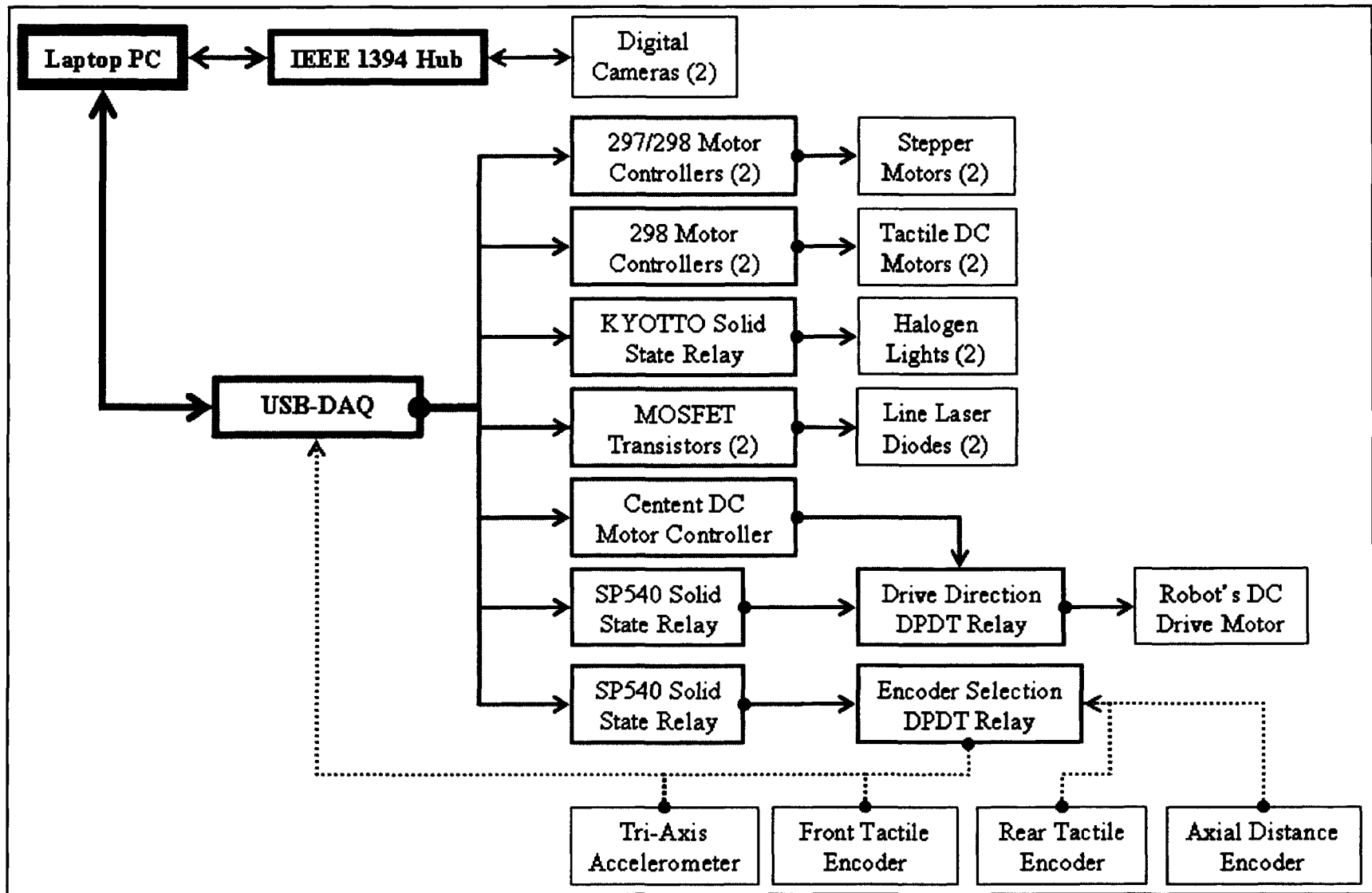


Figure 5.3 Data Flow Chart for Electrical Components on Prototype Robot

### **5.1.2 USB Data Acquisition Card and LabVIEW™ Software**

The USB DAQ selected for this project was model USB-6009 from National Instruments. The USB-6009 is a small, low-cost, portable device capable of 14-bit input resolution, sampling rates up to 48 kS/s, two analog output channels, eight analog input lines, twelve digital input/output lines, a 32-bit event counter, and plug-and-play USB connectivity. The USB DAQ was installed in the grey electronics box on the top of the robot and is shown in Figure 5.4.

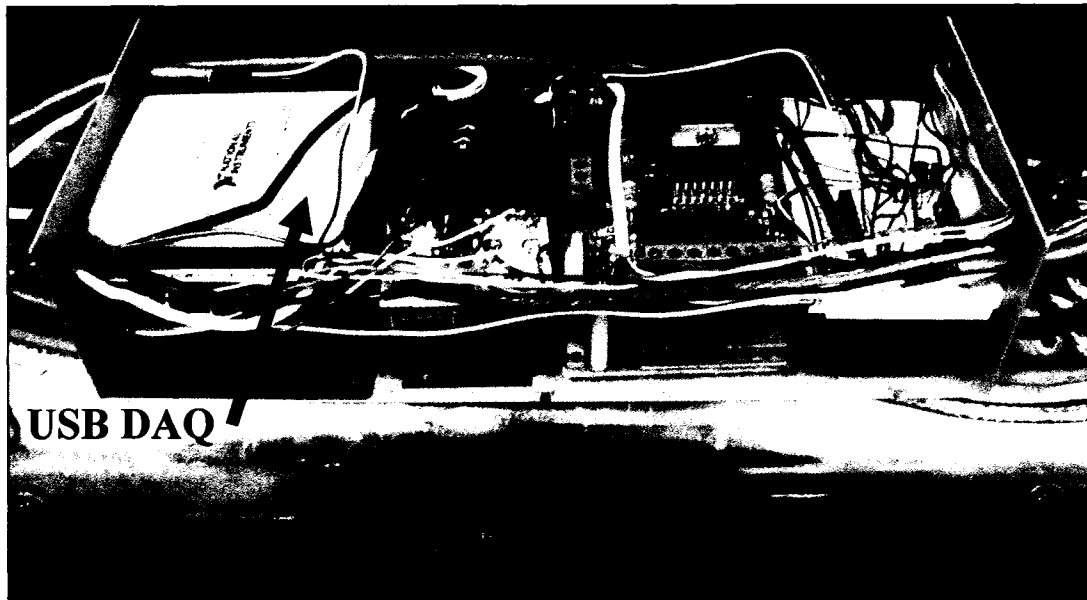


Figure 5.4 USB-6009 DAQ Mounted on Prototype Robot

The USB-6009 DAQ was designed to operate with National Instrument's LabVIEW™ software, and LabVIEW™ was used to automate the data collection process. The LabVIEW™ name is an acronym which stands for Laboratory Virtual Instrumentation Engineering Workbench and is a visual programming language known as "G". G is a dataflow language where program execution is determined by the structure of

a graphical block diagram on which the programmer connects different function nodes by drawing wires. The wires propagate variables and nodes execute as soon as all of its input data is available.

LabVIEW™ creates user interfaces called front panels which feature controls and indicators linked to the block diagram. LabVIEW™ programs, or sub-routines, are called virtual instruments (VIs). Each VI has a front panel, a block diagram and a connector pane. The connector pane is used to link VIs to other VIs with wires. LabVIEW™ also provides many libraries with a number of functions for data acquisition, signal generation, mathematics, statistics, signal conditioning, data analysis and digital image processing each of which were used in the programming of this prototype. The actual LabVIEW™ code developed for this project is described in detail in Chapter 6.

## **5.2 Original Pipe Repair/Inspection Robot**

### **5.2.1 Purpose and Background of the Original Robot**

The original robot, donated by SCOOTER Video Inspection Systems, was designed to perform as a “find-and-fix” pipeline repair robot. The robot would be deployed from a service vehicle, usually a van, and controlled via a tether. Besides carrying electrical signals to and from the robot, the tether also conveyed compressed air and water. A closed circuit television (CCTV) camera, mounted to the front of the robot, visually located the area in the pipe requiring repair. Typically, the type of repair made by this robot involved epoxy injection into a cracked pipe segment or joint. An epoxy injecting tool was attached to the front of the robot and maneuvered into place via hydraulic cylinders and a gear train. A trowel at the top of the tool featured an air jet

which cleared debris and water from the damaged area. Figure 5.5 shows a picture of the joint and crack repair attachment.



Figure 5.5 Joint and Crack Repair Attachment

After the epoxy was injected, the joint and crack repair attachment would be removed and replaced with the grinding attachment. The pneumatically operated grinding attachment was used to remove superfluous epoxy from the repair site. Two water jets mounted on the front of the robot were used to remove heat during the grinding process and cleaned the repair site to ensure adequate repair. Figure 5.6 shows a picture of the grinding attachment.

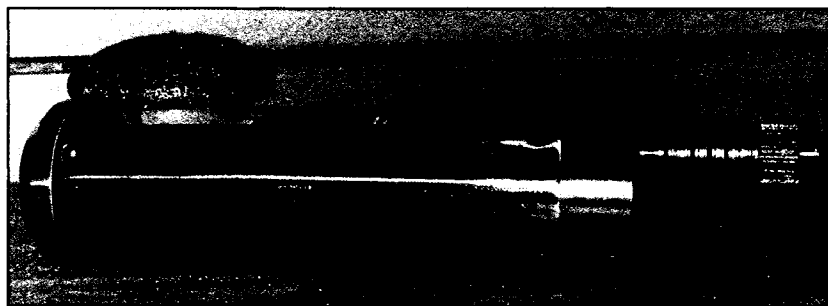


Figure 5.6 Grinding Arm Attachment

Since the joint and crack repair attachment and the grinding arm attachment were not needed for this research project, they were removed from the robot. Figure 5.7 shows

a picture of the original robot with the attachments removed. This robotic platform provided an adequate base for a prototype pipe profiler.



Figure 5.7 Original Robot with Attachments Removed

### **5.2.2 Robot Speed and Direction Controls**

The original robot's drive mechanism was comprised of a permanent magnet, DC motor and a gear train providing all wheel drive operation. The motor was manufactured by Motor Technology Inc., rated at 27 VDC, consumed a maximum of 5 amps, and provided 1632oz-in of torque. The motor was connected to a planetary speed reduction box with a speed ratio of 1:170 which served to increase the torque applied at the wheels. This high amount of torque was necessary to drag the long and cumbersome tether through the pipe and more than adequately powered the new prototype profiler.

To control the speed of the robot, the original motor controller was removed in favor of a new Centent CN0105 DC motor controller. The CN0105 is a compact, high efficiency switching type speed controller. It varies motor speed by varying the switching rate of a field effect transistor network. The CN0105 has a supply voltage range of 12-40 VDC and is rated for 10 amps maximum load current. The speed control input voltage

ranges from 0-5 VDC and was connected to channel AO0 of the USB DAQ. A detailed drawing provided by the manufacturer is shown in Figure 5.8.

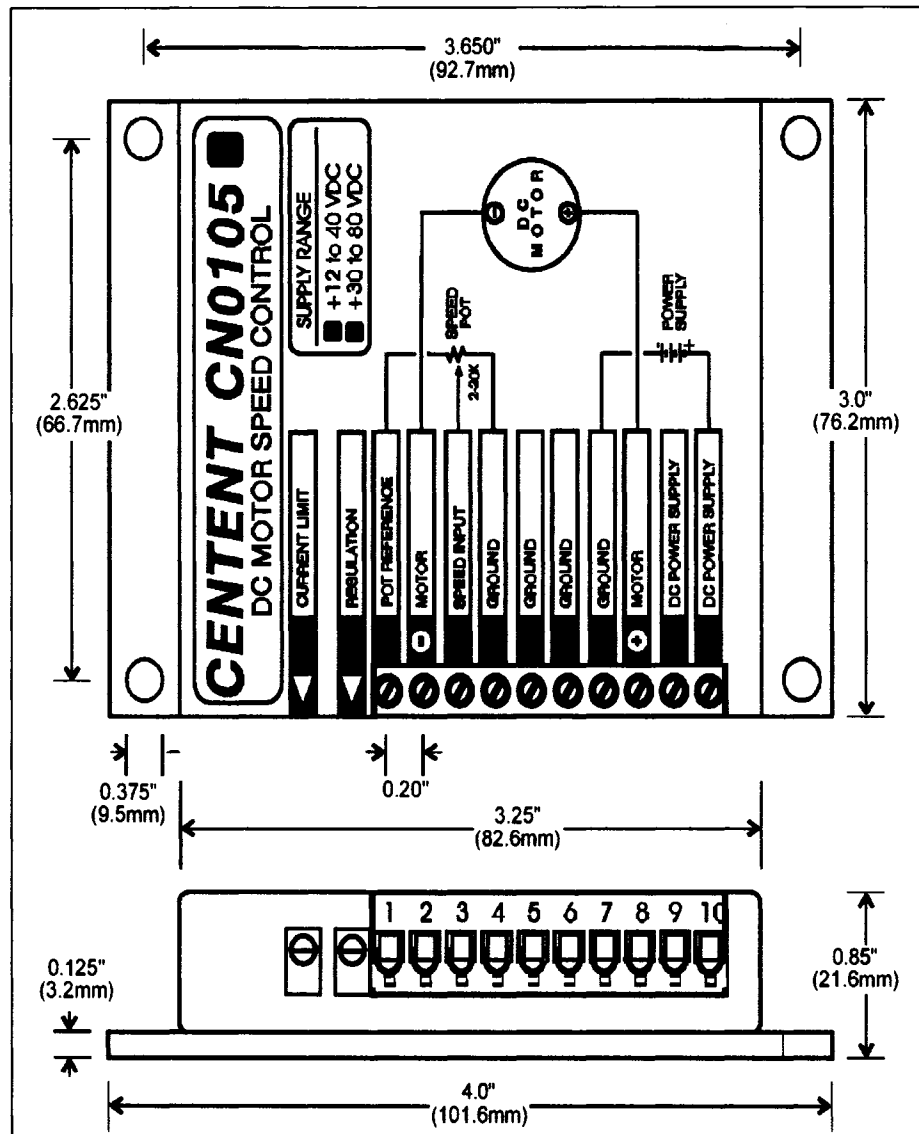


Figure 5.8 Centent CN0105 DC Motor Controller Drawing

An electromagnetic relay was used to control the prototype's direction of travel. Since both poles of the robot motor needed to be switched at the same time, a double-pole, double-throw (DPDT) manufactured by RAYEX Electric was selected. The relay was a LB2 type with a coil voltage of 24 VDC. The contacts were rated at 240 VAC or

30 VDC at 12 amps. A schematic showing the dimensions and wiring diagram of the LB2 relay is shown in Figure 5.9.

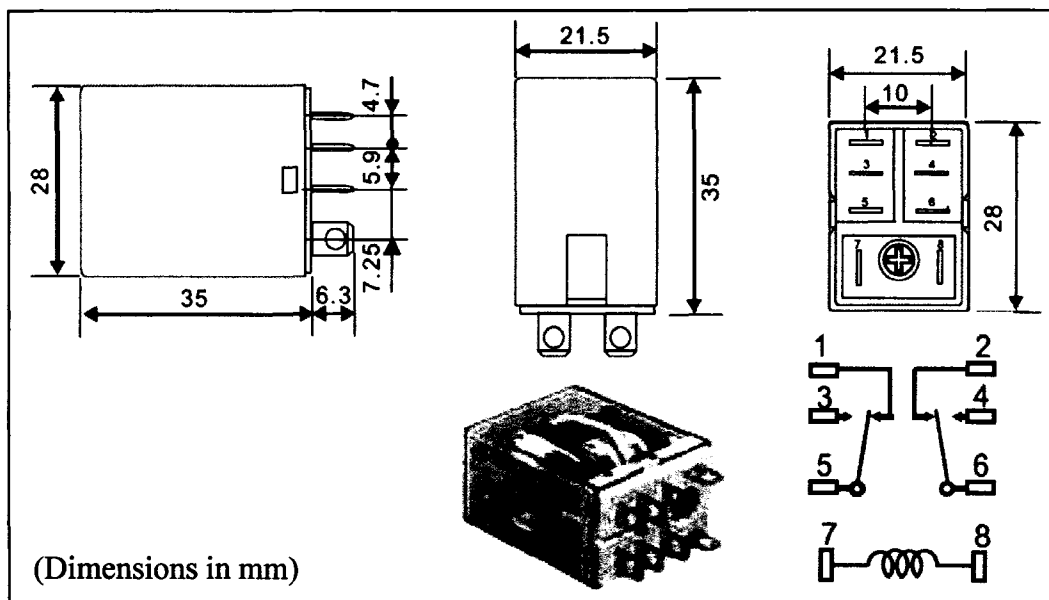


Figure 5.9 RAYEX LB2 DPDT Electromagnetic Relay

The two poles of the robot's DC drive motor were connected to pins 1 and 2 on the LB2 relay. Pins 3 and 6 and pins 4 and 5 were connected together with jumpers. The LB2 coil, pins 7 and 8, required 37 mA at 24 VDC which was beyond the capabilities of the USB DAQ. Therefore, a single-pole, single-throw, (SPST) solid state relay was selected to provide digital control of the LB2 relay from the USB DAQ.

The SPST relay chosen was the SP540-X by Solid State Optronics. This relay consists of an integrated circuit which drives an enhancement type double-diffused metal oxide semiconductor (DMOS) transistor. The integrated circuit is optically coupled to a light emitting diode. It features high input-to-output isolation, low input control power consumption, 750 mA maximum continuous load current, and 2 ohms maximum on-resistance. Figure 5.10 shows a picture of the SP540-X along with a wiring schematic.

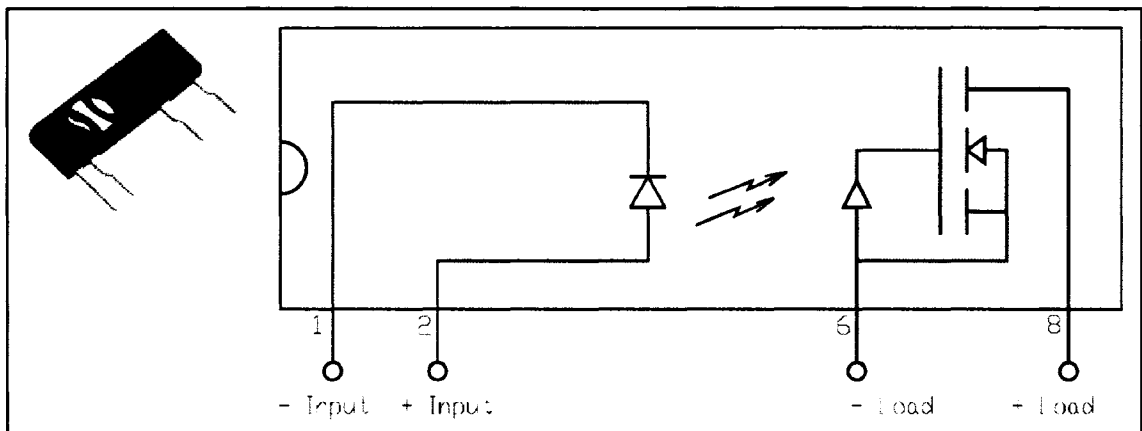


Figure 5.10 SP540-X Solid State Relay

When a digital input/output (DIO) channel on the USB DAQ supplies voltage to pins 1 and 2 of the SP540-X relay, the LED turns on. Light produced by the LED is sensed by the load circuit which electrically couples pins 6 and 8. This closes the circuit between a 24 VDC power supply and the LB2 relay.

A variable power supply was used to power the robot's DC motor and energize the LB2 relay coil. An S-240-24 single output, switching power supply, manufactured by Mean Well was selected. It is low weight, compact, and features a built-in electromagnetic filter. It is capable of supplying 0-24 VDC at 10 amps with low ripple noise. The S-240-24 power supply also features an automatic cooling fan to maintain the temperature and short circuit/over-load/over-temperature protection. The power supply is shown in Figure 5.11.



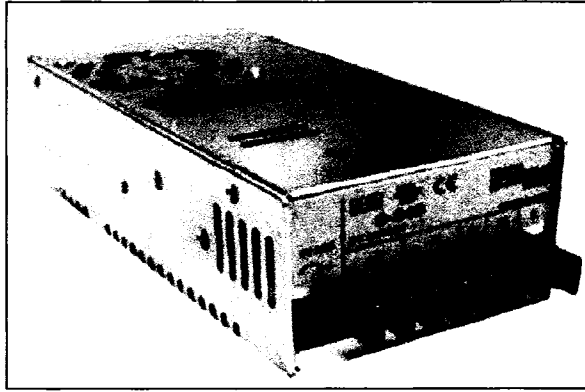


Figure 5.11 Power Supply for Robot Drive Motor and 24VDC Relays

In summary, the original robot's DC motor was utilized, but a new DC motor controller was constructed. The new controller featured 0-5 VDC analog speed control with digital control of drive direction. This allowed the prototype's speed and direction to be easily controlled by the USB DAQ and the automation software described in Chapter 6.

### **5.3 Global Orientation and Axial Position Measuring Systems**

#### **5.3.1 Accelerometer and Custom Bracket**

A tri-axis accelerometer was employed as a two axis roll sensor to monitor the pitch and roll of the robot with respect to gravity. The integrated circuit selected for this task was the LI33L02AS4 manufactured by STMicroelectronics. It is a MEMS inertial sensor configured as a three-axis linear accelerometer. Figure 5.12 shows a picture of the LI33L02AS4 chip highlighting the direction of detectable accelerations and the pin-out diagram.

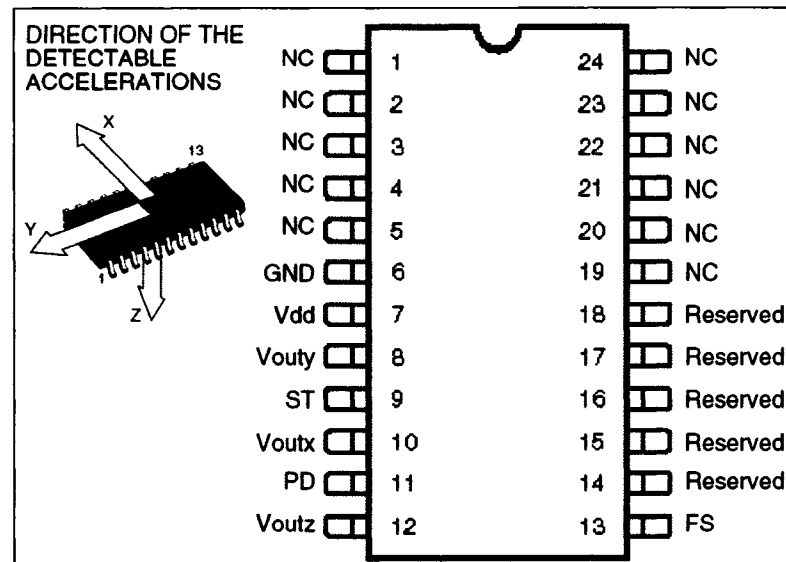


Figure 5.12 Tri-axis Accelerometer Pin-out and Coordinate System

The accelerometer provides three pins, Voutx, Vouty, and Voutz, which each send an analog signal proportional to the acceleration along one of its three axes. Using the earth's gravitational field, the accelerometer's output varies with its global orientation. Six different orientations, along with the respective analog output from the accelerometer, are shown in Figure 5.13.

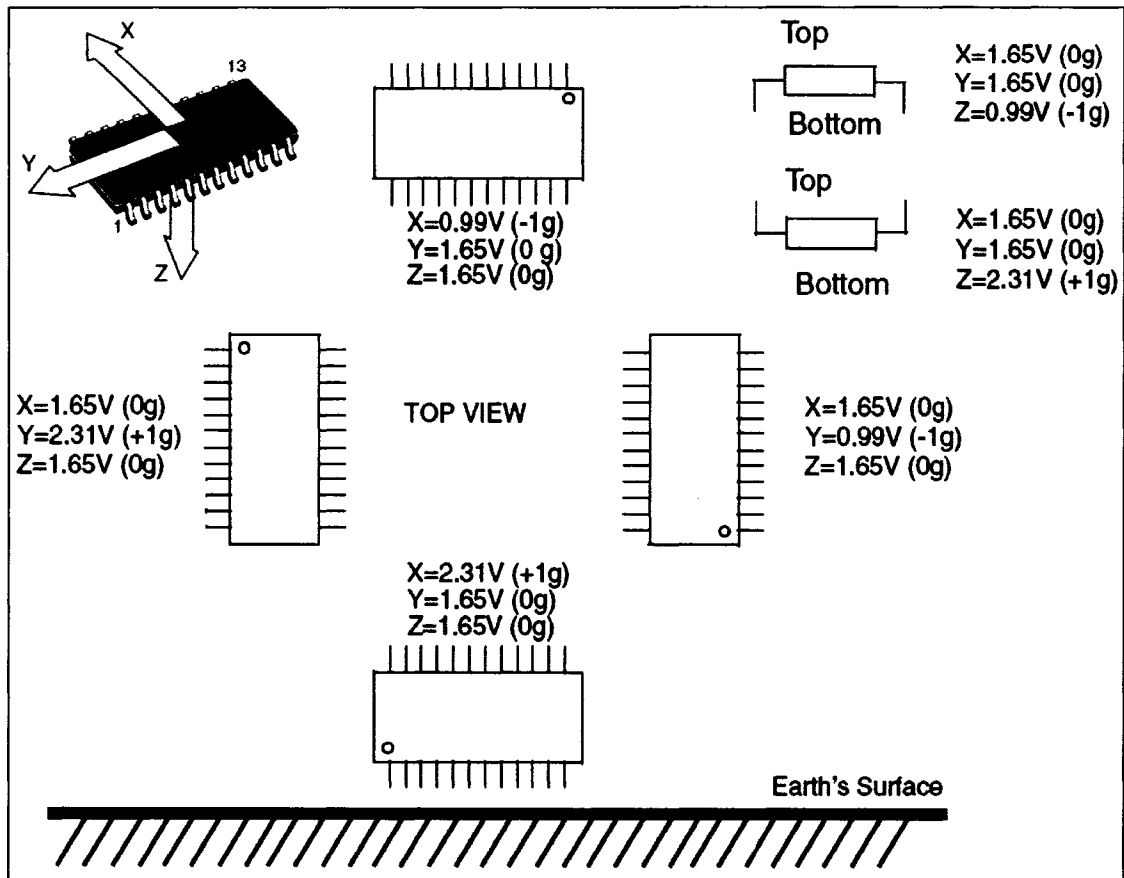


Figure 5.13 Tri-axis Accelerometer Output Response vs. Orientation

A custom aluminum bracket was fashioned for the accelerometer circuit board and was attached to the top of the prototype. The mounting location and custom bracket are shown in Figure 5.14.

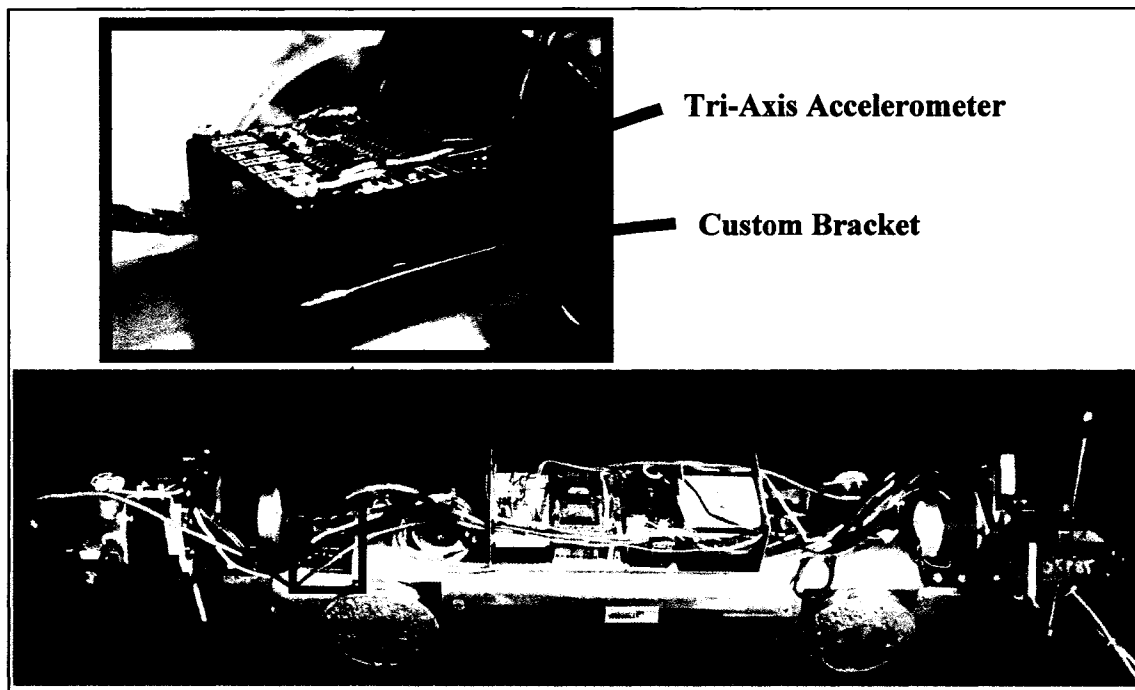


Figure 5.14 Accelerometer Mounting Location and Custom Bracket

### **5.3.2 Axial Position Encoder**

A rotary optical encoder attached to the robot's drive wheel was used to measure the axial distance traveled by the prototype down the pipe. An H5S-900-I encoder from US Digital Corporation was selected for its small size, low cost, and two-channel quadrature TTL square wave outputs. By using quadrature logic, the prototype's position and direction of travel could be determined. A custom, spring-loaded bracket was fashioned for the encoder to provide adequate contact pressure between the encoder wheel and the robot wheel. A plastic encoder wheel with a rubber o-ring was attached to the encoder shaft. The encoder assembly is shown in Figure 5.15.

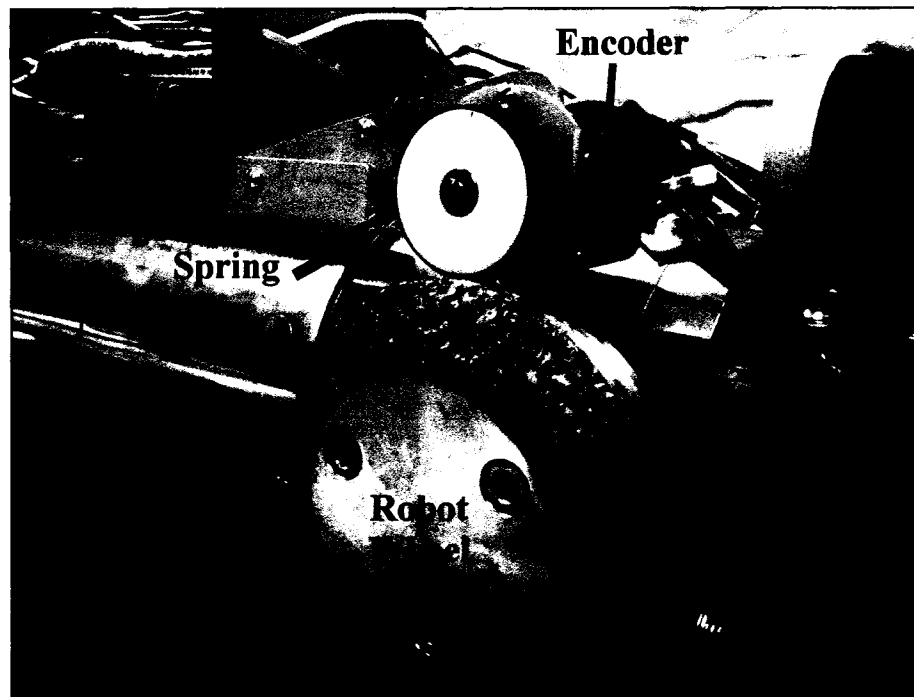


Figure 5.15 Spring Loaded Axial Distance Encoder Assembly

#### **5.4 Optical Triangulation Measuring System**

The prototype optical measuring system was comprised of two separate camera-laser systems. One camera-laser system was attached to the front of the prototype and one to the rear. IEEE 1394 digital cameras were used to capture images during the data collection process. Halogen lights were used to provide illumination during the collection of pipe images, and line lasers were used to provide reference planes for radial measurements. Twelve custom brackets were designed and constructed to provide adjustment capability and structural support for the two camera-laser systems. Stepper motors were utilized to incrementally rotate and position the camera-laser assemblies during the pipe scanning process.

### **5.4.1 Stepper Motors and Supporting Hardware**

The stepper motors chosen to rotate the camera-laser assemblies were type 57BYG084 from JAMECO®. The motors were NEMA 23 style and rotated 1.8° per step. Each coil required 12VDC at 0.6 amps. Both of the stepper motors were bolted into NEMA 23 stepper motor brackets from CyberResearch Inc. These brackets provided a mounting plane 90° from the stepper motor face. Figure 5.16 shows a picture of the stepper motor mounted in the black NEMA 23 bracket.

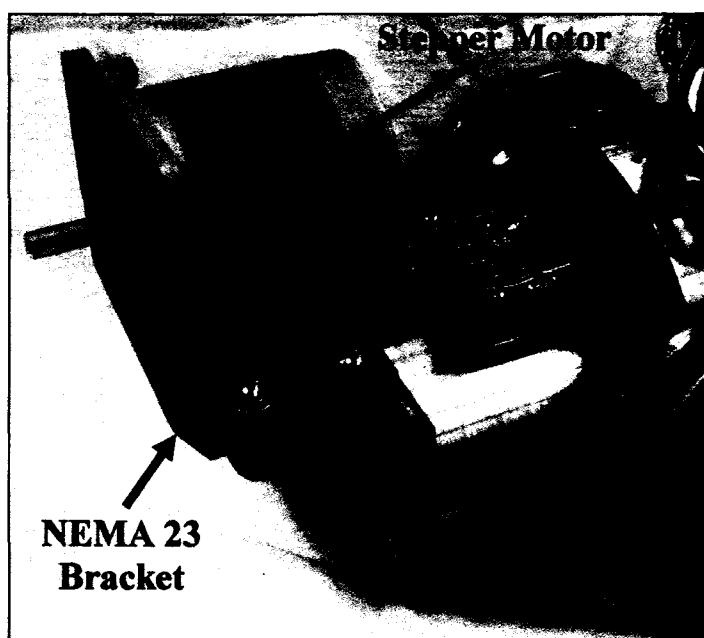


Figure 5.16 Stepper Motor and NEMA 23 Bracket on Front of Robot

Two custom brackets were designed and constructed to support the NEMA 23 brackets to the front and rear of the prototype. The brackets were constructed from 1/8 inch steel and featured three support webs to minimize deflection. The ends of the robot were drilled and tapped to provide secure attachment points for each of the brackets. Pictures of the two custom brackets are shown in Figure 5.17.



Figure 5.17 Custom Stepper Motor Support Brackets

Control of the stepper motors was achieved through the use of a controller-amplifier combination kit which utilized L297 and L298N integrated circuits. The L297/L298N kits were purchased from Square 1 Electronics. This kit controlled the direction, speed, and stepping mode with three digital inputs. Direction control and half or full step control is set by a digital high or low signal. Speed control is achieved through the use of a clocked square wave input from the USB DAQ. By incorporating the L297 chip with a L298N dual bridge driver, the L297/L298N kit can control stepper motors with phases up to 36 VDC and 2 amps. Figure 5.18 shows a picture of the 297/298 kit, and Figure 5.19 shows its circuit diagram.

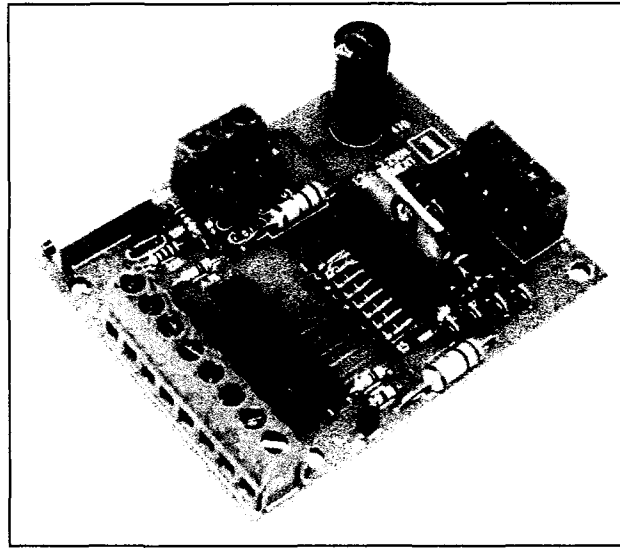


Figure 5.18 Stepper Motor Controller Kit L297/L298N

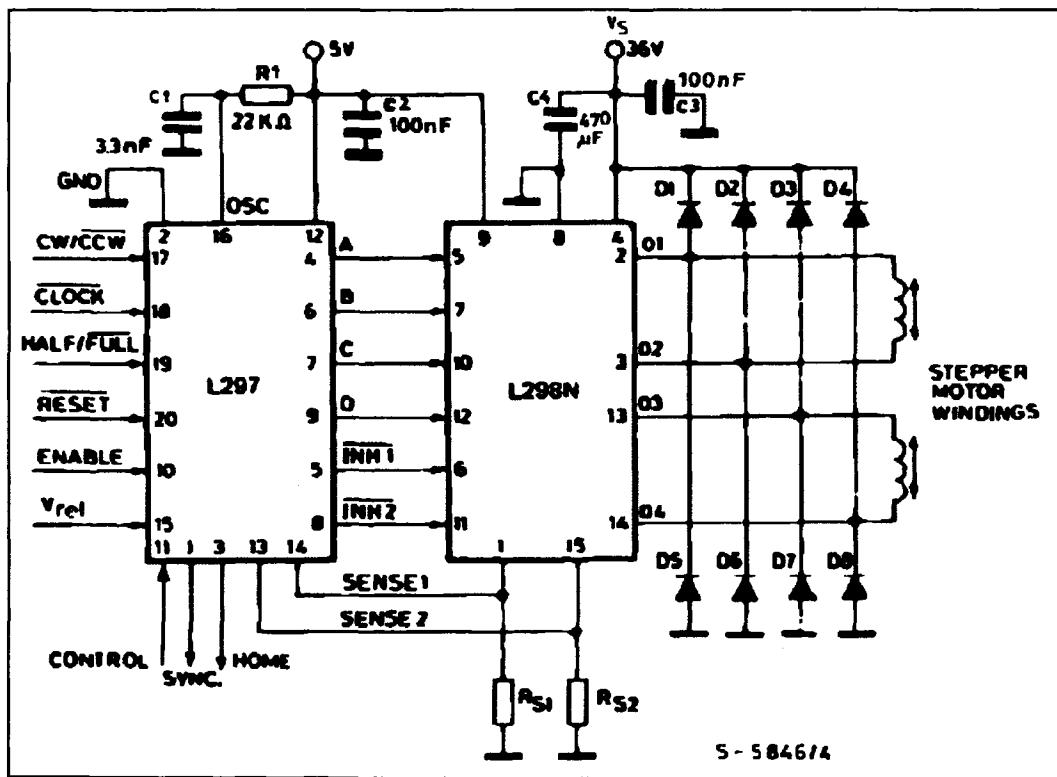


Figure 5.19 Circuit Diagram for L297/L298N Stepper Motor Control Kit



### **5.4.2 Digital Cameras and Supporting Hardware**

The cameras selected for the prototype were MicroPix C-1024 digital color cameras. The cameras utilized a progressive scan 1/3 inch CCD sensor and had a resolution of 1024 x 768 pixels. The C-1024 could be externally triggered, was network capable through IEEE 1394, captured up to 30 frames per second, and output 24 BIT RGB color. Pictures of the C-1024 camera are shown in Figure 5.20.

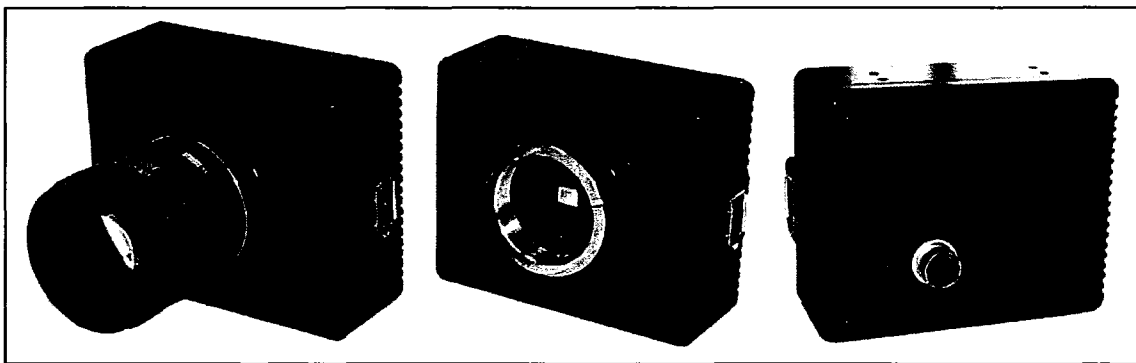


Figure 5.20 MicroPix C-1024 Digital Camera

Each camera was connected to an IEEE 1394 hub located in the electronics housing box on top of the robot. The hub selected for this project was the HFW410 by Koutech. The low-profiled hub featured four ports, three downstream and one upstream. The HFW410 FireWire hub also supported external bus power. This was required because the laptop PC, used to control the prototype, did not have a 12 VDC supply in the IEEE 1394 bus. A picture of the HFW410 FireWire hub is shown in Figure 5.21.

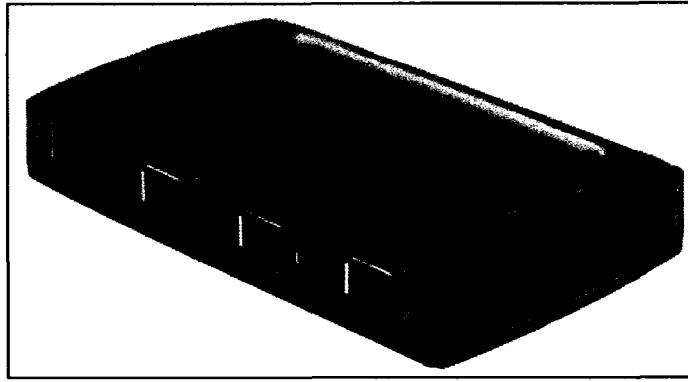


Figure 5.21 IEEE 1394 Hub for Digital Cameras

Ten custom aluminum brackets were designed and constructed to attach the cameras and lasers to the stepper motors. The brackets were designed to ensure the camera-laser system could be easily adjusted and calibrated. The ten custom brackets consisted of the following pieces:

- Four shaft couplers with adjustable set screws
- Two wedge-shaped mounting plates
- Two camera support wings
- Two laser mount spacers

Two shaft couplers were bolted together to help distribute the cantilevered load on each of the stepper motor shafts. Two holes were drilled and tapped into each of the four shaft couplers. Set screws were inserted into these holes to provide perpendicular alignment of the shaft coupler to the stepper motor shaft. A picture of two shaft couplers attached to the front stepper motor is shown in Figure 5.22.

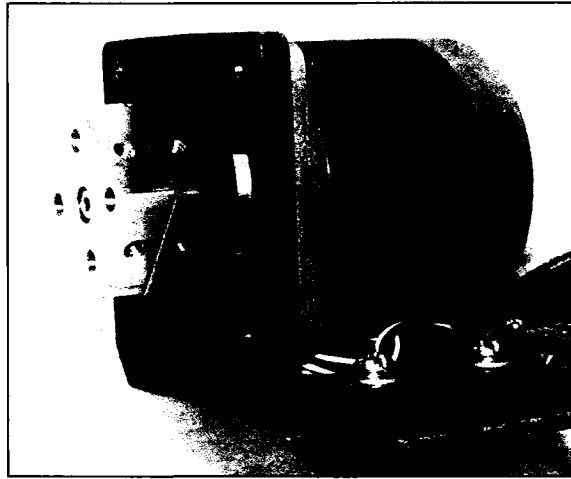


Figure 5.22 Custom Shaft Couplers Attached to Front Stepper Motor

The two wedge-shaped mounting plates were attached to the outer shaft couplers on each stepper motor. The plates provided sturdy mounting locations for the laser mount spacer and the camera support wings. Figure 5.23 shows a picture of the front wedge-shaped plate bolted to the outer shaft coupler.



Figure 5.23 Wedge-Shaped Mounting Plate Attached to Front Stepper Motor

Figure 5.24 shows a picture of the camera support wing and laser mount spacer bolted to the wedge-shaped plate.

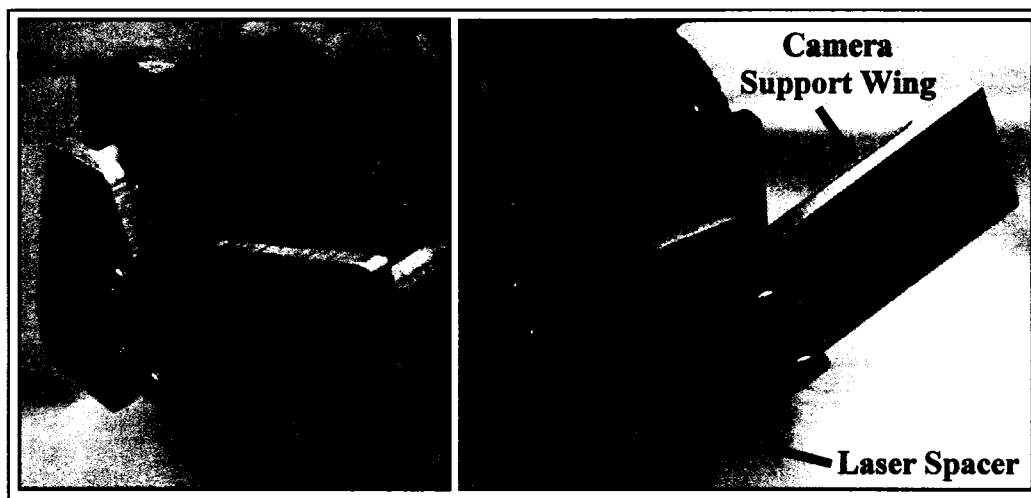


Figure 5.24 Camera Support Wing and Laser Mount Spacer

Figure 5.25 shows a picture of the assembly with the MicroPix C-1024 camera and line laser installed.

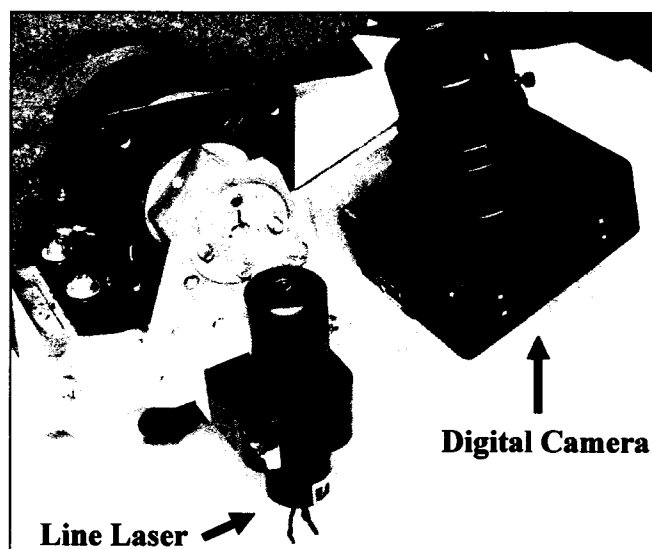


Figure 5.25 Front Camera-Laser Support Assembly

#### **5.4.3 Lasers and Transistors for Brightness Control**

Structured light in the form of a line laser provided a reference plane for accurate pipe radii measurements. The laser module selected for this project was a 650nm line

laser from JAMECO® model 143845CG. The line laser featured an adjustable lens with a set screw, a 5mW power rating, and operated on 3-5 VDC. A laser clamp, JAMECO® part 143853CG was used to attach the line laser to the laser spacer mounted on the wedge-shaped plate.

The brightness of the line laser was controlled by varying its input voltage. Since the power requirements of the lasers were higher than that supplied by the USB DAQ, two MOSFET transistors were utilized to vary the voltage across the line lasers. The MOSFET transistors selected for this task were 2N7000 n-channel transistors manufactured by PHILIPS. Each line laser was connected in series with a 5 VDC source and placed between the source and drain of the MOSFET. The USB DAQ AO1 channel was connected to the MOSFET gate, and the USB DAQ ground was connected to the MOSFET source. This allowed a low current analog signal from the USB DAQ to control the brightness of the laser. Figure 5.26 shows a picture of the MOSFET and its wiring diagram.

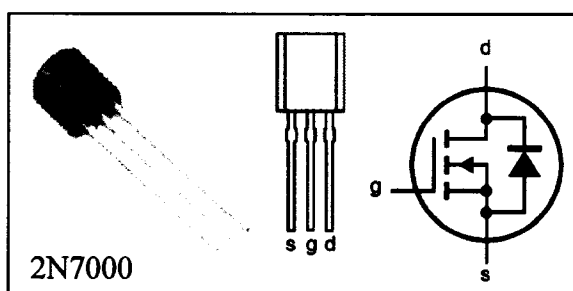


Figure 5.26 MOSFET Transistor for Laser Brightness Control

#### **5.4.4 Halogen Backlights and Solid State Relay**

Whenever a pipe is profiled, it is desirable to also capture lighted images of the interior surface of the pipe for visual inspection. To accomplish this, two 12 VDC

halogen lights were used to periodically illuminate the pipe after the laser line modules were turned off. The lights were mounted on the tactile probe spacer. A picture of the halogen light mounted on the rear tactile spacer is shown in Figure 5.27.



Figure 5.27 Halogen Light Mounted on Rear Tactile Probe Spacer

The halogen lights each required 3 amps at 12VDC. Therefore, a high powered solid-state relay was used to allow the USB DAQ to control the lights. The KG1010D by KYOTTO was selected for its ability to provide 3-32 VDC at 10 amps with a digital input signal from the USB DAQ. The operation of the KG1010D is similar to the SP540-X solid state relay. An internal LED triggers a photo detector which closes the output circuit. Figure 5.28 shows a picture and wiring diagram of the KG1010D solid state relay.

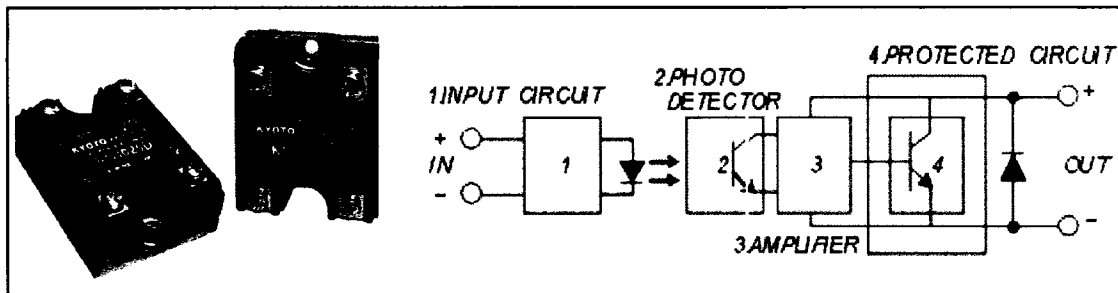


Figure 5.28 KG1010D Solid State Relay for Halogen Light Control

### 5.5 Tactile Measuring System

The prototype pipe profiler was outfitted with a set of custom tactile probe measuring systems. Each probe consisted of a rack and pinion mechanism which physically made contact with the inner pipe wall when driven outward radially. One tactile probe was attached to the front camera-laser measuring system and one to the rear. This provided a rigid link between the measuring systems and allowed the stepper motors to position both measuring systems simultaneously. The tactile probe assemblies were comprised of twenty off-the-shelf components and ten custom brackets. A picture of the tactile probe assembly is shown in Figure 5.29, and each piece of hardware used in the construction is described in detail in the sections that follow.

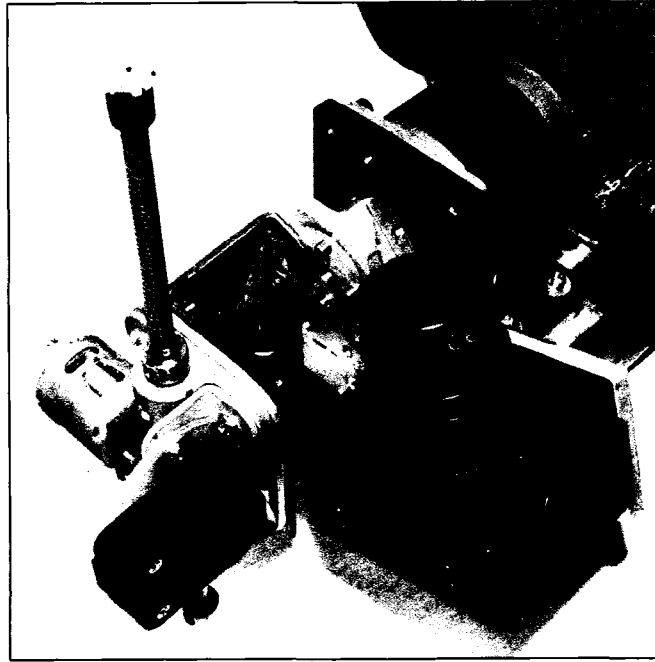


Figure 5.29 Tactile Probe Assembly Attached to the Optical Measuring System

### **5.5.1 Tactile Probe Hardware**

The tactile probe consists of a rotary encoder attached to a rack and pinion mechanism driven by a DC motor. When the DC motor is driven forward, the rack is thrust radially outward from the robot until it makes contact with the inner surface of the pipe. A small spur gear on the encoder shaft rests on the pinion gear, and the encoder measures the distance traveled by the tactile probe. The polarity of the DC motor then reverses, and the rack retracts from the surface of the pipe, providing clearance for the probe to be rotated to its next stop.

The round rack chosen had a 0.25 inch diameter, 18 inch length, a diametral pitch of 48, a pressure angle of 20°, and was made of #416 stainless steel. The rack was purchased from Stock Drive Products, and the part number was S1807Y-RA-3P. The 18 inch rack was cut in half. Therefore, each tactile probe was 9 inches in length. Rubber tips were installed on the racks to prevent high impact loading on the surface of the pipe.



Shaft collars were installed at appropriate locations on both ends of each rack. These collars prevented the rack from traveling beyond the range of measurement. The stainless steel collars selected for use were part #A 7X 2-11608 from Stock Drive Products. Each rack was mounted inside of a flanged brass bushing to ensure smooth, low friction operation. The brass bushings selected were part #A 7Z 4-P2408 from Stock Drive Products.

The encoder selected for use on the tactile probe was very similar to the axial distance encoder used on the robot wheel. The tactile encoder selected was part H5S-192-I from US Digital Corporation. A steel spur gear, part # S1166Z-048S020 from Stock Drive Products, was installed on the shaft of the tactile encoder. The stainless steel encoder gear featured 20 teeth and a diametral pitch of 48. The DC motor used on each tactile probe was an MD5-12160 from JAMECO®. The motor required 12-24 VDC at 0.3 amps, rotated at 4000 RPM, and supplied 34.3 g-cm of torque (at maximum efficiency). Plastic spur gears, or pinions, were attached to the DC motor shafts to drive the racks. The plastic spur gear used was part #A 1M 2-TA48010 from Stock Drive Products. It featured 10 teeth and a diametral pitch of 48. Each of the off-the-shelf components used in the construction of the tactile probe are shown in Figure 5.30.

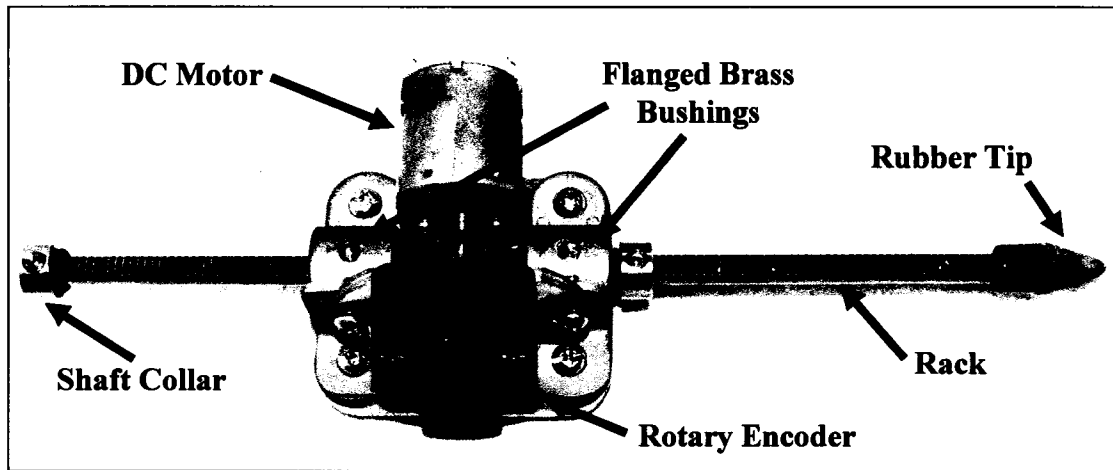


Figure 5.30 Tactile Probe Off-the-Shelf Components

Ten custom steel and aluminum brackets were designed and constructed to attach the tactile probes to the optical measuring systems. The ten custom brackets consisted of the following pieces:

- Four steel brackets to attach the encoders to the brass bushings
- Two steel DC motor mounts
- Two aluminum plates to hold the flanged brass bushings
- Two steel U-brackets to attach the tactile probe assemblies to the optical measuring systems

Each of the custom brackets fashioned for the tactile probe are shown in Figure 5.31.

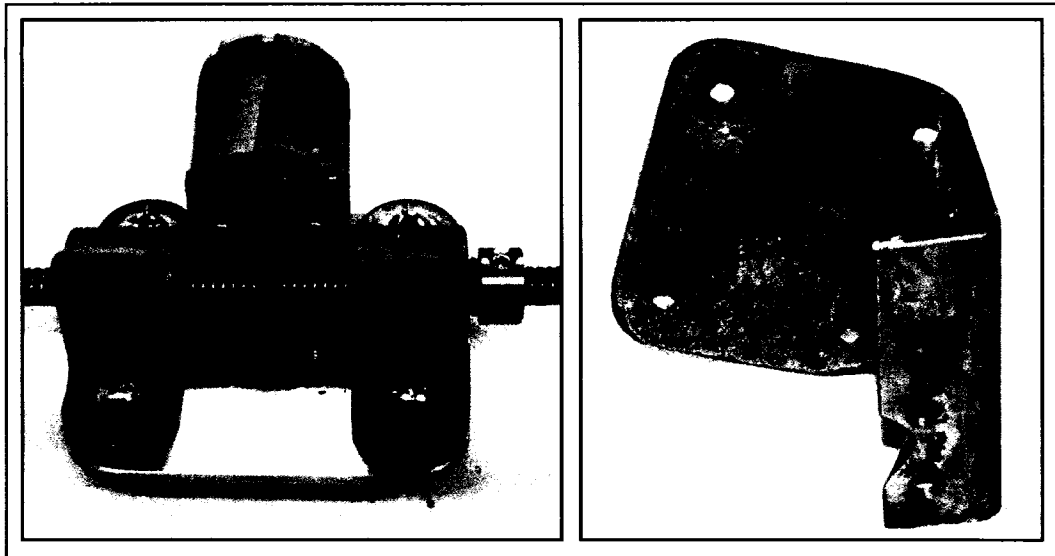


Figure 5.31 Custom Brackets for the Tactile Probe

Control of the DC tactile probe motors was achieved through the use of a L298 Motor Driver from Solarbotics Ltd. This compact driver is capable of controlling two DC motors simultaneously. The L298 can supply 6-26 VDC at 4 amps. The DC motors can be driven forward or reverse by two digital inputs to the L298 kit. This allowed for seamless integration with the USB DAQ. The L298 kit also featured a 5 VDC regulated power source and supplied power to all three of the rotary encoders on the prototype robot. A picture of the L298 kit is shown in Figure 5.32 and the details of the L298 chip are shown in Figure 5.33.

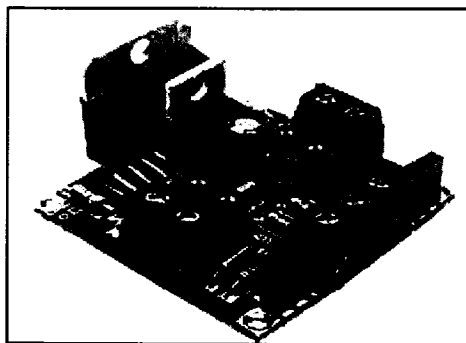


Figure 5.32 L298 DC Motor Driver Kit

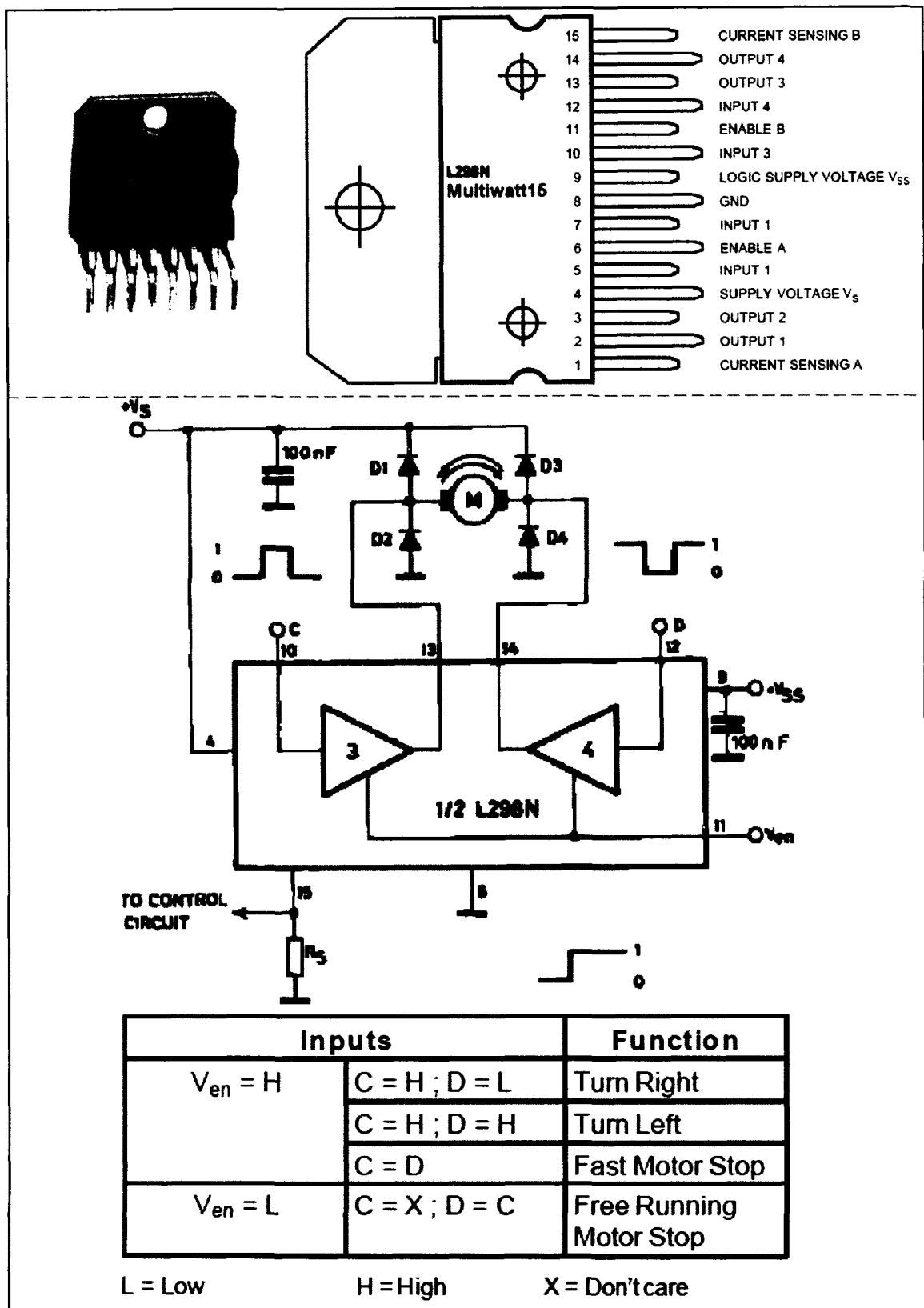


Figure 5.33 L298 Pin-out, Wiring Diagram, and Logic Table for Tactile DC Motor

## **5.6 Conclusions**

In summary, the new position and orientation estimation technique, as presented in Chapter 4, drove the design of the prototype robot. The base robot, donated by SCOOTER Video Inspection Systems, provided an adequate foundation for the new prototype profiler. Minor modifications were made to the original robot, and several new systems were added including the following:

- Digital controls and customized software were developed in lieu of the existing analog controller.
- A longitudinal position sensor was mounted on a custom spring loaded lever arm.
- A tri-axis accelerometer, mounted on a custom bracket, was attached to the top of the robot.
- Two custom optical measuring systems comprised of line lasers, halogen lights, and digital cameras were designed and installed at each end of the robot.
- Two custom tactile probe measuring systems utilizing a DC motor, rack and pinion drive mechanism, and an optical encoder were installed at each end of the robot.
- An electronics housing box was attached to the top of the robot to provide mounting locations for the USB DAQ, IEEE 1394 hub, breadboard, stepper motor controllers, tactile drive motor controllers, five relays, two MOSFET transistors, and the robot drive motor controller.

## CHAPTER 6

### EXPERIMENTAL SETUP AND AUTOMATED PROTOTYPE SOFTWARE DEVELOPMENT

#### **6.1 Experimental Preparation and Procedures**

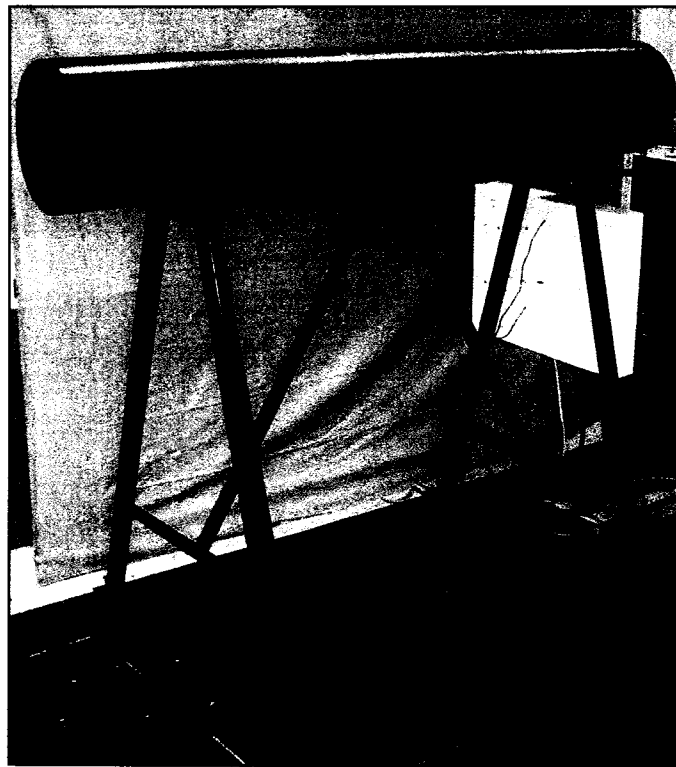
Experimental procedures and software were developed to demonstrate the position and orientation estimation technique on the prototype robot. An adjustable test stand was designed and constructed, and a 72 inch long, 12 inch diameter, 0.5 inch thick wall, steel pipe was selected to be profiled. Two vertical planes on the robot were defined and aligned to provide perpendicular datums for the radial measurements taken during the tests. The tri-axis accelerometer was calibrated to provide accurate pitch and roll angles with respect to gravity. The optical measuring systems were both calibrated using a custom camera calibration jig, and the tactile probes were calibrated using a Mitutoyo digital caliper.

The entire pipe was scanned from one end to the other with the prototype robot using both the tactile and optical radial measuring systems. This data set provided a basis of comparison for future data sets. A total of 17,600 tactile probe measurements were collected, and 17,600 digital images were captured during the scan of the laboratory test pipe. Next, the prototype robot was held stationary in the pipe and systematically placed on thirteen different bumps. For each bump the prototype collected one ring of pipe radii

measurements at each of its ends with the optical measuring systems. The tactile probe measuring system was not used during the pipe scans involving the robot on the bump due to the limited clearance inside the pipe.

### **6.1.1 Pipe Test Stand**

The pipe selected for use during the profiling experiments was a 72 inch x 12 inch x 0.5 inch steel pipe. A sturdy test stand was designed and constructed from 1.25 inch square, 1/16 inch walled tubing. The test stand featured dual A-frame legs and adjustable feet. This allowed the pipe to be leveled with respect to gravity during the experimental data collection process. Figure 6.1 shows a picture of the test stand with the pipe installed.



**Figure 6.1 Test Stand and Pipe Used for Experimental Data Collection**

### **6.1.2 Alignment of Robot's Reference Planes**

Two vertical reference planes were defined on the prototype robot. These planes were used as horizontal references for calibration of the tactile and optical measurement systems. The first reference plane was defined by the alignment of two faces on the side of the robot behind the wheels. These two faces are shown in Figure 6.2.

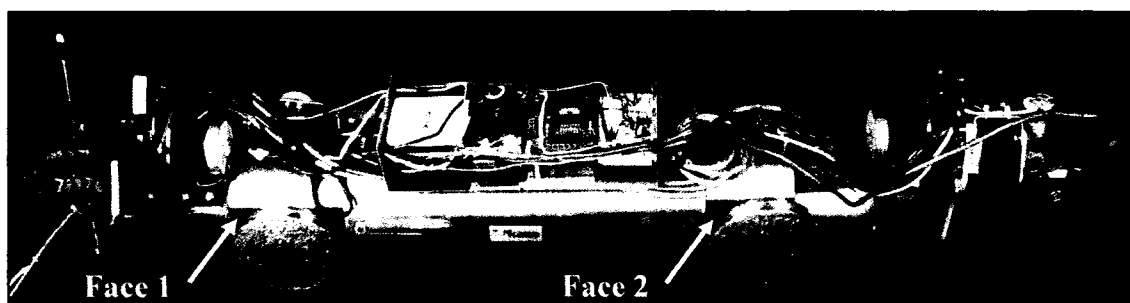


Figure 6.2 Faces Aligned on the Side of the Robot

The robot had to be partially disassembled to provide alignment of the two faces. The wheels and drive shafts were removed, and the central cylindrical portion of the robot was loosened to provide adjustability of the faces. Two hardened, ground steel parallel bars were used in conjunction with a high-precision, cast iron surface plate to provide references for the alignment of the two faces. After the faces were aligned, the robot was reassembled. The rear faces of each stepper motor defined a second vertical reference plane. The faces were aligned parallel to one another with a Mitutoyo caliper. The stepper motors were shimmed and adjusted to provide alignment of their rear faces. The two vertical planes remained stationary throughout the duration of the data collection process and experimental preparation.



### 6.1.3 Tactile Probe Calibration

The tactile probe measuring systems were calibrated after the two vertical reference planes were defined. The first step in the calibration process involved relating the known planes to the tactile probe center of rotation. Point  $P_t$  represents the rear tactile probe center of rotation, and point  $Q_t$  represents the front tactile probe center of rotation. These points and their dimensions are shown in Figure 6.3.

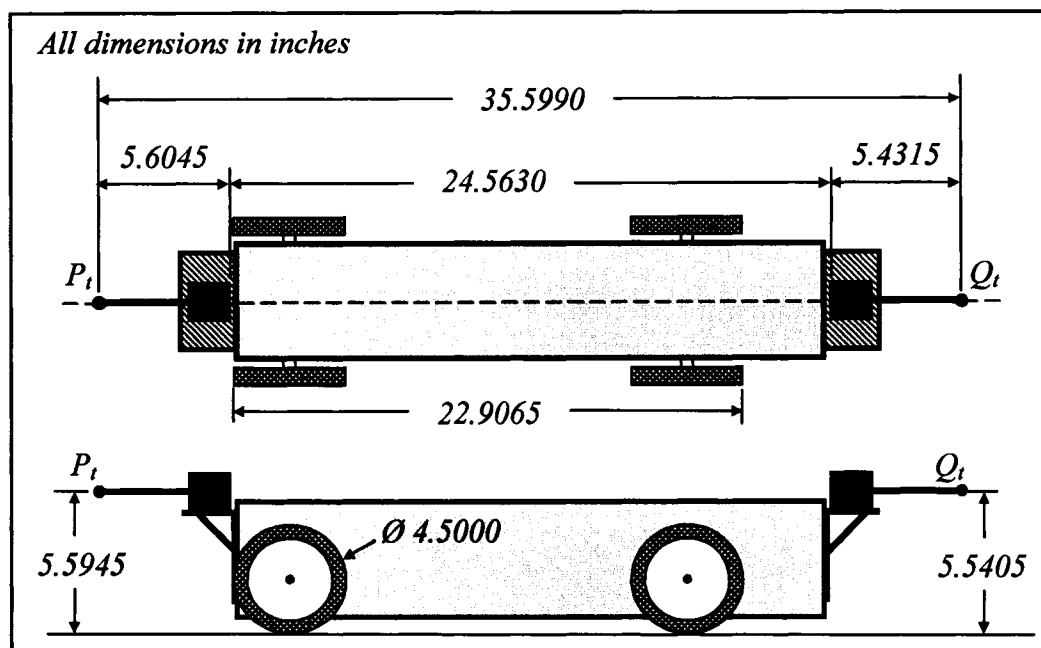


Figure 6.3 Tactile Measuring Point References

Next, the tactile probes were analytically calibrated to relate the number of rotary encoder pulses to inches of travel of the rack. The tactile probe's gears and rack each had a diametral pitch of 48 (the number of teeth per inch of pitch diameter). The rotary encoders each delivered 192 pulses per revolution and featured steel spur gears with 20 teeth. The encoder and rack were each installed on opposite sides of the DC drive motor

gear. Therefore, a 1:1 gear ratio was achieved. This enabled the final pulse to inch ratio to be expressed as Eq. (6.1).

$$\frac{1 \text{ rev}}{192 \text{ pulses}} \times \frac{20 \text{ teeth}}{1 \text{ rev}} \times \left( \frac{\pi}{48} \right) \frac{\text{in}}{\text{teeth}} = \frac{5\pi}{2304} \frac{\text{in}}{\text{pulses}} \approx 146.677 \frac{\text{pulses}}{\text{inch}} \quad (6.1)$$

The tactile probe encoder featured quadrature logic. Implementation of the quadrature logic was performed using the G code displayed in Figure 6.4.

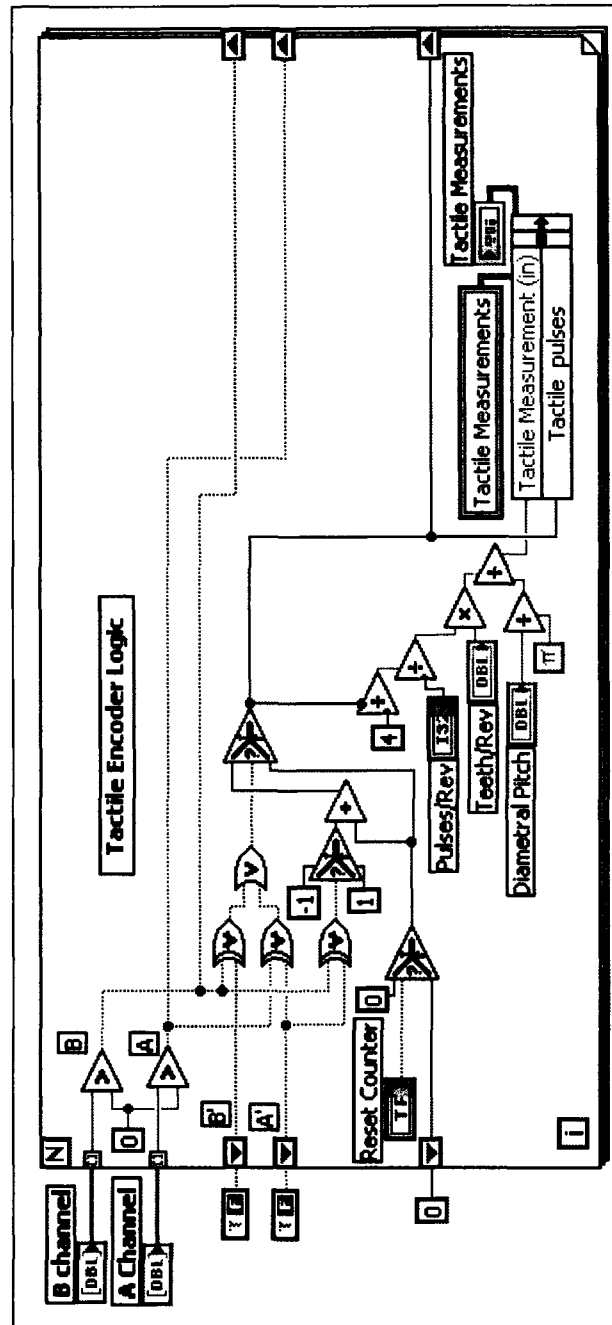


Figure 6.4 Tactile Probe Encoder VI Block Diagram

#### 6.1.4 Camera and Laser Calibration

Calibration of the camera-laser systems was the next step in preparation for experimental data collection. The camera locations were measured and recorded. Point  $P_c$

represents the rear camera center of rotation, and point  $Q_c$  represents the front camera center of rotation. These points and their dimensions are shown in Figure 6.5.

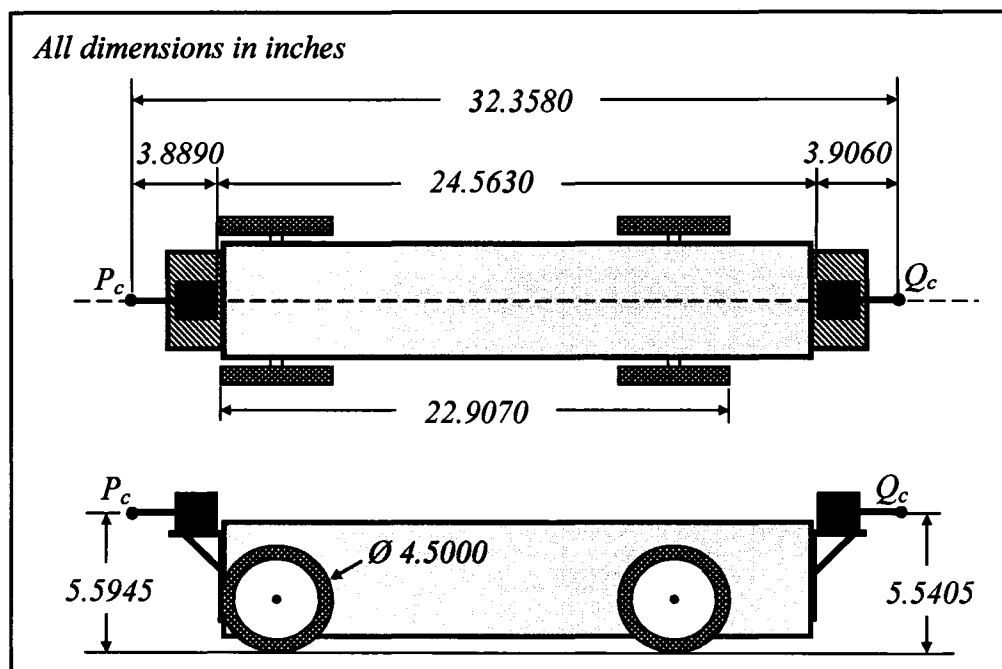


Figure 6.5. Dimensions of Robot Highlighting Camera/Laser Measuring Points

Each camera was calibrated to provide a pixel per inch translation of the laser line location in each image. A custom jig was constructed capable of adjustability along one axis. The sliding axis was aligned perpendicularly to the robot and parallel to the laser plane. The line laser was projected onto an aluminum block on the adjustable jig. Digital images of the intersection between the aluminum block and the laser were captured at various distances from the robot. A picture of the camera calibration jig is shown in Figure 6.6.

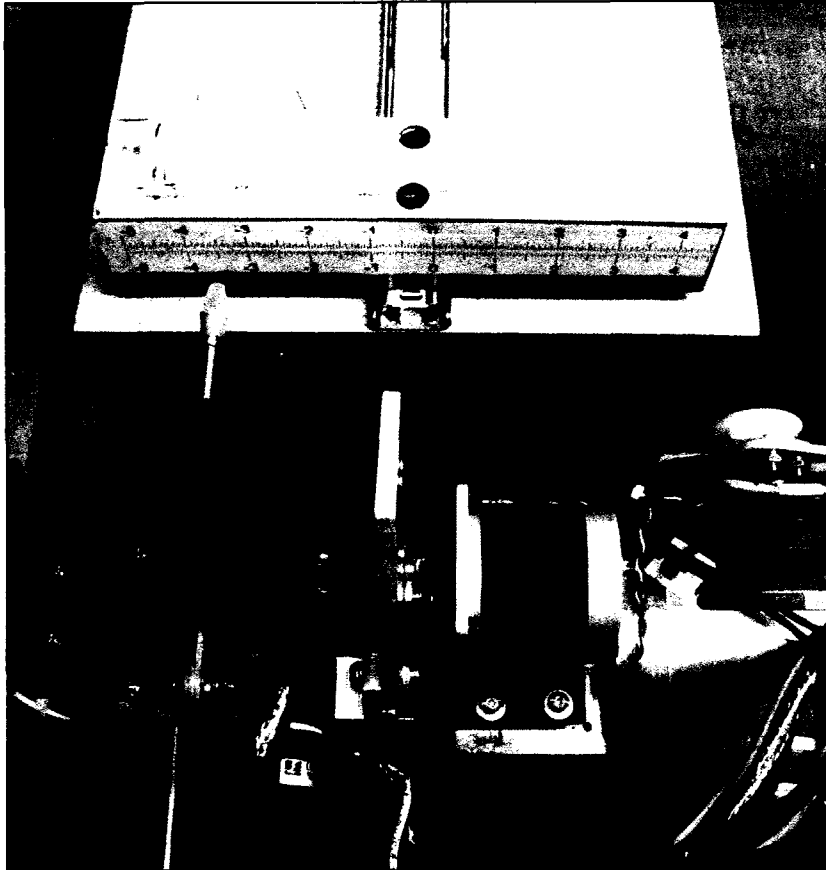


Figure 6.6 Camera Calibration Jig (Top View)

The front and rear camera-laser systems were calibrated over a range of 4.50-7.25 inches with 27 increments for a total of 54 images. The calibration measurements were made with the 24 inch Mitutoyo digital caliper. The 54 digital images were saved on the PC hard drive with a consecutive numbering scheme and then analyzed to determine the center pixel location.

A LabVIEW™ VI automatically extracted the center red pixel values for a series of digital images. The VI's inputs included a path to the location of an image or series of images to be analyzed, the base name of the images (minus the image's index), the starting and ending image index numbers, the quadratic's peak width, and red pixel value

threshold. The inputs are shown on the VI's front panel in Figure 6.7. Its associated block diagram is shown in Figure 6.8.

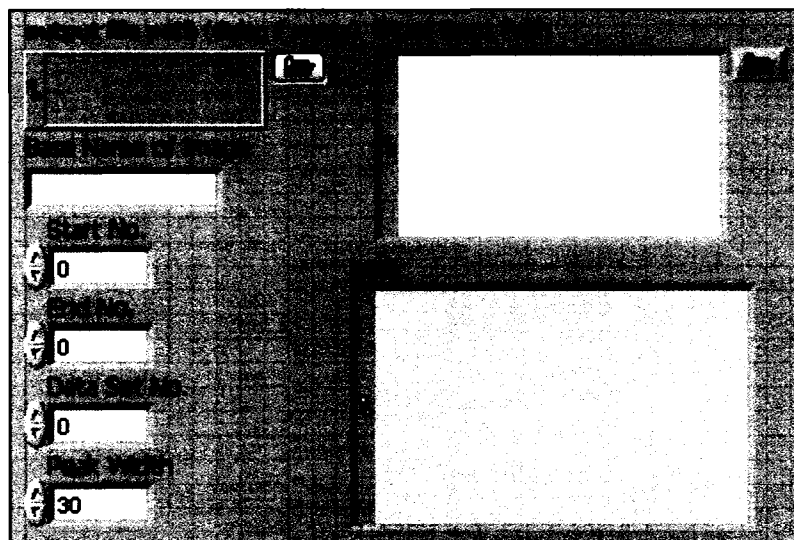


Figure 6.7 Parse Image Set for Camera Calibration Front Panel

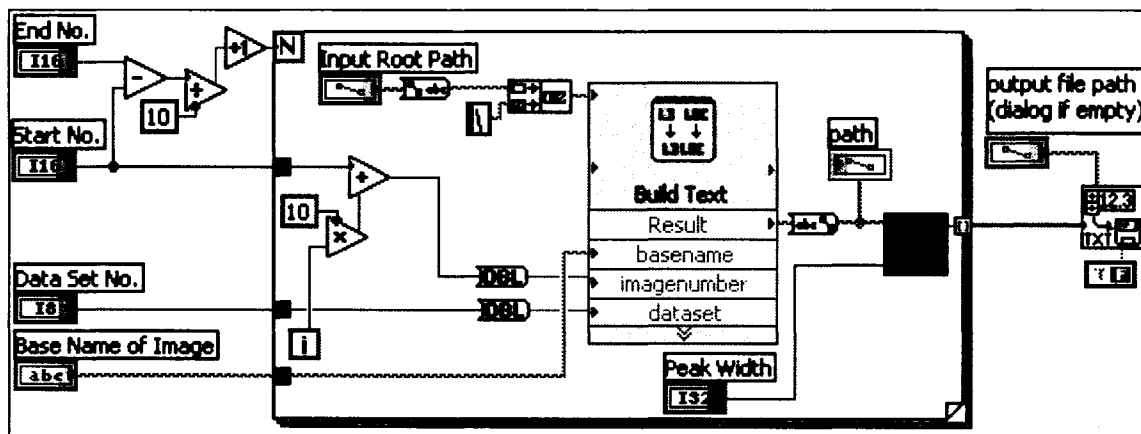


Figure 6.8 Parse Image Set for Camera Calibration Block Diagram

The programming structure of the “Parse Image Set” VI utilized a FOR LOOP which executed the “Peak Finder Looped” sub-VI for each of the 54 calibration images. The “Build Text” express VI in the “Parse Image Set” VI was used to incrementally

adjust the name of the image for each program loop. The “Parse Image Set” VI processed the 27 rear calibration images and the 27 front calibration images.

The “Peak Finder Looped” VI opened a single image file, converted the image to a two dimensional array of three clusters representing the RGB values of each pixel and extracted the red values from each pixel. The center of the camera represented the point of measurement. Therefore, the VI analyzed the red values in the center raster of the image. The images were 768 pixels tall, thus 384<sup>th</sup> raster was analyzed. The “Peak Detector” algorithm, as described in Chapter 2, operated on the 384<sup>th</sup> raster and determined the location of the peak(s). If no peak was found, the peak width was decremented and the peak detector repeated the search. If more than one peak was found, the peak with the maximum amplitude was saved. The “Peak Finder Looped” block diagram is shown in Figure 6.9.

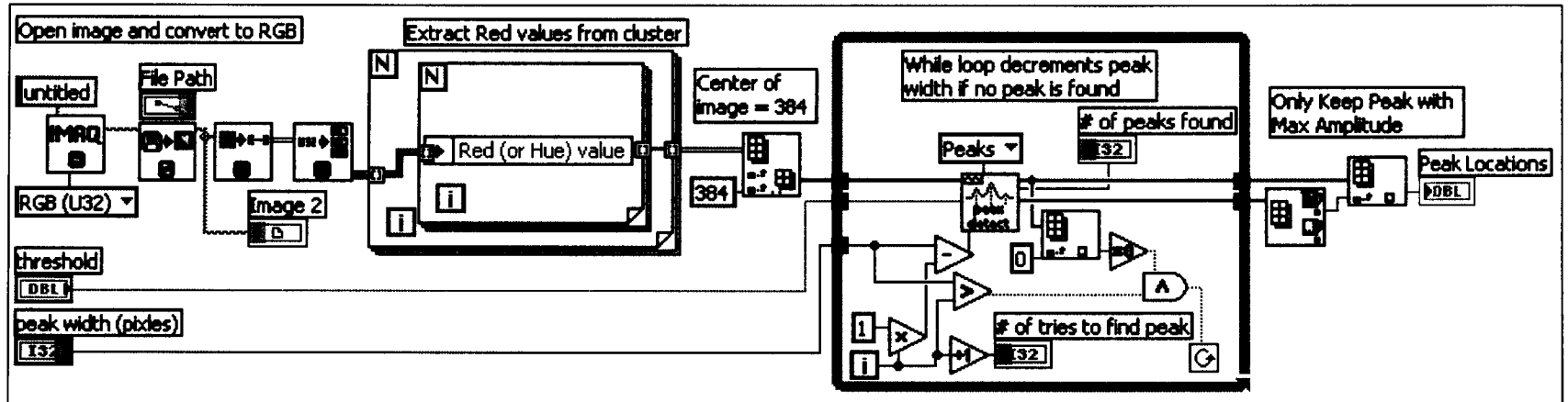


Figure 6.9 Peak Finder Looped VI Block Diagram



The peak pixel values for the front and rear calibration images were plotted versus the caliper measurements taken on the calibration jig. A third-degree polynomial was fitted to each set of calibration data to provide a function which converts the pixel values to a radial distance in inches. The results from the front and rear camera calibration procedure are shown in Figure 6.10.

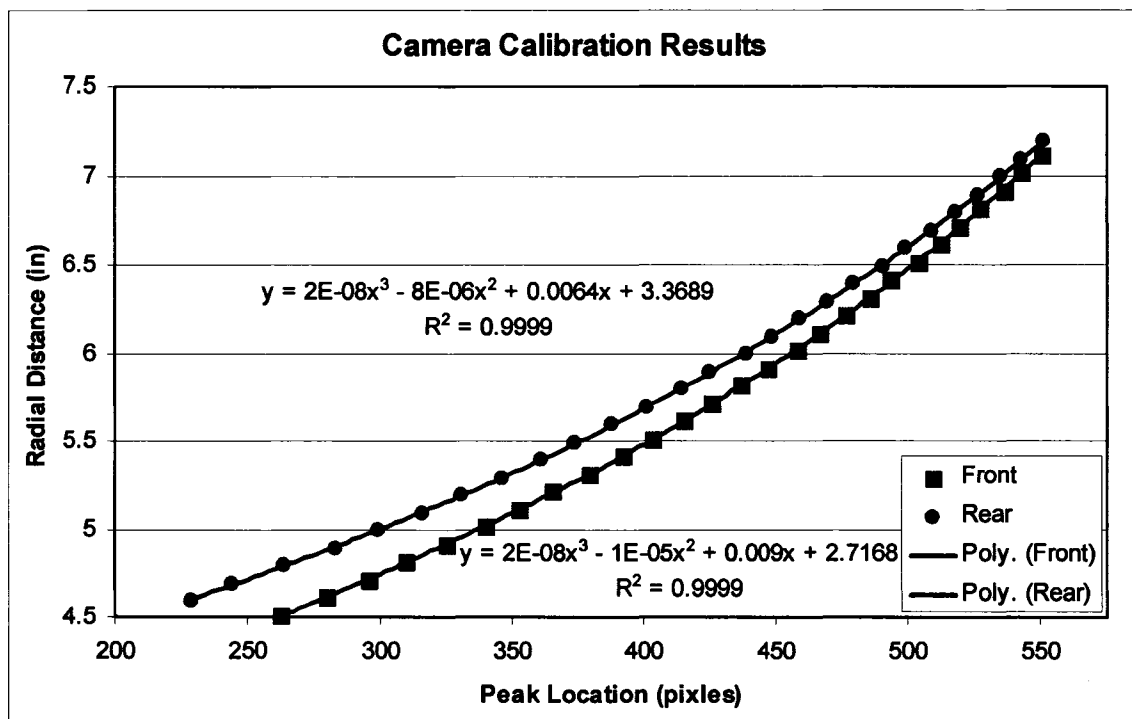


Figure 6.10 Camera Calibration Curves and Equations

### 6.1.5 Accelerometer Normalization and Calibration

The tri-axis accelerometer was used to calculate the pitch and roll angles of the robot relative to gravity. The angles were calculated from the raw analog voltages from accelerometer. Each of the raw output voltages,  $V_{outx}$ ,  $V_{outy}$ , and  $V_{outz}$ , varied proportionately according to the accelerometer's orientation relative to gravity. These

voltages can be treated as three components of a vector representing gravity and are expressed as Eq. (6.2).

$$\begin{bmatrix} V_{outx} \\ V_{outy} \\ V_{outz} \end{bmatrix} \quad (6.2)$$

These raw voltages were normalized to values between -1 and 1 using Eq. (6.3).

$$\left( \frac{2(V_{outx} - V_{\min})}{V_{\max} - V_{\min}} - 1 \right) = V_{normx} \quad (6.3)$$

where  $V_{\min} = -1$ ; and  $V_{\max} = 1$ . Likewise,  $V_{outy}$  and  $V_{outz}$  are normalized using Eq. (6.3).

Since the accelerometer's coordinate system was not perfectly aligned with the robot's coordinate system, the two coordinate systems were related to each other by the angles between each of their axes. This was achieved by setting the robot on a level surface and taking voltage output readings from the accelerometer. Since the robot was level, the normalized output from the accelerometer multiplied by a transformation matrix should be equal to a vector pointing toward gravity. This can be represented by Eq. (6.4).

$$\begin{bmatrix} V_{normx} \\ V_{normy} \\ V_{normz} \end{bmatrix} \cdot \begin{bmatrix} l_1 & m_1 & n_1 \\ l_2 & m_2 & n_2 \\ l_3 & m_3 & n_3 \end{bmatrix} = \begin{bmatrix} 0 \\ 0 \\ -1 \end{bmatrix} \quad (6.4)$$

where  $l$ ,  $m$ , and  $n$  are direction cosines of the angles between the robot's coordinate system and the accelerometer's coordinates system.

Since the direction cosine matrix is unknown, Eq. (6.4) yields three equations with nine unknowns. Six more equations are necessary to solve for the nine direction

cosines. Since the accelerometer's coordinate system and the robot's coordinate system are rectangular and have a common origin, Eqs. (6.5) and (6.6) can be written [74].

*For the Row Elements:*

$$\begin{aligned}
 l_i^2 + l_i^2 + l_i^2 = 1, \quad i = 1,2,3, \quad \text{and} \quad & l_1 l_2 + m_1 m_2 + n_1 n_2 = 0, \\
 & l_1 l_3 + m_1 m_3 + n_1 n_3 = 0, \\
 & l_2 l_3 + m_2 m_3 + n_2 n_3 = 0
 \end{aligned} \tag{6.5}$$

*For the Column Elements:*

$$\begin{aligned}
 l_1^2 + l_2^2 + l_3^2 = 1, \quad & l_1 m_1 + l_2 m_2 + l_3 m_3 = 0, \\
 m_1^2 + m_2^2 + m_3^2 = 1, \quad \text{and} \quad & l_1 n_1 + l_2 n_2 + l_3 n_3 = 0, \\
 n_1^2 + n_2^2 + n_3^2 = 1, \quad & m_1 n_1 + m_2 n_2 + m_3 n_3 = 0
 \end{aligned} \tag{6.6}$$

A Mathcad® solve block was utilized to simultaneously solve Eq. (6.4) and five of the nine relations listed in Eqs. (6.5) and (6.6) for the nine unknown direction cosines.

This resulted in the Eq. (6.7).

$$\begin{bmatrix} l_1 & m_1 & n_1 \\ l_2 & m_2 & n_2 \\ l_3 & m_3 & n_3 \end{bmatrix} = \begin{bmatrix} 0.9922 & -0.1233 & -0.0182 \\ 0.1232 & 0.9924 & -5.5546 \cdot 10^{-3} \\ 0.0191 & 3.0409 \cdot 10^{-3} & 1.0225 \end{bmatrix} \tag{6.7}$$

The direction cosines were used to transform the three normalized voltages in Eq. (6.2). This provided three primed voltages which represent the gravity vector relative to the robot's coordinate system noted in Eq. (6.8).

$$\begin{bmatrix} V_{normx} \\ V_{normy} \\ V_{normz} \end{bmatrix} \cdot \begin{bmatrix} 0.9922 & -0.1233 & -0.0182 \\ 0.1232 & 0.9924 & -5.5546 \cdot 10^{-3} \\ 0.0191 & 3.0409 \cdot 10^{-3} & 1.0225 \end{bmatrix} = \begin{bmatrix} V_{x'} \\ V_{y'} \\ V_{z'} \end{bmatrix} \tag{6.8}$$

The relationship between the three primed voltages,  $V_{x'}$ ,  $V_{y'}$ , and  $V_{z'}$ , and the pitch and roll angles of the robot relative to gravity are shown in Figures 6.11 and 6.12.

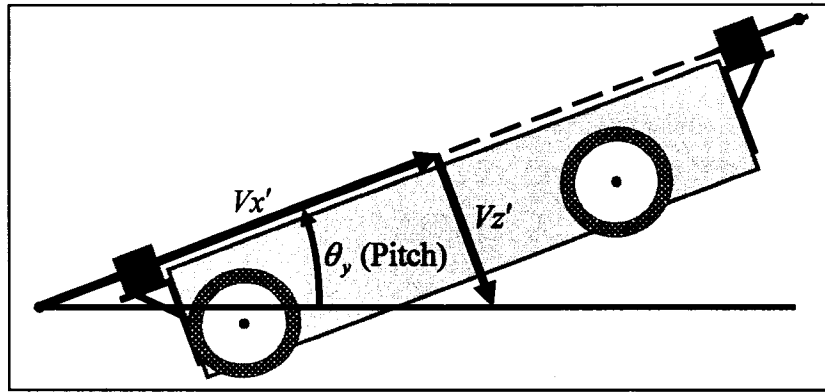


Figure 6.11 Robot Pitch Angle Related to Accelerometer Output Voltages

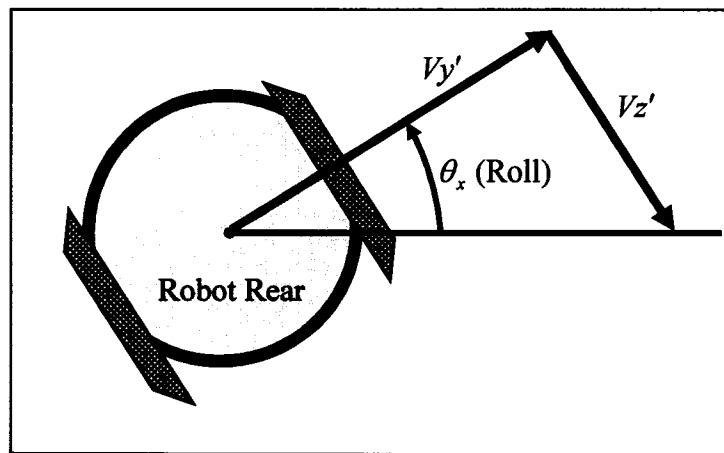


Figure 6.12 Robot Roll Angle Related to Accelerometer Output Voltages

The geometric relationships shown in Figures 6.12 and 6.13 were quantified with directional cosine equations noted in Eqs. (6.9) and (6.10).

$$\theta_y = \cos^{-1} \left( \frac{V_{x'}}{\sqrt{(V_{x'})^2 + (V_{z'})^2}} \right) \quad (6.9)$$

$$\theta_x = \cos^{-1} \left( \frac{V_{y'}}{\sqrt{(V_{y'})^2 + (V_{z'})^2}} \right) \quad (6.10)$$

### **6.1.6 Axial Distance Encoder and Robot Drive Motor Calibration**

The rotary encoder, used to measure the axial distance traveled by the robot down the pipe, was also calibrated before the data collection phase of the project. A conversion was necessary to translate the number of pulses sensed by the encoder to the distance actually traveled by the robot. The axial distance encoder delivered 900 pulses per revolution and had a 1.6 inch diameter plastic wheel attached to the shaft. The robot wheel had a diameter of 4.5 inches, therefore, the final pulse to inch ratio was Eq. (6.11).

$$\frac{1 \text{ rev}}{900 \text{ pulses}} \times \frac{1.6 \text{ in}}{4.5 \text{ in}} \times \frac{4.5 \cdot \pi \text{ in}}{1 \text{ rev}} \approx 0.005585 \frac{\text{in}}{\text{pulse}} \approx 179.049 \frac{\text{pulses}}{\text{in}} \quad (6.11)$$

The axial distance sensor was used to *measure* how far the robot had traveled after it had already moved. The axial distance sensor was not used to *control* how far the robot traveled. This simplified the programming code required for automatic data collection. The distance traveled by the robot was assumed to be a function of two variables: voltage and time. A certain level of voltage for a specified length of time would drive the robot a certain distance. Since the data collection process would involve a constant driving speed, only one data point needed to be calibrated with the drive motor. Thus, the robot's DC drive motor voltage was varied until it moved 1.5 inches per second. The voltage required was 0.681 volts and was applied during the experimental data collection. The robot drive motor ceased motion after a specified length of time had passed based on the desired distance between stops. For more details on how this scheme was implemented during data collection, see Section 6.2.3.

### **6.1.7 Experimental Procedure for Full-Length Pipe Scan**

Before the full-pipe scan was performed with the prototype profiler, a set of detailed experimental procedures was developed to avoid potential mistakes. The procedures for the full-length pipe scan are as follows:

1. Double-check all of the measurements between the tactile probes and camera-laser systems to ensure the alignment of the critical planes.
2. Level the robot and ensure calibration of the accelerometer by measuring its output voltages.
3. Ensure the correct voltages were supplied to the prototype profiler power systems. These included two 5 VDC sources, one 12 VDC source, and one 24 VDC source.
4. Verify proper operation of the cameras, USB DAQ, and their drivers by running the Measurement and Automation Explorer (NiMAX) program.
5. Clean any dust or residue off of the tactile probe racks and ensure smooth operation by manually moving each probe. Lubricate tactile gears if necessary.
6. Clean any dust or residue off of the camera lenses and verify the focus adjustments and iris adjustments were correct.
7. Ensure all cords and wires were clear of any moving parts on the prototype.
8. Ensure the pipe is clear of any c-clamps or other devices used during set-up.
9. Level the steel pipe on the test stand.
10. Close any other programs running on the laptop PC to free up system resources.
11. Load the “Master Control” VI, set the “total distance to scan” to 72 inches, set the “distance between stops” to 0.5 inches, set the robot “drive speed” to 1.5 in/sec,

enable both the front and rear measuring systems, set the “stepping mode” to “half step”, set the “ring resolution” to 200 steps/rev, set the “laser brightness” to maximum, and choose a file name and path for the data storage location.

#### **6.1.8 Acquiring Optical Scans for Incremental Bump-Height Measurements**

Before the multiple optical scans were performed with the prototype profiler for various bump-heights, detailed experimental procedures were developed to avoid potential mistakes. The procedures for these experiments are the same as those presented in Section 6.1.7 for the full-length pipe scan except for step 11 and the addition of a 12<sup>th</sup> step.

11. Load the “Master Control” VI, set the “total distance to scan” to 0 inches, set the “distance between stops” to 0 inches, set the robot “drive speed” to 0 in/sec, enable both the front and rear camera-laser systems, set the “stepping mode” to “half step”, set the “ring resolution” to 200 steps/rev, set the “laser brightness” to maximum, and choose a file name and path for the data storage location.
12. Repeat step 11 for the next bump.

#### **6.1.9 Experimental Procedure for Caliper Measurements of Pipe Diameter**

A single ring of diameter measurements were taken with a 24 inch Mitutoyo digital caliper to provide a control set of data. This control set was used as a basis of comparison to the measurements taken with the tactile probes and the camera-laser systems. A flexible tape measure was wrapped around the circumference of the test pipe,

and one-hundred diameter measurements were recorded with the digital caliper. A picture of this process is shown in Figure 6.13.

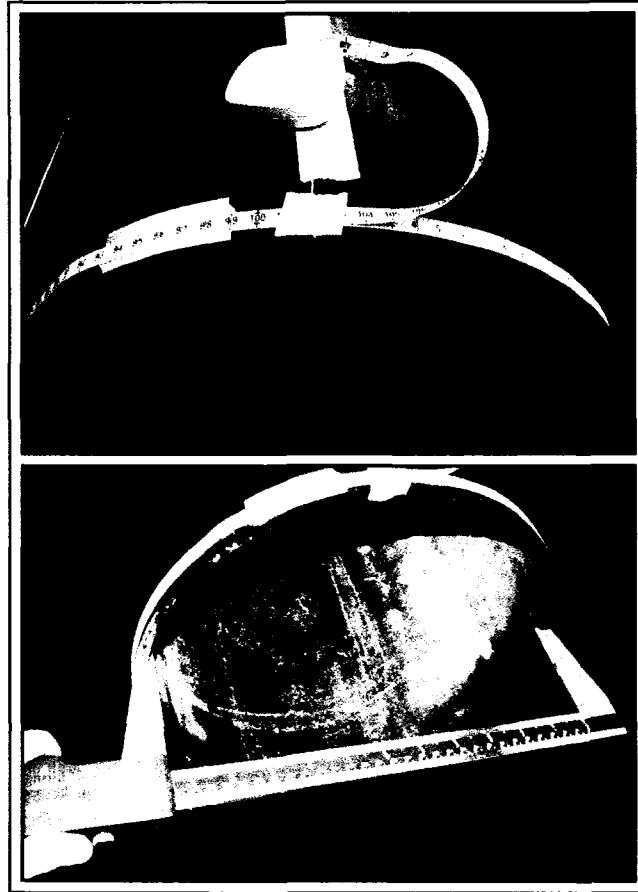


Figure 6.13 Caliper Measurements of Pipe Diameter

## **6.2 Software Design and Implementation for Automated Data Collection**

Customized software was developed using National Instrument's LabVIEW™ to control the prototype and log sensor data during the data collection phases of the project. Thirty-one custom programs (VIs) were created for data collection. Since each VI has a user interface (front panel) and a block diagram, not all of the VIs are displayed in this chapter. Only the relevant and unique front panels and block diagrams will be shown, but



all the VIs are discussed in the sections that follow. A VI hierarchy diagram displaying the 31 VIs used for data collection and each dependant sub-VI is shown in Figure 6.14.

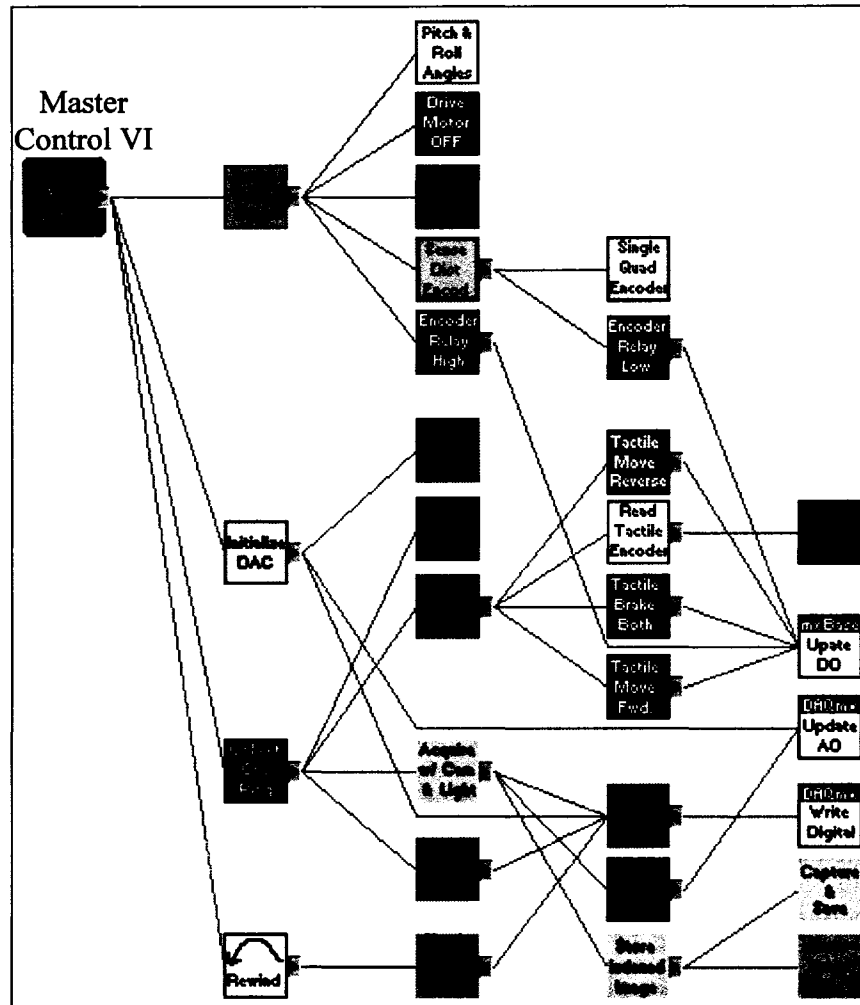


Figure 6.14 VI Hierarchy for Automated Data Collection Process

The software design was based on the following control methodology:

- The prototype robot would profile a certain length of pipe by driving a specified distance, stopping, and scanning one ring of radial data with the front measuring system and one ring of radial data with the rear. The stepper motors would “reset”

by reversing direction and stopping in their original position. This process would repeat until the desired length of pipe to profile had been reached by the robot.

### **6.2.1 Master Control VI**

The “Master Control” VI was written to implement the overarching control methodology, and it calls four sub-VIs in the process. The “Initialize DAC” VI executes, and then the “Sense, Drive, Stop” VI, the “Collect One Ring” VI, and the “Rewind” VI are each executed in sequence and repeated in a WHILE LOOP until a stop button is pressed or the total distance to scan is reached or exceeded. A picture of the “Master Control” VI block diagram is shown in Figure 6.15.

information and includes indicators making the operator aware of the current test

The "Master Control" VI front panel allows a user to input several pieces of

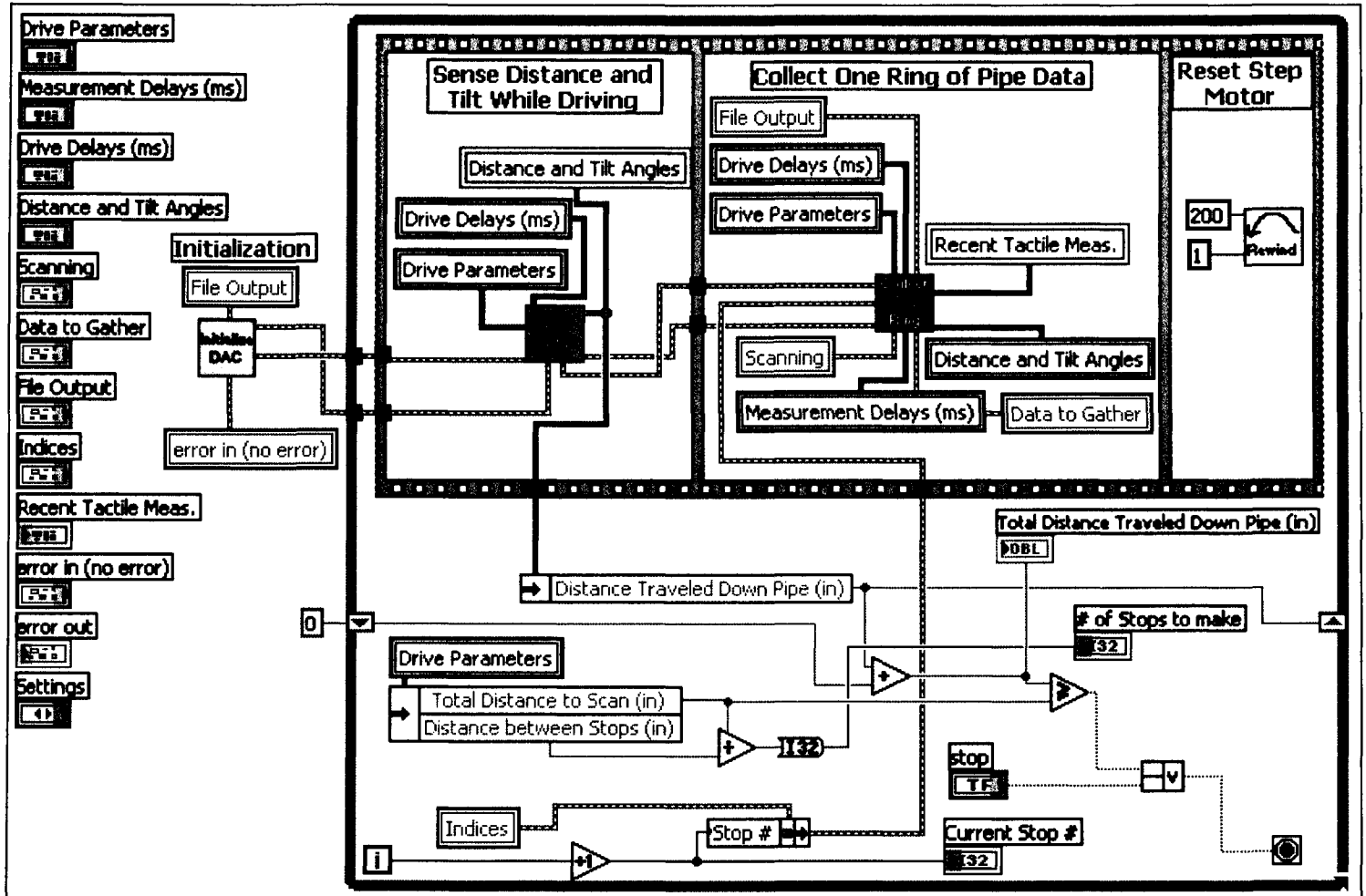


Figure 6.15 Master Control VI Block Diagram

conditions and progress. Input parameters on the master control include the total length of pipe to scan, distance between stops, robot drive speed, type of measurements to take, half/full step mode, number of steps (or measurements taken) per revolution, laser brightness, measurement delays, drive delays, filename and path for data storage.

Indicators on the “Master Control” VI include the current robot stop number, the number of stops to make, the total distance traveled by the robot during the current scan, the incremental distance traveled from the last stop, and the robot’s global pitch and roll angles from the accelerometer. A picture of the “Master Control” front panel and six nested front panel tabs are shown in Figures 6.16-6.19.

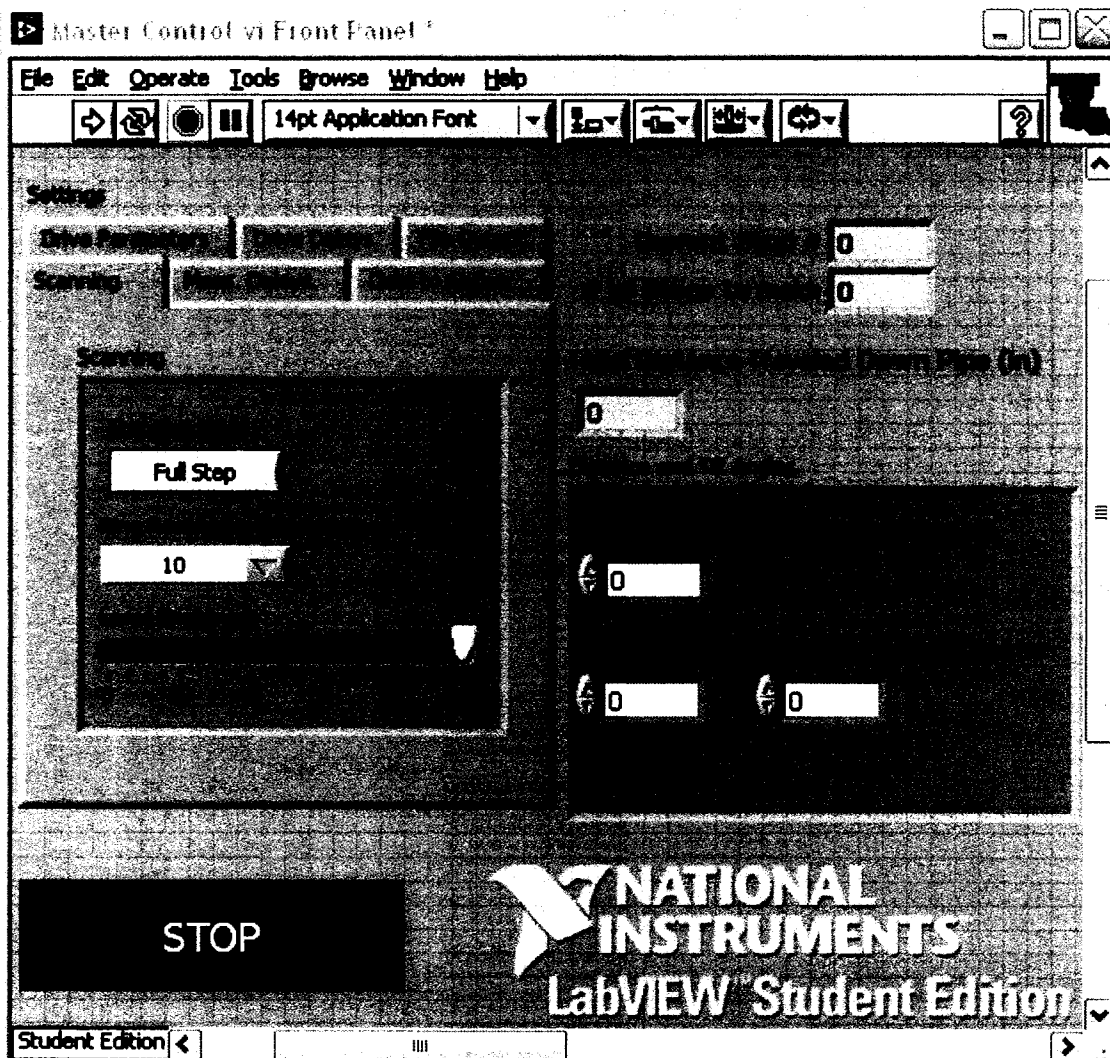


Figure 6.16 Master Control VI Front Panel

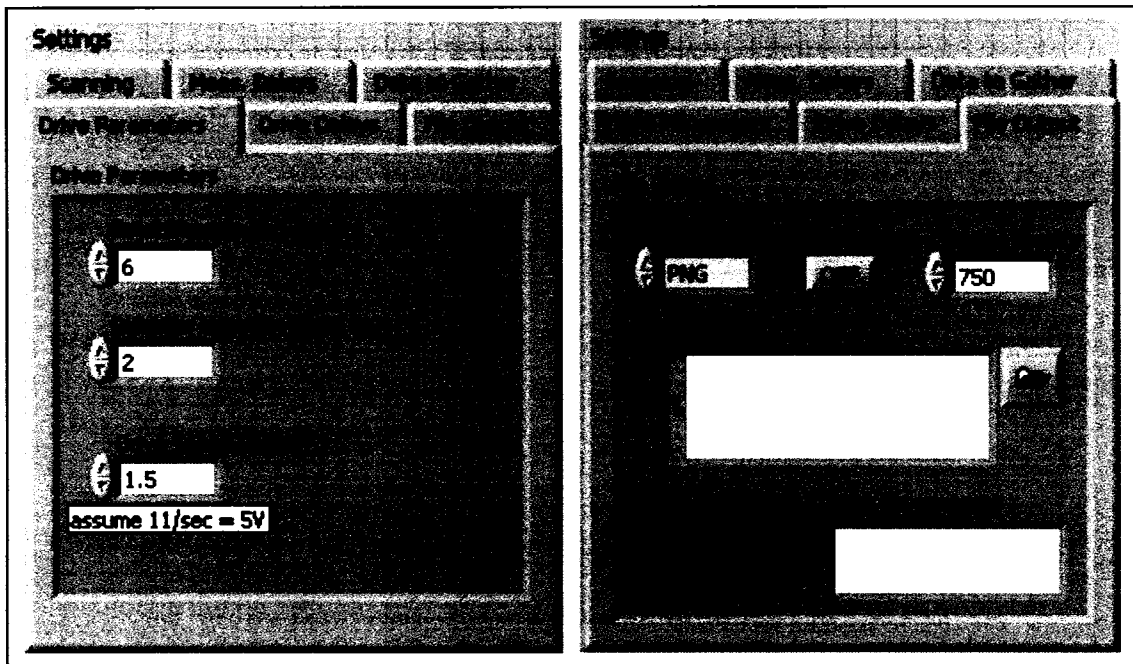


Figure 6.17 Drive Parameters and File Output Tabs on Master Control VI Front Panel

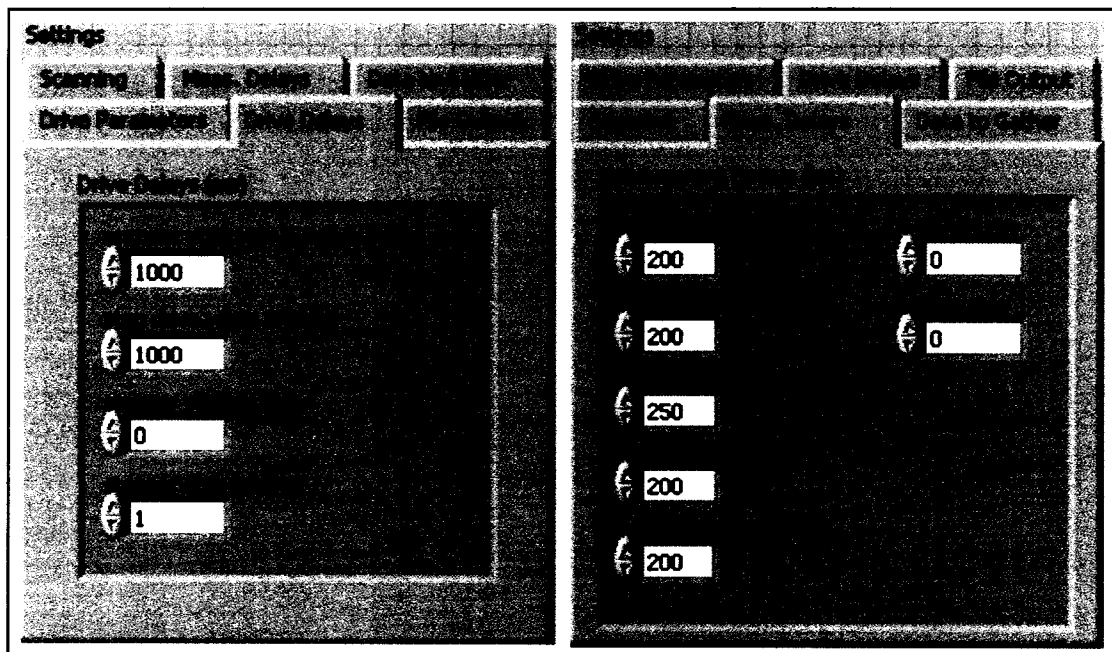


Figure 6.18 Drive and Measurement Delay Tabs on Master Control VI Front Panel

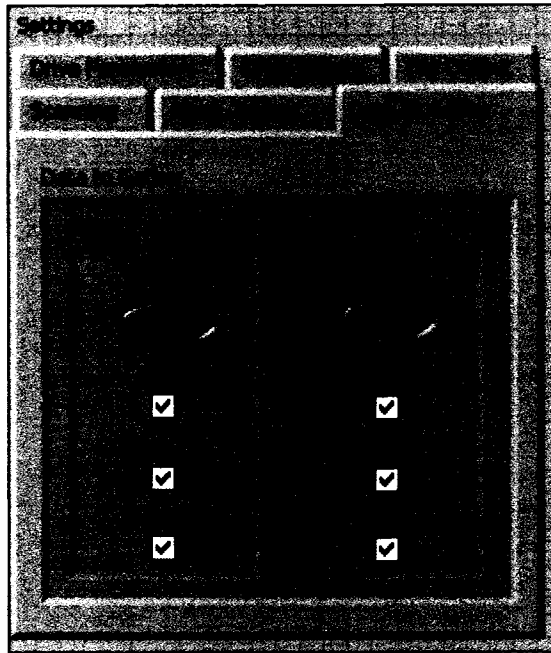


Figure 6.19 Data to Gather Tab on Master Control VI Front Panel

### **6.2.2 Initialize DAC VI and its Sub-VIs**

The first sub-VI executed in the “Master Control” VI is the “Initialize DAC” VI. The purpose of this VI is to initialize a data output file, set the analog output channels on the USB DAQ to zero, and initialize the digital output lines by setting them all to zero except one. The “Initialize DAC” VI calls 3 other sub-VIs to accomplish these tasks including the “Initialize File” VI, the “Update AO” VI, and the “Boolean Cluster to Port” VI. The block diagram of the “Initialize DAC” VI is shown in Figure 6.20.

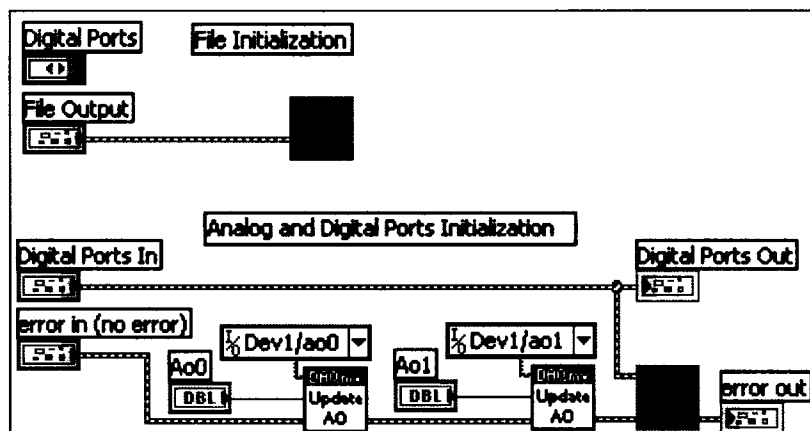


Figure 6.20 Initialize DAC VI Block Diagram

The “Initialize File” VI was designed to create a new text or csv file for storing the tactile radial measurements, the robot stop number during the scan, the angular stop number by each stepper motor, the incremental distance traveled by the robot between stops, and the pitch and roll angles at each stop. The “Initialize File” VI inserts a time/date stamp into the new file and the type of image saved by the IEEE 1394 cameras (JPG, PNG, or BMP). The “Initialize File” VI block diagram is shown in Figure 6.21.



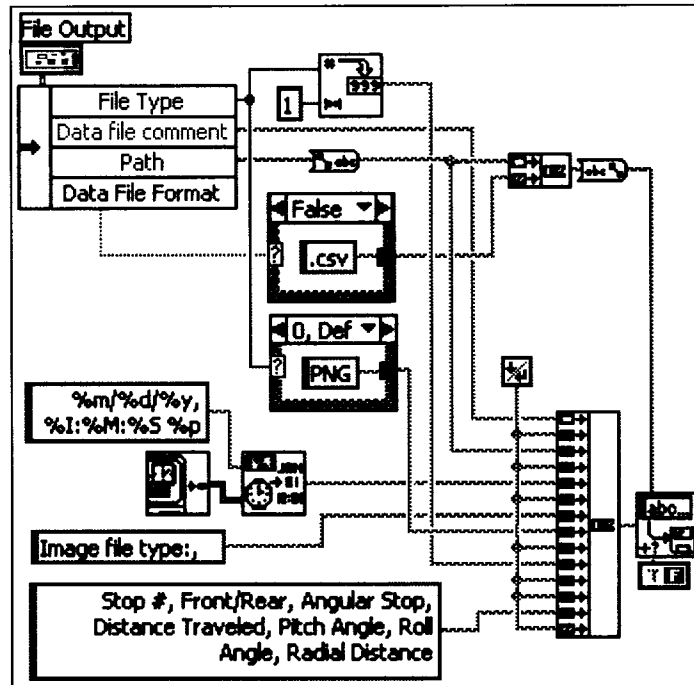


Figure 6.21 Initialize DAC VI Block Diagram

The “Update AO” VI was written to set an individual analog output channel on the USB DAQ to a user defined value. The physical DAQ channel, min and max voltage range, and desired output voltage were specified. This block diagram incorporates the use of National Instrument’s mxBase drivers which must be installed prior to use of this VI. The “Update AO” VI is shown in Figure 6.22.

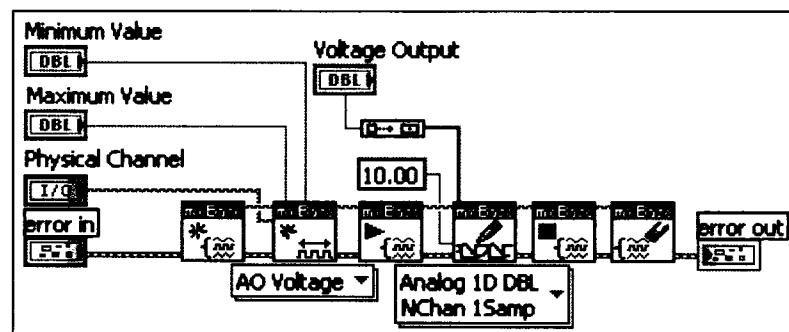


Figure 6.22 Update AO VI Block Diagram

Since the mxBase drivers only allow port level access to the digital inputs and outputs, the “Boolean Cluster to Port” VI was written to provide single digital channel access for writing Boolean data to the “Write Digital” VI. Port 0 on the USB DAQ has 8 bits, and Port 1 has 4 bits. Each bit was assigned to a toggle switch for Boolean control in the “Boolean Cluster to Port” VI Front Panel as shown in Figures 6.23 and 6.24.

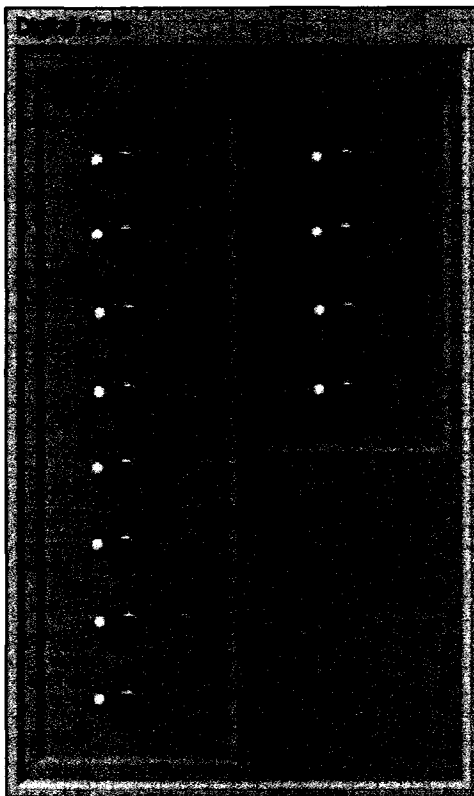


Figure 6.23 Boolean Cluster to Port VI Front Panel

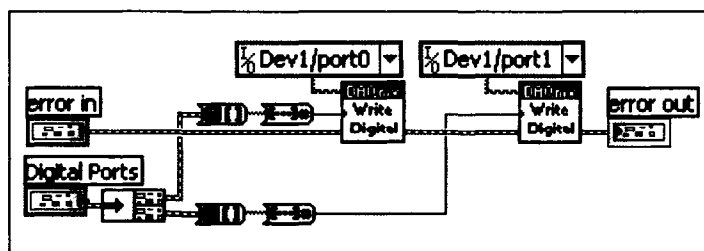


Figure 6.24 Boolean Cluster to Port VI Block Diagram

The “Write Digital” VI was designed to convert the Boolean cluster to a hexadecimal number and to send that number to the USB DAQ DIO ports via the mxBase drivers. The “Write Digital” VI block diagram is shown Figure 6.25.

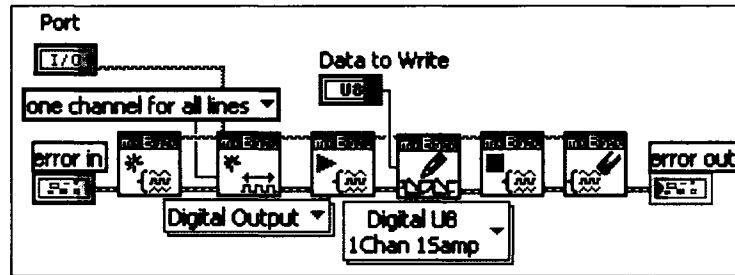


Figure 6.25 Write Digital VI Block Diagram

### **6.2.3 Sense, Drive, Stop VI and its Sub-VIs**

The “Sense, Drive, Stop” VI is the first of three sub-VIs called in the “Master Control” VI WHILE LOOP. The purpose of the “Sense, Drive, Stop” VI is to sample the axial distance encoder, drive the robot to its next stop for in preparation for radial measurements, sample the voltage output from the tri-axis accelerometer, and report the pitch and roll angles of the robot with respect to gravity. The “Sense, Drive, Stop” VI accepts the user inputs from the “Master Control” VI drive parameter tab and drive delay tab. The “Sense, Drive, Stop” VI outputs the distance traveled down the pipe, the global pitch angle, and global roll angle. The “Sense, Drive, Stop” VI block diagram is shown in Figures 6.26 and 6.27.

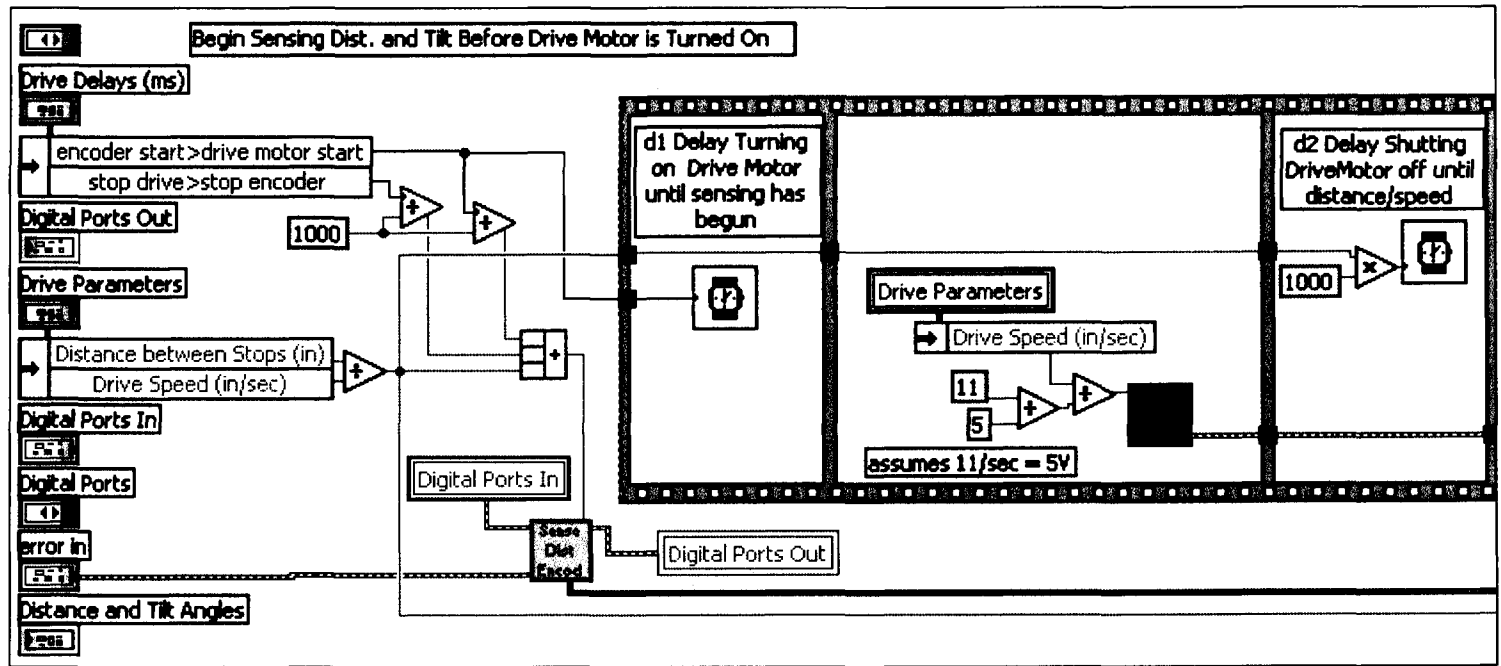


Figure 6.26 Sense, Drive, Stop VI Block Diagram (1 of 2)

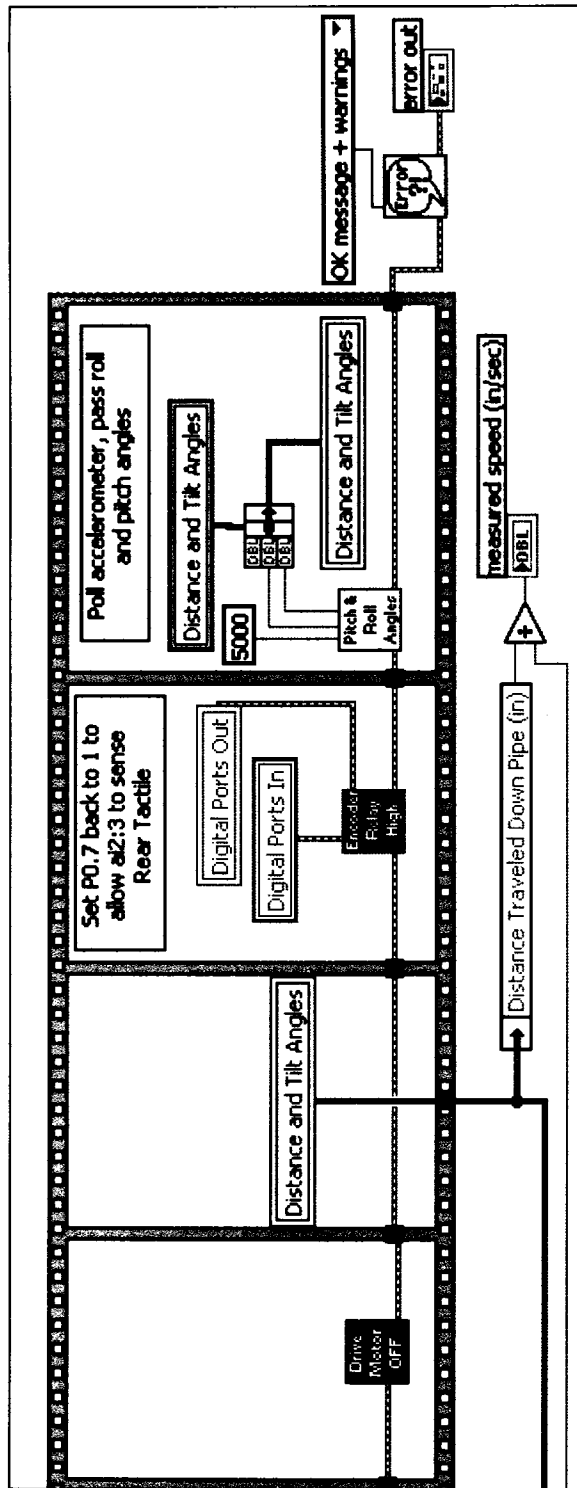


Figure 6.27 Sense, Drive, Stop VI Block Diagram (2 of 2)

The first sub-VI executed in the “Sense, Drive, Stop” VI is the “Sense Distance Encoder” VI. This VI is responsible for setting the encoder relay low, sampling the axial

distance encoder, processing the quadrature encoder logic, and reporting the distance traveled down the pipe. The sampling duration allotted for the axial distance encoder is a sum of three components: 1) a delay starting the robot's DC drive motor until sensing can begin, 2) a delay to allow the robot to stop rolling after the drive motor has been turned off, and 3) the time calculated from two user inputs including the distance between stops and the drive speed noted in Eq. (6.12).

$$\frac{\text{Distance between stops (in)}}{\text{Drive Speed (in/sec)}} = \text{seconds to sample axial distance encoder} \quad (6.12)$$

The sampling rate was set to 11 kHz per channel which was the maximum allowed by the USB DAQ. The "Sense Distance Encoder" VI block diagram is shown in Figure 6.28.

Encoder” VI is to process the quadrature encoder logic from the axial distance sensor and

The purpose of the “Single Quad Encoder” sub-VI in the “Sense Distance

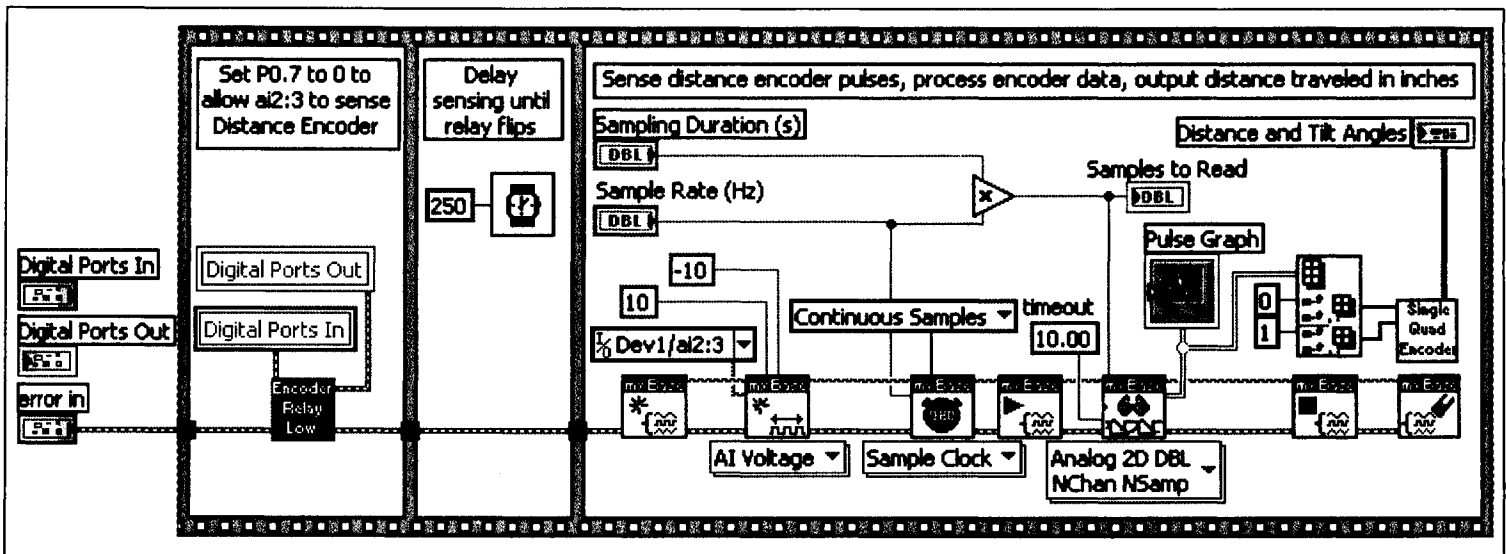


Figure 6.28 Sense Distance Encoder VI Block Diagram

apply the axial distance calibration equation. The “Single Quad Encoder” VI reads two one-dimensional arrays of encoder pulses, one pulse at a time, and converts them to inches traveled by the robot. The “Single Quad Encoder” VI block diagram is shown in Figure 6.29.



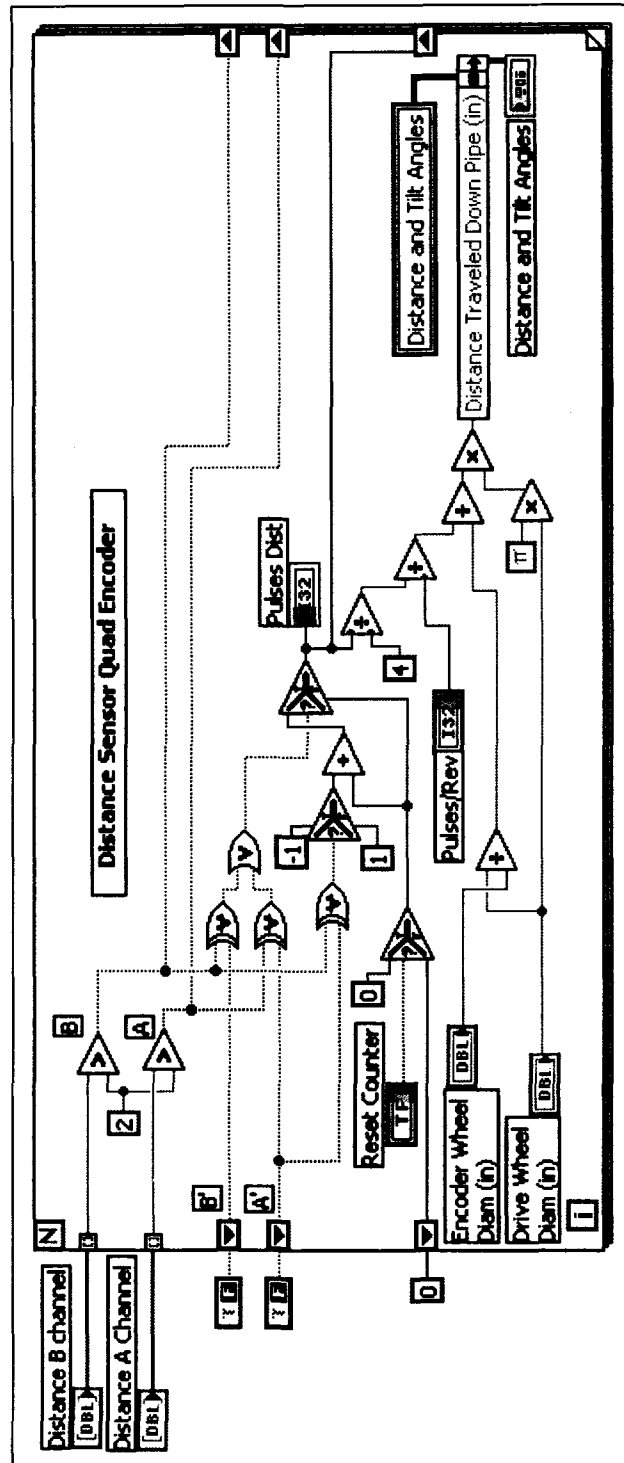


Figure 6.29 Single Quad Encoder VI Block Diagram

After the “Sense Distance Encoder” VI begins, the drive speed input is divided by the robot drive motor calibration equation to calculate the analog drive speed voltage for the DC drive motor controller. This is accomplished in the “Set Drive Speed” sub-VI.

The drive motor shuts off after its appointed time, the encoder relay is set to high, and the “Pitch and Roll” sub-VI executes.

The purpose of the “Pitch and Roll” VI was to sample the three analog voltages from the tri-axis accelerometer, normalize the voltages to range from -1 to 1, apply the accelerometer calibration equation, and calculate the pitch and roll angles of the robot with respect to gravity. The “Pitch and Roll” VI block diagram is shown in Figures 6.30 and 6.31.

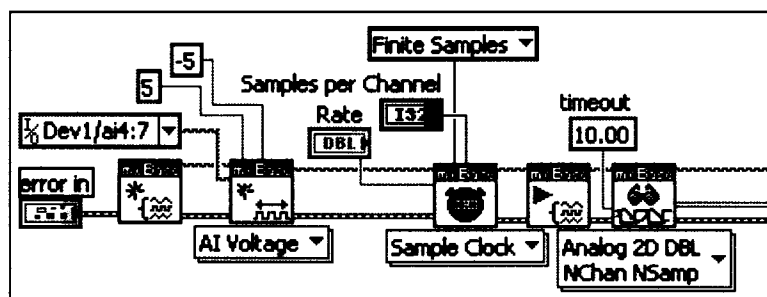


Figure 6.30 Pitch and Roll VI Block Diagram (1 of 2)

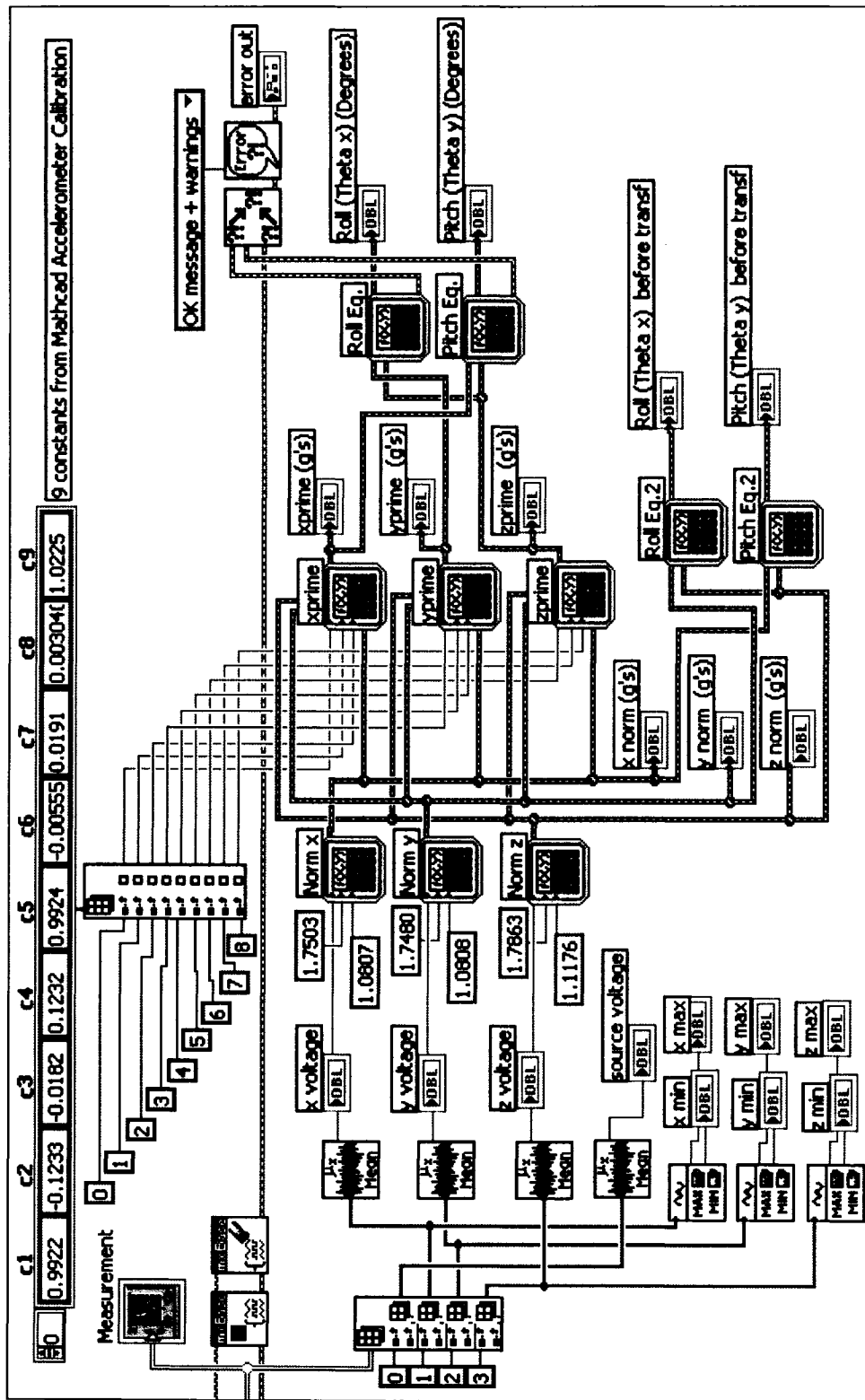


Figure 6.31 Pitch and Roll VI Block Diagram (2 of 2)

#### **6.2.4 Collect One Ring VI and its Sub-VIs**

The “Collect One Ring” VI is the second of three sub-VIs called in the “Master Control” VI WHILE LOOP. The purpose of the “Collect One Ring” VI is to collect radial measurements with the tactile probes and with the camera-laser systems, write the tactile probe measurements to a data file, acquire backlit images with the cameras, index the stepper motor, and then repeat the process until the user defined “measurements per revolution” is achieved. The “Collect One Ring” VI block diagram is shown in Figures 6.32, 6.33 and 6.34.

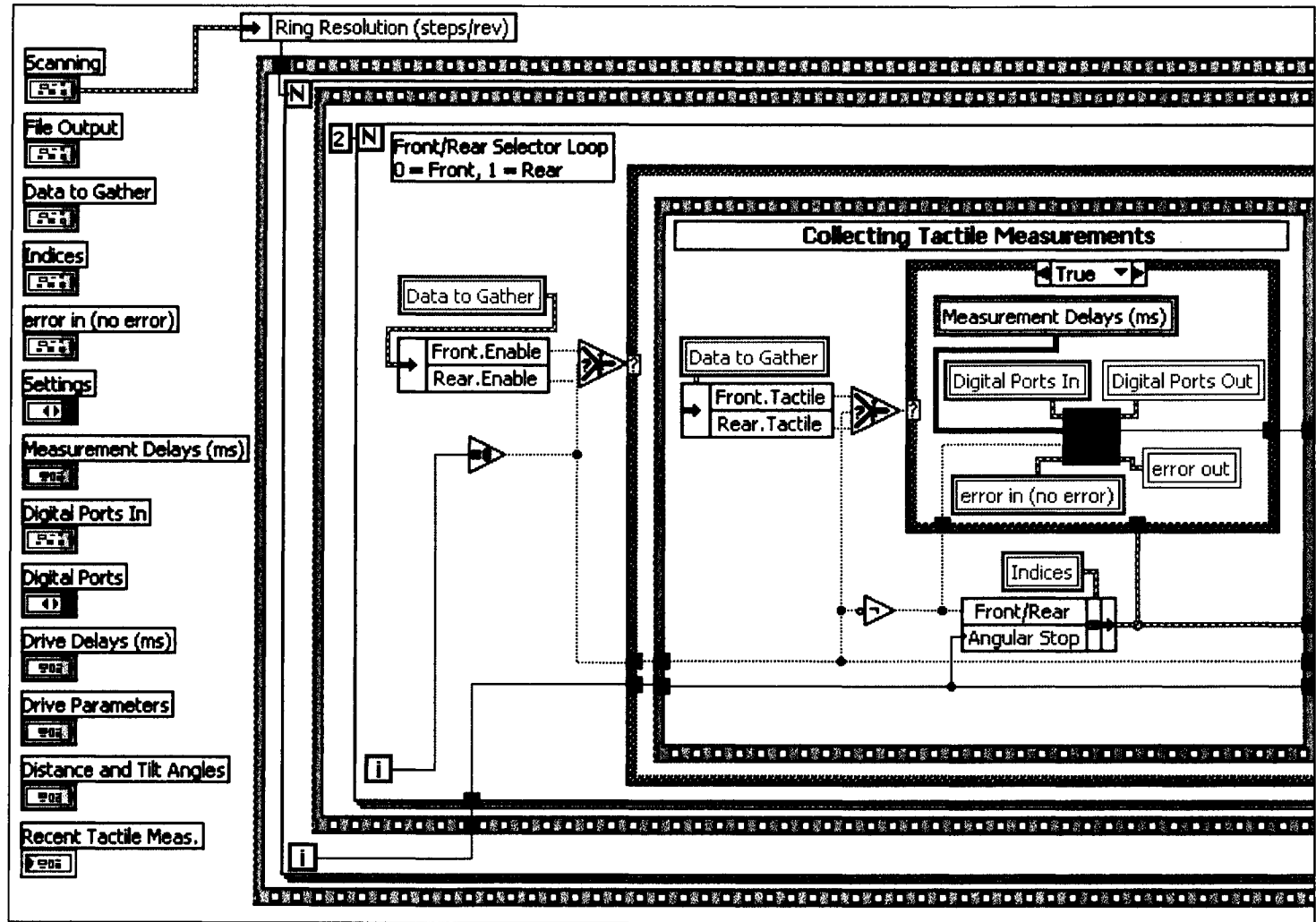


Figure 6.32 Collect One Ring VI Block Diagram (1 of 3)

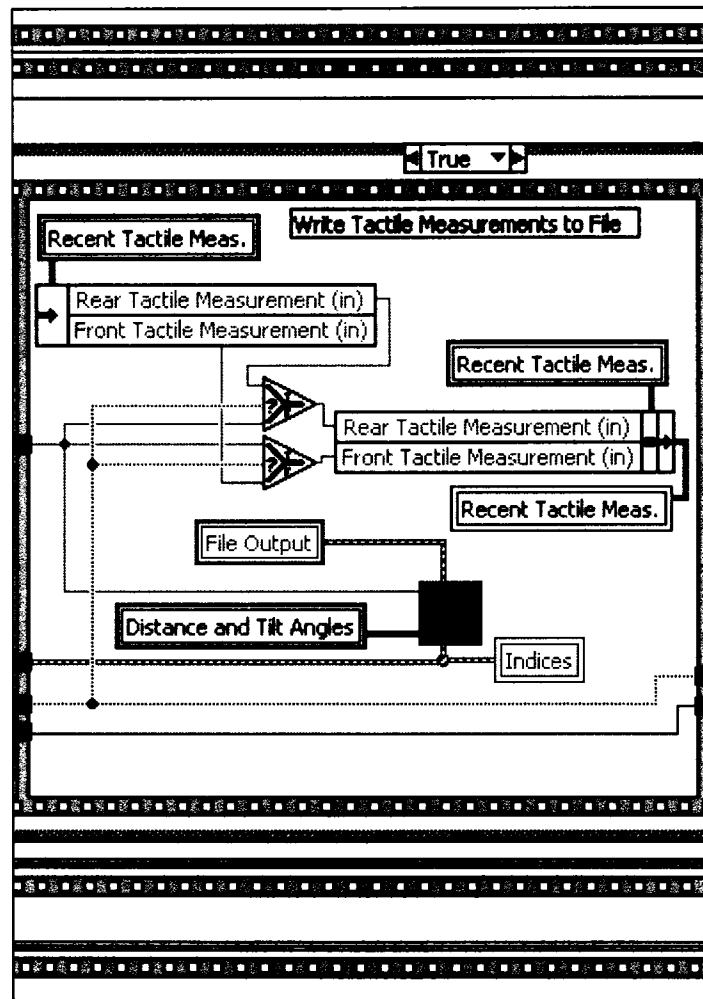


Figure 6.33 Collect One Ring VI Block Diagram (2 of 3)

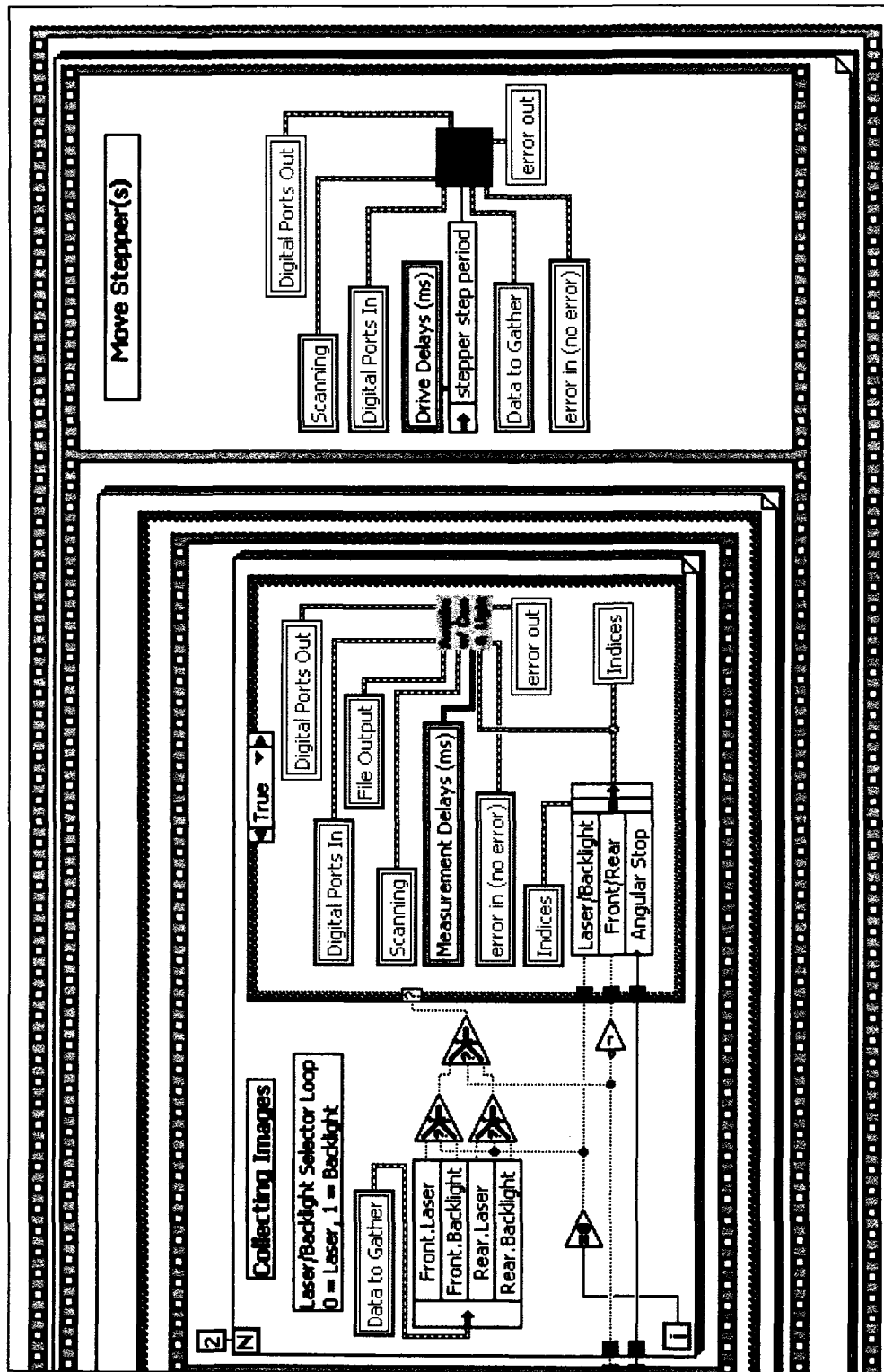


Figure 6.34 Collect One Ring VI Block Diagram (3 of 3)

The first sub-VI to execute in the “Collect One Ring” VI is the “Tactile Sense & Motion” VI. This VI was designed to drive a tactile probe outward for a preset time

duration, sample the tactile encoder to record a radial measurement, and then retract the tactile probe. The “Tactile Sense and Motion” VI is shown in Figures 6.35 and 6.36.

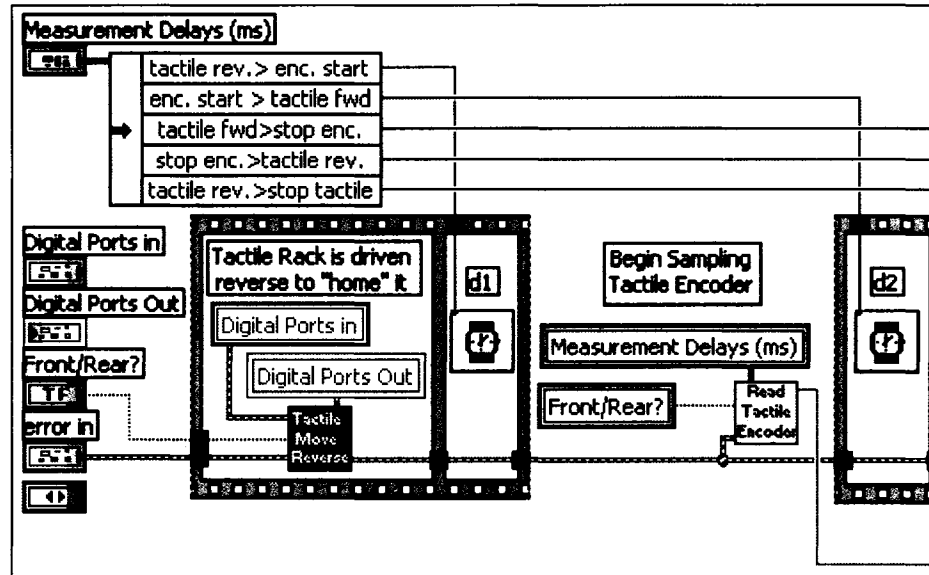


Figure 6.35 Tactile Sense and Motion VI Block Diagram (1 of 2)



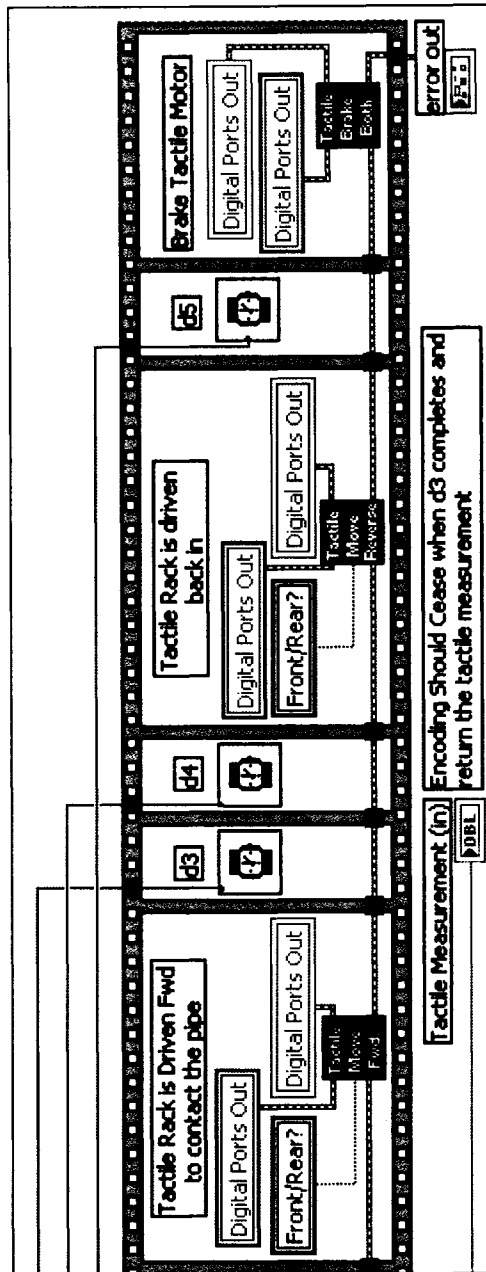


Figure 6.36 Tactile Sense and Motion VI Block Diagram (2 of 2)

Three sub-VIs are responsible for moving the tactile probes. This is achieved by sending digital signals to the tactile DC motor controllers via the USB DAQ. This is performed using the “Boolean Cluster to Port” VI. The “Read Tactile Encoder” sub-VI is very similar to the “Sense Distance Encoder” VI except for the encoder calibration equation. The “Read Tactile Encoder” VI applies the tactile encoder calibration equation

developed in Section 6.1.3. The tactile probe quadrature logic and calibration equation is applied in a sub-VI called the “Single Quad Encoder Linear” VI and is shown in Figure 6.37.

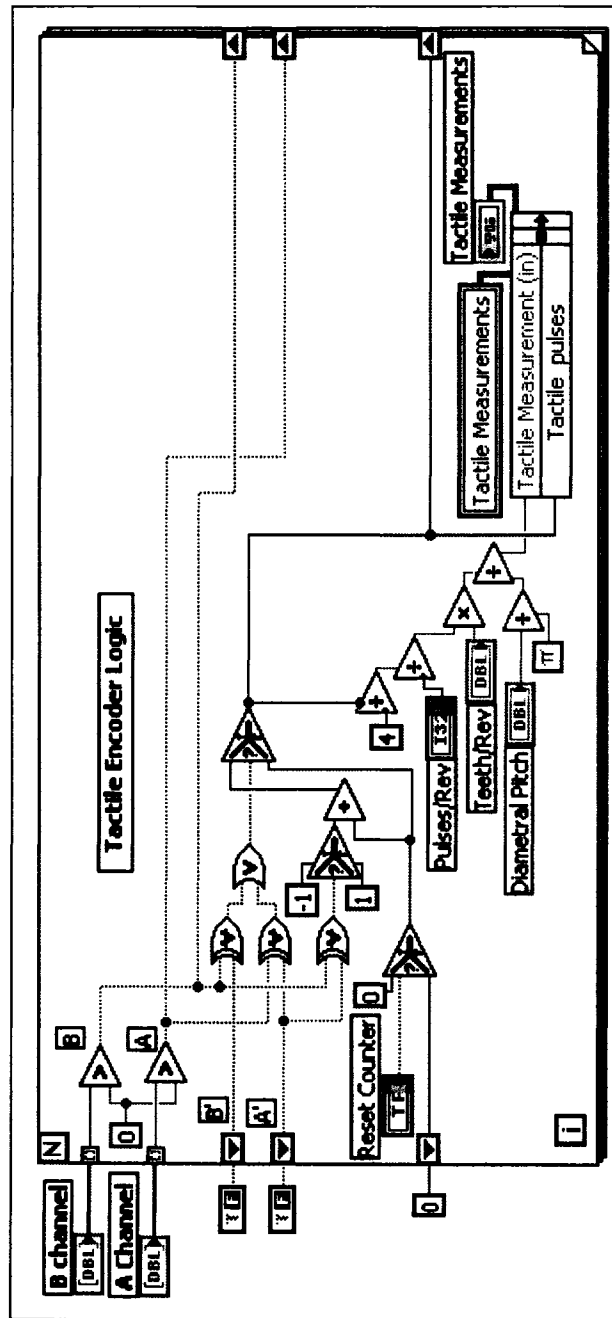


Figure 6.37 Single Quad Encoder Linear VI Block Diagram

The next sub-VI to execute in the “Collect One Ring” VI is the “Add File Line” VI. This VI was designed to open the initialized data file, write seven pieces of information including: the current stop number, an “F” or “R” to indicate whether the tactile measurement was taken at the rear or front probe, the incremental distance traveled by the robot down the pipe, the roll angle, pitch angle, and tactile probe measurement. The “Add File Line” VI block diagram is shown in Figure 6.38.

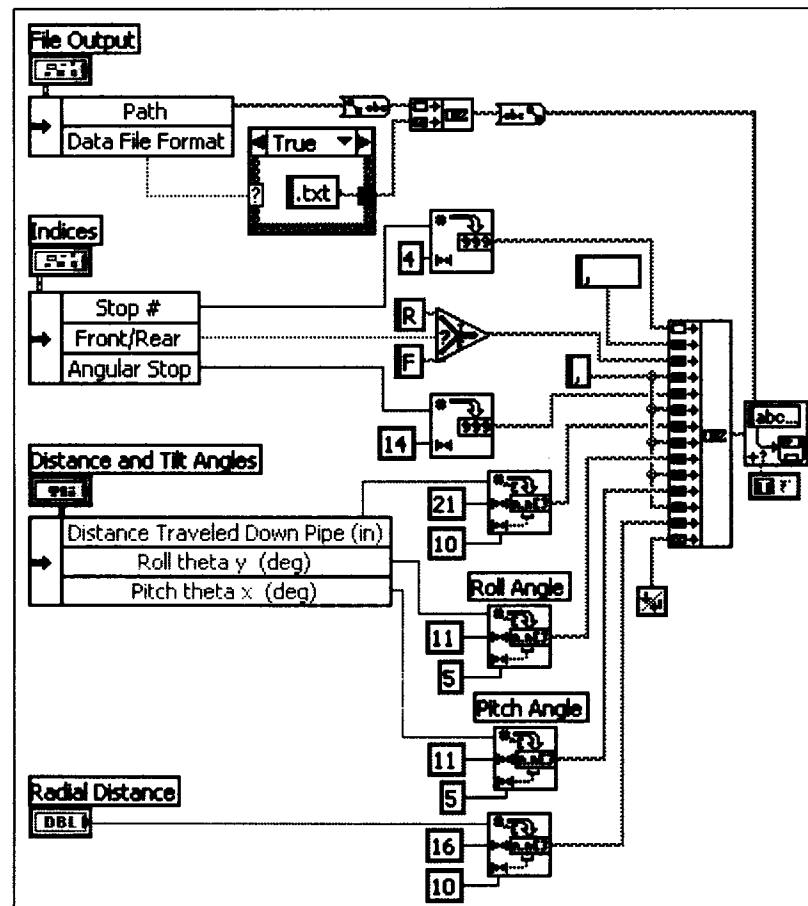


Figure 6.38 Add File Line VI Block Diagram

The next sub-VI to execute in the “Collect One Ring” VI is the “Acquire with Camera & Light” VI. This VI was designed to turn the backlights on, store an image, turn

the back lights off, turn the lasers on, store an image, and turn the lasers off. The “Acquire with Camera & Light” VI block diagram is shown in Figures 6.39 and 6.40.

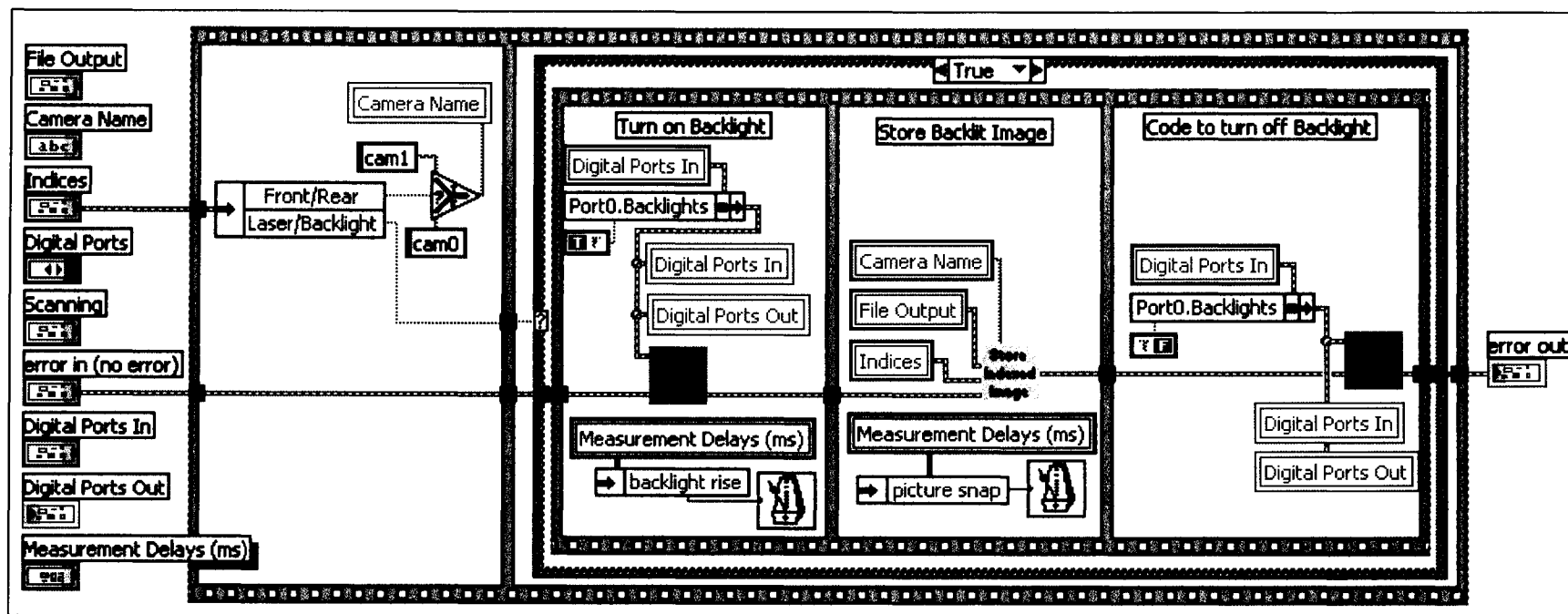


Figure 6.39 Acquire with Camera and Light VI Block Diagram in Backlight Mode

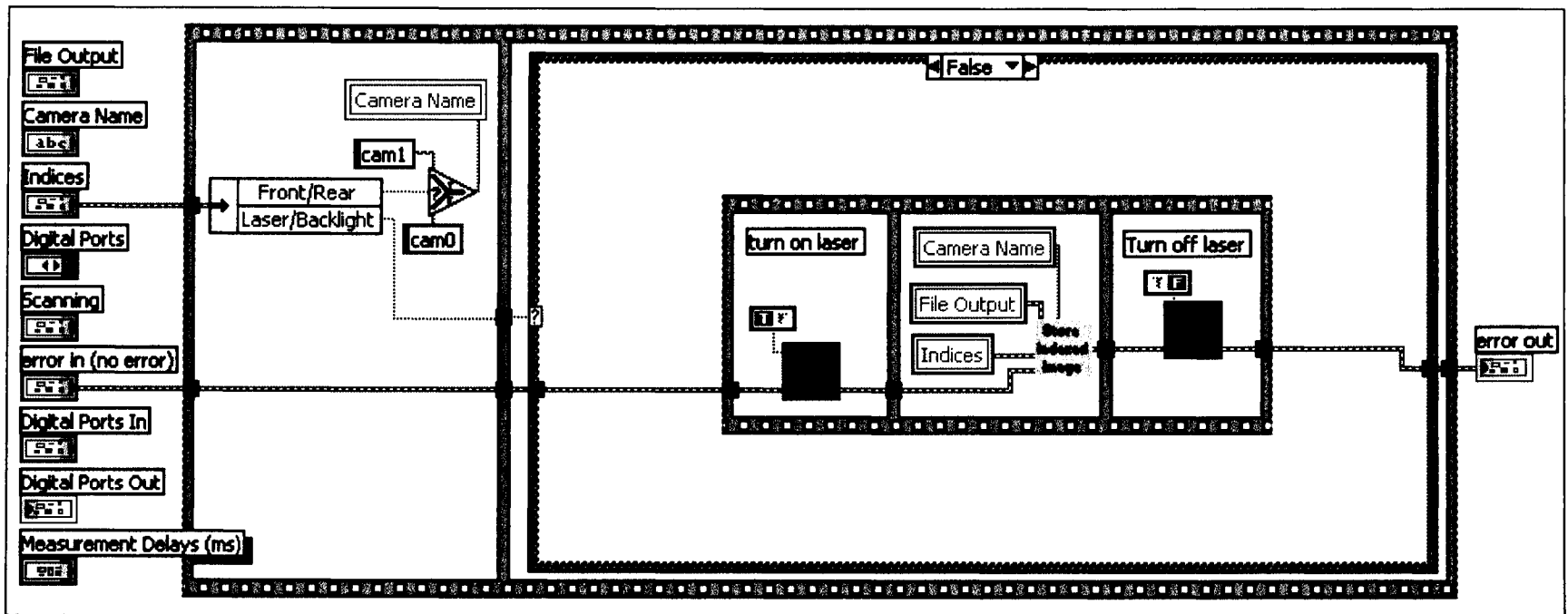


Figure 6.40 Acquire with Camera and Light VI Block Diagram in Laser Mode

The backlight control utilizes the “Boolean Cluster to Port” VI to send the appropriate digital signals to the USB DAQ. The “Laser Control” sub-VI sends an analog signal to the MOSFET transistors illuminating both lasers. The “Store Indexed Image” sub-VI in the “Acquire with Camera and Light” VI was designed to name the image file, capture the image, and save it to disk. The “Store Indexed Image” VI is shown in Figure 6.41.

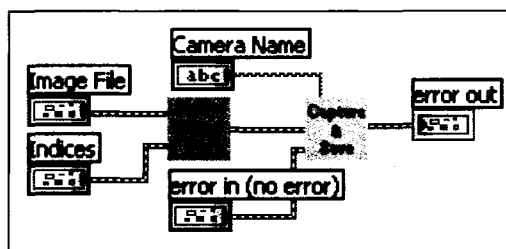


Figure 6.41 Store Indexed Image VI Block Diagram

The “Name Image File” sub-VI in the “Store Indexed Image” VI was designed to create a file path and name for an image file. The file path and name was based on six pieces of information including:

1. The user defined path for data storage in the “Master Control” VI front panel
2. An image file extension of .bmp, .jpg, or .png based on the user input
3. The current robot stop number
4. A “R” or “F” indicating an image taken with the front or rear camera
5. A “B” or “L” indicating an image taken with the backlight or laser
6. The current stepper motor angular stop

The “Name Image File” VI block diagram is shown in Figure 6.42.

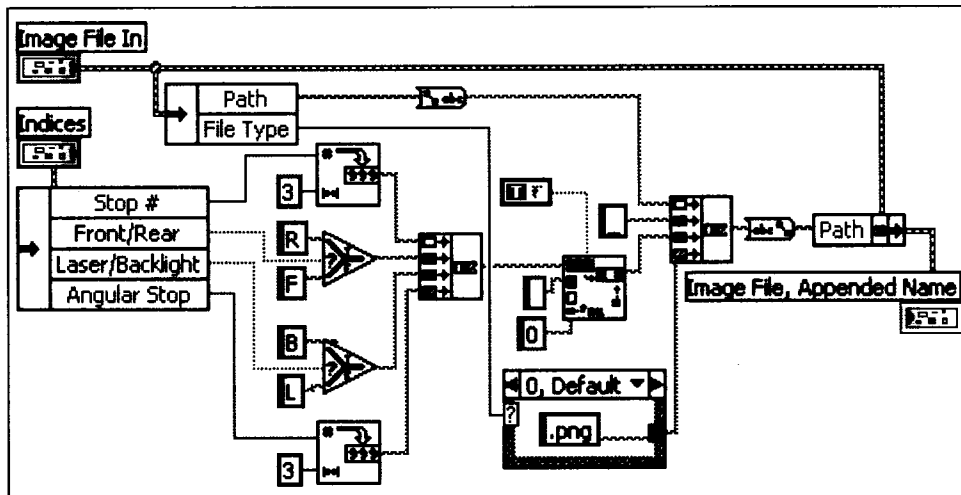


Figure 6.42 Name Image File VI Block Diagram

The “Capture and Save” sub-VI in the “Store Indexed Image” VI was designed to capture and save an image based on the information passed from “Name Image File” VI. The “Capture and Save” VI initializes an IEEE 1394 Camera, snaps an image, writes the image to disk, closes the camera session, and removes the image from memory. The “Capture and Save” VI block diagram is shown in Figure 6.43.

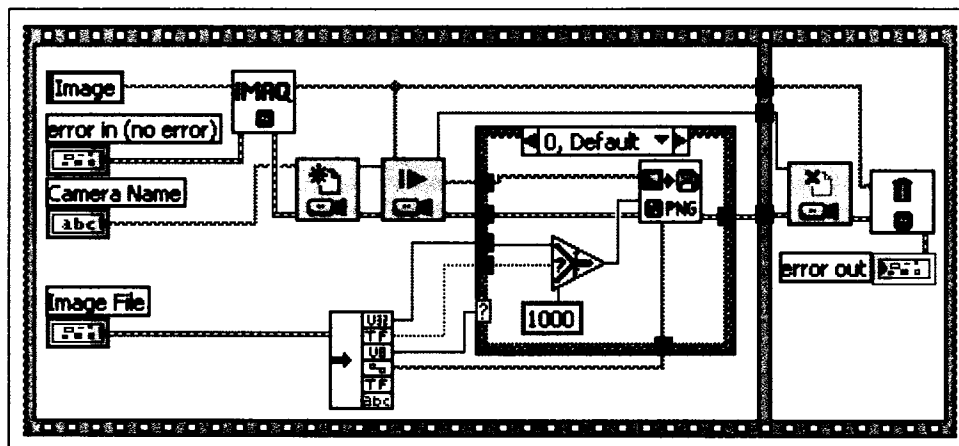


Figure 6.43 Capture and Save VI Block Diagram





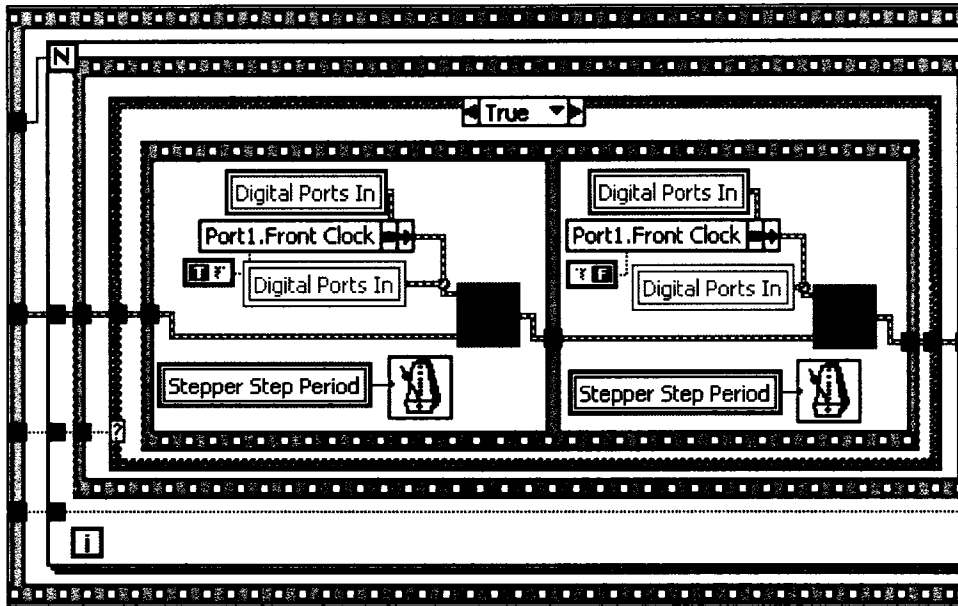


Figure 6.45 Stepper ++ VI Block Diagram (2 of 3)

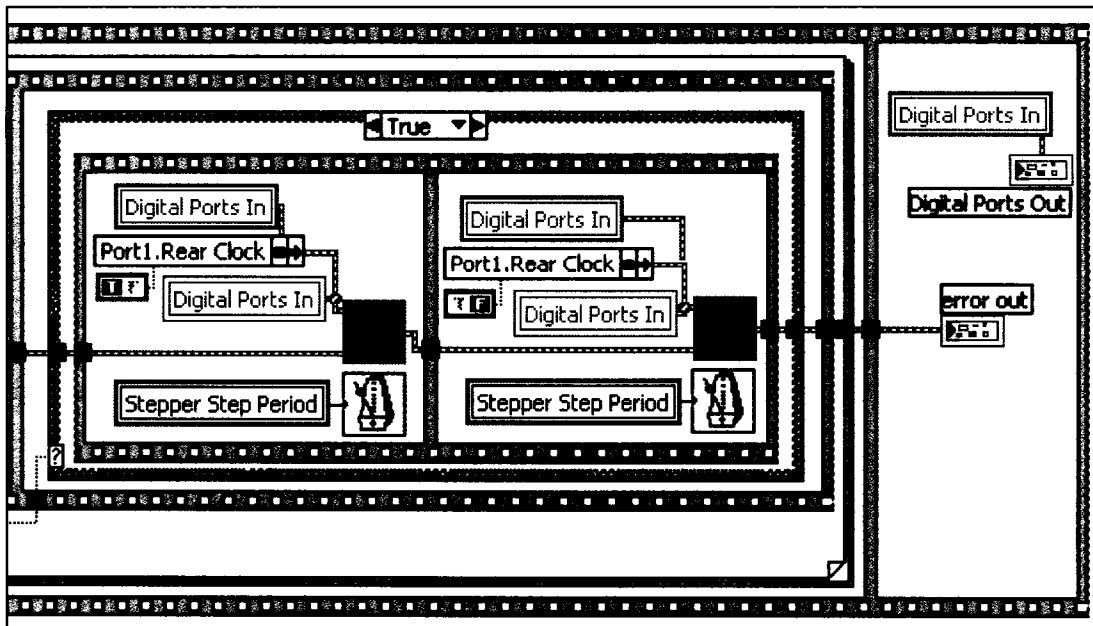


Figure 6.46 Stepper ++ VI Block Diagram (3 of 3)

### 6.2.5 Rewind VI and its Sub-VIs

The last sub-VI to run in the “Master Control” VI’s WHILE LOOP is the “Rewind” VI. This VI was designed to reset the stepper motor’s position by reversing the

stepper motor's drive direction and sending it an appropriate number of pulses to return it to its original position. The "Rewind" VI utilizes a sub-VI called "Simple Stepper ++" which is very similar to the Stepper ++ but sends pulses to both stepper motors simultaneously. The "Rewind" VI and "Simple Stepper" VI are shown in Figures 6.47 and 6.48.

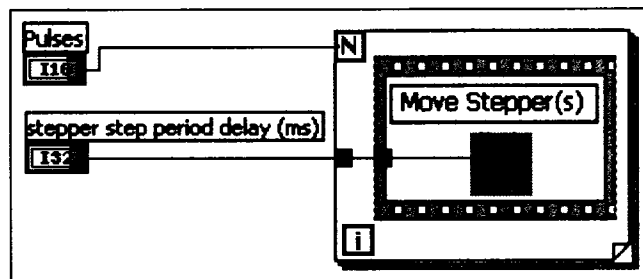


Figure 6.47 Rewind VI Block Diagram

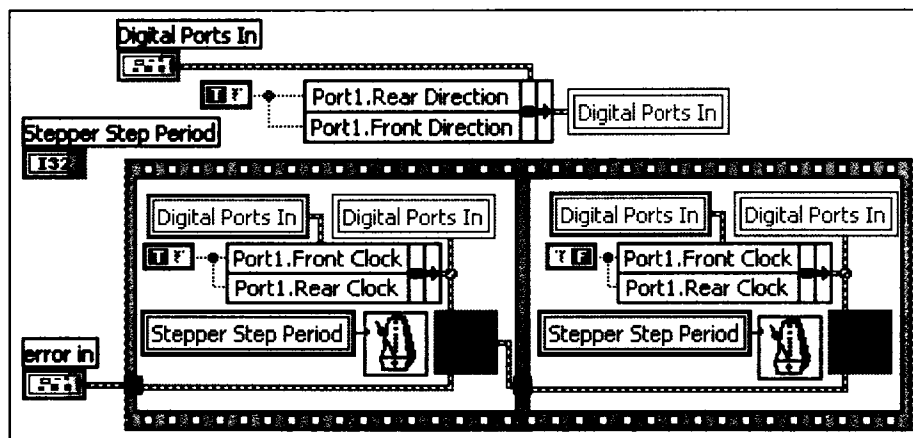


Figure 6.48 Simple Stepper ++ VI Block Diagram

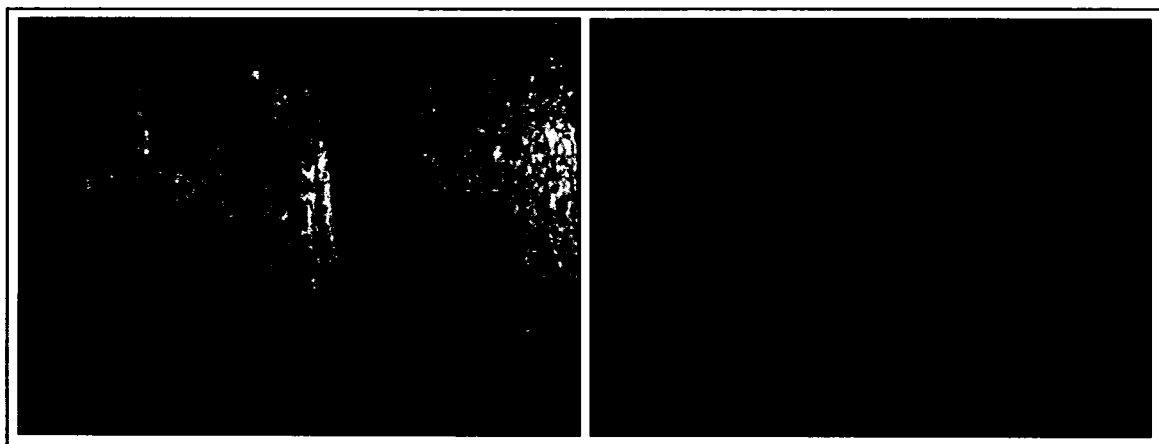
This concludes the description of the automated data collection software as presented in the programming sequence in the "Master Control" VI. The aforementioned sequence would repeat in the "Master Control" VI's WHILE LOOP until a stop button is pressed or the total distance to scan is reached or exceeded.

### **6.3 Data Collection Preliminary Results**

A total of 22,800 tactile probe measurements and laser-images were captured during the data collection phases. This includes the full-length, 72-inch pipe scan and the thirteen scans with the robot on a bump. The images were approximately 2.3 MB each resulting in the need for 53 GB of hard disk space. The laptop PC, used to run the LabVIEW™ code during data collection, had a 3.2GHz Pentium 4-HT processor, 2GB of RAM, and 100GB hard disk.

The full-length pipe was scanned with approximately 0.5 inch increments. Since it took about 18 minutes to scan one ring of data with the front and one with the rear, approximately 11 hours were required to complete the full-length, 72-inch scan. The thirteen scans involving the robot on the bump took approximately two hours to complete since the scans involved the use of the optical measuring systems and not the tactile probes.

Sample images taken with the laser and with the backlight during the data collection process are shown in Figure 6.49.



**Figure 6.49 Sample Images Taken During Data Collection**

The data file written by the VIs during data collection stored several pieces of information including: the filename and path, the time and date, the image file type, the current stop number, an “F” or “R” to indicate whether the tactile measurement was taken at the rear or front probe, the incremental distance traveled by the robot down the pipe, the roll angle, the pitch angle, and the tactile probe measurement. Table 6.1 shows a sample data file.

Table 6.1 Sample Raw Data File from Data Collection Process

C:\Documents and Settings\andydettmer\Desktop\Data Collection 36in 2006_10_26\2nd set\36in_scan_set2_raw.csv						
10/26/2006 08:28:09 PM						
Image file type: PNG						
Stop #	Front/ Rear	Angular Stop	Distance Traveled	Roll Angle	Pitch Angle	Tactile Probe Measurement
1	F	0	5.74E-01	-1.13E+00	-2.54E-01	9.94E-01
1	R	0	5.74E-01	-1.13E+00	-2.54E-01	9.00E-01
1	F	1	5.74E-01	-1.13E+00	-2.54E-01	1.01E+00
1	R	1	5.74E-01	-1.13E+00	-2.54E-01	9.02E-01
1	F	2	5.74E-01	-1.13E+00	-2.54E-01	1.01E+00
1	R	2	5.74E-01	-1.13E+00	-2.54E-01	9.03E-01
1	F	3	5.74E-01	-1.13E+00	-2.54E-01	1.00E+00
1	R	3	5.74E-01	-1.13E+00	-2.54E-01	8.95E-01
1	F	4	5.74E-01	-1.13E+00	-2.54E-01	9.97E-01
1	R	4	5.74E-01	-1.13E+00	-2.54E-01	9.02E-01

## 6.4 Conclusions

Chapter 6 presented the experimental preparation and procedures for the prototype profiler and the software developed for the data collection process. Several devices required calibration before the experiments could ensue including:

- The pipe test stand
- Several reference planes on the prototype robot

- Both tactile probes
- Both camera-laser systems
- The robot's drive motor
- The axial distance encoder
- The tri-axis accelerometer

All of the calibration data was implemented into LabVIEW™ VIs used to control the robot and collect radial measurement data.

A detailed set of experimental procedures were developed for the full pipe scan, the scans with the robot on incremental bump-heights, and the manual caliper measurements. Thirty-one custom VIs were written to automate the data collection process and provide full customization of the experimental variables with a friendly user interface. A total of 22,800 tactile probe measurements and laser-images were captured during the data collection phases. This includes the full-length, 72-inch pipe scan and the thirteen scans with the robot on an incremental bump. The data collection phase was successful, but the raw data required post processing for interpretation and analysis.

## CHAPTER 7

### EXPERIMENTAL DATA POST-PROCESSING AND ERROR ANALYSIS

The purpose of this chapter is to demonstrate how the new position and orientation technique, developed in Chapter 4 and implemented on a prototype robot, was used to experimentally verify the ovality prediction equations developed in Chapter 3. The uncertainties of the radial measurements taken by the prototype are quantified in this chapter to make statistical inferences about the results.

Experimental verification of the ovality prediction equation, Eq. (3.21), was achieved by placing the prototype profiling robot in 13 known orientations within a pipe, implementing coordinate transformations based on information from the prototype's sensors, and comparing the measured erroneous ovality to the predicted erroneous ovality for each bump. Both radial measuring systems were verified to have statistically significant repeatability, and both were shown to cause low uncertainty propagation through the ovality calculations using the Kline-McClintock method.

Equation (3.21) was used to predict the erroneous ovality produced by a pipe profiler in a perfectly cylindrical pipe. Since the laboratory test pipe was assumed to have some ovality, full-pipe scans were first performed with the tactile probes and camera-laser systems. These scans provided accurate measures of the true dimensions of the pipe

and were used as datums for comparison of the 13 scans performed with the robot on various bumps.

During the full-pipe scans, 17,600 data points were collected with the tactile probes and 17,600 data points with the camera-laser systems. The transformation equations, developed in Chapter 4, were applied to each of the 35,200 data points to correct for the robot's pitch, meander and roll and for the pitch of the pipe relative to gravity. Two three-dimensional plots were used to display the pipe wireframes before and after the transformations were applied. The two data sets collected during the full-pipe scans were found to be almost identical. These measurements formed the basis of the pipe's true dimensions and were used to calculate the laboratory test pipe's ovality.

After the 13 data sets were collected with the robot on the bump, the measured ovalities were compared with the ovality prediction equation developed in Chapter 3. After adding the average ovality from the full pipe scans, the measured ovalities showed a strong correlation to the predicted ovality, thus demonstrating the validity of the ovality prediction equation from Chapter 3.

The accuracy of the tactile probe measurements and camera-laser measurements were also examined using statistical techniques. Fifty sample measurements were taken with the tactile probe to examine repeatability and accuracy. A regression analysis was also performed on the 27 calibration points for the camera-laser system. This analysis showed that a 3<sup>rd</sup> order polynomial was an optimum least-squares-fit with a 95% confidence level.

The uncertainty propagation through the ovality equations was quantified using the Kline-McClintock method. The measurement uncertainties for the camera-laser



systems and partial derivatives of the ASTM ovality equation were used as factors in determining the overall error propagation through the ovality equations. The uncertainties calculated with the Kline-McClintock method were low enough to be confident of the predicted positive correlation between ovality and robot pitch angle.

### **7.1 Experimental Data Post-Processing**

After the full-pipe scan and 13 varying bump-height scans, the raw data was post-processed to interpret and display the results. The post-processing involved three steps:

1. Format the raw measurements from the camera-laser system, tactile probes, accelerometer, and axial distance encoder.
2. Transform each data point from the robot's coordinate system to the world coordinate system using the equations developed in Chapter 4.
3. Compare the ovalities produced by the robot on the 13 bump heights to those predicted by the erroneous ovality equation developed in Chapter 3.

#### **7.1.1 Format Raw Data for Transformations**

After the data collection process was complete, several pieces of information necessitated formatting before the coordinate transformations could be applied. These include:

1. Add the incremental distances logged by the axial distance encoder to find the total length from the end of the pipe to the ring of data collected.
2. Process the digital images taken by the cameras to determine the location of the laser line within each image.
3. Apply the camera calibration equations to convert the pixel distances to inches.

4. Detect and remove outliers.
5. Convert the stepper motor pulses to angles.
6. Calculate the centroid of each ring of data using Green's Theorem.

The aforementioned tasks were performed by an algorithm incorporated into a VI which calls eight sub-VIs. This VI created a new data file which was used as the source for the coordinate transformations equations applied in Section 7.1.2. See Section 5.1.2 for a description of LabVIEW™ VIs. The main VI is called the Format Raw Data for Transformations VI, and its block diagram is shown in Figure 7.1.

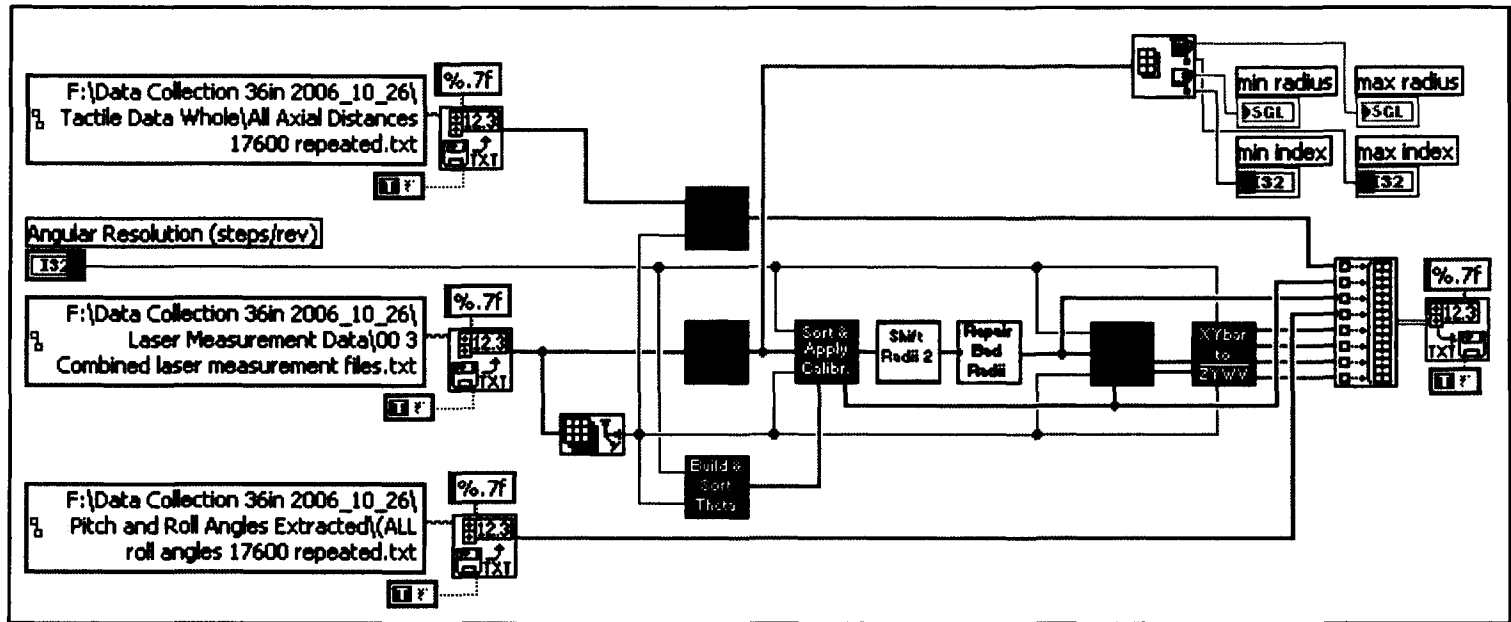


Figure 7.1 Format Raw Data for Transformations VI Block Diagram

### **7.1.1.1 Outlier Detection**

Before performing the coordinate transformations on the data, it was necessary to remove any radial measurements which did not seem consistent with the rest of the data. Outlier detection was performed both on the tactile probe data and on the camera-laser data.

During data collection, there were a few instances where the tactile probe encoder did not log a radial measurement. This was caused by lack of bandwidth to the USB DAQ or electrical noise within the system. Wherever a “zero” measurement was logged, the average of the two closest points were taken on the same ring. Wherever two “zero” measurements were logged in succession, the average of the two closest measurements on adjacent rings were taken.

The few outliers logged by the camera-laser system were caused by the laser line disappearing due to three holes in the steel laboratory test pipe. Whenever a hole was scanned by the laser, the laser line would disappear and the laser-peak-detection algorithm would not record a radial measurement. The same outlier correction algorithm as described with the tactile probe was used to detect and correct the camera-laser outliers.

### **7.1.2 Application of Transformation Equations**

After formatting the raw data, the transformation equations developed in Chapter 4 were applied to the data files produced by the Format Raw Data for Transformations VI. The data files were imported into Mathcad®, the transformation equations applied, and then a new data file was exported to LabVIEW™ to display three-dimensional parametric plots of the full-pipe scans.

To display the effects of the transformations, three-dimensional parametric plots are shown before and after the transformations were applied. The  $x$ - $y$ - $z$  plots feature the 88 rings of data collected by the tactile probes and the 88 rings of data collected by the camera-laser systems. Each ring has 200 radial measurements, and the color of each measurement point was varied according to its radial distance from the centroid. The data obtained with the camera-laser system is shown in Figure 7.2. The data obtained with the tactile probes is shown in Figure 7.3.

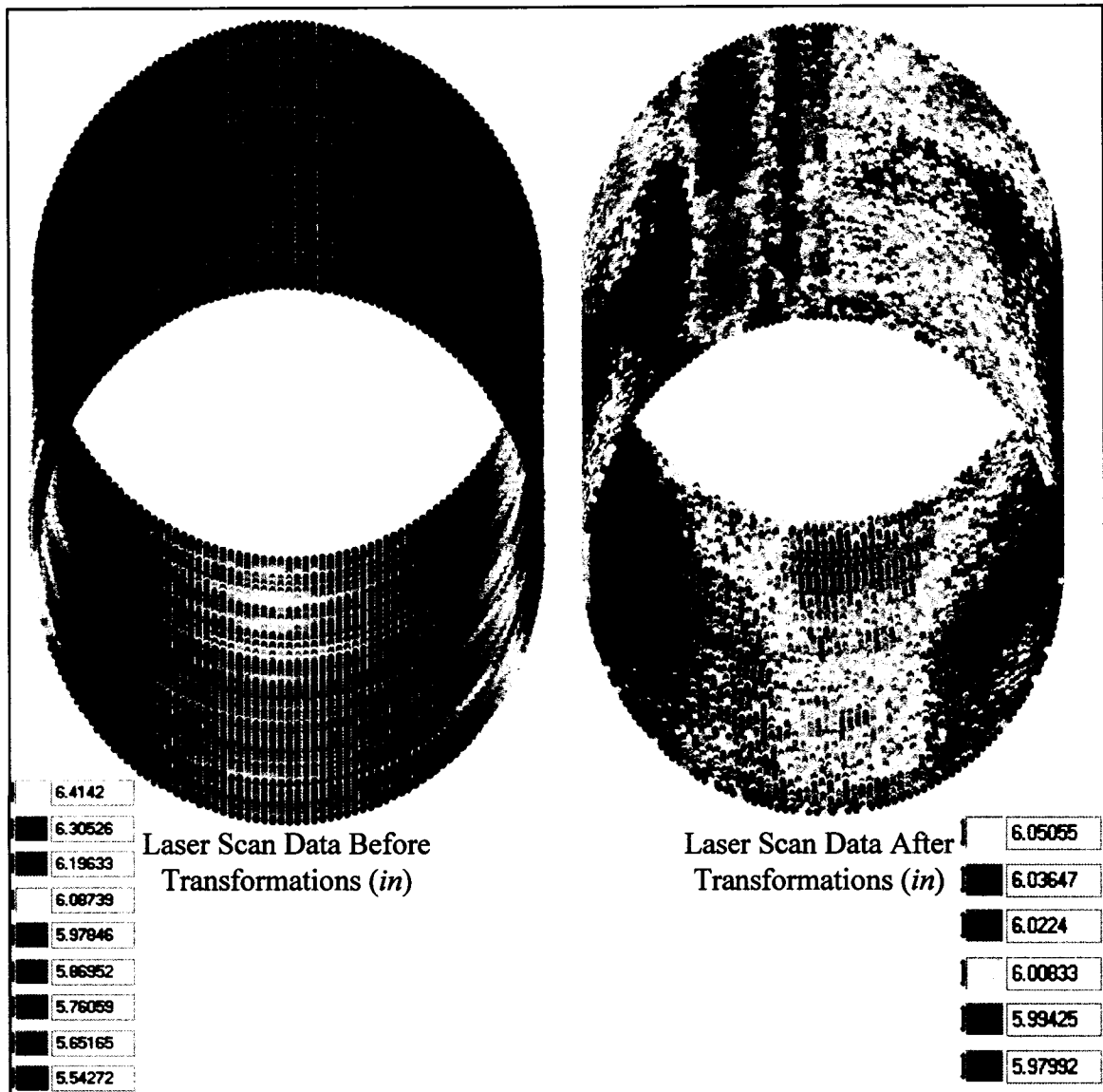


Figure 7.2 3-D Plots of Laser Radial Measurements for the Full-Pipe Scan

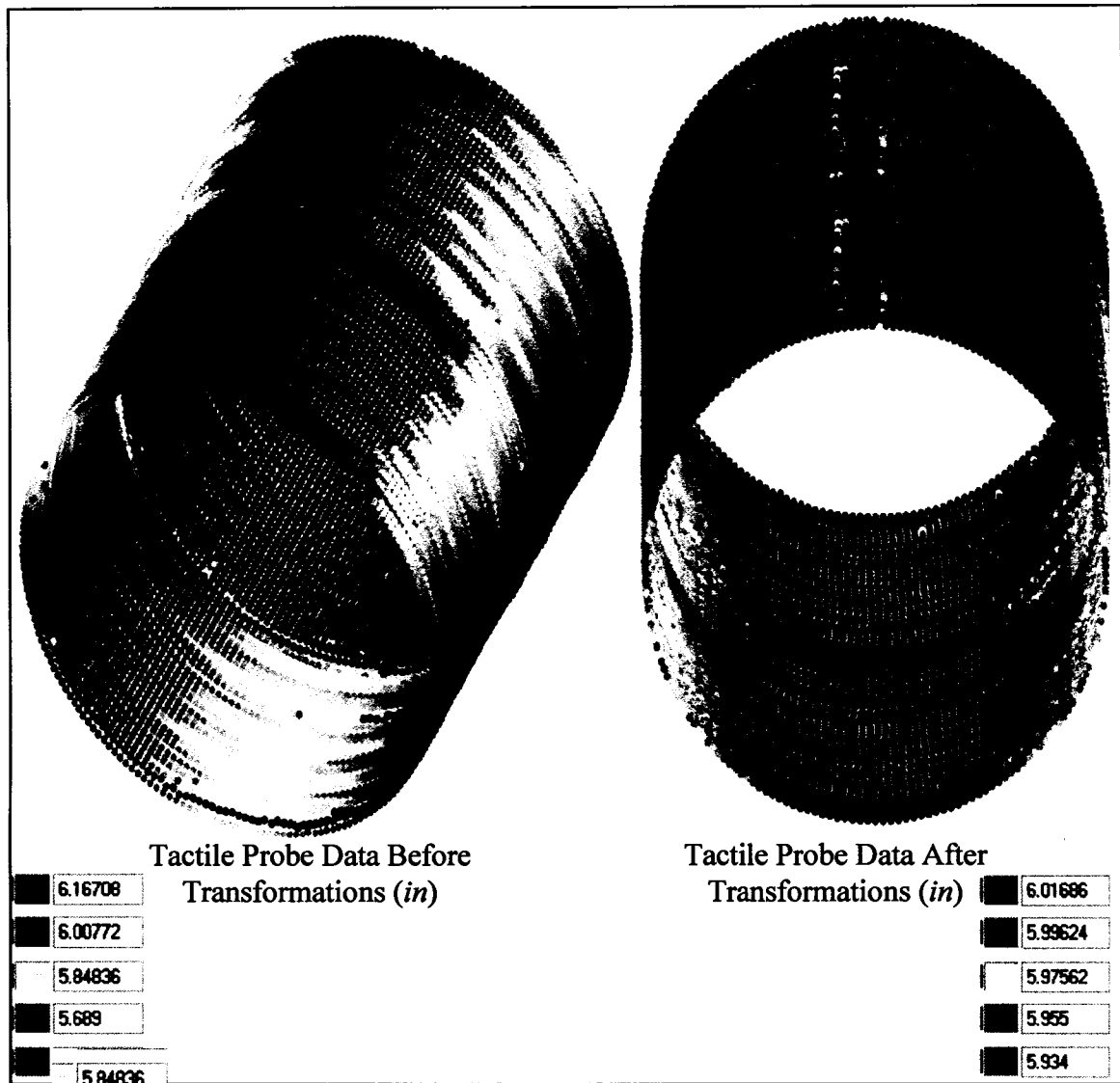


Figure 7.3 3-D Plots of Tactile Probe Radial Measurements for the Full-Pipe Scan

The most drastic change the transformations had on the plots is the vertical shift or  $\bar{y}$  term in the transformations. This is evident in the color maps associated with each plot. Before the transformations were applied, the largest radii measured were at the bottom of the pipe. This was due to the fact that the stepper motor's center of rotation was closer to the top of the pipe than the bottom. Another key feature which the final plots reveal is the longitudinal weld at the top of the pipe. This feature is especially

evident in the plots after the transformations were applied. The longitudinal weld was a region of larger radii at the top of the pipe depicted by the reddish colors.

### **7.1.3 Ovality Calculations for the Full-Pipe Scan**

To establish an average ovality for the laboratory pipe, the ovality at each ring of measurements was calculated for the tactile probes and for the camera-laser systems. The equation used to calculate ovality is specified in ASTM F1216-03 as Eq. (7.1).

$$q = 100 \cdot \frac{\text{Max Inside Diameter} - \text{Mean Inside Diameter}}{\text{Mean Inside Diameter}} \quad (7.1)$$

where  $q$  is the percentage ovality of the original pipe.

The average ovality for the full-pipe scan as measured by the tactile probes was  $0.3442\% \pm 7.894 \times 10^{-3} \%$ , whereas the average ovality measured by the camera-laser systems was  $0.3379\% \pm 1.551 \times 10^{-2} \%$ . The average ovalities were calculated based on the ovalities of each ring with a 95% confidence interval. Table 7.1 provides a comparison of the average ovalities as measured by both radial systems and the 24 inch caliper.

Table 7.1 Percent Difference Comparison between Types of Measuring Devices

<b>% difference Between Measuring Systems</b>			
	Caliper	Tactile Probe	Camera-Laser
Caliper	-	1.081%	0.767%
Tactile Probe	1.081%	-	1.847%
Camera-Laser	0.767%	1.847%	-

These low percent difference calculations give reasonable assurance that all three measuring systems report similar ovality for the laboratory test pipe. It is important to note that percent difference is a separate quantity than percent ovality.



#### **7.1.4 Comparison of Measured Ovality to Predicted Ovality**

Equation (3.25) which computes the erroneous ovality of a pipe based on robot pitch angle  $\theta_v$  and yaw angle  $\theta_h$  is verified experimentally here by placing the robot on bumps centered horizontally in the pipe. A total of 13 bump heights ranging from 0 to 1.25 inches were used to systematically alter the pitch angle to determine the ovality “perceived” by the prototype profiler employing the camera-laser system with no active position and orientation correction. The major and minor diameters for each pitch angle were computed based on the maximum and minimum separation of opposing radial coordinates, and these radii were inserted in the ASTM F1216-03 ovality equation (Eq. 2.1) to compute the ovality perceived by the profiler.

Since the robot was centered horizontally in the pipe, the yaw angle  $\theta_h$  was set to zero for all analytical estimates of ovality. Inserting this zero yaw angle into Eq. (3.25) for erroneous ovality and adding the actual pipe ovality of 0.3379% yields Eq. (7.2).

$$q = q_e + q_{actual} = 100 \times \frac{\left[ 1 + \tan\left(\sin^{-1} \frac{h}{l}\right)^2 \right]^{\frac{1}{2}} - 1}{\left[ 1 + \tan\left(\sin^{-1} \frac{h}{l}\right)^2 \right]^{\frac{1}{2}} + 1} + 0.3379\% \quad (7.2)$$

where  $h$  is the bump height and  $l$  is the robot length. Plotting the ovalities measured by the prototype profiler alongside the ovalities computed using Eq. (7.2) results in Figure 7.4.

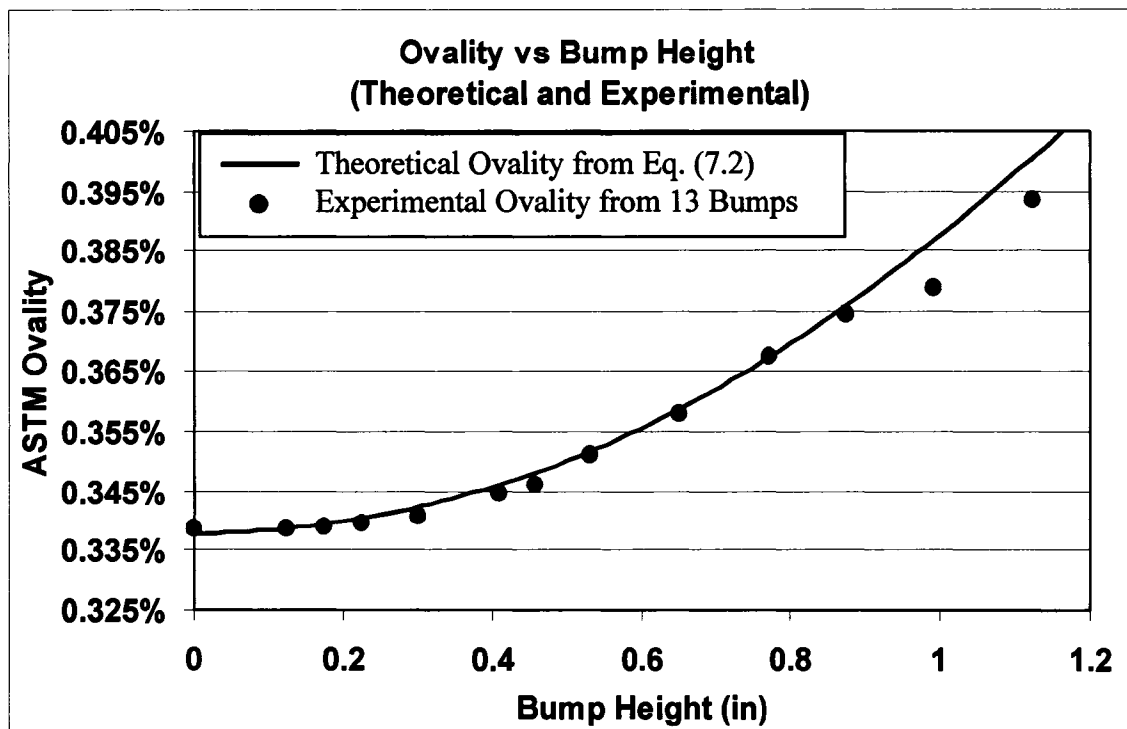


Figure 7.4 Theoretical and Experimental Ovality Due to a Robot on a Bump

Figure 7.4 reveals that the experimental data closely follows the predicted trend line, with some difference for bump heights greater than one inch. Since there are uncertainties associated with the measurements made with the camera-laser system, a more thorough analysis of this figure and its associated error analysis is performed in Section 7.2.

## 7.2 Error and Uncertainty Analysis

### 7.2.1 Error in Camera-Laser Measurements

The error associated with the camera-laser system was assumed to be only a function of how well the 3<sup>rd</sup> order polynomial fit described the calibration data as presented in Chapter 6. This assumption is adopted since the width of the laser line, the orientation angles and distances of the camera-laser setup, and the camera resolution are

identical when the camera-laser system is being calibrated and when the system is mounted to the robot; that is, the camera-laser system is moved as a unit from the calibration setup to the robot setup. Since the polynomial fit was not a perfect fit, the residuals in the regression analysis were used as estimates of the measurement error.

The polynomial fit was performed using Microsoft Excel's LINEST function by specifying a multiple linear regression with four coefficients as in Eq. (7.3).

$$y = a_3x^3 + a_2x^2 + a_1x + a_0 \quad (7.3)$$

The results from the regression analysis are given in Table 7.2.

Table 7.2 Regression Analysis on the Camera Calibration Data

	a3	a2	a1	a0
<b>Coefficients</b>	1.696E-08	-7.254E-06	6.148E-03	3.096E+00
<b>Standard Error of Coefs.</b>	1.380E-09	1.556E-06	5.603E-04	6.397E-02
<b>Observed t-values</b>	12.2963	-4.6633	10.9726	48.3982
t <sub>crit</sub> (99% conf level)	2.7707			
R <sup>2</sup>	0.99994			
Standard Error of Regression	0.007513			
Sum of Squares Regression	24.7985			
Sum of Squares Residual	0.001524			
DOF	24			
F	146442			
F <sub>crit</sub> (99% conf level)	4.6009			

Each of the four polynomial coefficients was deemed statistically different than zero as evidenced by the absolute values of the observed t-values being higher than t<sub>crit</sub>. The high R<sup>2</sup> value was a good indication that the polynomial was a good fit to the data, and the high F value was a good indication that that the high R<sup>2</sup> value did not happen by chance.

The residual sum of squares is small but important since it quantifies the sum of the squared error which remains unexplained by the polynomial fit. The following relationship was used to find the average error for the camera measurements in Eq. (7.4).

$$\text{Average Camera-Laser Error} = \pm \frac{\sqrt{SS_{\text{residual}}}}{n} \quad (7.4)$$

Substituting  $SS_{\text{residual}}$  from Table 7.1 and the number of calibration points  $n$  into Eq. (7.4) gives Eq. (7.5).

$$\text{Average Camera-Laser Error} = \pm \frac{\sqrt{0.001524}}{27} = \pm 0.001446 \text{ inches} \quad (7.5)$$

### **7.2.2 Error in Tactile Probe Measurements**

The average error in the tactile probe measurements was quantified by examining the repeatability of its measurements. Fifty measurements of the same radius were taken with a tactile probe and the results examined statistically. A 95% confidence level was applied to the mean ( $\bar{x}$ ) and standard deviation ( $\sigma$ ) of the 50 measurements to establish the average error. This average error was calculated using the following confidence interval equation in Eq. (7.6).

$$\text{Confidence interval} = \bar{x} \pm 1.96 \left( \frac{\sigma}{\sqrt{n}} \right) \quad (7.6)$$

where the average error was noted in Eq. (7.7).

$$\pm 1.96 \left( \frac{\sigma}{\sqrt{n}} \right) \quad (7.7)$$

Substituting the standard deviation and number of trials from the tactile probe experiments into Eq. (7.7) gives Eq. (7.8)

$$\text{Tactile Probe Average Error} = \pm 1.96 \left( \frac{0.003494}{\sqrt{50}} \right) = 9.685 \times 10^{-4} \text{ inches} \quad (7.8)$$

### **7.2.3 Uncertainty Propagation** **Using Kline-McClintock**

The previous sections described the amount of error associated with each of the measuring devices used on the prototype profiler. However, there is an additional source of uncertainty stemming from the calculation of ovality based on quantities with their own uncertainty. This is especially important when comparing the ovality measured with the camera-laser systems when the robot was placed on 13 different bumps. This second source of uncertainty occurs in the calculation of ovality from the mean and maximum diameters.

The Kline-McClintock equation is a widely accepted method to calculate uncertainty in the calculation of a multivariate function whose inputs have defined uncertainties. The Kline-McClintock equation for a multivariate function's uncertainty is Eq. (7.9).

$$\pm U_{\bar{y}} = \pm \sqrt{\sum_i \left[ \left( \left. \frac{\partial y}{\partial x_i} \right|_{x_i = \bar{x}_i} U_{\bar{x}_i} \right)^2 \right]} \quad (7.9)$$

where  $U_{\bar{y}}$  is the total uncertainty in the calculation and  $x$  is the variable which is known with an uncertainty of  $U_{\bar{x}_i}$ . The Kline-McClintock method is useful in the case of calculating the uncertainty of ASTM ovality since the function's inputs, the mean and maximum diameters, have defined uncertainties of their own as measured with the camera-laser system. Since the equation for ASTM ovality is Eq. (7.10).

$$q = 100 \times \frac{D_{\max} - \bar{D}}{\bar{D}} \quad (7.10)$$

the uncertainty in the computation of ovality  $q$  is given by Eq. (7.11).

$$\pm U_{\bar{q}} = \sqrt{\left( \frac{\partial q}{\partial D_{\max}} \cdot U_{D_{\max}} \right)^2 + \left( \frac{\partial q}{\partial \bar{D}} \cdot U_{\bar{D}} \right)^2} \quad (7.11)$$

where

$$\frac{\partial q}{\partial D_{\max}} = \frac{100}{\bar{D}},$$

$$\frac{\partial q}{\partial \bar{D}} = \frac{-100 D_{\max}}{\bar{D}^2},$$

and  $U_{D_{\max}} = U_{\bar{D}} = \text{Average Camera-Laser Error} = \pm 0.001446 \text{in.}$

The uncertainty of each ovality calculation from the scans with the robot on 13 bumps was calculated using Eq (7.11) and expressed in the error bars for each experimental data point in Figure 7.5.

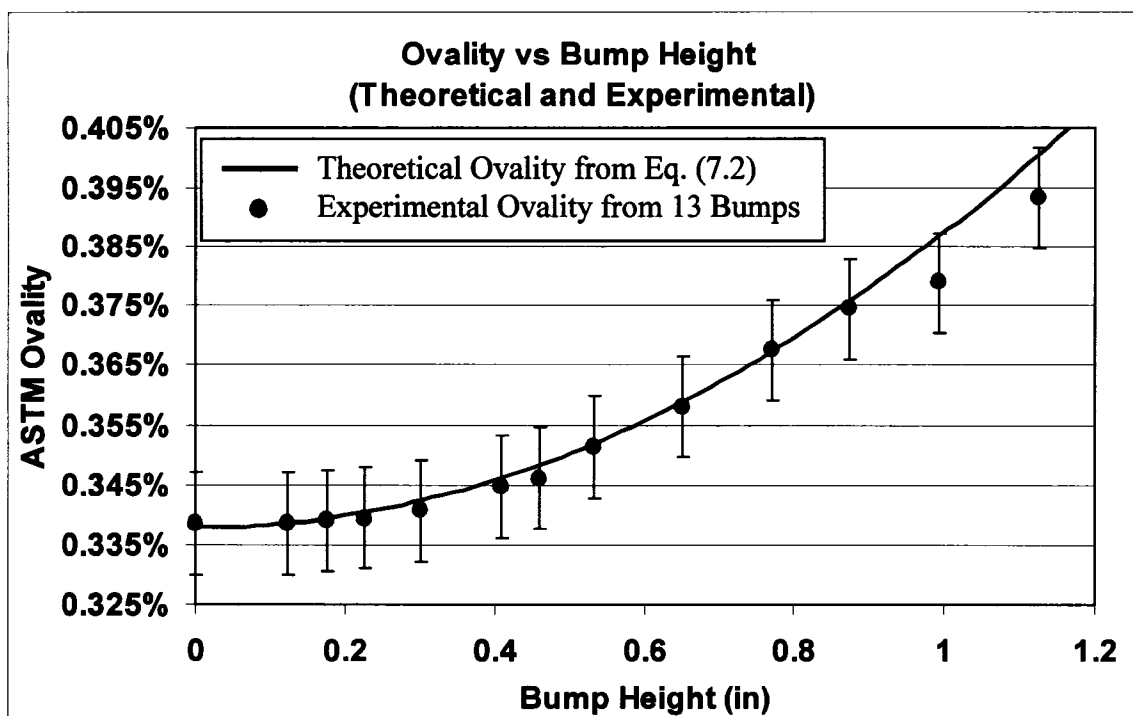


Figure 7.5 Theoretical and Experimental Ovality Due to a Robot on a Bump with Error Bars

For Figure 7.5, the uncertainty in ovality ranges from 0.01703% to 0.01704%.

The error associated with each data point clearly spans the predicted ovality function for all points except for a one-inch bump height. The data from this chart effectively verifies the theory posed in Chapter 3 where ovality was calculated as a function of bump height.

### 7.3 Conclusions

This chapter demonstrated how the new position and orientation technique, developed in Chapter 4 and implemented on a prototype robot, experimentally verified the ovality prediction equation developed in Chapter 3. Equation (3.21) was confirmed by placing the prototype profiling robot in 13 known orientations within a pipe, implementing coordinate transformations based on information from the prototype's

sensors, and comparing the measured erroneous ovality to the predicted erroneous ovality for each bump.

The accuracy of the tactile probe measurements and camera-laser measurements were also examined using statistical techniques. Fifty sample measurements were taken with the tactile probe to examine repeatability and accuracy. A regression analysis was also performed on the 27 calibration points for the camera-laser system. This analysis showed that a 3<sup>rd</sup> order polynomial was an optimum least-squares-fit with a 95% confidence level.

The uncertainty propagation through the ovality equations was also quantified using the Kline-McClintock method. The measurement uncertainties for the camera-laser systems and partial derivatives of the ASTM ovality equation were used as factors in determining the overall error propagation through the ovality equations. The uncertainties calculated with the Kline-McClintock method were low enough to be confident of the predicted positive correlation between pipe ovality and the robot pitch angle relative to the pipe.



## CHAPTER 8

### CONCLUSIONS, RESEARCH IMPLICATIONS AND RECOMMENDATIONS

#### **8.1 Research Conclusions**

Sewer systems are prevalent, important, valuable, unnoticed, and often in a state of disrepair. Many sewer systems are failing catastrophically and are in need of inspection and renovation. In-pipe assessment is necessary for observing and predicting pipeline failure and is useful in verifying whether proper installation methods were used for new flexible walled pipes. Pipe inspection is often government mandated and is now required of many municipalities complying with GASB 34 accounting standards. Pipe inspection robots are routinely used to inspect underground pipelines for cracks, deformations, leaks, blockages and other anomalies. Pipe profilers incorporate advanced sensors allowing for the measurement of pipe radii. Accurate radial measurements permit the calculation of several important pipe parameters which aid in the determination of pipe condition and prediction of time to failure. Ovality measurements of the host-pipe are used in the design of thin walled pipe liners and in the determination of the quality of backfill around a new plastic pipe installation. A pipe's flow parameters are vital in the evaluation of a sewer system's capacity, and tracking the rate of pipe deformation can help determine the remaining life of a system. Significant research work has been

completed in North America, Europe, Asia and Australia aimed at improving the accuracy and automation of the pipe inspection process. However, the current commercialized systems are in their infant stages of maturity and may require further development.

The objective of this research was to quantify the measurement error incurred by a pipe profiler's misalignment with the pipe axis, present a new methodology to correct the measurement error, develop a prototype profiler to verify the equations derived herein, and to further the development of pipe profiler technology. Equations were developed relating the position and orientation of a profiling robot in a cylindrical pipe to the measurement error causing erroneous ovality and three-dimensional wireframe distortion. A new mathematical model to estimate the position and orientation of the pipe profiler was then developed and presented. This model was verified experimentally via a prototype pipe profiling robot developed exclusively for this research. To fulfill this objective the research program was comprised of the following activities:

- Conduct a thorough literature review of the following topics: material demonstrating the need for the accurate determination of pipe condition, past and present pipe inspection research, and techniques used for position and orientation estimation of robots in pipelines.
- Derive equations for erroneous ovality and three-dimensional wireframe distortion as functions of a robot's misalignment with the pipe axis. This derivation was extended to include the effects on CIPP liner design and the length chosen for pipe profiling robots.

- Develop homogenous coordinate transformations to correct for the robot's misalignment with the pipe axis, and provide the steps necessary to implement the technique on existing pipe profilers.
- Apply the coordinate transformations to simulated radial measurements to demonstrate the new position and orientation technique, effectively correcting for the position, pitch and yaw of the robot with respect to the pipe and the pitch and roll of the robot with respect to gravity.
- Design and construct a prototype pipe profiling robot with two types of radial measuring devices at each end demonstrating the new position and orientation estimation technique.
- Develop customized software with National Instrument's LabVIEW™ to automate the data collection process with the prototype pipe profiling robot.
- Perform comparisons and error analyses of both types of radial data collected. The data set taken with the tactile probes was compared to the data set taken with the camera-laser systems. The uncertainty propagation of the radial measurements through the ASTM ovality equation was also quantified using the Kline-McClintock method.

## **8.2 Research Implications**

There are several important implications for the asset manager evaluating the use of pipe profiling technology. This research project addressed some of these concerns and ignored others. Therefore, it is helpful to summarize items which may be of interest to asset managers as pipe profiling technology continues to develop in the future.

One of the most important considerations in choosing a pipe profiling method is the amount of error introduced by the system. Pipe profiling is prone to several types of error including:

1. Calibration of the camera, laser (or radial measuring device), and other sensors on the profiler can have serious effects on measurement accuracy. Calibration must be carried out on a routine basis to help minimize measurement error.
2. The position and orientation of the camera and laser relative to each other and relative to the robot have profound effects on measurement accuracy [75]. Robust profiler performance in harsh field conditions is essential, since misalignment of critical components may occur during handling and use.
3. Radial measurement accuracy is not constant across the camera (CCD sensor) as shown by Swanbom's work [75]. Measurement error is a function of the camera's resolution, the width of the laser line, and the configuration of the camera-laser system.
4. Color variation in the images collected can affect where the machine vision system determines the location of the laser line.
5. Laser light scatter or sonar scatter caused by varying conditions in the pipe can cause the pipe radii to be measured inaccurately.
6. Various artifacts in the pipe and irregular cross sections can make the centroid location difficult to establish, leading to difficulty in proper estimation of ovality.
7. The misalignment of the pipe profiler with respect to the axis of the pipe can cause erroneous ovality and distance measurement error.

The seven sources of error introduced by a pipe profiler are by no means a comprehensive list. It simply illustrates that the error quantified in Chapter 3, the error introduced by a robot's meander and pitch relative to the pipe, is only one type of error.

The magnitude of the error quantified in Chapter 3 was shown to be small for robot misalignments expected in profiling applications. Since the magnitude of the erroneous ovality was small, CIPP liner over-design was not a significant problem in terms of added thickness (10% over-design for a 20° misalignment). Likewise, the magnitude of the distance measurement error causes only slight distortions in the three-dimensional wireframes of pipes. This is not to say that all ovality measurements taken using pipe profiling systems are accurate; clearly, the cumulative influence of multiple error sources may lead to significant errors. As pipe profiling technology continues to advance, more and more types of error should be taken into account to minimize the variance between multiple scans of the same pipe. This is especially important for municipalities considering employment of pipe profiling technology to comply with GASB 34 which states: "municipalities must perform a condition assessment of sewer assets at least every three years using a consistent basis of measurement and scale that can be repeated."

The author firmly believes that inspection systems which quantify the coordinates of underground infrastructure are becoming an essential part of asset management. Standard calibration, verification, reporting and analysis practices must be developed for pipe profilers if coordinate profiling data is to be effectively included in the long-term management of pipeline assets. Technology is constantly changing, critical infrastructure is continuously decaying, and the demand for accurate inspection techniques will

continue to increase as assessment management programs are adopted. It is vital to develop inspection methods which demonstrate accuracy and repeatability, and the research presented here contributes to this endeavor.

### **8.3 Recommendations for Further Research**

After completing the research presented in this dissertation, the author would like to make the following recommendations to those who desire to continue in this field of study:

1. Develop standard procedures for calibration, verification, reporting and analysis practices for pipe profilers. This is essential if coordinate profiling data is to be effectively included in the long-term management of pipeline assets.
2. Document the robot's pitch and yaw angles with respect to the pipe for typical pipeline inspections. This will determine the magnitude of one type of error experienced by pipe profilers.
3. Develop algorithms which can quantify the measurement error using only one radial measuring system. It may be impractical to implement two radial measuring devices as presented in this research.
4. Investigate the applicability of using measurements made with laser interferometry at different locations within the pipe to establish the position and orientation of the robot with respect to the pipe.
5. Sewer inspection vehicles are difficult to market if they are expensive. Developing a low-cost alternative would be well received by the industry.

6. Trialability is a major concern in the adaptation of new technology. Developing inspection technology which is easy for end-users to try would be quickly accepted.
7. Develop an automated inspection robot which can be left alone in the sewers for days, weeks, or even months. Conceptually, a system could roam the sewers, periodically uploading condition information to provide constant asset monitoring.

## REFERENCES

1. Logan, G. and P. Anderson, *Lasers and Machine Vision for Pipeline Precision Measurement*. 2003, CleanFlow Systems Limited: Albany, Auckland, New Zealand.
2. Ouellet, M. and C. Senecal. "3-D Profiling and Software Modeling for Pipe Qualification." in *North American Society for Trenchless Technology (NASTT) NO-DIG*. 2004. New Orleans, LA, USA.
3. Wade, M., *Controlling Inflow and Infiltration in Wastewater Collection Systems*. 2002, Wade and Associates, Inc.: Lawrence, KS.
4. EPA, *Guide for Evaluating Capacity, Management, Operation, and Maintenance (CMOM) Programs at Sanitary Sewer Collection Systems*. 2005, Office of Enforcement and Compliance Assurance, United States Environmental Protection Agency.
5. Ghosh, S., *Sewer Rehab Trends*, in *Trenchless Technology*. 2006. p. 38-41.
6. Sinha, S. and M. Knight, "Intelligent System for Condition Monitoring of Underground Pipelines." *Computer-Aided Civil and Infrastructure Engineering*, 2004. p. 42-53.
7. VanDine, M., *Maximizing Asset Value: The Paradigm Shift in Today's Wastewater Industry*, in *Trenchless Technology*. 2005. p. 40-41.
8. ASCE, *Infrastructure Report Card*. 2005, American Society of Civil Engineers.
9. EPA, *Report to Congress on Impacts and Control of Combined Sewer Overflows and Sanitary Sewer Overflows*. 2004.
10. Carter&Burgess, *Protecting the Public Investment: GASB Statements 34/35 Make Government More Accountable*, in *Technically Speaking*. 2001.
11. EPA. *Asset Management*. 2006 [cited 5/23/2006]; Online: <http://www.epa.gov/owm/assetmanage/index.htm>.
12. EPA, *Effective Water Sector Utility Management Statement of Intent*, United States Environmental Protection Agency, Editor. 2006, Water Environment Federation (WEF).



13. Sinha, S. "A Multi-Sensory Approach to Structural Health Monitoring of Buried Sewer Pipelines Infrastructure System." in *Pipelines Conference*. 2004. San Diego, California, USA: ASCE.
14. Burn, L., Eiswirth, M., DeSilva, D., and Davis, P. "Condition Monitoring and Its Role in Asset Planning." in *Pipes Wagga Wagga*. 2001. Australia.
15. Deb., A. and Y. Hasit, *Quantifying Future Rehabilitation and Replacement Needs of Water Mains* 1998, AWWARF.
16. Burn, L., P. Davis, and D. DeSilva. "The Role of Planning Models in Pipeline Rehabilitation." in *Plastic Pipes XI*. 2001. Munic, Germany.
17. Makar, J., "Diagnostic Techniques for Sewer Systems." *Journal of Infrastructure Systems*, 1999. p. 69-78.
18. EPA, *Wastewater Primer*. 1998, Office of Water Management (4204), United States Environmental Protection Agency.
19. EPA, *Protecting the Nation's Waters through Effective NPDES Permits: A Strategic Plan FY 2001 and Beyond*. 2001, Office of Water, United States Environmental Protection Agency.
20. WEF, *The O & M in CMOM: "Operation & Maintenance."* 2006, Water Environment Federation.
21. Gokhale, S., J. Graham, and S. Bowns, *Sanitary Sewer Evaluation Surveys: Why and How (Part 1)*, in *Trenchless Technology*. 2005. p. 48-56.
22. Carter&Burgess, *In the Public Interest: GASB 34/35*, in *Carter & Burgess's Quarterly*. 2002.
23. McLendon, R. *Florida Culverts & Pipe Advisory Group*. 2006 [cited 2/19/2006]; Online: <http://www.dot.state.fl.us/rddesign/dr/Advisory-Groups.htm>.
24. AZDOT, *Corrugated High Density Polyethylene Plastic Pipe General Requirements*, Highways, Roads, and Design, Editors. 2005, AZDOT.
25. WRc, *Sewers for Adoption*. 2006: WRc Publications.
26. CleanFlowSystems (2006) *Latest News*. [cited 12/03/2006]; Online: <http://www.cleanflowsystems.com/LatestNews.html>.
27. ASTM, *Standard Practice for Rehabilitation of Existing Pipelines and Conduits by the Inversion and Curing of a Resin-Impregnated Tube*. 2003, American Society for Testing Materials.

28. Gumbel, J. "New Approach to Design of Circular Liner Pipe to Resist External Hydrostatic Pressure." in *Pipelines 2001*. 2001. San Diego, California, USA: ASCE.
29. WRc, *Cleanflow Systems Ltd: WRc Approved*. 2005. p. 39.
30. Bennet, D. and L. Corkill. "CCTV in the United States." in *North American Society for Trenchless Technology (NASTT), NO-DIG*. 2006. Nashville, Tennessee, USA.
31. Kirkham, R., P. Kearney, and K. Rogers, "PIRAT-a System for Quantitative Sewer Pipe Assessment." *The International Journal of Robotics Research*, 2000. p. 1033-1053.
32. Wirahadikusumah, R., D. Abraham, and T. Iseley, "Assessment Technologies for Sewer System Rehabilitation." *Automation in Construction*, 1998. p. 259-270.
33. Eiswirth, M., C. Heske, and H. Hotzl. "Pipe Defect Characterisation by Multi-Sensor Systems." in *International No-Dig*. 2000. Perth, Australia.
34. Xu, K., A. Luxmoore, and T. Davies, "Sewer Pipe Deformation Assessment by Image Analysis of Video Surveys." *Pattern Recognition*, 1998. p. 169-180.
35. Henry, R. and A. Luxmoore, "A Pipe-Profiling Adapter for CCTV Inspection Cameras: Development of a Pipe-Profiling Instrument." *Measurement Science & Technology*, 1996. p. 495-504.
36. CEITEC-CERF, *Evaluation of Sset: The Sewer Scanner & Evaluation Technology*. 2001, Civil Engineering Research Foundation.
37. Pantsar, T. and J. Korkealaakso. "Recovery of the 3-D Structure of a Sewer Pipeline Using Computer Vision." in *No-Dig*. 2002. Montreal, Canada.
38. Gokhale, S., J. Graham, and S. Bowns, *Sanitary Sewer Evaluation Surveys: Why and How? (Part 2)*, in *Trenchless Technology*. 2005. p. 38-42.
39. Hunger, W. "Panoramo a New Step Forward in Optical Sewer Inspection." in *International Society of Trenchless Technology (ISTT) NO-DIG 2002*. 2002. Montreal, Canada.
40. IBAK (2006) *Panoramo 3-D Spherical Opto-Scanner System*. RapidView Inspection Systems
41. Graham, J. "Rehabilitation of Large Concrete Sewer Interceptors with the Aid of Laser Profiling and Other Investigative and Analytical Techniques." in *North American Society of Trenchless Technology (NASTT) NO-DIG*. 2006. Nashville, Tennessee, USA.

42. Optical Metrology Centre. *OMC Project Description - Sewer Profiling*. 2006 [cited 12/19/2006]; Online: [http://www.optical-metrology-centre.com/Downloads/Projects/Project\\_Description-Sewer\\_Profiling.pdf](http://www.optical-metrology-centre.com/Downloads/Projects/Project_Description-Sewer_Profiling.pdf).
43. Howard, B. and G. Brown. "Novel Measurement Techniques for Assessment of Geometrical Variations in the Reeling Process." in *Deep Offshore Technology*. 2003. Marseille, France
44. Clarke, T., *The Development of an Optical Triangulation Pipe Profiling Instrument*, in *Optical 3-D Measurement Techniques*. 1995, Wichmann. p. 331-340.
45. Gooch, R., and T. Ellis. "A Semi-Autonomous Sewer Surveillance and Inspection Vehicle." in *Proc IEEE Intelligent Vehicles*. 1996. Japan.
46. Clarke, T., *A Review of Tunnel Profiling Methods*. 1996, Optical Metrology Centre.
47. Lightman, A., *Sewer Assessment in Fort Worth, Texas*, in *Trenchless Technology*. 2006. p. 32-34.
48. RedZone-Robotics. *Responder Robotic Platform Laser Sensor*. 2006 [cited 12/20/2006]; Online: [http://www.redzone.com/downloads/rzr\\_dfs-laser.pdf](http://www.redzone.com/downloads/rzr_dfs-laser.pdf).
49. Tsubouchi, T., Y. Kawaguchi, and S. Takaki. "A Straight Pipe Observation from the inside by Laser Spot Array and a TV Camera. 2000. Takamatsu: Institute of Electrical and Electronics Engineers, Inc.
50. Kirkham, R., P. Kearney, and K. Rogers. "PIRAT-A System for Quantitative Sewer Assessment." in *International Conference of Field and Service Robotics*. 1999. Pittsburg, PA, USA.
51. Kirkham, R. (2006) *PIRAT Sewer Inspection System*. Machine Vision-CSIRO Manufacturing & Infrastructure Technology,
52. Hibino, Y., T. Nomura, and S. Ohta, "Laser Scanner for Tunnel Inspections." *International Water Power and Dam Construction*, 1994. p. 34-36.
53. Pan, X., T. Ellis, and T. Clarke, *Robust Tracking of Circular Features*, in *Proceedings of the 6th British Conference on Machine Vision (Vol. 2)*. 1995, BMVA Press: Birmingham, United Kingdom.
54. Hartrumpf, M. and R. Munser, "Optical Three-Dimensional Measurements by Radially Symmetric Structured Light Projection." *Applied Optics*, 1997. p. 2923.
55. Pridmore, T., D. Cooper, and N. Taylor, "Estimating Camera Orientation from Vanishing Point Location During Sewer Surveys." *Automation in Construction*, 1997. p. 407-419.

56. Cooper, D., T. Pridmore, and N. Taylor, "Towards the Recovery of Extrinsic Camera Parameters from Video Records of Sewer Surveys." *Machine Vision and Applications*, 1998. p. 53-63.
57. Cooper, D., T. Pridmore, and N. Taylor, "Assessment of a Camera Pose Algorithm Using Images of Brick Sewers." *Automation in Construction*, 2001. p. 527-540.
58. Kampfer, W., R. Bartzke, and W. Ziehl. "Flexible Mobile Robot System for Smart Optical Pipe Inspection. 1998. San Antonio, Texas, USA: The International Society for Optical Engineering.
59. Kuntze, H. and H. Haffner. "Experiences with the Development of a Robot for Smart Multisensoric Pipe Inspection. 1998. Leuven, Belgium: IEEE, Piscataway, New Jersey, USA.
60. Eiswirth, M., C. Frey, and J. Herbst. "Sewer Assessment by Multi-Sensor Systems." in *IWA 2. World Water Conference*. 2001. Berlin, Germany.
61. Zhang, W. and B. Zhuang, "Non-Contact Laser Inspection for the Inner Wall Surface of a Pipe." *Measurement Science & Technology*, 1998. p. 1380-1387.
62. Berns, K. and K. Scholl. "A Mechatronic Concept for a Sewer Inspection Robot." in *International Conference on Advanced Intelligent Mechatronics*. 1999. Atlanta, GA, USA.
63. Kolesnik, M. and G. Baratoff. "Online Distance Recovery for a Sewer Inspection Robot. 2000.
64. Adria, O. and J. Hertzberg, "Dynamic Replanning in Uncertain Environments for a Sewer Inspection Robot." *International Journal of Advanced Robotic Systems*, 2004. p. 33-38.
65. Kolesnik, M., "View-Based Method for Relative Orientation in the Pipe." *Proceedings of SPIE - The International Society for Optical Engineering*, 1999. p. 70-78.
66. Kolesnik, M. and G. Baratoff. "3-D Interpretation of Sewer Circular Structures. 2000. San Francisco, CA, USA: Institute of Electrical and Electronics Engineers, Inc., Piscataway, NJ, USA.
67. Roberts, R., "Laser Profilometry for Tube Inspection." *The Online Journal of Nondestructive Testing & Ultrasonics*, 1999.
68. Duran, O., K. Althofer, and L.D. Seneviratne, "Pipe Inspection Using a Laser-Based Transducer and Automated Analysis Techniques." *IEEE/ASME Transactions on Mechatronics*, 2003. p. 401-409.

69. Duran, O., K. Althoefer, and L. Seneviratne. "Automated Sewer Inspection Using Image Processing and a Neural Classifier. 2002. Honolulu, Hawaii: Institute of Electrical and Electronics Engineers, Inc.
70. Gomez, F., K. Althoefer, and L.D. Seneviratne. "An Ultrasonic Profiling Method for Sewer Inspection. 2004. New Orleans, Louisiana, USA: Institute of Electrical and Electronics Engineers Inc., Piscataway, USA.
71. Price, T. "Inspecting Buried Plastic Pipe Using a Rotating Sonic Caliper." in *2nd International Conference on Advances in Underground Pipeline Engineering*. 1995.
72. Weisstein, E. *Inverse Trigonometric Functions*. 2006 [cited 6/12/2006]; Online: <http://mathworld.wolfram.com/InverseTrigonometricFunctions.html>
73. Mathsoft<sup>(R)</sup>, *Mathcad 12<sup>(R)</sup>*. 2004, Mathsoft<sup>(R)</sup> Engineering & Education.
74. Boresi, A., Schmidt, R., Sidebottom, O., *Advanced Mechanics of Materials*. 5th Ed. ed. 1993, New York: John Wiley & Sons, Inc.
75. Swanbom, M., *Evaluation of the Effects of Geometric Parameters on the Accuracy of Structured Light Pipe-Profiling Instruments*. 2007, Ph.D. dissertation, Louisiana Tech University.